AD-A275 237

TGAL-93-7

# STATISTICAL CHARACTERIZATION OF RUGGED PROPAGATION PATHS WITH APPLICATION TO Rg SCATTERING STUDY

Rong-Song Jih

Teledyne Geotech Alexandria Laboratory
314 Montgomery Street
Alexandria, Virginia 22314-1581

NOVEMBER 1993

| | |
|---|---|
| SEMI-ANNUL REPORT: | No.4 (20 September 1993 - 5 November 1993) |
| ARPA ORDER NO.: | 6731 |
| PROJECT TITLE: | Statistical Study of Soviet Explosion Magnitudes and Yields Using Heavily Censored Historical Yields, Soviet-released Analog Waveforms, and Digital Data Recorded at Modern Arrays |
| CONTRACT NO.: | F29601-91-C-DB23 |

Approved for Public Release; Distribution Unlimited

Prepared for:
UNITED STATES AIR FORCE
AIR FORCE MATERIEL COMMAND
PHILLIPS LABORATORY (PL)
KIRTLAND AFB, NM 87117-6008

Monitored by:
ADVANCED RESEARCH PROJECTS AGENCY
NUCLEAR MONITORING RESEARCH OFFICE
3701 NORTH FAIRFAX DRIVE
ARLINGTON, VA 22203-1714

DTIC
ELECTE
FEB 02 1994
S B D

The views and conclusions contained in this report are those of the author and should not be interpreted as representing the official policies, either expressed or implied, of the Advanced Research Projects Agency or the U.S. Government.

94-03129

94 1 31 223

# REPORT DOCUMENTATION PAGE

Form Approved
OMB No. 0704-0188

Public reporting burden for this collection of information is estimated to average 1 hour per response, including the time for reviewing instructions, searching existing data sources, gathering and maintaining the data needed, and completing and reviewing the collection of information. Send comments regarding this burden estimate or any other aspect of this collection of information, including suggestions for reducing this burden, to Washington Headquarters Services, Directorate for Information Operations and Reports, 1215 Jefferson Davis Highway, Suite 1204, Arlington, VA 22202-4302, and to the Office of Management and Budget, Paperwork Reduction Project (0704-0188), Washington, DC 20503.

| 1. AGENCY USE ONLY (Leave blank) | 2. REPORT DATE | 3. REPORT TYPE AND DATES COVERED |
|---|---|---|
| | 5 November 1993 | Semi-Annul Report, 20 Sept. 1993 - 5 Nov. 1993 |

**4. TITLE AND SUBTITLE**

Statistical Characterization of Rugged Propagation Paths with Application to Rg Scattering Study

**5. FUNDING NUMBERS**

Contract F29601-91-C-DB23

PE 62101F
PR 7600
TA 09
WU AT

**6. AUTHOR(S)**

R.-S. Jih

**7. PERFORMING ORGANIZATION NAME(S) AND ADDRESS(ES)**

Teledyne Geotech Alexandria Laboratory
314 Montgomery Street
Alexandria, VA 22314-1581

**8. PERFORMING ORGANIZATION REPORT NUMBER**

TGAL-93-07

**9. SPONSORING/MONITORING AGENCY NAME(S) AND ADDRESS(ES)**

ARPA/NMRO (Attn. Dr. Alan Ryall, Jr.)
3701 North Fairfax Drive
Arlington, VA 22203-1714

**10. SPONSORING/MONITORING AGENCY REPORT NUMBER**

**11. SUPPLEMENTARY NOTES**

**12a. DISTRIBUTION/AVAILABILITY STATEMENT**

Approved for Public Release; Distributic Unlimited

**12b. DISTRIBUTION CODE**

**13. ABSTRACT** *(Maximum 200 words)*

Motivated by many observations of correlation between the free-surface topography and the coda generation at teleseismic and regional distances, seven simple statistics have been tested whether they can fully characterize the roughness of an arbitrary rugged free-surface topography. Based on 2-dimensional finite-difference simulations, the normalized arc length and *Durbin-Watson number* are identified as the best and the poorest, respectively, roughness measures, in terms of correlating with the propagation behavior of $R_g$. The numerical experiments show that rougher topography causes stronger attenuation (as expected), that reflection is an efficient process, and that the bulk of the energy which is not transmitted across the topography is either converted to body waves or reflected back. The scattered *P* and *S* waves are radiated as coda to teleseismic distances and some *P–SV* energy ccould be trapped in the crustal waveguide. The scattered body waves appear to radiate from the changes in slope and to first order can be visualized as from point diffractors along the rugged free-surface. $R_g$-to-*S* conversion is more efficient than that of $R_g$-to-*P*. The spatial *Q* values associated with rough topographic profiles range from 15 to 80, which are in excellent agreement with $Q_\beta$ of the uppermost crust in many places of the world. The attenuation coefficient, $\gamma$, and the scattering loss can be asymptotically represented as linear functions of the roughness parameters. This work offers a promising approach to quantify effects of scattering by topography and heterogeneity upon other regional phases.

**14. SUBJECT TERMS**

$R_g$, Topography, Wave Propagation, Scattering, Roughness, $L_g$, Path Effects, Discrimination

**15. NUMBER OF PAGES**

**16. PRICE CODE**

| 17. SECURITY CLASSIFICATION OF REPORT | 18. SECURITY CLASSIFICATION OF THIS PAGE | 19. SECURITY CLASSIFICATION OF ABSTRACT | 20. LIMITATION OF ABSTRACT |
|---|---|---|---|
| Unclassified | Unclassified | Unclassified | UL |

(THIS PAGE INTENTIONALLY LEFT BLANK)

# SUMMARY

The primary objective of this project is to develop and apply improved statistical methodologies for nuclear monitoring. During the past two years, our major efforts have been
[A] Measure the teleseismic *P*-wave magnitudes of historical Soviet explosions as well as explosions from other foreign test sites recorded at the optimal distance range from 20° to 95°.
[B] Perform various statistical analyses of the raw mb and obtain the optimal network mb values. Conduct the maximum-likelihood magnitude-yield regressions and analyze the source-depth scaling relationship.
[C] Conduct a theoretical study to investigate relevant issues. Improve and document the statistical as well as the forward-modeling tools currently in use.

This semi-annual report summarizes our results obtained under Task [C] during the period September 20, 1993, through November 5, 1993.

An accurate prediction of the regional phases due to explosion sources in areas of high proliferation concern requires a decent understanding of the attenuation/scattering mechanisms along the propagation paths. Motivated by many observations of correlation between the free-surface topography and the coda generation at teleseismic and regional distances, seven simple statistics have been presented and analyzed in this study to test whether they can fully characterize the roughness of an arbitrary rugged free-surface topography. The definitions of these parameters are very natural, and some of parameters might be suitable to quantify the roughness of realistic profiles. The normalized arc length and *Durbin-Watson number (von Neumann ratio)* are identified as the best and the poorest, respectively, roughness measures, in terms of correlating with the propagation behavior of $R_g$ (see Figures 95-102 for the regressions). 2-dimensional finite-difference simulations are then conducted to investigate short-period Rayleigh wave scattering by these 27 topographic profiles. The numerical experiments show that rougher topography causes stronger attenuation (as expected), that reflection is an efficient process, and that the bulk of the energy which is not transmitted across the topography is either converted to body waves or reflected back. The scattered *P* and *S* waves are radiated as coda to teleseismic distances and some *P–SV* energy is trapped in the crustal waveguide as $P_g$, Sg, and $L_g$. The body waves appear to radiate from the changes in slope and to first order can be visualized as from point diffractors along the rugged free-surface. For most models tested in this study, the $R_g$-to-*S* conversion is more efficient than that of $R_g$-to-*P* (see Figures 103-129). Particle motion plots of the scattered bodywaves can help to illustrate this point too (see Figure 130-156). The displacement synthetics of the scattered bodywaves, which makes the synthetics can be compared easily. This approach is more convenient than another one which presents the scattered wavefield in strain units. The spatial *Q* values associated with rough topographic profiles, inferred from the logarithm of the transmitted power spectrum, range from 15 to 80, which are in excellent agreement with the $Q_\beta$ of the uppermost crust in many places of the world. Regression results also suggest that both the attenuation coefficient, $\gamma$, and the scattering loss can be represented as linear functions of the roughness parameters. This work offers a promising approach to quantify effects of scattering by topography and heterogeneity upon other regional phases.

(THIS PAGE INTENTIONALLY LEFT BLANK)

# Table of Contents


Summary ..... iii

1. Introduction ..... 1

2. Roughness Statistics ..... 4

    2.1 Generation of Random Topography ..... 4

    2.2 Definition of Various Roughness Measures ..... 4

    2.3 Correlation between Various Roughness Measures ..... 7

3. Numerical Experiments ..... 8

    3.1 Finite-difference Scheme ..... 8

    3.2 Half-space Experiment ..... 9

    3.3 Experiments with Rough Topography ..... 9

    3.4 Scattered Body Waves ..... 13

4. Discussion and Conclusions ..... 14

5. Acknowledgement ..... 16

6. References ..... 16

7. Figure Captions ..... 21

Distribution List ..... 179



DTIC QUALITY INSPECTED 3

Accession For
NTIS GRA&I
DTIC TAB
Unannounced
Justification
By
Distribution/
Availability Codes
Dist | Avail and/or Special
A-1

(THIS PAGE INTENTIONALLY LEFT BLANK)

## 1. INTRODUCTION

The problem of short-period fundamental-mode Rayleigh waves (or $R_g$) scattered by topography is important and interesting for many reasons. A significant fraction of the elastic energy generated by a shallow explosion is contained in short-period Rayleigh waves. These short-period Rayleigh waves are the largest phase on the near-source seismogram. However, very often they are attenuated rather rapidly with spatial $Q$'s at 1 Hz in the range of 20 to 200. Such attenuation can be due to intrinsic shear attenuation in the near surface, or it can be accomplished by scattering from shallow heterogeneity and topography. If the energy is scattered then it must be observed as coda in the near-source, regional, and/or teleseismic seismogram.

The scattering of short-period Rayleigh waves by topography has been proposed as a mechanism for the generation of teleseismic $P$ coda by Greenfield (1971). Gupta and Blandford (1987) (and Gupta and Wagner, 1992) propose that such $P$ coda may be diagnostic of the near source medium. The ability of using teleseismic complexity for discriminating explosions from earthquakes can be accounted for by an explanation that the emergent earthquake teleseismic coda is comprised of $pP$ and of $S$-to-$P$ conversions at relatively sharp interfaces, whereas the emergent explosion coda is comprised of $R_g$-to-$P$ conversions. Thus the coda in emergent explosion signals would have more of a "rolling" character which can be distinguished from the "impulsive" coda of emergent earthquakes (Blandford, 1993). Adushkin *et al.* (1990) find $R_g$ from Soviet's Semipalatinsk nuclear test site a very stable yield estimator. With the focus of nuclear monitoring research moving from the yield estimation to seismic event identification, an assessment needs to be made of the maximum range at which $R_g$ could be used to discriminate small events in various geologic/tectonic environments (DARPA, 1992). $P$ coda observed at arrays is often partly composed of Rayleigh waves generated by $P$ waves steeply incident upon shallow heterogeneity or topography. Key (1967 and 1968) identified such Rayleigh waves within the $P$ coda at the EKA array (Eskdalemuir, Scotland) for certain azimuths of arrival. Dainty (1986) shows by use of frequency-wavenumber analysis that $P$ coda at the small NORESS array (southern Norway) is often composed of fundamental short-period Rayleigh waves. Both the coherency of such coda and its persistence are closely related to the scattering of the Rayleigh waves by topography and shallow heterogeneity. Aki and Chouet (1975) proposed three simple models for the generation and propagation of short-period coda from local earthquakes. They considered the case of scattered surface waves as well as scattered body waves. Although the coda of local earthquakes appears to be dominated by $S$ waves, it is clear that trapped modes and surface waves are also present (Phillips and Aki, 1986). A portion of the regional $L_g$ phase and its coda is composed of fundamental and higher mode Rayleigh waves trapped in the crustal waveguide. Der *et al.* (1984) propose that a significant portion of the $L_g$ coda is composed of short-period fundamental Rayleigh waves that concentrate energy near the surface and are multiply scattered, contributing to the long $L_g$ coda observed on regional seismograms. Baumgardt (1990) proposes that $L_g$ from Eastern Kazakh incident upon the Urals produces observable teleseismic $P$ coda at NORSAR. All of these problems have in common a need to estimate the effects of scattering on short-period surface waves due to shallow heterogeneity and topography.

Topographic scattering through a right-angle step was addressed by deBremaecker (1958) and continues as a topic of interest. Numerous workers have examined the incident Rayleigh or Love wave upon welded quarter spaces (see for example, Mal and Knopoff, 1965; McGarr and Alsop, 1967; Drake, 1972; Munasinghe and Farnell, 1973; Tuan and Li, 1974; Martel *et al.*, 1977; Sabina and Willis, 1977; Chen and Alsop, 1979; Fuyuki and Matsumoto, 1980; Drake and Bolt, 1980; Momoi, 1985; Fuyuki and Nakano, 1984; Wojcik and Mak, 1985; and Nakano *et al.*, 1988). Ultrasonic modeling was used by Bullit and Toksoz (1985) and Toksoz *et al.* (1986) to examine the obliquely incident Rayleigh wave transmission and reflection by sloping topography.

Most previous research concerned with the scattering of Rayleigh waves has dealt with the simplest geometric configurations (quarter-space, three-quarter space, a trench or a vertical step) where the boundaries are always parallel or perpendicular to the grid axis. The present study concentrates on more general topographic profiles, as a follow-up of our previous study summarized in McLaughlin and Jih (1986 and 1987). Linear Finite-Difference (LFD) modeling is chosen simply out of convenience. The method has the advantages that the solution contains all conversions (*P–SV*, *SV–P*) and all orders of multiple scattering. We use the 2nd-order formulation of Kelley *et al.* (1976) with absorbing boundary conditions described by Clayton and Engquist (1977) and 1st-order free-surface boundary conditions for topographic surfaces described by Jih *et al.* (1988) and Jih (1993a). The method permits examination of fairly general 2-D models. Surface waves are introduced as initial conditions within the half-space grid. There is now a considerable body of work covering many aspects of scattering using 2-D LFD methods.

McLaughlin and Jih (1987) examined the interaction of incident Rayleigh waves upon a 2-D shallow heterogeneous layer of various thicknesses, scale lengths, and rms velocity fluctuations embedded in a homogeneous half space using 2-dimensional LFD. In this paper, we explore the stability of planar Rayleigh waves incident upon 2-D topography using the same method of analysis. The goal is to determine some basic quantities such as scattering strength, conversion efficiency, and backscattering strength of the topographic relief. These quantities are needed in order to compose models for coda observed near the surface of the Earth. Although the present study tackles the same problem as was treated in our previous work (McLaughlin and Jih; 1986) (hereafter [1]), there are several fundamental improvements. No clear (*i.e.*, quantitative) relationship between the roughness measures and the propagation characteristics was found in [1], because the rough topographic profiles used in [1] did not cover a wide range of profile types. The scattered body waves were described in non-directional strain in [1], which made the synthetics more difficult for direct comparison. In the present work, more roughness measures are tested with a suite of realistic profiles. Furthermore, the scattered body waves are presented in the same displacement unit, with direction of each ray clearly identified.

We first examine the problem of transmission and the partitioning of energy by the scattering process. It is demonstrated as expected that rougher topography produces larger attenuation. Reflection (backscattering) is observed to be an efficient process for all cases examined. In this way the rough topography is characterized by a spatial $Q$ and several other roughness statistics. We use the converted body wave field at depth in the half-space as a measure of the simulated far-field $P$ and S coda.

Attenuation of the short-period Rayleigh wave is found to be strong by moderately rough topography, and Rayleigh-to-body wave conversion is seen to dominate the attenuation process. Examination of the converted body wave field in the half-space leads us to conclude that a significant fraction of the converted *SV* energy will be trapped in the crust as $L_g$.

## 2. ROUGHNESS STATISTICS

### 2.1 Generation of Random Topography

In this study, it is assumed that the rough topography can be approximated by level elevations separated by sections of 45° slope. Topographic profiles are generated with a random number generator which produces a Markov sequence of values 0, 1, and -1, according to an arbitrarily assigned probability of the "state" 1, hereafter denoted as Pr[1]. We assume $0 < Pr[-1] = Pr[1] < 0.5$ and $Pr[0] = 1 - Pr[1] - Pr[-1]$. The sequence of 0, 1 and -1 is regarded as the successive elevation change in the topography. That is, the integral of this Markov sequence represents a profile suitable for forward modeling experiments. Larger Pr[1] would cause more frequent elevation changes in the resulting topographic profile, and hence it is an indication of rougher topography. In this study, both smooth and extremely rugged topography are examined, with Pr[1] ranging from 5% to 35%. Initially, the values 1 and -1 are assumed to have the same probability. Nevertheless, the selection of the current "state" of the Markov chain is governed not only by the preset probability but also by the previous state. For instance, given a previous value of 1, the current value can only be 0 or 1. This Markov condition is imposed to make sure that the topography, as a piecewise-linear polygon, has at least two subsegments of the same slope in each of its linear segment, and to prevent the occurrence of sudden changes such as from 1 to -1 and *vice versa*.

27 rough topographic profiles thus generated were inserted into the grid with flat ground concatenated on both sides. Figure 1 through 9 show the rugged profile, H(x), of the 27 models on the left, log-amplitude wavenumber spectra of the topography in the center, and several corresponding roughness statistics (which are to be defined in the following section) listed on the right of topographic profiles numbered 11 through 73. Only the rugged portion of each profile is shown. In all these models, the rugged portion has a lateral span, X, approximately 30 km.

### 2.2 Definition of Various Roughness Measures

In searching for quantitative measures to characterize the roughness of a topographic profile, one would expect to seek parameters which are easy to compute once the profile is digitized. Note that each discretized profile is just a time series of equal spatial spacing in the lateral direction, and therefore many techniques used in time series analysis might be suitable for our need. Several statistics which appear to be natural candidates of the roughness measure are defined and tested in this study.

The *"normalized total variation"*, $\Omega_1$, is defined as $\Omega_1 \equiv \sum|H_i - H_{i-1}|/X$ where $H_i$ is the elevation (in km) at the ith column of the nontrivial portion of the topography. This statistic reflects the idea that in a smooth time series the differences between successive points are all small, and hence the numerator will be small. The denominator is simply a scaling factor. $\Omega_1$ is nothing but the *"normalized* $L^1$ *norm"* of the elevation change. This parameter turns out to be equivalent to the total *"probability of elevation change"* of the topographic profile. Another roughness measure, which is very similar to $\Omega_1$, is the *"normalized* $L^2$ *norm"* of the elevation change, $\Omega_2$, defined as $\sqrt{\sum(H_i - H_{i-1})^2}/X$. When each elevation change

is limited to have at most one unit step (as in all the examples used in this study), $\Omega_2$ is equivalent to $\Omega_1$ (up to a constant). This is not true in the more general case, and hence both quantities ought to be tested. The *"Root-mean-squared elevation"*, $\Omega_3$, is defined as $\sqrt{\sum(H_i-\bar{H})^2 / N}$ with $\bar{H}$ the average elevation of the topography, and N the number of subintervals. $\Omega_4 \equiv \sum(H_i-H_{i-1})^2/\sum(H_i-\bar{H})^2$, is also called the *"Durbin-Watson statistic"* or the *"von Neumann ratio"* (*cf*. Bloomfield, 1975). The peak wavenumber spectrum, K(0), is denoted as $\Omega_5$. The *"number of slope changes per unit length"* (*i.e.*, the average number of corners per km) is denoted as $\Omega_6$. Note that $\Omega_6$ is directly proportional to the *"probability of slope change"*, whereas $\Omega_1$ reflects the *"probability of elevation change"*. In calculus terms, $\Omega_1$ and $\Omega_6$ are closely related to the first and second spatial derivatives, respectively, of the topographic profile, H. $\Omega_5$, the peak wavenumber spectrum K(0), is a measure of the mean elevation, $\bar{H}$, whereas $\Omega_3$ is a measure of the deviation from the mean. The arc length (normalized by the total span), $\Omega_7$, is computed as $\sum\sqrt{[\Delta X^2 + (H_i-H_{i-1})^2]}/X$ where $\Delta X$ is the spacing (in km) in the horizontal direction. For a flat profile, $\Omega_7$ equals to 1. There exist simple relationships among some of the roughness measures. For instance,

$$\Omega_2 = \sqrt{\Delta Z \cdot \Omega_1 / X}\ ; \text{ and } \Omega_4 = N \cdot (\Delta X \cdot \Omega_2 / \Omega_3)^2.$$

Table 1 lists various roughness measures of 27 profiles numbered from 11 to 73 with increasing Pr[1]. In each case, the random number generator is initialized with the seed number being the truncated system clock time at the time the profile was generated. These seed numbers are also included in Table 1, and hence all the profiles can be duplicated on SUN4 computers. The preset probability of state 1 varies from 5% (models 11 through 13) to 35% (models 71 through 73). Larger Pr[1] yields more frequent recurrence of states 1 and -1, which means more elevation variations and hence a rougher topography. Intuitively any arbitrary sequence of 0, 1, -1 should suffice to generate a corresponding random profile. In our LFD calculations, however, the profile needs to be sampled well enough so that each segment consists of at least two subintervals with the same slope. As a result, the "actual" probability of states 1 and -1 is slightly smaller than that of the input. It is interesting to note that $\Omega_1$ happens to represent the "actual" probability of states 1 and -1 combined, which is slightly smaller than twice that of Pr[1]. Most statistics as defined above show an increasing trend with the increasing Pr[1], except $\Omega_4$ which seems to exhibit no clear pattern at all.

| Table 1. Roughness Statistics of 27 Topographic Profiles | | | | | | | | | |
|---|---|---|---|---|---|---|---|---|---|
| Model | $\Omega_1$ | $\Omega_2$ | $\Omega_3$ | $\Omega_4$ | $\Omega_5$ | $\Omega_6$ | $\Omega_7$ | Pr[1] | Seed |
| 11 | 0.091 | 0.0178 | 0.215 | 0.0198 | 0.240 | 0.839 | 1.038 | 0.050 | 22887 |
| 12 | 0.097 | 0.0186 | 0.487 | 0.0041 | 0.511 | 1.004 | 1.040 | 0.050 | 22892 |
| 13 | 0.097 | 0.0190 | 0.218 | 0.0203 | 0.260 | 0.967 | 1.040 | 0.050 | 85995 |
| 14 | 0.146 | 0.0225 | 0.234 | 0.0266 | 0.266 | 1.389 | 1.060 | 0.070 | 91333 |
| 15 | 0.144 | 0.0228 | 0.209 | 0.0329 | 0.310 | 1.439 | 1.060 | 0.070 | 91350 |
| 16 | 0.127 | 0.0218 | 0.265 | 0.0181 | 0.209 | 1.194 | 1.053 | 0.070 | 91285 |
| 21 | 0.180 | 0.0245 | 0.686 | 0.0038 | 0.528 | 1.600 | 1.075 | 0.100 | 93337 |
| 22 | 0.182 | 0.0248 | 0.557 | 0.0059 | 0.638 | 1.757 | 1.076 | 0.100 | 93347 |
| 23 | 0.150 | 0.0231 | 0.435 | 0.0079 | 0.370 | 1.429 | 1.062 | 0.100 | 93356 |
| 31 | 0.310 | 0.0323 | 1.329 | 0.0018 | 0.981 | 2.357 | 1.128 | 0.150 | 748546615 |
| 32 | 0.230 | 0.0283 | 0.234 | 0.0421 | 0.317 | 1.742 | 1.095 | 0.150 | 20333 |
| 33 | 0.233 | 0.0282 | 0.408 | 0.0140 | 0.303 | 2.192 | 1.096 | 0.150 | 86016 |
| 41 | 0.283 | 0.0309 | 0.756 | 0.0049 | 0.599 | 2.357 | 1.117 | 0.200 | 93397 |
| 42 | 0.298 | 0.0318 | 0.878 | 0.0039 | 0.751 | 2.508 | 1.124 | 0.200 | 93407 |
| 43 | 0.316 | 0.0324 | 0.751 | 0.0056 | 0.819 | 2.392 | 1.131 | 0.200 | 12345 |
| 51 | 0.401 | 0.0366 | 0.469 | 0.0183 | 0.584 | 2.609 | 1.166 | 0.250 | 21691 |
| 52 | 0.361 | 0.0348 | 0.553 | 0.0118 | 0.549 | 2.742 | 1.150 | 0.250 | 21696 |
| 53 | 0.399 | 0.0364 | 0.506 | 0.0156 | 0.633 | 2.591 | 1.165 | 0.250 | 86037 |
| 61 | 0.478 | 0.0400 | 1.003 | 0.0048 | 1.741 | 2.676 | 1.198 | 0.300 | 93459 |
| 62 | 0.437 | 0.0386 | 1.160 | 0.0032 | 1.153 | 2.662 | 1.181 | 0.300 | 93468 |
| 63 | 0.438 | 0.0383 | 0.745 | 0.0079 | 1.112 | 2.274 | 1.181 | 0.300 | 93479 |
| 64 | 0.477 | 0.0400 | 0.539 | 0.0164 | 0.663 | 2.685 | 1.197 | 0.320 | 55473 |
| 65 | 0.483 | 0.0405 | 0.934 | 0.0055 | 1.207 | 2.585 | 1.200 | 0.320 | 55499 |
| 66 | 0.512 | 0.0421 | 0.604 | 0.0140 | 0.795 | 2.699 | 1.212 | 0.320 | 55446 |
| 71 | 0.502 | 0.0410 | 0.538 | 0.0174 | 0.749 | 2.475 | 1.208 | 0.350 | 22192 |
| 72 | 0.595 | 0.0444 | 0.728 | 0.0112 | 0.777 | 1.993 | 1.246 | 0.350 | 31087 |
| 73 | 0.555 | 0.0431 | 0.863 | 0.0075 | 1.129 | 2.341 | 1.230 | 0.350 | 86061 |

### 2.3 Correlation Between Various Roughness Measures

The correlation coefficients between various roughness measures are listed in Table 2. As would be expected from Table 1, almost all of the parameters are positively correlated with each other with the exception of $\Omega_4$. Thus it may be anticipated that, except for $\Omega_4$, a profile which is "rough" in one sense would probably be rough in another sense as well. The question is, then, which parameter can optimally characterize the wave propagation phenomenon. That is, which one of the roughness parameters is the best statistic to use in predicting the amplitude decay when some previously uncalibrated rugged paths are involved. The answer to such a question could well be dependent on the seismic phases of interest, since different seismic phase might interact with the rough topography differently. Throughout this study, $R_g$ wave packet is injected into the model as the incident source, and the transmitted, reflected and the scattered synthetics are then analyzed. The ultimate output of this exercise would be some calibration curves which may be suitable for predicting the $R_g$ amplitudes, given an arbitrary rugged profile. The same procedure should be repeated for other crustal phases to establish the associated relationship with the roughness measures, which will be addressed in the follow-up report.

Table 2.Correlation Coefficients Between Roughness Parameters

| | $\Omega_2$ | $\Omega_3$ | $\Omega_4$ | $\Omega_5$ | $\Omega_6$ | $\Omega_7$ | Pr[1] |
|---|---|---|---|---|---|---|---|
| $\Omega_1$ | 0.99 | 0.58 | -0.27 | 0.73 | 0.82 | 1.00 | 0.99 |
| $\Omega_2$ | ___ | 0.60 | -0.27 | 0.73 | 0.87 | 0.99 | 0.99 |
| $\Omega_3$ | ___ | ___ | -0.76 | 0.84 | 0.64 | 0.58 | 0.55 |
| $\Omega_4$ | ___ | ___ | ___ | -0.58 | -0.35 | -0.27 | -0.27 |
| $\Omega_5$ | ___ | ___ | ___ | ___ | 0.67 | 0.73 | 0.72 |
| $\Omega_6$ | ___ | ___ | ___ | ___ | ___ | 0.82 | 0.84 |
| $\Omega_7$ | ___ | ___ | ___ | ___ | ___ | ___ | 0.99 |

## 3. NUMERICAL EXPERIMENTS

### 3.1 Finite-difference Scheme

The 2-D linear finite-difference (LFD) scheme popularized by Kelly *et al.* (1976) is used with the Clayton and Engquist (1977) (Emerman and Stephen, 1983) absorbing boundary conditions on both the sides and the bottom of the grid. Even with the absorbing boundary conditions, the simulations are run with large enough grids such that for the duration of the simulations reflections from the sides do not seriously contaminate the results. The free-surface boundary conditions follow from the work of Jih *et al.* (1988) and Jih (1993a) which allows for the introduction of arbitrary polygonal topography into the wave propagation simulations and which has been applied by McLaughlin and Jih (1988) for the modeling of teleseismic *P* waves from explosive line sources under realistic topographic surfaces. These boundary conditions are extensions to those of Ilan (1975 and 1977). Recently a number of techniques have been pursued in an effort to improve the computational performance of LFD solutions to wave equations. These include variable grids, higher order schemes, or implicit rather than explicit methods. Jih *et al.* (1988) have found that none of these methods provide significant improvement over the traditional explicit second order centered LFD schemes described by Alterman, Boore, and Kelly when rough topographic profiles are used at the free surface.

In the present experiments, the medium has *P*– and *S*–wave velocities of 5.02 and 2.898 km/sec respectively, corresponding to a Poisson's ratio of 0.35 and a Rayleigh wave velocity of 2.665 km/sec. The formulation generating the incident pure Rayleigh wave packet is analogous to Boore (1970) or Munasinghe and Farnell (1973) which has been used extensively by Martel *et al.* (1977), Fuyuki and Matsumoto (1980), Fuyuki and Nakano (1984), Levander (1985), and McLaughlin and Jih (1986 and 1987). The initial waveform is the fundamental mode Rayleigh wave in the homogeneous half space with a Ricker wavelet shape. This method is superior to another approach which shakes several mesh points on the free surface or the grid edge to generate the incident Rayleigh wave, since the latter would excite undesirable body waves as well. The pure Rayleigh wave packet of Ricker-wavelet shape is particularly suitable for the numerical modeling study, since it is well localized in both the time and wavenumber spaces. To reduce the grid dispersion, we have oversampled the incident wave packet by choosing the dominant wavelength to be 3.2 km = 32 $\Delta X$, where $\Delta X$ =0.1 km is the grid spacing in the horizontal direction. The dominant wavenumber is 2.358 radians/km which corresponds to a wavelength of 2.665 km at 1Hz. Thus the energy of our incident $R_g$ wave packet is centered at 1 Hz.

The grids used in LFD simulations are 60 km in length and 50 km in depth, with a grid spacing of 0.1 km in both X and Z directions. The initial incident waveform, the reflected and the transmitted waveforms were then measured at free-surface "sensors". Transmission coefficients and the attenuation factor $Q(f)$ were then computed in the frequency domain. The useful bandwidth is limited to frequencies below 2.4 Hz due to the limitation of 2nd order LFD scheme. Although we quote dimensions in km and velocities in km/s, it is possible to scale these simulations to higher or lower frequencies as desired. As explained earlier, the LFD scheme must discretize the topography into well-sampled polygons, which is exactly the reason for adopting a Markov sequence rather than a white sequence.

Therefore the smallest scale length of the topography is always twice the horizontal grid spacing. The largest scale length is limited by the total span of the rugged profile used in the simulation.

### 3.2 Half-space Experiment

Experiments were first conducted to justify that, in the case of a homogeneous half-space, the grid dispersion only slightly modulates the spectra of the propagating Rayleigh wave. A particularly informative way to visualize wave propagation through the models is by using numerical Schlieren diagrams. These "snapshots" of the wavefield traveling through the grid are generated by saving the displacement (or strain) at each grid point for a given time step. Figure 10 shows the snapshots of the displacement field at time incidents of 4 seconds apart. Shading in each snapshot is proportional to $\sqrt{U^2 + W^2}$ where U and W are the displacement along the X and Z directions, respectively, of the grid. The darkness of the plot is normalized to the maximum in each frame. No significant attenuation of the Rayleigh wave could be measured for the half-space in the frequency band of interest (Figure 11).

### 3.3 Experiments with Rough Topography

Following this check, we conducted 27 simulations with the random topographic profiles listed in Table 1. Each simulation took 4000 time steps. As in the half-space case, Figures 12 through 38 show snapshots of the displacement field due to a Rayleigh wave incident upon various topographic profiles. Successive frames are separated by intervals of 4 seconds, and the incident Rayleigh wave always travels from left to right. In general, the diffraction pattern becomes much more complicated when the the topography is rougher. This is obvious in comparing Figure 13 (for model No.12) and Figure 32 (for model No.63), for instance. In all cases the corners act as point sources radiating converted body waves (mainly *S* wave).

Thirty sensors numbered from No.1 through No.30 are placed 2 km apart along the free surface to record the displacement. Figures 39 through 66 show the seismic section of the vertical component of each model with the maximum zero-to-peak amplitude shown on the right. The distance between each sensor and the "epicenter" of the initial Rayleigh wave packet is also shown. Smoother models tend to have longer reflected wave trains than do rougher models. Also, the peak amplitude of the transmitted signal, which is measured with trace No.29 of each model, drops significantly as the model becomes rougher. The reflected waves systematically consist of multiply reflected Rayleigh waves which last 22 seconds or longer, which is the time required for the $R_g$ packet to cross the whole profile and then bounce back. On the other hand, the transmitted synthetic is dominated by very few cycles of Rayleigh waves. In the following, these qualitative observations are further elaborated in a quantitative manner.

The power spectra of traces No.2 and No.29 of each model are measured to represent the reflected and transmitted signal. We define the Rayleigh wave energy transmission coefficient, T, as $T(f) = Power_{trans}(f)/Power_{inc}(f)$ where $Power_{inc}(f)$ is the power spectrum of the incident Rayleigh wave. The reflection coefficient, R, is defined in an analogous way: $R(f) = Power_{refl}(f)/Power_{inc}(f)$. Table 2 gives the statistics of all 27 topographic profiles used and the corresponding attenuation factor $Q$ at 1 Hz, which is the dominant frequency of the incident $R_g$ packet. Here the quality factor, $Q$, is computed

via $\gamma = Q^{-1}(f) = -\ln(T(f)) \cdot (V_R/2\pi fX)$ as in McLaughlin and Jih (1986 and 1987).

Table 3. Transmission/Reflection/Scattering Statistics

| Model | T(1Hz) | R(1Hz) | 1-T-R | Q(1Hz) | γ |
|---|---|---|---|---|---|
| 11 | 0.360 | 0.181 | 0.459 | 65.6 | 0.0153 |
| 12 | 0.345 | 0.251 | 0.404 | 72.0 | 0.0139 |
| 13 | 0.371 | 0.207 | 0.422 | 81.1 | 0.0123 |
| 14 | 0.174 | 0.198 | 0.628 | 40.4 | 0.0248 |
| 15 | 0.320 | 0.207 | 0.473 | 58.2 | 0.0172 |
| 16 | 0.284 | 0.225 | 0.491 | 52.4 | 0.0191 |
| 21 | 0.138 | 0.237 | 0.625 | 33.9 | 0.0295 |
| 22 | 0.217 | 0.289 | 0.494 | 50.5 | 0.0198 |
| 23 | 0.148 | 0.188 | 0.664 | 37.1 | 0.0269 |
| 31 | 0.041 | 0.130 | 0.829 | 22.3 | 0.0449 |
| 32 | 0.076 | 0.249 | 0.675 | 28.2 | 0.0354 |
| 33 | 0.189 | 0.193 | 0.618 | 46.4 | 0.0215 |
| 41 | 0.063 | 0.181 | 0.756 | 26.0 | 0.0385 |
| 42 | 0.049 | 0.160 | 0.791 | 27.0 | 0.0371 |
| 43 | 0.165 | 0.143 | 0.692 | 44.0 | 0.0227 |
| 51 | 0.084 | 0.101 | 0.815 | 31.3 | 0.0320 |
| 52 | 0.047 | 0.229 | 0.724 | 22.8 | 0.0439 |
| 53 | 0.189 | 0.256 | 0.555 | 44.3 | 0.0226 |
| 61 | 0.209 | 0.073 | 0.718 | 64.9 | 0.0154 |
| 62 | 0.123 | 0.112 | 0.765 | 37.6 | 0.0266 |
| 63 | 0.053 | 0.064 | 0.883 | 23.7 | 0.0422 |
| 64 | 0.050 | 0.051 | 0.899 | 22.2 | 0.0450 |
| 65 | 0.133 | 0.079 | 0.788 | 35.1 | 0.0285 |
| 66 | 0.066 | 0.043 | 0.891 | 26.3 | 0.0380 |
| 71 | 0.091 | 0.068 | 0.841 | 32.3 | 0.0309 |
| 72 | 0.011 | 0.059 | 0.930 | 16.8 | 0.0596 |
| 73 | 0.006 | 0.047 | 0.947 | 15.2 | 0.0658 |

A significant conclusion is immediately apparent from Table 3, that the reflected energy and transmitted energy is far from 100% of the incident energy, and that body wave conversion must be very efficient. Even the smoothest model (such as model No.12) caused a scattering loss of at least 40%. In the extreme case of model No.73, nearly 95% of the Rayleigh wave energy is lost to body wave conversion, which results in a very low quality factor. The model which yields the highest value of $Q$ has a

transmission coefficient of about 37%, and about 42% of $R_g$ energy is lost to scattering. The spatial $Q$ values associated with rough topography as listed in Table 3 are in the same range as the $Q_\beta$ of the uppermost crust in many places including the Arabian shield (Mokhtar, *et al.*, 1988), the eastern folded region of the Arabian Peninsula (Seber and Mitchell, 1991), Maine (Al-Eqabi and Herrmann, 1993), and different portions of New England (Saikia *et al.*, 1990; Saikia, 1992).

The nature of the reflected and transmitted signals can be determined with the polarity. Figures 68 through 94 show the synthetics at surface sensors No.2 and No.29, which have been used to represent the reflected and transmitted waves, respectively, in Table 3. Vertical and horizontal components are plotted in solid and dashed lines, respectively. The particle motion shown on the left clearly exhibits the retrograde motion. For comparison, the synthetics recorded at a deep sensor are shown at the bottom of each figure. This sensor, being 37.5 km in depth, records only the scattered body waves, as is indicated by the nearly linear particle motions.

The four propagation parameters, namely $\gamma$, T, R, and 1-T-R, have been regressed against each individual roughness coefficients separately, as shown in Figures 95 through 103. Table 4 summarizes the correlation between various roughness measures and the $R_g$ propagation characteristics. $\Omega_1$ and $\Omega_2$ have the highest correlation (0.87 and 0.88, respectively) with the scattering loss. This is also illustrated in lower-right plot of Figures 95 through 103. Note that $\Omega_1$ and $\Omega_2$ perform better in predicting the scattering loss than in predicting the transmission or reflection alone. For a practical monitoring situation, however, it might be desirable to infer the transmission coefficient, T, of an uncalibrated path in order to gain some information about how the seismic wave behaves. On this regard, $\Omega_1$, $\Omega_2$, and $\Omega_6$ might serve the purpose equally well, with the correlation coefficients around 0.73-0.76. $\Omega_4$, the Durbin-Watson number or the von Neumann ratio, turns out to be the poorest statistics in all tests. The correlation coefficient between $\Omega_4$ and any of the propagation statistics is always no higher than 0.27 (Figure 98). As discussed earlier, $\Omega_4$ is essentially the square of the quotient of two other roughness measures, namely $\Omega_2$ and $\Omega_3$. Thus combining these two parameters offers no advantage at all. That $\Omega_4$ is negatively correlated to all other roughness measures (*cf.* Table 2), scatter loss, as well as $\gamma$, would suggest that $\Omega_4$ is not a good candidate for quantifying the roughness. Several systematic patterns can be observed from the regression results: both $\gamma$ and the scattering loss (1-T-R) increase with the roughness coefficients (except $\Omega_4$), whereas T and R decrease with the roughness coefficients.

Table 4.Correlation Between Roughness and Propagation Characteristics

| | T(1Hz) | R(1Hz) | 1-T-R | $\Omega_1$ | $\Omega_2$ | $\Omega_3$ | $\Omega_4$ | $\Omega_5$ | $\Omega_6$ | $\Omega_7$ | Pr[1] |
|---|---|---|---|---|---|---|---|---|---|---|---|
| $\gamma$ | -0.88 | -0.54 | 0.84 | 0.67 | 0.66 | 0.42 | -0.17 | 0.31 | 0.49 | 0.66 | 0.64 |
| T(1Hz) | ___ | 0.54 | -0.92 | -0.73 | -0.76 | -0.54 | 0.24 | -0.43 | -0.74 | -0.73 | -0.73 |
| R(1Hz) | ___ | ___ | -0.83 | -0.81 | -0.79 | -0.49 | 0.24 | -0.65 | -0.57 | -0.81 | -0.80 |
| 1-T-R | ___ | ___ | ___ | 0.87 | 0.88 | 0.59 | -0.27 | 0.59 | 0.76 | 0.86 | 0.86 |

| Table 5. Regression Results | | | | | |
|---|---|---|---|---|---|
| X | Y | Slope | Intercept | σ(Y) | ρ |
| $\Omega_1$ | γ | 0.057±0.013 | 0.013±0.004 | 0.010 | 0.67 |
| $\Omega_1$ | T(1Hz) | -0.501±0.095 | 0.306±0.033 | 0.077 | -.73 |
| $\Omega_1$ | R(1Hz) | -0.393±0.056 | 0.280±0.020 | 0.045 | -.81 |
| $\Omega_1$ | 1-T-R | 0.894±0.104 | 0.413±0.036 | 0.084 | 0.87 |
| $\Omega_2$ | γ | 1.069±0.242 | -0.003±0.008 | 0.010 | 0.66 |
| $\Omega_2$ | T(1Hz) | -9.915±1.686 | 0.462±0.055 | 0.072 | -.76 |
| $\Omega_2$ | R(1Hz) | -7.206±1.117 | 0.384±0.037 | 0.048 | -.79 |
| $\Omega_2$ | 1-T-R | 17.121±1.869 | 0.154±0.061 | 0.080 | 0.88 |
| $\Omega_3$ | γ | 0.019±0.008 | 0.019±0.006 | 0.013 | 0.42 |
| $\Omega_3$ | T(1Hz) | -0.199±0.062 | 0.268±0.041 | 0.094 | -.54 |
| $\Omega_3$ | R(1Hz) | -0.127±0.045 | 0.233±0.030 | 0.068 | -.49 |
| $\Omega_3$ | 1-T-R | 0.326±0.089 | 0.499±0.060 | 0.135 | 0.59 |
| $\Omega_4$ | γ | -0.234±0.274 | 0.034±0.004 | 0.014 | -.17 |
| $\Omega_4$ | T(1Hz) | 2.667±2.181 | 0.114±0.035 | 0.108 | 0.24 |
| $\Omega_4$ | R(1Hz) | 1.878±1.527 | 0.132±0.024 | 0.076 | 0.24 |
| $\Omega_4$ | 1-T-R | -4.546±3.239 | 0.754±0.052 | 0.161 | -.27 |
| $\Omega_5$ | γ | 0.011±0.007 | 0.023±0.005 | 0.013 | 0.31 |
| $\Omega_5$ | T(1Hz) | -0.127±0.054 | 0.234±0.041 | 0.101 | -.43 |
| $\Omega_5$ | R(1Hz) | -0.136±0.032 | 0.248±0.024 | 0.059 | -.65 |
| $\Omega_5$ | 1-T-R | 0.263±0.072 | 0.518±0.055 | 0.135 | 0.59 |
| $\Omega_6$ | γ | 0.011±0.004 | 0.009±0.008 | 0.012 | 0.49 |
| $\Omega_6$ | T(1Hz) | -0.131±0.024 | 0.418±0.051 | 0.075 | -.74 |
| $\Omega_6$ | R(1Hz) | -0.070±0.020 | 0.301±0.044 | 0.064 | -.57 |
| $\Omega_6$ | 1-T-R | 0.202±0.035 | 0.281±0.074 | 0.109 | 0.76 |
| $\Omega_7$ | γ | 0.137±0.031 | -0.124±0.035 | 0.010 | 0.66 |
| $\Omega_7$ | T(1Hz) | -1.210±0.229 | 1.517±0.259 | 0.077 | -.73 |
| $\Omega_7$ | R(1Hz) | -0.949±0.136 | 1.229±0.154 | 0.046 | -.81 |
| $\Omega_7$ | 1-T-R | 2.159±0.251 | -1.746±0.284 | 0.084 | 0.86 |
| Pr[1] | γ | 0.080±0.019 | 0.015±0.004 | 0.011 | 0.64 |
| Pr[1] | T(1Hz) | -0.734±0.139 | 0.294±0.031 | 0.077 | -.73 |
| Pr[1] | R(1Hz) | -0.566±0.085 | 0.269±0.019 | 0.047 | -.80 |
| Pr[1] | 1-T-R | 1.300±0.156 | 0.437±0.035 | 0.086 | 0.86 |

### 3.5 Scattered Body Waves

A horizontal array is formed of 30 sensors spaced 2 km apart at a depth of 37.5 km to record the converted *P* and *SV* wavefields. Figures 103 through 129 give the seismic sections of the converted *P* wave (top) and *S* wave (bottom) displacements for each model. The take-off angle as well as the zero-to-peak amplitude of each synthetic are shown on the right. The seismic sections are plotted in a uniform scale. Note that the converted *SV* waves typically have a peak amplitude two to three times larger than that of the the converted *P* waves. The *P* and *S* wavefields can be seen to be radiated from numerous point diffractors along the topographic profile, as was already suggested by the snapshots (Figures 12-38). For the lower portion of the seismic section, *i.e.*, synthetics numbered 50 and on, the take-off angles are generally more oblique than 30°. If a velocity gradient were introduced into the model, most of these rays would pass the critical angle and could well be multiply reflected in the crustal waveguide.

In plotting the seismic sections, each synthetic seismogram is steered towards its ray direction which is determined with the particle motion within an appropriate time window. To illustrate the robustness of this approach in separating *P* and *SV* components, Figures 130 through 156 display three synthetic seismograms for each model. The particle motion throughout the whole LFD simulation (*i.e.*, 40-second window) is shown on the left, with the *P* and *SV* components shown in solid and dashed lines, respectively, on the right. Traces 31, 40, and 59 of each model are plotted from top to bottom. The take-off angle of each ray is determined by the *P* onset, and it turns out that within the initial *P* window (typically from 10 to 15 seconds), the *SV* component is nearly negligible. On the other hand, the later arrivals (*e.g.*, 20 seconds and on) are dominated by *SV* component with peak amplitude a few times larger than that of the *P* waves, except for the obliquely scattered trace (*e.g.*, the synthetic No.59) of a few models.

Although the topography is embedded in the central portion of the grid, the scattered *S* wave field is far from isotropic. The backscattered *S* waves have steeper take-off angles and longer duration, whereas the forward scattered *S* waves have more compact wavetrains. There are twice as many sensors that recorded forward-scattered *S* waves. Furthermore, many of them have very oblique take-off angles. This is in support of the interpretation that we are observing a series of *S*-wave point sources spread along the free surface which are "triggered" in the forward direction. Thus even if we assume that the subsurface geology is perfectly homogeneous and isotropic, the scattered *S* wavefield will not be as symmetric. Both the forward and backward directions have about the same number of rays that would penetrate into the deeper earth. However, there is always a significant amount of energy which is favorably trapped in the crustal waveguide in the forward direction.

## 4. DISCUSSION AND CONCLUSIONS

In this study, we have performed 2-D numerical Rayleigh-wave scattering experiments upon complicated random topographies. The simulations show that reflection is an efficient process and that the bulk of the energy which is not transmitted across the topography is either converted to body waves or reflected back. Through the simulations, we illustrate that *P* and *S* waves are radiated as coda to teleseismic distances, and some *P–SV* energy is trapped in the crustal waveguide as $P_g$, $S_g$, and $L_g$. The body waves appear to radiate from the changes in slope and to first order can be visualized as being from point-force diffractors. All these observations are consistent with our previous study (McLaughlin and Jih, 1986 and 1987; Jih and McLaughlin, 1988).

The spatial *Q* values associated with rough topography obtained in this study are in the same range as the $Q_\beta$ of the uppermost crust in many places including the Arabian shield (Mokhtar, *et al.*, 1988), the eastern folded region of Arabian Peninsula (Seber and Mitchell, 1991), and Maine (Al-Eqabi and Herrmann, 1993). Saikia (1992) (and Saikia *et al.*, 1990) also finds that a low $Q_\beta$ of 15 is needed in order to match his $R_g$ synthetics with the data observed at southwestern New England. An accurate characterization/prediction of the propagation of regional phases due to explosion sources in regions of high proliferation concern requires an accurate regionalized map of the attenuation coefficient. Although a global $L_g$ coda Q map is available for much of Eurasia and some other regions of the world, the identification of small seismic events has raised a need to refine such a map for a more detailed regionalization for complex areas. It is known that changes in the quality factor of the propagation path can have a significant influence on magnitude estimates and therefore on network performance estimates (*e.g.*, Jih and Lynnes, 1993). Regionalized Q maps (for different phases) need to be established and must be coupled with the appropriate source model for the distinct geologies.

A major issue for the Non-Proliferation Treaty is the discrimination of large chemical explosions from possible clandestine or small nuclear tests. Unless discrimination is possible, the numerous mining blasts could give ample opportunity for concealing clandestine tests. Rippled-fired explosions are commonly used to fragment rocks during quarry and open-pit mining. Through LFD calculations, Jih (1993b) finds that ripple firing could excite directionally dependent $R_g$ and S*. Thus the lack of $R_g$ may not be always indicative of a deep source. Rather, it could also be due to the shot pattern. However, the enhanced $R_g$ in the forward direction of ripple firing can be strongly attenuated by lateral heterogeneity and surface topography, as is illustrated in the present study. The scattered $R_g$ energy could then couple into the crustal waveguide as $L_g$ and other phases. Since such scattering mechanisms are commonly present in many quarry sites or mines, it is not surprising that the directional enhancement of $R_g$ may not be always observable. The spall could obscure the azimuthal dependency of $R_g$ as well. LFD modeling studies suggest that the $R_g$-to-*S* scattering is in general stronger than that of $R_g$-to-*P*, which could provide a plausible explanation of why quarry blasts and mining blasts should discriminate less well from earthquakes than would contained nuclear explosions.

The $L_g$ phase has an increasingly prominent role in nuclear test detection, discrimination, and yield estimation. Regional $L_g$ phase is a short-period guided wave, composed mainly of a sequence of

multiply reflected postcritical *S*–waves trapped in the crustal waveguide. The formation of $L_g$ requires a significant amount of energy propagating as *S* waves, either directly radiated from the source or converted from other phases, and these *S* waves must be properly trapped in the crustal wave guide (Xie and Lay, 1993; Frankel, 1989; and others). Shallow explosions are strong $R_g$ generators, and these explosion-generated $R_g$ waves can contribute to $L_g$ via scattering at rough topohraphy. LFD simulations using a pure $R_g$ packet as the initial condition offers a promising approach to quantify effects of scattering by topography and heterogeneity upon surface waves, as illustrated in this study. A complete exploration of the problem will require variation of the *P* and *S* velocities, near surface velocity gradients, as well as crustal velocity heterogeneity, since the low-*Q* sediments can be equally attenuative, as reported by Mitchell and Hwang (1987). Adding any of these mechanisms to the numerical experiments can only increase the *S* coupling (*cf.* Aki, 1992). Thus we can anticipate that in a more realistic geological environment, the Rayleigh-to-$L_g$ conversion would be more profound than in the case of a half space. Recently Patton and Taylor (1993) observed $L_g$ spectral null around 0.55 Hz for Yucca Flat explosions, which could be due to the null in excitation of $R_g$ by a CLVD source as a function of depth. The null can not be accounted for by the delay between P and spall slapdown when those differ for shots at constant depth but different yield. Thus the scattering of large amplitude $R_g$ waves in the near field may be the most important source of $L_g$ waves with frequencies near 1 Hz for explosions on Yucca Flat or mountainous site.

Zhang and Lay (1993) found the $S_n/L_g$ amplitude ratio to be strongly dependent on some roughness measures of paths from Semipalatinsk to several Eurasian stations. Perhaps $S_n$ interacts with the irregular Moho topography in a way very similar to that of $R_g$ with the free-surface topography. Thus this may suggest that energy partitioning in the regional wavefield is controlled by waveguide structure and attenuation variations which are manifested in the surface topography. Further investigation along this line with numerical modeling techniques as presented in this study would be very useful. A distinct advantage of using a source-free Rayleigh wave packet in the simulation (as adopted in this study) is that the interaction with certain types of heterogeneity (such as the topography) can be isolated. Scaling our results with other source-dependent relationships (such as the depth-dependence of $R_g$ excitation) is straightforward.

The simple functional relationship between some of the roughness parameters might lead us to regard some of the roughness parameters as redundant. However, it turns out that the performance of these roughness measures could be different. This simply means that by applying appropriate "transformation" on the data, we might be able to find a better linear regression. A useful family of transformations for this purpose is the family of *Box-Cox transformations* (see, for example, Johnson and Wichern, 1992). When we regress $\gamma$ and the transmission power (T(1Hz)) on any of the roughness measures, say $\Omega_1$, it should not be surprising to see that a linear fit is appropriate for $\gamma$, but not T(1Hz). Converting T(1Hz) to $\gamma$ with a simple logarithmic operation is a typical example of the Box-Cox transformation. Such an exercise of transforming nonnormal data into more nearly "normal looking" data (around the calibration curve) is a standard practice in the statistics field, and it may be worth exploring.

## 5. ACKNOWLEDGEMENTS

The author is indebted to Bob Blandford, Alan Ryall, Anton Dainty, and Howard Patton for helpful discussions. Wilmer Rivers' review and comments on the original manuscript are gratefully acknowledged. This research also benefited from a previous study which was performed with the collaboration from Keith L. McLaughlin and Zoltan A. Der. This study was supported under Phillips Laboratory contract F29601-91-C-DB23. The views and conclusions contained in this paper are those of the author and should not be interpreted as representing the official policies, either expressed or implied, of the U.S. Air Force, the Advanced Research Projects Agency or the U.S. Government.

## 6. REFERENCES

Adushkin, V. V., V. I. Kulikov, F. F. Safonov, and A. A. Solomonov (1990). Method for determining power of underground explosion from seismic wave parameters in near seismic zone, *Izvestiya,* **26,** 1002-1009.

Aki, K. and B. Chouet (1975). Origin of coda waves: source, attenuation, and scattering effects, *J. Geophys. Res.,* **80,** 3322-3342.

Aki, K. (1992). Scattering conversions *P* to *S* versus *S* to *P*, *Bull. Seism. Soc. Am.,* **82,** 1969-1972.

Al-Eqabi, G. I. and R. B. Herrmann (1993). Ground roll: a potential tool for constraining shallow shear-wave structure, *Geophysics,* **58,** 713-719.

Baumgardt, D. R. (1990). Causes of $L_g$ amplitude variations and scattering in the Eurasian continental craton, *Proceedings of 12th DARPA/GL Seismic Research Symposium (18-20 Sept. 1990, Key West, FL. 33040),* 224-233.

Blandford, R. R. (1993). Discrimination of earthquakes and explosions at regional distances using complexity, *Report AFTAC-TR-93-044,* HQ AFTAC/TT, Patrick AFB, FL.

Bloomfield, P. (1975). *Fourier Analysis of Time Series: An Introduction,* John Wiley and Sons, Inc., New York.

Boore, D. (1970). Love waves in nonuniform wave guides: finite-difference calculations, *J. Geophys. Res.,* **75,** 1512-1527.

Boore, D., Harmsen, S. C., Harding, S. (1981). Wave scattering from a step change in surface topography, *Bull. Seism. Soc. Am.,* **71,** 117-125.

Bouchon, M. (1973). Effect of topography on surface motion, *Bull. Seism. Soc. Am.,* **63,** 615-632.

deBremaecker, J. Cl. (1958). Transmission and reflection of Rayleigh waves by corners, *Geophysics,* **23,** 1701-1731.

Bullit, J. T. and M. N. Toksoz (1985). Three-dimensional ultrasonic modeling of Rayleigh wave propagation, *Bull. Seism. Soc. Am.,* **75,** 1087-1104.

Chen, T. C. and L. E. Alsop (1979). Reflection and transmission of obliquely incident Rayleigh waves at a vertical discontinuity between two welded quarter-spaces, *Bull. Seism. Soc. Am.,* **69,** 1409-1423.

Cheng, C.-C. and B. J. Mitchell (1981). Crustal *Q* structure in the United States from multi-mode

surface waves, *Bull. Seism. Soc. Am.*, **71**, 161-181.

Clayton, R. and B. Engquist (1977). Absorbing boundary conditions for acoustic and elastic wave equations, *Bull. Seism. Soc. Am.*, **67**, 1529-1540.

DARPA/NMRO (1992). Report on the DARPA seismic identification workshop, 18-19 May 1992. (Blandford, R. R., A. Dainty, R. Lacoss, R. Maxion, A. Ryall, B. Stump, C. Thurber, and T. Wallace edt.), *DARPA/NMRO Special Topical Report*, 28 pp.

Dainty, A. M. (1986). Coda observed at NORSAR and NORESS, *Report AFGL-TR-85-0199*, Air Force Geophysics Laboratory, Hanscom AFB, MA.

Dainty, A. M., R. M. Duckworth, and A. Tie (1987). Attenuation and backscattering from local coda, *Bull. Seism. Soc. Am.*, **77**, 1728-1747.

Der, Z. A., M. E. Marshall, A. O'Donnell, and T. W. McElfresh (1984). Spatial coherence structure and attenuation of the $L_g$ phase, site effects, and the interpretation of the $L_g$ coda, *Bull. Seism. Soc. Am.*, **74**, 1125-1147.

Drake, L. A. (1972). Rayleigh waves at a continental boundary by the finite element method, *Bull. Seism. Soc. Am.*, **62**, 1259-1268.

Drake, L. A. and B. A. Bolt (1980). Love waves normally incident at a continental boundary, *Bull. Seism. Soc. Am.*, **70**, 1103-1123.

Emerman, S. and R. Stephen (1983). Comment on "Absorbing boundary conditions for acoustic and elastic wave equations", by R. Clayton and B. Engquist, *Bull. Seism. Soc. Am.*, **73**, 661-665.

Frankel, A. (1989). Effects of source depth and crustal structure on the spectra of regional phases determined from synthetic seismograms, *Proceedings of AFTAC/DARPA 1989 Seismic Research Review* (28-29 Nov 1989, Patrick AFB, Florida), 97-118.

Fuyuki, M. and Y. Matsumoto (1980). Finite-difference analysis of Rayleigh wave scattering at a trench, *Bull. Seism. Soc. Am.*, **70**, 2051-2069.

Fuyuki, M. and N. Nakano (1984). Finite-difference analysis of Rayleigh wave transmission past an upward step change, *Bull. Seism. Soc. Am.*, **74**, 893-911.

Greenfield, R. J. (1971). Short-period *P*-wave generation by Rayleigh-wave scattering at Novaya Zemlya, *J. Geophys. Res.*, **76**, 7988-8002.

Gupta, I. N. and R. R. Blandford (1987). A study of *P* waves from NTS explosions: near-source information from teleseismic observations? *Bull. Seism. Soc. Am.*, **77**, 1041-1056.

Gupta, I. N. and R. A. Wagner (1992). Evidence of $R_g$-to-*P* scattering in teleseismic *P* coda of East Kazakh explosions, *Bull. Seism. Soc. Am.*, **82**, 2139-2152

Hudson, J. A. and A. Douglas (1975). Rayleigh wave spectra and group velocity minima, and the resonance of *P* waves in layered structure, *Geophys. J. R. astr. Soc.*, **42**, 175-188.

Hudson, J. A. and L. Knopoff (1967). Statistical properties of Rayleigh waves due to scattering by topography, *Bull. Seism. Soc. Am.*, **57**, 83-90.

Ilan, A., A. Ungar, and Z. Alterman (1975). An improved representation of boundary conditions in finite-difference schemes for seismological problems, *Geophys. J. R. astr. Soc.*, **43**, 727-745.

Ilan, A. (1977). Finite-difference modeling for P-pulse propagation in elastic media with arbitrary polygonal surface, *J. Geophys.*, **43**, 41-58.

Jih, R.-S. (1993a). User's manual of FD2: a software package for modeling seismological problems with 2-dimensional linear finite-difference method, *Report TGAL-93-06*, Teledyne Geotech, Alexandria, VA.

Jih, R.-S. (1993b). Directional excitation of $R_g$ due to ripple-fired explosions: 2-dimensional finite-difference calculations, *EOS, Trans. Am. Geophys. Union*, **74-16**, 213. (also presented at *DoE/LANL Numerical Modeling for Underground Nuclear Test Monitoring Symposium*, March 23-25, Durango, CO.)

Jih, R.-S. and C. S. Lynnes (1993). Studies of regional phase propagation in Eurasia. *Report PL-TR-93-2003*, Phillips Laboratory, Hanscom AFB, MA.

Jih, R.-S. and K. L. McLaughlin (1988). Investigation of explosion generated *SV* $L_g$ waves in 2-D heterogeneous crustal models by finite-difference method, *Report AFGL-TR-88-0025*, Air Force Geophysics Laboratory, Hanscom AFB, MA.

Jih, R.-S., K. L. McLaughlin and Z. A. Der (1988). Free boundary conditions of arbitrary polygonal topography in a 2-D explicit elastic finite difference scheme, *Geophysics*, **53**, 1045-1055.

Johnson, R. A. and D. W. Wichern (1992). *Applied Multivariate Statistical Analysis*, Prentice-Hall International, Inc., London, U.K.

Kafka, A. L. (1990). $R_g$ as a depth discriminant for earthquakes and explosions: a case study in New England, *Bull. Seism. Soc. Am.*, **80**, 373-394.

Kelly, K. R., R. W. Ward, S. Treitel, and M. Alford (1976). Synthetic seismograms: a finite-difference approach, *Geophysics*, **41**, 2-27.

Key, F. A. (1967). Signal-generated noise recorded at Eskdalemuir seismometer array station. *Bull. Seism. Soc. Am.*, **57**, 27-37.

Key, F. A. (1968). Some observations and analyses of signal-generated noise. *Geophys. J. R. astr. Soc.*, **15**, 377-392.

Lay, T. (1987). Analysis of near-source contributions to early P-wave coda for underground explosions. III. Inversion for isotropic scatterers, *Bull. Seism. Soc. Am.*, **77**, 1767-1783.

Levander, A. (1985). Finite-difference calculations of dispersive Rayleigh wave propagation, *Tectonophysics*, **113**, 1-30.

Levander, A. (1990). Seismic scattering near the earth's surface, *PAGEOPH*, **132**, 21-47.

Lynnes, C. S. and T. Lay (1989). Inversion of *P* coda for isotropic scatterers at the Yucca Flat Test Site, *Bull. Seism. Soc. Am.*, **79**, 790-804.

Mal, A. K. and L. Knopoff (1965). Transmission of Rayleigh waves past a step change in elevation, *Bull. Seism. Soc. Am.*, **55**, 319-334.

Malin, P. E. and R. A. Phinney (1985). On the relative scattering of *P* and *S* waves, *Geophys. J. Roy. astr. Soc.* **80**, 603-618.

Martel, L., M. Munasinghe, and G. W. Farnell (1977). Transmission and reflection of Rayleigh wave through a step, *Bull. Seism. Soc. Am.*, **67**, 1277-1290.

McGarr, A. and L. E. Alsop (1967). Transmission and reflection of Rayleigh waves at vertical boundaries, *J. Geophys. Res.*, **72**, 2169-2180.

McLaughlin, K. L. and R.-S. Jih (1986). Finite-difference simulations of Rayleigh wave scattering by 2-D rough topography, *Report AFGL-TR-86-0269*, Air Force Geophysics Laboratory, Hanscom AFB, MA.

McLaughlin, K. L. and R.-S. Jih (1987). Finite-difference simulations of Rayleigh wave scattering by shallow heterogeneity. *Report AFGL-TR-87-0322*, Air Force Geophysics Laboratory, Hanscom AFB, MA.

McLaughlin, K. L. and R.-S. Jih (1988). Scattering from near-source topography: teleseismic observations and numerical 2-D explosive line source simulations, **78**, 1399-1414.

Mitchell, B. J. and H. J. Hwang (1987). Effect of low $Q$ sediments and crustal $Q$ on $L_g$ attenuation in the United States, *Bull. Seism. Soc. Am.*, **77**, 1197-1210.

Mitchell, B. J., J. Xie, and W. Lin (1992). Attenuation of multiphase surface waves in the Basin and Range Province, Part II: Fundamental-mode surface waves, in *Semiannual Technical Report 07/91-01/92*, Saint Louis University, Saint Louis, Mo.

Mokhtar, T. A., R. B. Herrmann, and D. R. Russell (1988). Seismic velocity and $Q$ model for the shallow structure of the Arabian shield from short-period Rayleigh waves, *Geophysics*, **53**, 1379-1387.

Momoi, T. (1985). Scattering of Rayleigh waves in an elastic three-quarter space, *J. Phys. Earth*, **33**, 323-343.

Munasinghe, M. and G. Farnell (1973). Finite-difference analysis of Rayleigh wave scattering at vertical discontinuities, *J. Geophys. Res.*, **78**, 2454-2466.

Nakano, M., K. Fujii, and S. Takeuchi (1988). Rayleigh wave scattering at wedge corners with major wedge angles, *PAGEOH*, **128**, 119-132.

Ohtsuki, A. and H. Yamahara (1984). Effect of topography and subsurface inhomogeneity on seismic Rayleigh wave, *Earthquake Eng. Struct. Dyn.*, **12**, 37-58.

Patton, H. J. and S. R. Taylor (1993). Analysis of $L_g$ spectral ratios from NTS explosions: implications for the source mechanisms of spall and the generation of $L_g$ waves (submitted to *Bull. Seism. Soc. Am.)*.

Phillips, S. W. and K. Aki (1986). Site amplification of coda waves from local earthquakes in central California, *Bull. Seism. Soc. Am.*, **76**, 627-648.

Sabina, F. J. and J. R. Willis (1977). Scattering of Rayleigh waves by a ridge, *J. Geophys*, **43**, 401-419.

Saikia, C. K. (1992). Numerical study of quarry generated $R_g$ as a discriminant for earthquakes and explosions: modeling of $R_g$ in southwestern New England, *J. Geophys. Res.*, **97**, 11057-11072.

Saikia, C. K., A. L. Kafka, S. C. Gnewuch, and J. W. McTigue (1990). Shear velocity and intrinsic $Q$ structure of the shallow crust in southeastern New England from $R_g$ wave dispersion, *J. Geophys. Res.*, **95**, 8527-8541.

Seber, D. and B. J. Mitchell (1991). Attenuation of surface waves across the Arabian Peninsula, in *Report PL-TR-91-2286*, Phillips Laboratory, Hanscom AFB, MA.

Toksoz, M. N., A. M. Dainty, and E. E. Charrette (1986). Development of ultrasonic modeling techniques for the study of seismic wave scattering due to crustal inhomogeneities, *Report AFGL-TR-86-0078*, Air Force Geophysics Laboratory, Hanscom AFB, MA.

Tuan, H. S. and R. C. M. Li (1974). Rayleigh-wave reflection from groove and step discontinuities: *J. Acoust. Soc. Am.*, **55**, 1212-1217.

Wojcik, L. W. and R. Mak (1985). A numerical study of diffraction in reentrant geologic structure, *Report AFGL-TR-85-0158*, Air Force Geophysics Laboratory, Hanscom AFB, MA.

Xie, X.-B. and T. Lay (1993). The excitation of $L_g$ waves by explosions: a finite-difference investigation *(manuscript submitted for publication)*.

Zhang, T. and T. Lay (1993). Analysis of short-period regional phase path effects associated with topography in Eurasia *(manuscript submitted for publication)*.

## 7. FIGURE CAPTIONS

**Figure 1:** 3 rugged profiles corresponding to models No.11 through No.13, respectively, are shown on the left, with the log-amplitude wavenumber spectra of the topography in the center, and statistics characterizing the topography listed on the right. The log-amplitude wavenumber spectra are normalized by the peak value of the spectra (which is shown at the right as K(0)). The seed number and the preassigned probability of state 1, which determine the random topography, are printed under the profile.

**Figures 2-9:** Same as Figure 1 except for models No.14 through No.73.

**Figure 10** The snapshots of the displacement field at time incidents of 4 seconds apart. Shading in each snapshot is proportional to $\sqrt{U^2 + W^2}$ where U and W are the displacement along the X and Z directions, respectively, of the grid. The darkness of the plot is normalized to the maximum in each frame.

**Figure 11:** Spectral ratio of the transmitted Rayleigh waves over the incident Rayleigh waves in a homogeneous half-space. Grid dispersion only modulates the spectra slightly. The frequency band of interest in this study is around 1 Hz. No significant attenuation of the Rayleigh wave could be measured for the half-space in the frequency band of interest.

**Figure 12:** The snapshots of the displacement field due to a Rayleigh wave incident upon topographic profile No.11.

**Figures 13-38:** Same as Figures 10 and 12 except for models No.12 through No.73. In general, the diffraction pattern becomes much more complicated when the the topography is rougher. This is obvious in comparing Figure 13 (for model No.12) and Figure 32 (for model No.63), for instance. In all cases the corners act as point sources radiating converted body waves (mainly *S* wave).

**Figure 39:** The seismic section of the vertical component of the half-space model. The sensors are evenly distributed (2 km apart) along the free-surface. The maximum zero-to-peak amplitude of each trace is shown on the right.

**Figures 40-66:** Same as Figure 39 except for models No.12 through No.73. Smoother models tend to have longer reflected wave trains than do rougher models. Also, the peak amplitude of the transmitted signal, which is measured with trace No.29 of each model, drops significantly as the model becomes rougher. In the following, these qualitative observations are further elaborated in a quantitative manner.

**Figure 67:** The synthetics for the half-space model at three different distances are shown on the right with the vertical and horizontal components are plotted in solid and dashed lines, respectively. The particle motion is plotted at the left. Note the clear retrograde motion.

**Figure 68:** The synthetics at surface sensors No.2 and No.29, which have been used to represent the reflected and transmitted waves, respectively, in Table 3. Same as in Figure 67, the vertical and horizontal components are plotted in solid and dashed lines, respectively. The reflected waves (top) is composed of multiply reflected Rayleigh waves. On the other hand, the transmitted synthetic (middle) is dominated by very few cycles of Rayleigh waves. The particle motion shown on the left clearly exhibits the retrograde motion. For comparison, the synthetics recorded at a deep sensor are shown at the bottom of each figure. This sensor, being 37.5 km in depth, records only the scattered body waves, as is indicated by the nearly linear particle

motions.

**Figures 69-94:** Same as Figure 68 except for models No.12 through No.73.

**Figure 95:** The four propagation parameters ($\gamma$, T, R, and 1-T-R) are regressed against $\Omega_1$. The correlation of 0.87 between $\Omega_1$ and the scattering loss is statistically significant.

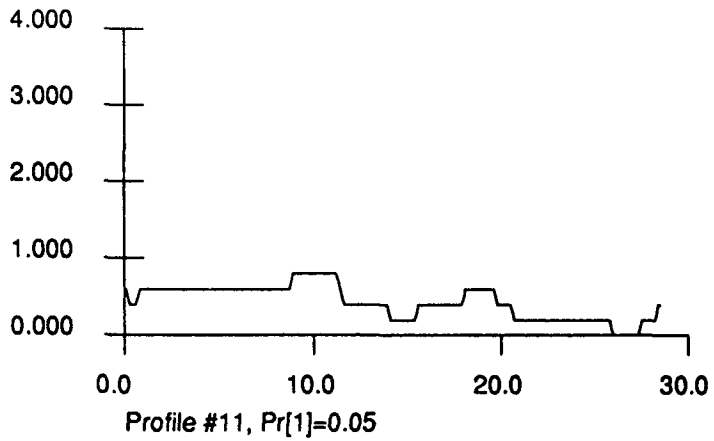
**Figures 96-102:** Same as Figure 95 except for different roughness measures. $\Omega_1$ and $\Omega_2$ perform better in predicting the scattering loss than in predicting the transmission or reflection alone. $\Omega_4$, the Durbin-Watson number or the von Neumann ratio, turns out to be the poorest statistics in all tests. The correlation coefficient between $\Omega_4$ and any of the propagation statistics is always no higher than 0.27 (Figure 98). Several systematic patterns can be observed from the regression results: both $\gamma$ and the scattering loss (1-T-R) increase with the roughness coefficients (except $\Omega_4$), whereas T and R decrease with the roughness coefficients.

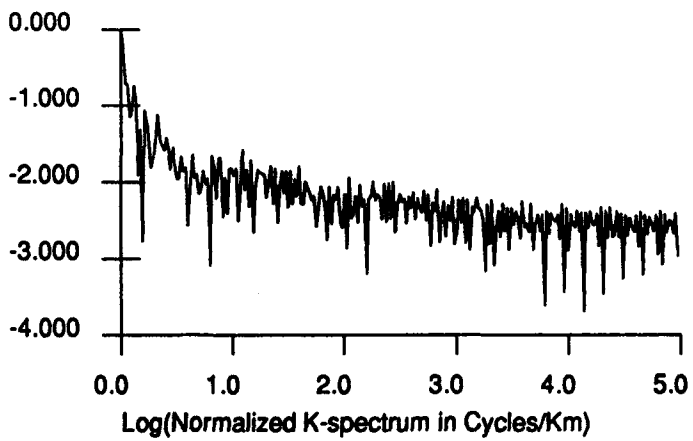
**Figure 103:** The seismic sections of the converted *P* wave (top) and *S* wave (bottom) displacements of model No.11. The take-off angle and the zero-to-peak amplitude of each synthetic are shown on the right.

**Figures 104-129:** Same as Figure 103 except for models No.12 through No.73. Note that the converted *SV* waves typically have a peak amplitude two to three times larger than that of the the converted *P* waves. For the lower portion of the seismic section, *i.e.*, synthetics numbered 50 and on, the take-off angles are generally more oblique than 30°.

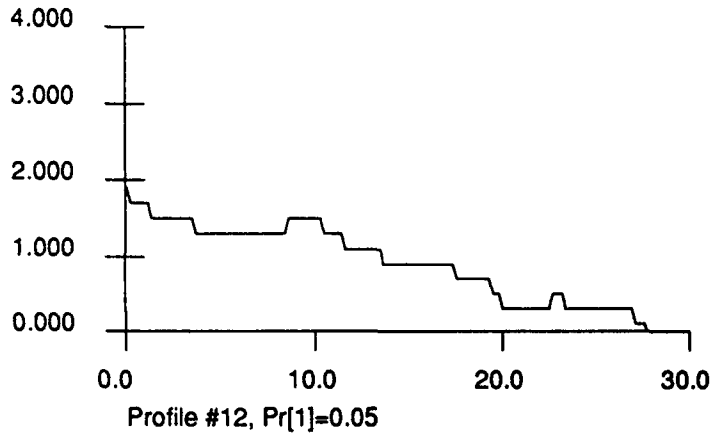
**Figure 130:** Three (rotated) synthetic seismograms, (traces No.31 (top), No.40 (middle), and No.59 (bottom)), generated with model No.11. The *P* and *SV* components are shown in solid and dashed lines, respectively. The particle motion throughout the whole 40-second window is shown on the left. The take-off angle of each ray is determined by the *P* onset.

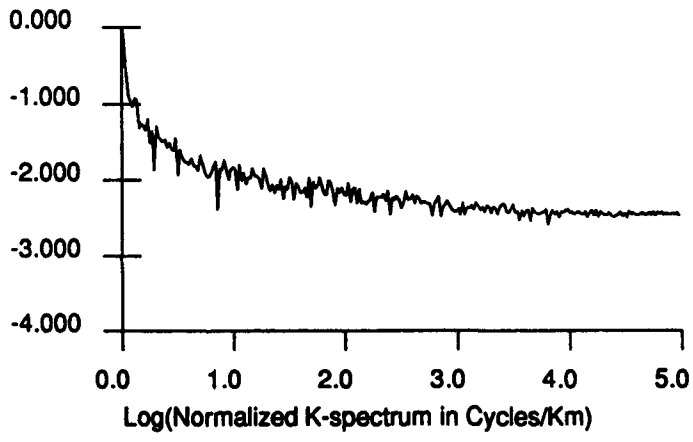
**Figures 131-156:** Same as Figure 130 except for models No.12 through No.73. Note that within the initial *P* window (typically from 10 to 15 seconds), the *SV* component is nearly negligible. Later arrivals (*e.g.*, 20 seconds and on) are dominated by *SV* component with the peak amplitude a few times larger than that of the *P* waves, except for the obliquely scattered trace (*e.g.*, the synthetic No.59) of a few models .



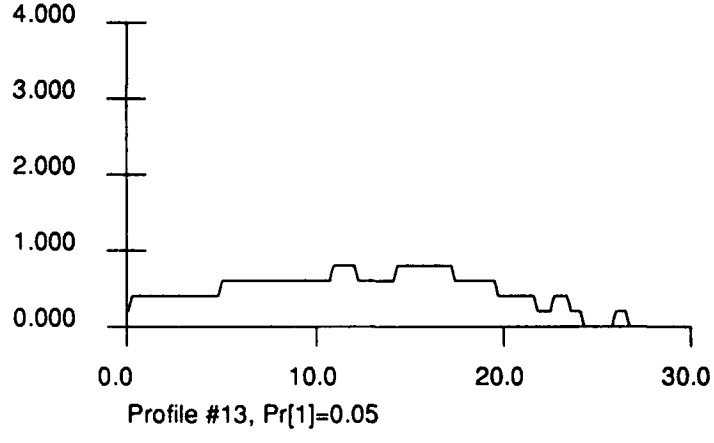



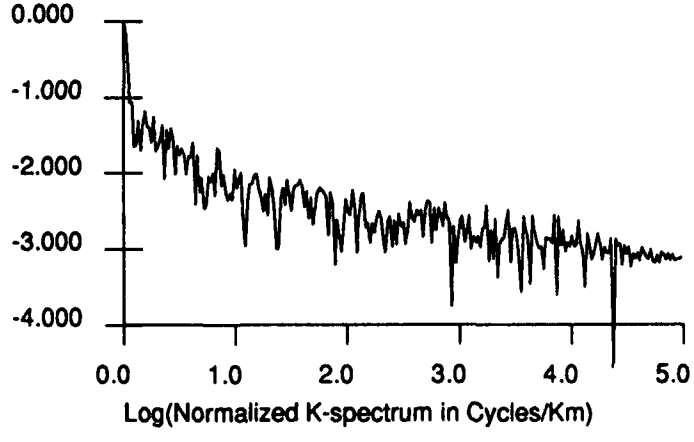

Pr[1] = 0.05 , Seed = 22887
[L1-jumps]/km = 0.0909
[L2-jumps]/km = 0.0178
RMS elevation = 0.2145
Durbin-Watson # = 0.0198
Peak K-Spectrum = K(0) = 0.2404
0.84 Corners/km
( 24 corners / 28.60km)
Normalized arc length= 1.038




Pr[1] = 0.05 , Seed = 22892
[L1-jumps]/km = 0.0968
[L2-jumps]/km = 0.0186
RMS elevation = 0.4866
Durbin-Watson # = 0.0041
Peak K-Spectrum = K(0) = 0.5113
1.00 Corners/km
( 28 corners / 27.90km)
Normalized arc length= 1.040




Pr[1] = 0.05 , Seed = 85995
[L1-jumps]/km = 0.0967
[L2-jumps]/km = 0.0190
RMS elevation = 0.2181
Durbin-Watson # = 0.0203
Peak K-Spectrum = K(0) = 0.2596
0.97 Corners/km
( 26 corners / 26.90km)
Normalized arc length= 1.040

**Figure 1**

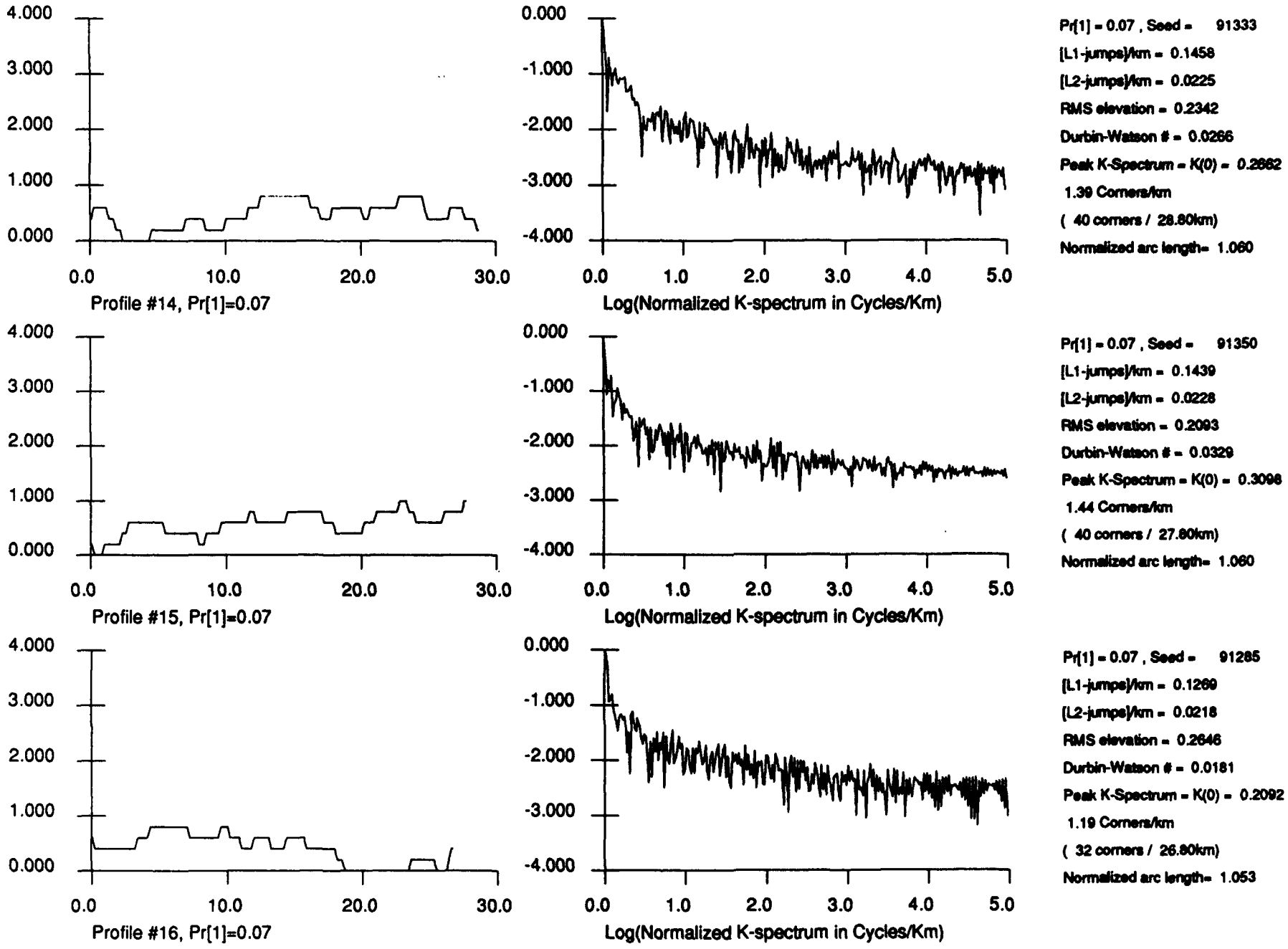
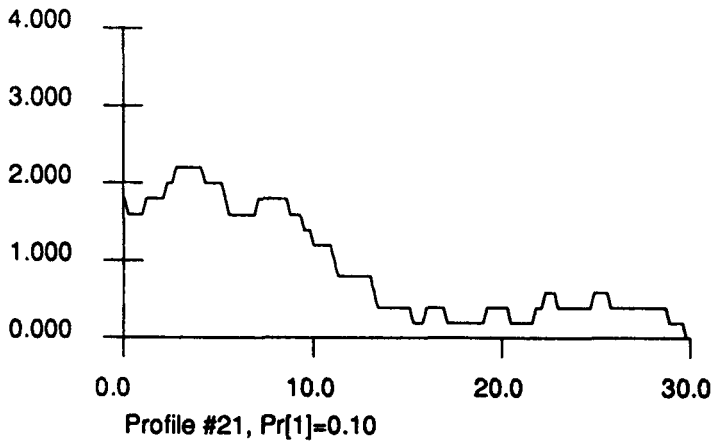
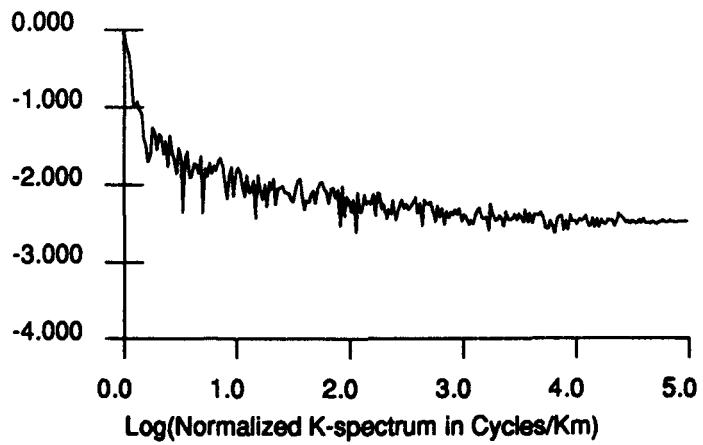
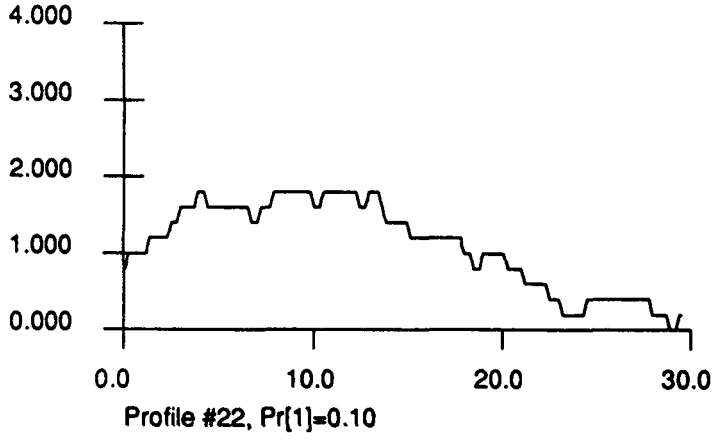

4.000
3.000
2.000
1.000
0.000
0.0
10.0
20.0
30.0
Profile #14, Pr[1]=0.07
0.000
-1.000
-2.000
-3.000
-4.000
0.0
1.0
2.0
3.0
4.0
5.0
Log(Normalized K-spectrum in Cycles/Km)
Pr[1] = 0.07 , Seed = 91333
[L1-jumps]/km = 0.1458
[L2-jumps]/km = 0.0225
RMS elevation = 0.2342
Durbin-Watson # = 0.0266
Peak K-Spectrum = K(0) = 0.2662
1.39 Corners/km
( 40 corners / 28.80km)
Normalized arc length= 1.060
Profile #15, Pr[1]=0.07
Log(Normalized K-spectrum in Cycles/Km)
Pr[1] = 0.07 , Seed = 91350
[L1-jumps]/km = 0.1439
[L2-jumps]/km = 0.0228
RMS elevation = 0.2093
Durbin-Watson # = 0.0329
Peak K-Spectrum = K(0) = 0.3096
1.44 Corners/km
( 40 corners / 27.80km)
Normalized arc length= 1.060
Profile #16, Pr[1]=0.07
Log(Normalized K-spectrum in Cycles/Km)
Pr[1] = 0.07 , Seed = 91285
[L1-jumps]/km = 0.1269
[L2-jumps]/km = 0.0218
RMS elevation = 0.2646
Durbin-Watson # = 0.0181
Peak K-Spectrum = K(0) = 0.2092
1.19 Corners/km
( 32 corners / 26.80km)
Normalized arc length= 1.053

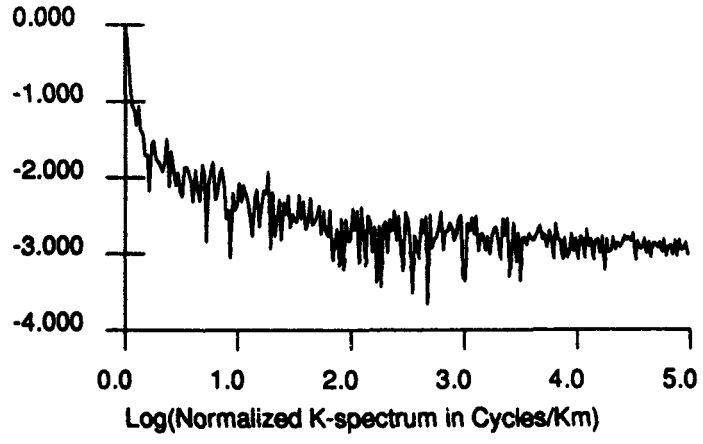
**Figure 2**



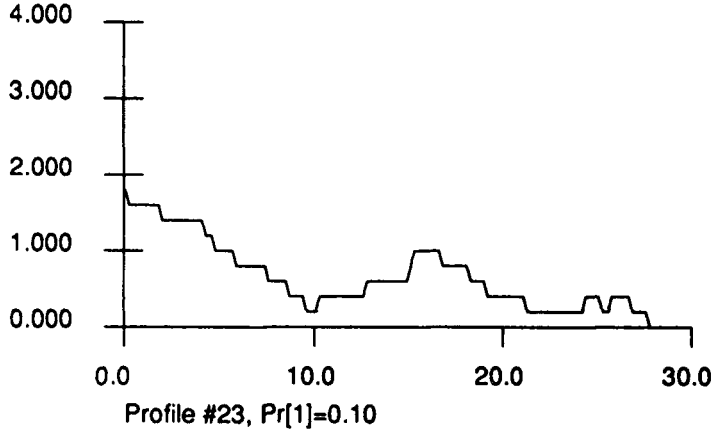



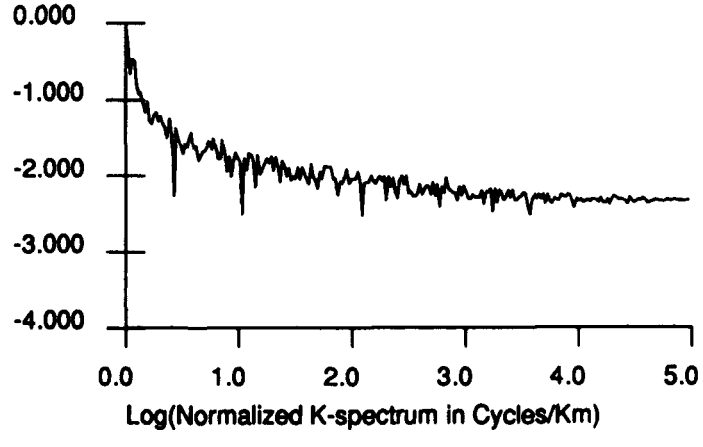

Pr[1] = 0.10 , Seed = 93337
[L1-jumps]/km = 0.1600
[L2-jumps]/km = 0.0245
RMS elevation = 0.6857
Durbin-Watson # = 0.0038
Peak K-Spectrum = K(0) = 0.5283
1.60 Corners/km
( 48 corners / 30.00km)
Normalized arc length= 1.075




Pr[1] = 0.10 , Seed = 93347
[L1-jumps]/km = 0.1824
[L2-jumps]/km = 0.0248
RMS elevation = 0.5573
Durbin-Watson # = 0.0069
Peak K-Spectrum = K(0) = 0.6385
1.76 Corners/km
( 52 corners / 29.60km)
Normalized arc length= 1.076




Pr[1] = 0.10 , Seed = 93356
[L1-jumps]/km = 0.1500
[L2-jumps]/km = 0.0231
RMS elevation = 0.4352
Durbin-Watson # = 0.0079
Peak K-Spectrum = K(0) = 0.3697
1.43 Corners/km
( 40 corners / 28.00km)
Normalized arc length= 1.062

Figure 3

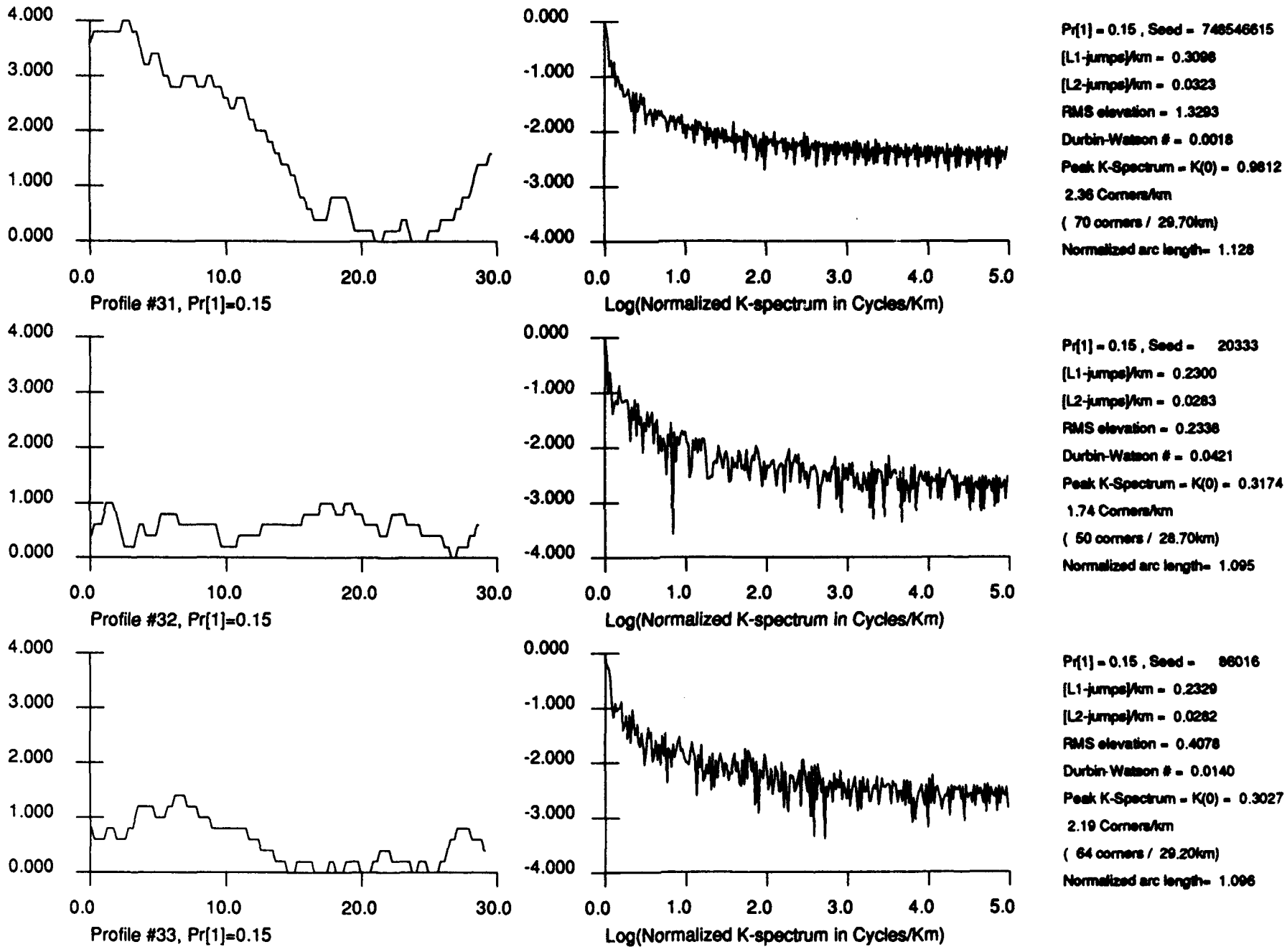
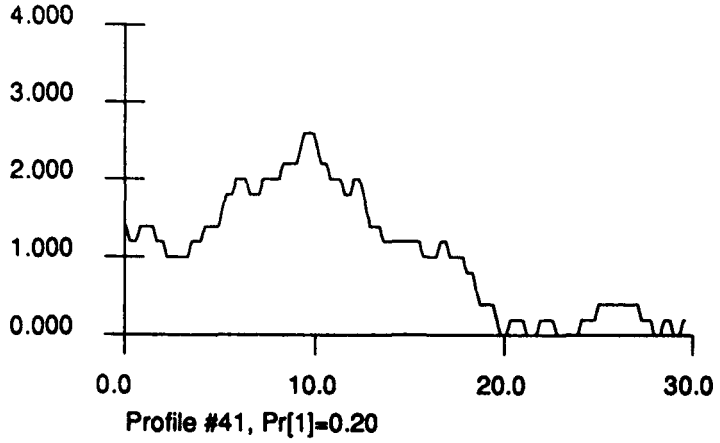
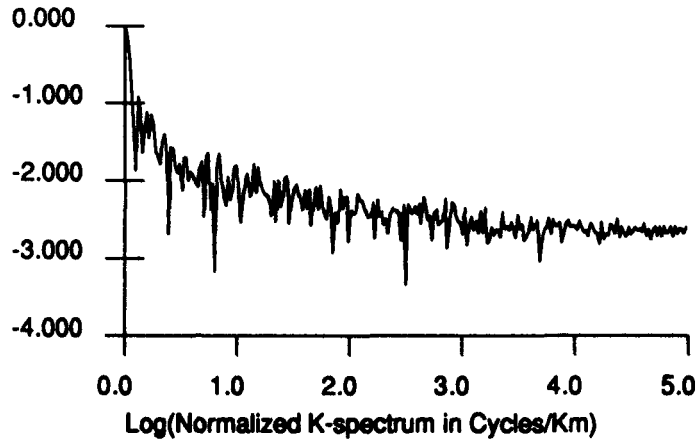
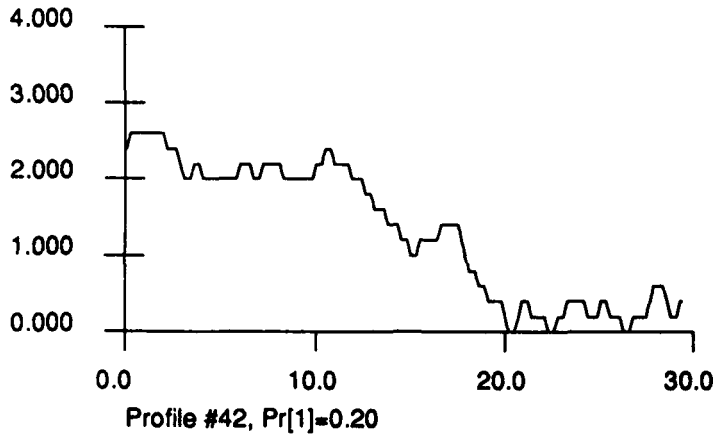

4.000
3.000
2.000
1.000
0.000
0.0
10.0
20.0
30.0
Profile #31, Pr[1]=0.15
0.000
-1.000
-2.000
-3.000
-4.000
0.0
1.0
2.0
3.0
4.0
5.0
Log(Normalized K-spectrum in Cycles/Km)
Pr[1] = 0.15 , Seed = 748546615
[L1-jumps]/km = 0.3096
[L2-jumps]/km = 0.0323
RMS elevation = 1.3293
Durbin-Watson # = 0.0018
Peak K-Spectrum = K(0) = 0.9612
2.36 Corners/km
( 70 corners / 29.70km)
Normalized arc length= 1.128
Profile #32, Pr[1]=0.15
Log(Normalized K-spectrum in Cycles/Km)
Pr[1] = 0.15 , Seed = 20333
[L1-jumps]/km = 0.2300
[L2-jumps]/km = 0.0283
RMS elevation = 0.2338
Durbin-Watson # = 0.0421
Peak K-Spectrum = K(0) = 0.3174
1.74 Corners/km
( 50 corners / 28.70km)
Normalized arc length= 1.095
Profile #33, Pr[1]=0.15
Log(Normalized K-spectrum in Cycles/Km)
Pr[1] = 0.15 , Seed = 86016
[L1-jumps]/km = 0.2329
[L2-jumps]/km = 0.0282
RMS elevation = 0.4078
Durbin-Watson # = 0.0140
Peak K-Spectrum = K(0) = 0.3027
2.19 Corners/km
( 64 corners / 29.20km)
Normalized arc length= 1.096

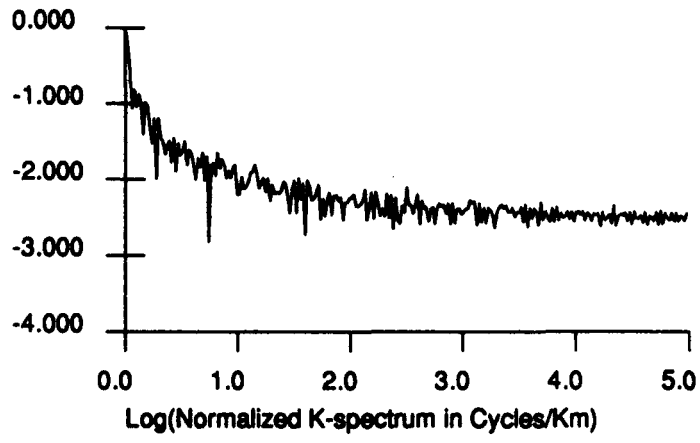
**Figure 4**



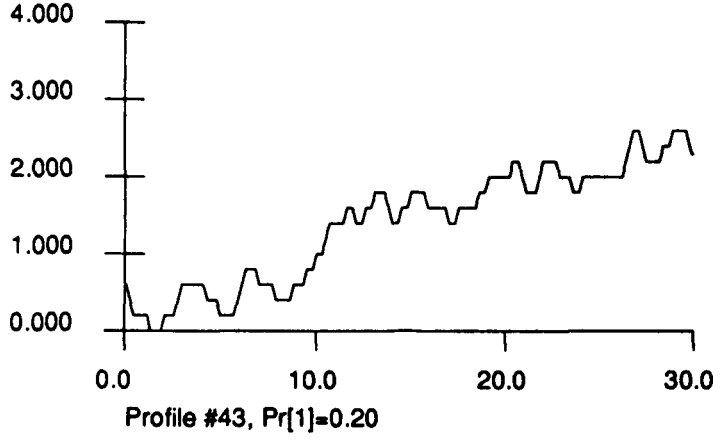



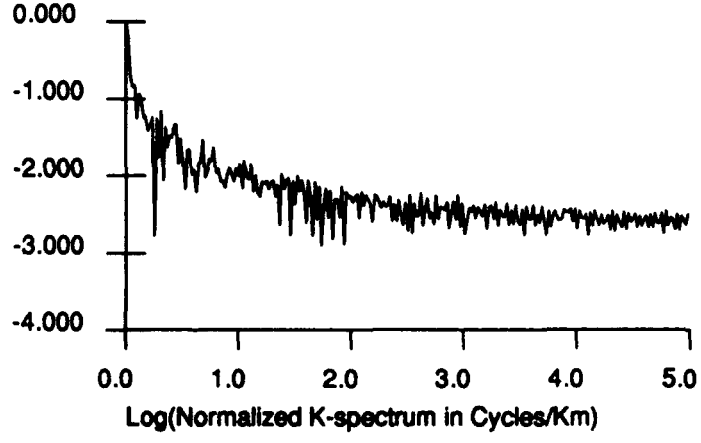

Pr[1] = 0.20 , Seed = 93397
[L1-jumps]/km = 0.2828
[L2-jumps]/km = 0.0309
RMS elevation = 0.7560
Durbin-Watson # = 0.0049
Peak K-Spectrum = K(0) = 0.5992
2.36 Corners/km
( 70 corners / 29.70km)
Normalized arc length= 1.117




Pr[1] = 0.20 , Seed = 93407
[L1-jumps]/km = 0.2983
[L2-jumps]/km = 0.0318
RMS elevation = 0.8779
Durbin-Watson # = 0.0039
Peak K-Spectrum = K(0) = 0.7512
2.51 Corners/km
( 74 corners / 29.50km)
Normalized arc length= 1.124




Pr[1] = 0.20 , Seed = 12345
[L1-jumps]/km = 0.3156
[L2-jumps]/km = 0.0324
RMS elevation = 0.7514
Durbin-Watson # = 0.0056
Peak K-Spectrum = K(0) = 0.8188
2.39 Corners/km
( 72 corners / 30.10km)
Normalized arc length= 1.131

**Figure 5**

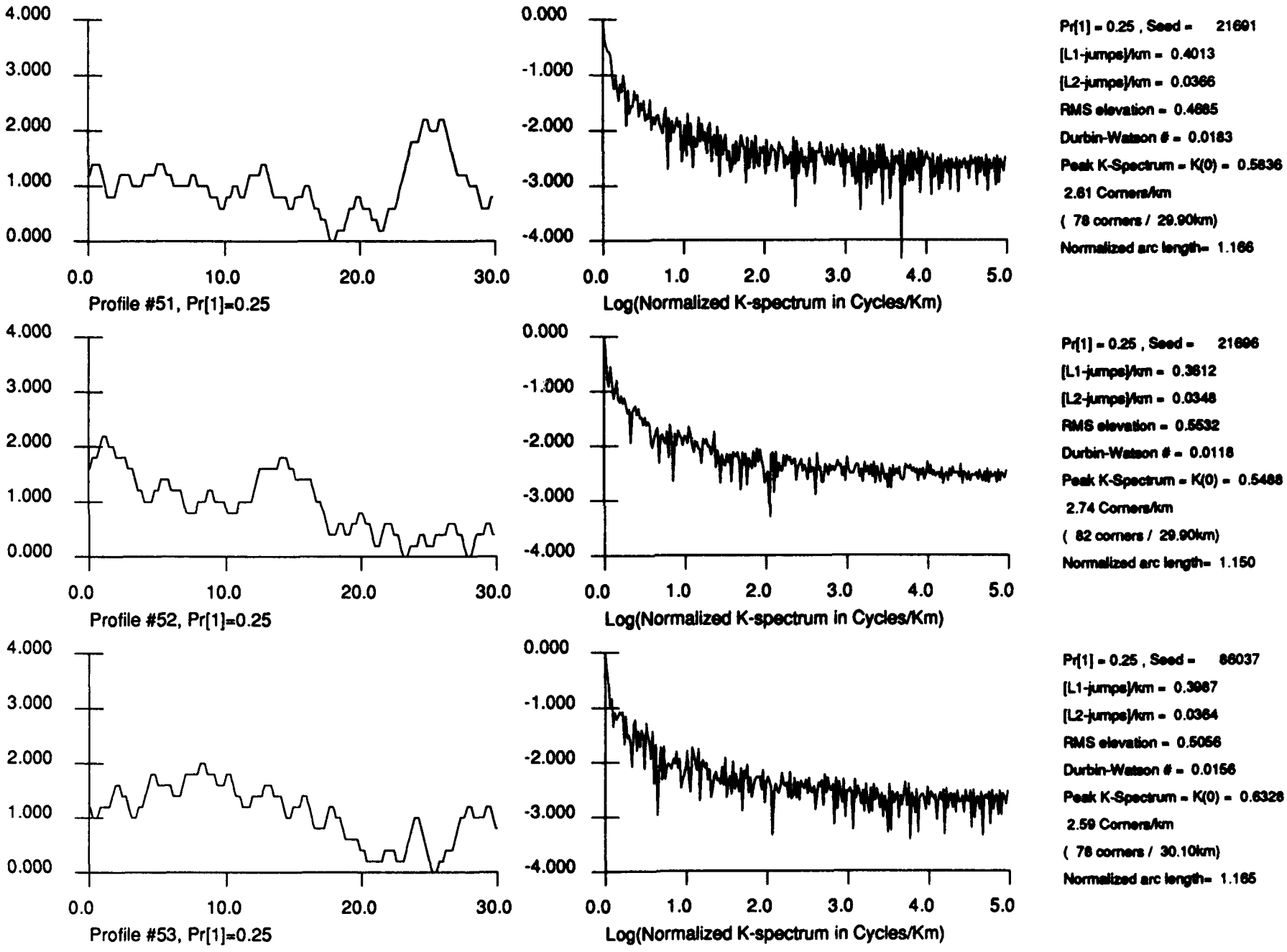

4.000
3.000
2.000
1.000
0.000
0.0
10.0
20.0
30.0
Profile #51, Pr[1]=0.25
0.000
-1.000
-2.000
-3.000
-4.000
0.0
1.0
2.0
3.0
4.0
5.0
Log(Normalized K-spectrum in Cycles/Km)
Pr[1] = 0.25 , Seed = 21691
[L1-jumps]/km = 0.4013
[L2-jumps]/km = 0.0366
RMS elevation = 0.4685
Durbin-Watson # = 0.0183
Peak K-Spectrum = K(0) = 0.5836
2.61 Corners/km
( 78 corners / 29.90km)
Normalized arc length= 1.166
Profile #52, Pr[1]=0.25
Log(Normalized K-spectrum in Cycles/Km)
Pr[1] = 0.25 , Seed = 21696
[L1-jumps]/km = 0.3612
[L2-jumps]/km = 0.0348
RMS elevation = 0.5532
Durbin-Watson # = 0.0118
Peak K-Spectrum = K(0) = 0.5488
2.74 Corners/km
( 82 corners / 29.90km)
Normalized arc length= 1.150
Profile #53, Pr[1]=0.25
Log(Normalized K-spectrum in Cycles/Km)
Pr[1] = 0.25 , Seed = 86037
[L1-jumps]/km = 0.3987
[L2-jumps]/km = 0.0364
RMS elevation = 0.5056
Durbin-Watson # = 0.0156
Peak K-Spectrum = K(0) = 0.6328
2.59 Corners/km
( 78 corners / 30.10km)
Normalized arc length= 1.165

Figure 6

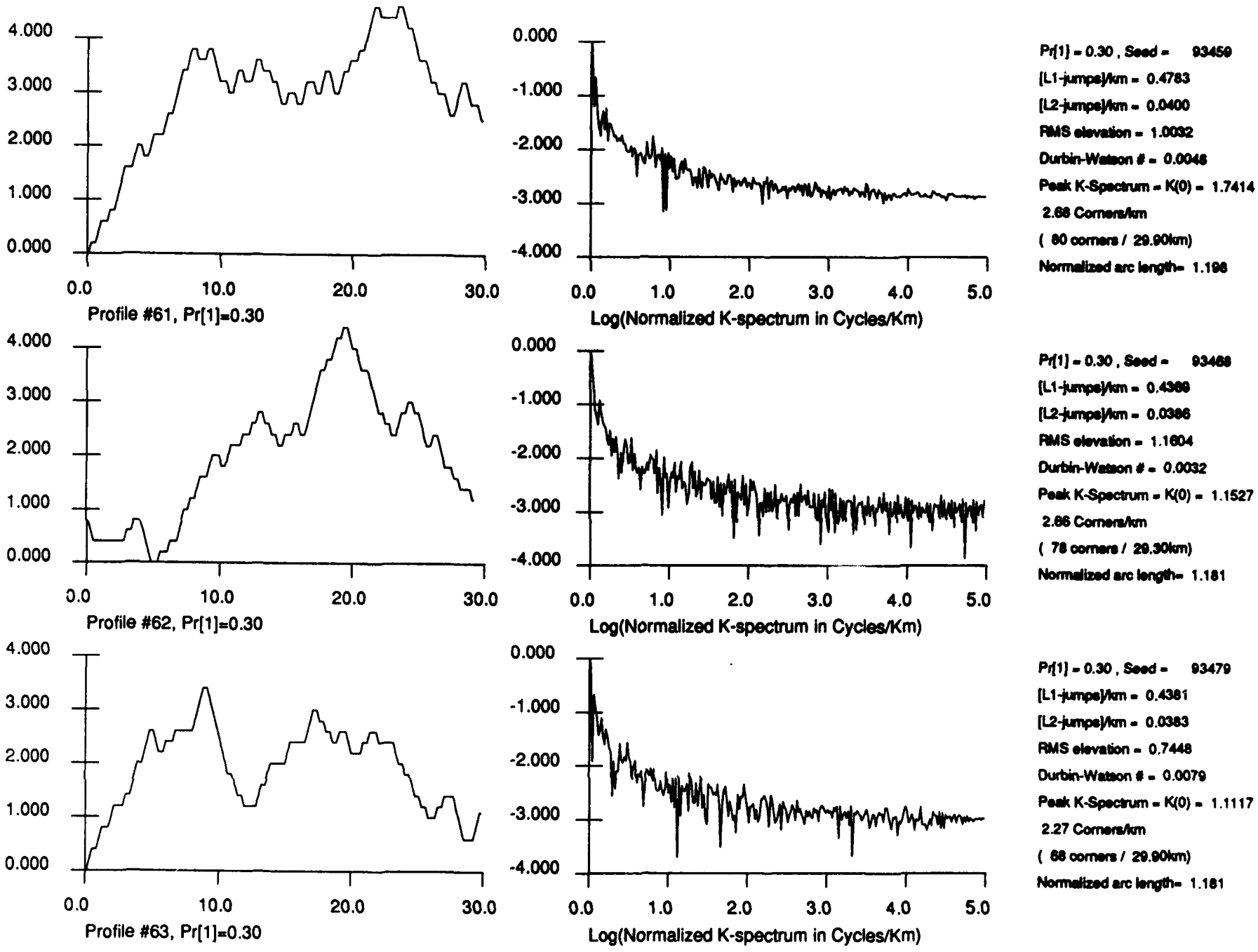

4.000
3.000
2.000
1.000
0.000
0.0
10.0
20.0
30.0
Profile #61, Pr[1]=0.30
0.000
-1.000
-2.000
-3.000
-4.000
0.0
1.0
2.0
3.0
4.0
5.0
Log(Normalized K-spectrum in Cycles/Km)
Pr[1] = 0.30 , Seed = 93459
[L1-jumps]/km = 0.4783
[L2-jumps]/km = 0.0400
RMS elevation = 1.0032
Durbin-Watson # = 0.0046
Peak K-Spectrum = K(0) = 1.7414
2.68 Corners/km
( 80 corners / 29.90km)
Normalized arc length= 1.198
Profile #62, Pr[1]=0.30
Log(Normalized K-spectrum in Cycles/Km)
Pr[1] = 0.30 , Seed = 93469
[L1-jumps]/km = 0.4369
[L2-jumps]/km = 0.0366
RMS elevation = 1.1604
Durbin-Watson # = 0.0032
Peak K-Spectrum = K(0) = 1.1527
2.66 Corners/km
( 78 corners / 29.30km)
Normalized arc length= 1.181
Profile #63, Pr[1]=0.30
Log(Normalized K-spectrum in Cycles/Km)
Pr[1] = 0.30 , Seed = 93479
[L1-jumps]/km = 0.4361
[L2-jumps]/km = 0.0383
RMS elevation = 0.7448
Durbin-Watson # = 0.0079
Peak K-Spectrum = K(0) = 1.1117
2.27 Corners/km
( 68 corners / 29.90km)
Normalized arc length= 1.181

Figure 7

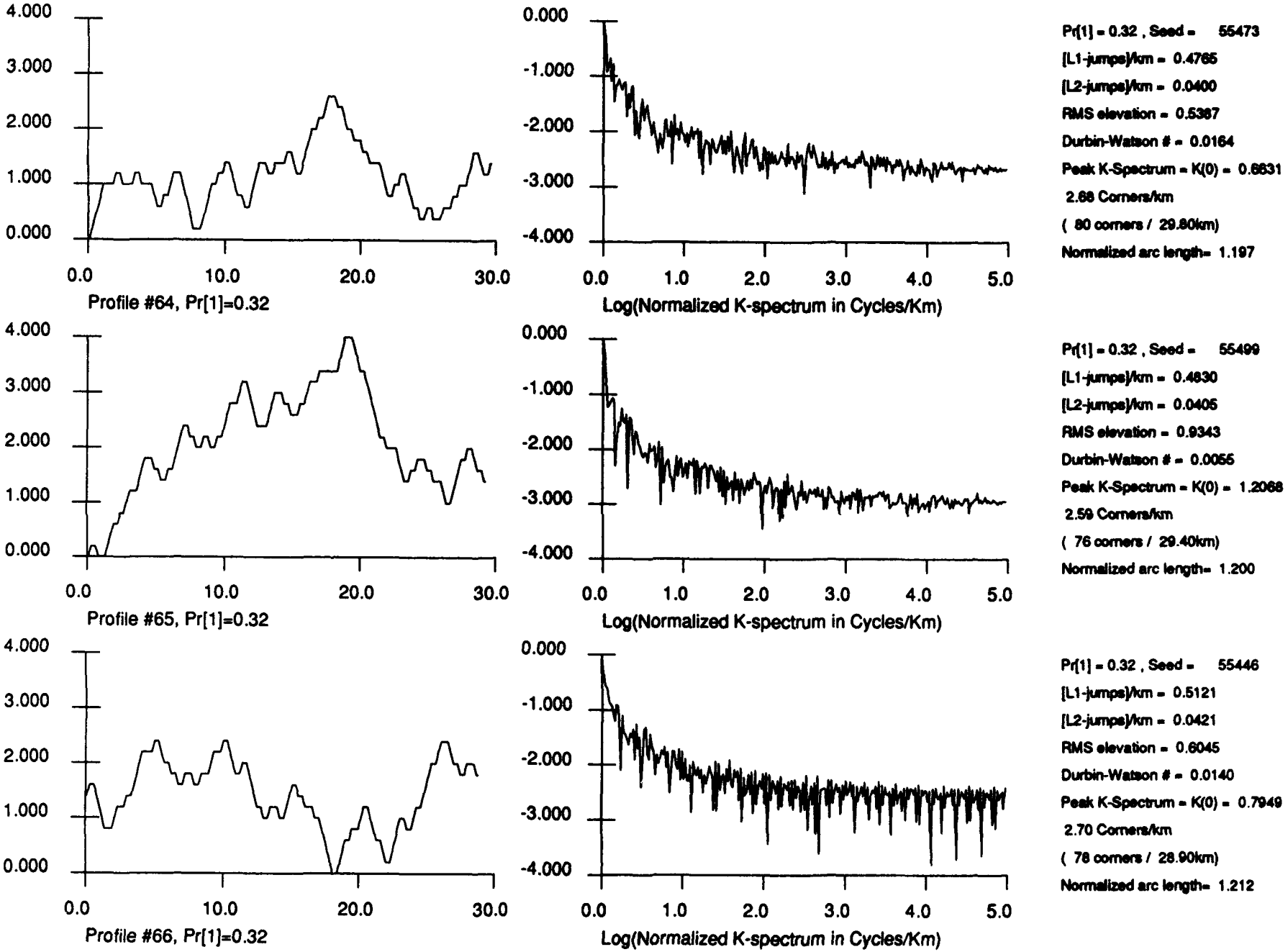

4.000
3.000
2.000
1.000
0.000
0.0
10.0
20.0
30.0
Profile #64, Pr[1]=0.32
0.000
-1.000
-2.000
-3.000
-4.000
0.0
1.0
2.0
3.0
4.0
5.0
Log(Normalized K-spectrum in Cycles/Km)
Pr[1] = 0.32 , Seed = 55473
[L1-jumps]/km = 0.4765
[L2-jumps]/km = 0.0400
RMS elevation = 0.5367
Durbin-Watson # = 0.0164
Peak K-Spectrum = K(0) = 0.6831
2.68 Corners/km
( 80 corners / 29.80km)
Normalized arc length= 1.197
Profile #65, Pr[1]=0.32
Log(Normalized K-spectrum in Cycles/Km)
Pr[1] = 0.32 , Seed = 55499
[L1-jumps]/km = 0.4830
[L2-jumps]/km = 0.0405
RMS elevation = 0.9343
Durbin-Watson # = 0.0055
Peak K-Spectrum = K(0) = 1.2068
2.59 Corners/km
( 76 corners / 29.40km)
Normalized arc length= 1.200
Profile #66, Pr[1]=0.32
Log(Normalized K-spectrum in Cycles/Km)
Pr[1] = 0.32 , Seed = 55446
[L1-jumps]/km = 0.5121
[L2-jumps]/km = 0.0421
RMS elevation = 0.6045
Durbin-Watson # = 0.0140
Peak K-Spectrum = K(0) = 0.7949
2.70 Corners/km
( 78 corners / 28.90km)
Normalized arc length= 1.212

**Figure 8**

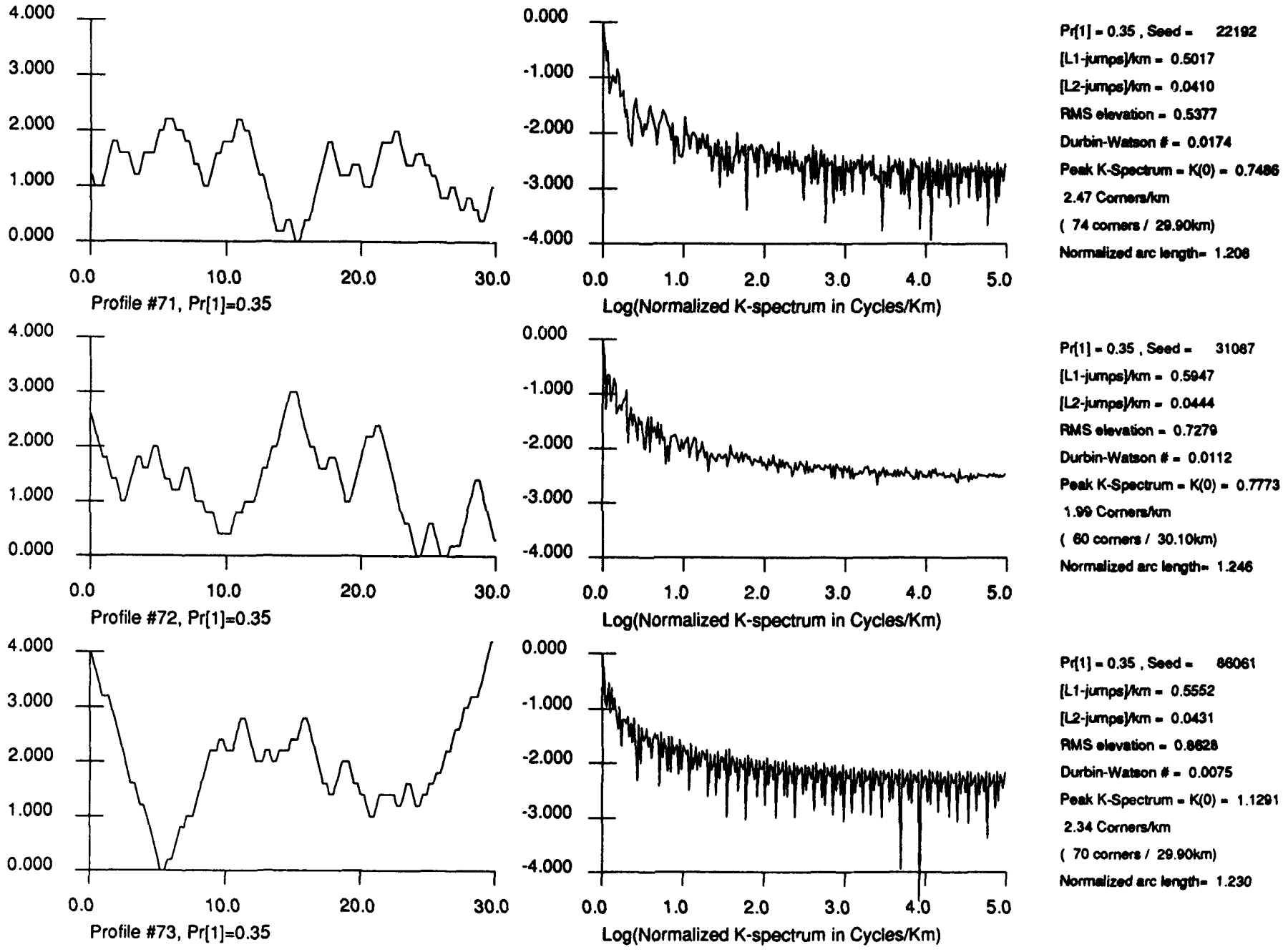
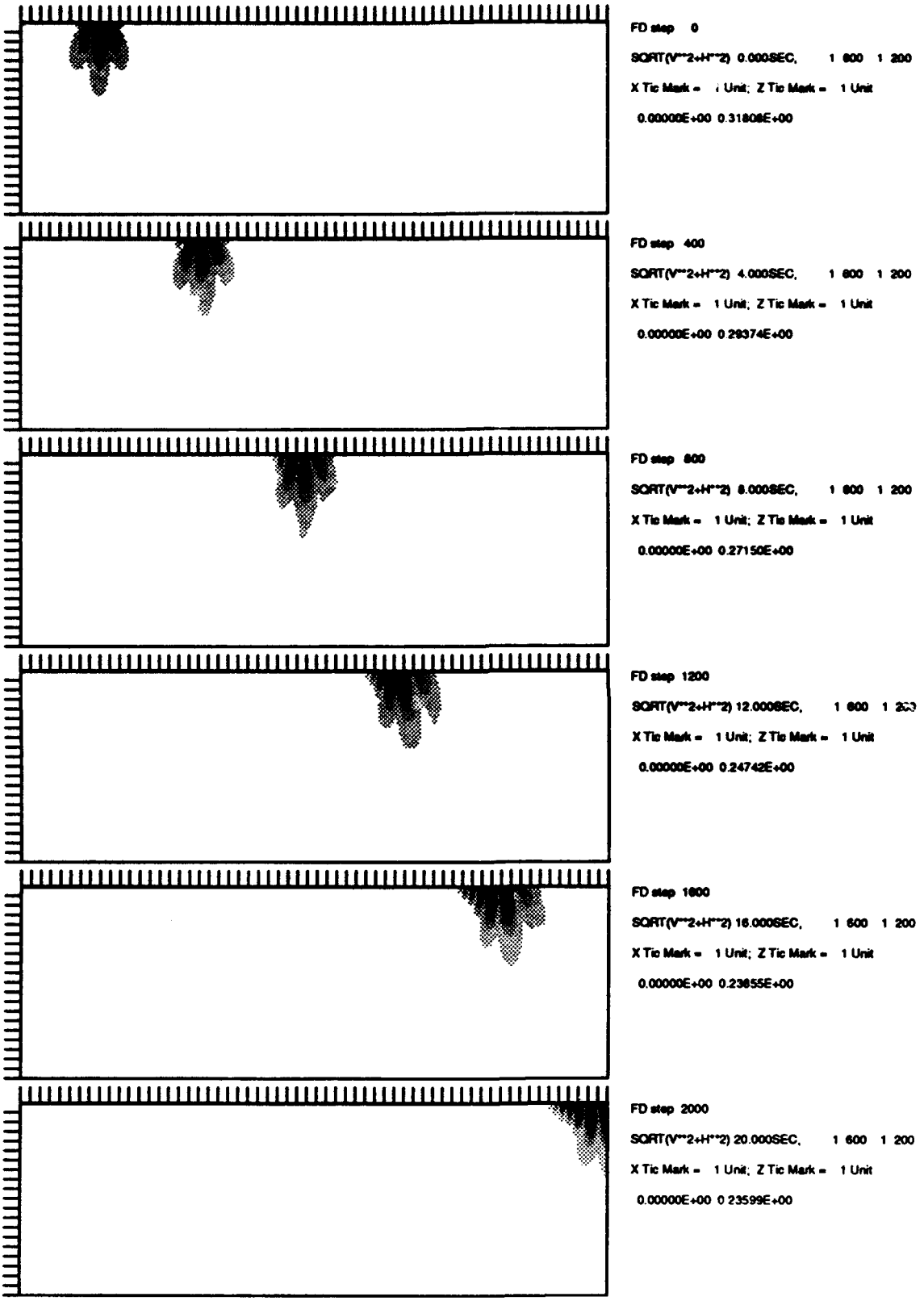

4.000
3.000
2.000
1.000
0.000
0.0
10.0
20.0
30.0
Profile #71, Pr[1]=0.35
0.000
-1.000
-2.000
-3.000
-4.000
0.0
1.0
2.0
3.0
4.0
5.0
Log(Normalized K-spectrum in Cycles/Km)
Pr[1] = 0.35 , Seed = 22192
[L1-jumps]/km = 0.5017
[L2-jumps]/km = 0.0410
RMS elevation = 0.5377
Durbin-Watson # = 0.0174
Peak K-Spectrum = K(0) = 0.7486
2.47 Corners/km
( 74 corners / 29.90km)
Normalized arc length= 1.208
Profile #72, Pr[1]=0.35
Log(Normalized K-spectrum in Cycles/Km)
Pr[1] = 0.35 , Seed = 31087
[L1-jumps]/km = 0.5947
[L2-jumps]/km = 0.0444
RMS elevation = 0.7279
Durbin-Watson # = 0.0112
Peak K-Spectrum = K(0) = 0.7773
1.99 Corners/km
( 60 corners / 30.10km)
Normalized arc length= 1.246
Profile #73, Pr[1]=0.35
Log(Normalized K-spectrum in Cycles/Km)
Pr[1] = 0.35 , Seed = 86061
[L1-jumps]/km = 0.5552
[L2-jumps]/km = 0.0431
RMS elevation = 0.8628
Durbin-Watson # = 0.0075
Peak K-Spectrum = K(0) = 1.1291
2.34 Corners/km
( 70 corners / 29.90km)
Normalized arc length= 1.230

Figure 9




Rg (1Hz:2.665km); Grid 600*500 [dx=0.1km,dt=10ms]
Profile 00 (seed 00, Pr(1)=00)

**Figure 10**

RATIO vers 1.5

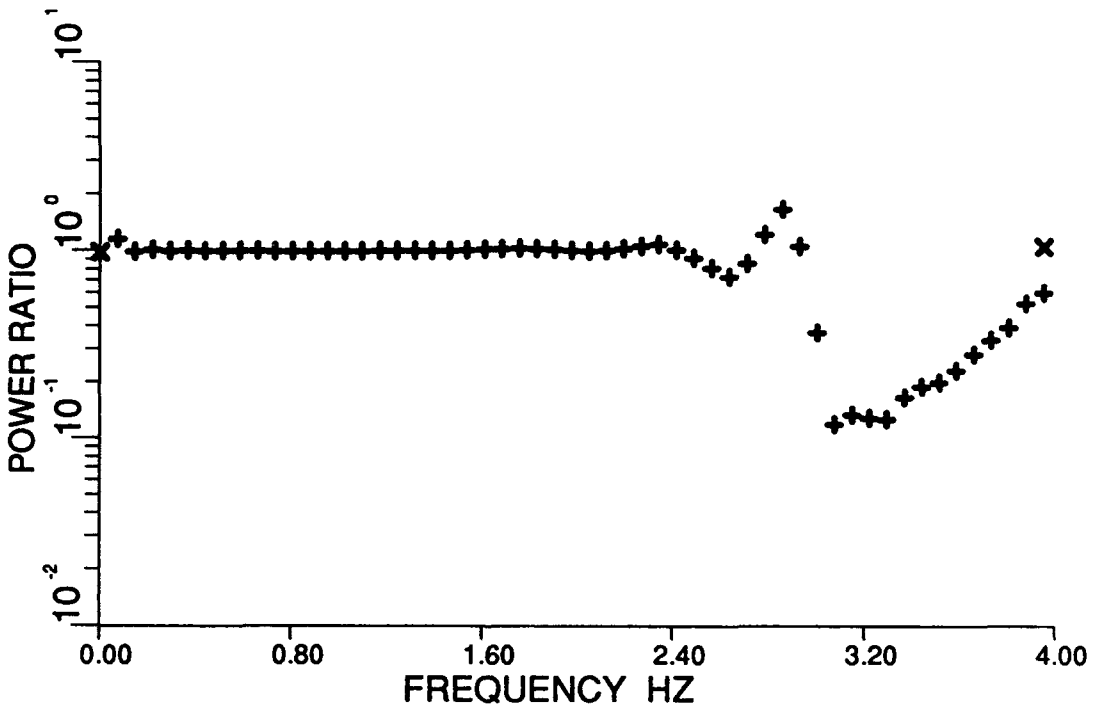
Wed Oct 27 10:16:11 1993

Model 00

NOISE POWER NOT SUBTRACTED FROM SIGNAL POWER

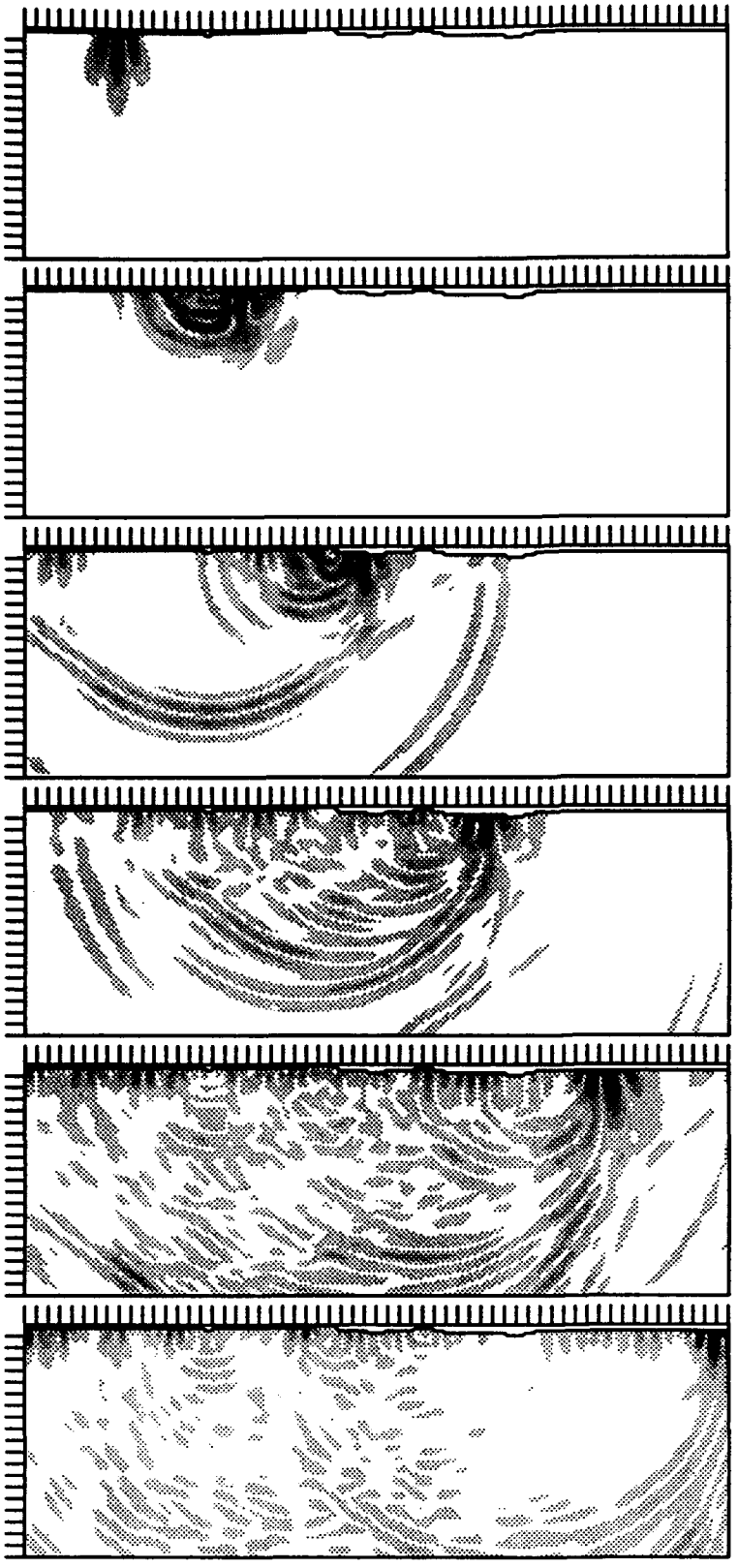
S/N POWER THRESHOLD = 2.0 N

NO SMOOTHING



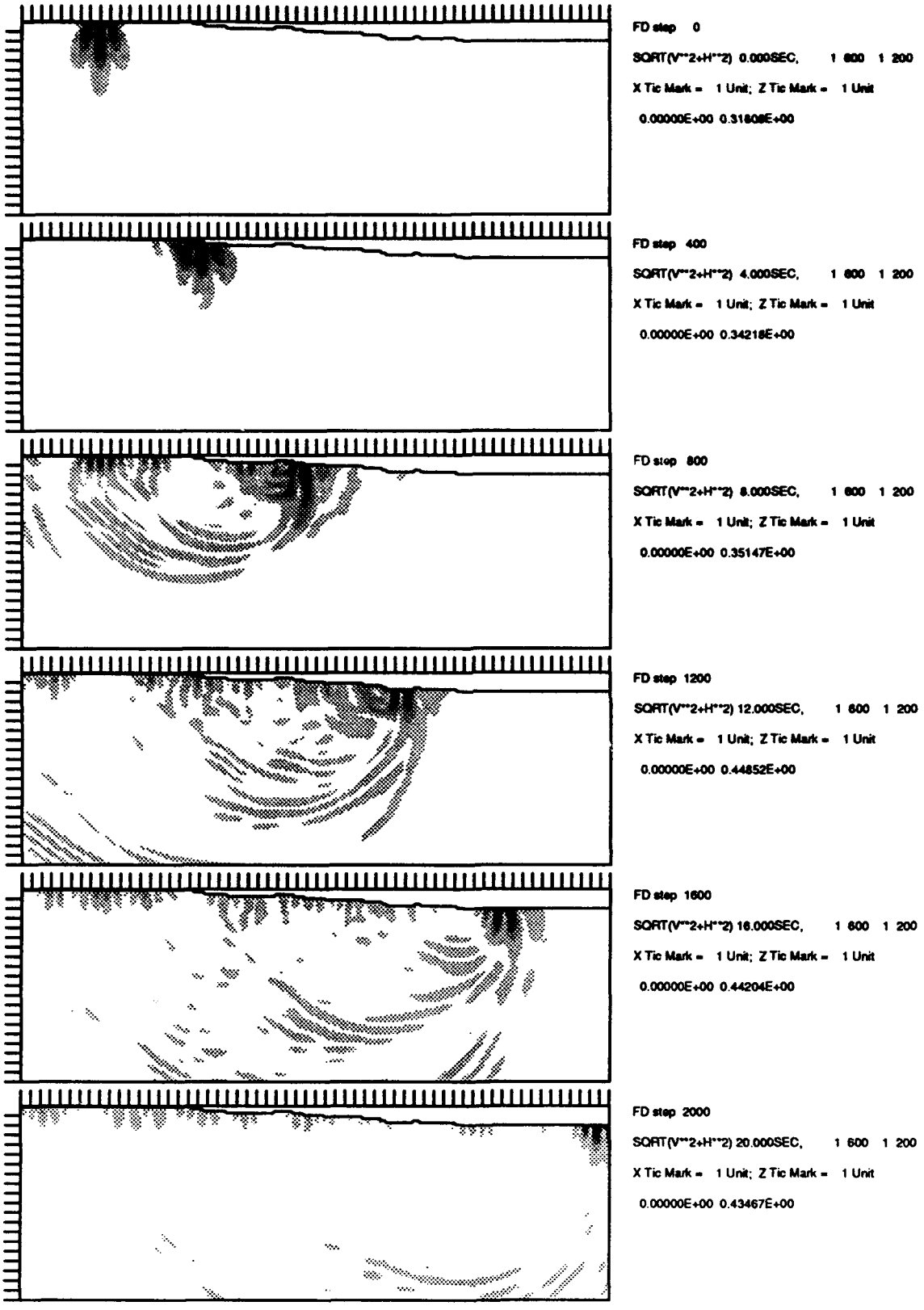

| FREQ BAND | SLOPE | +/- | Y INTERC | AV INTEG | AV RATIO | SD |
|---|---|---|---|---|---|---|
| 0.75-1.25 | 5.869e-03 | 1.118e-03 | 9.776e-01 | -3.947e-03 | -3.798e-03 | 1.040e-03 |
| 0.50-1.50 | 1.023e-03 | 1.011e-03 | 9.907e-01 | -3.047e-03 | -3.058e-03 | 1.201e-03 |
| 0.01-1.00 | -3.351e-02 | 1.422e-02 | 1.047e+00 | 2.943e-03 | 2.685e-03 | 1.747e-02 |
| 1.00-2.00 | 1.037e-02 | 3.236e-03 | 9.670e-01 | 9.790e-04 | 9.942e-04 | 4.884e-03 |
| 0.50-3.00 | 5.904e-03 | 1.235e-02 | 9.772e-01 | 3.371e-04 | 1.670e-04 | 5.272e-02 |

Figure 11




Rg (1Hz:2.665km); Grid 600*500 [dx=0.1km,dt=10ms]
Profile 11 (seed 22887, Pr(1)=0.05)

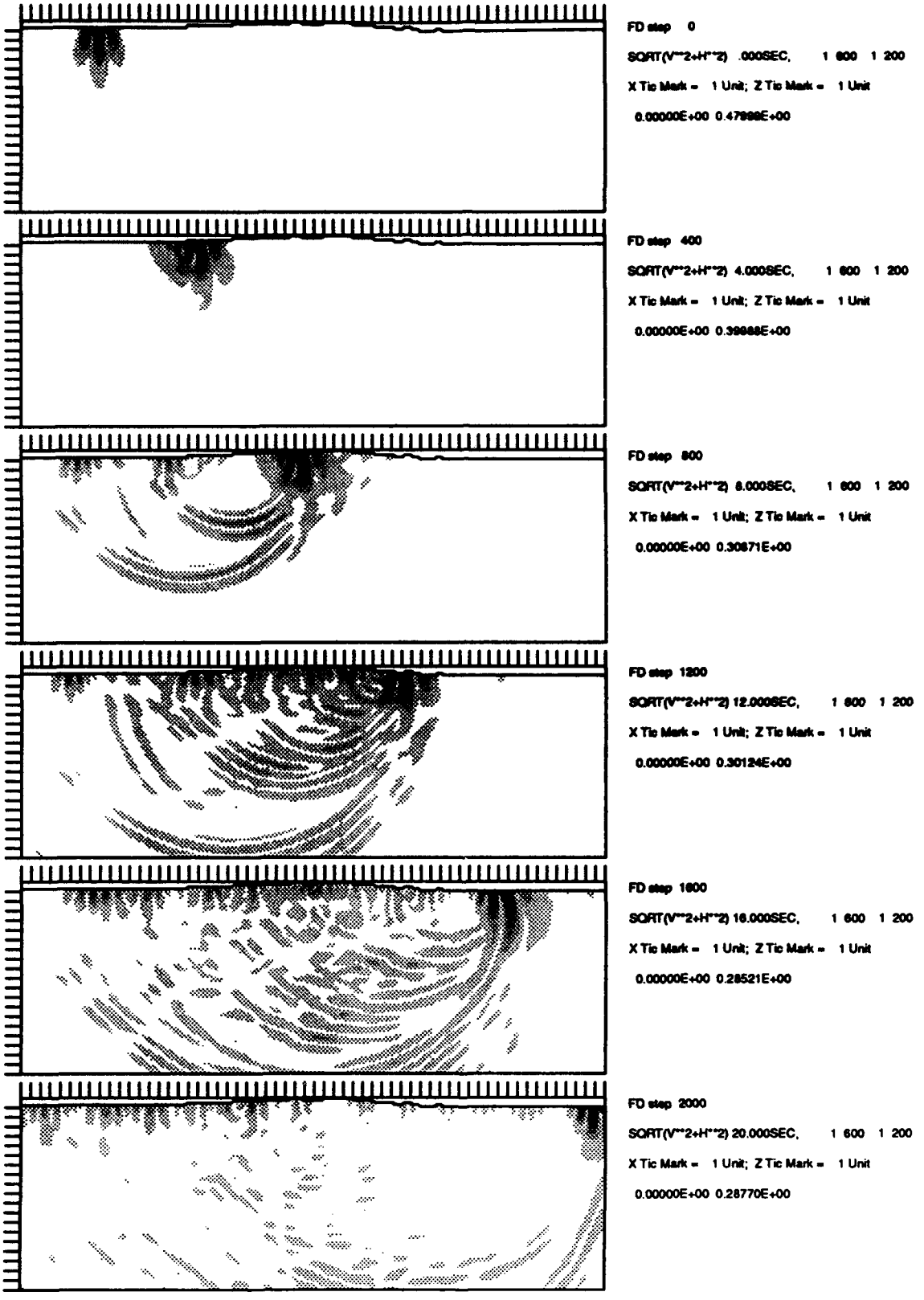
**Figure 12**




Rg (1Hz:2.665km); Grid 600*500 [dx=0.1km,dt=10ms]

Profile 12 (seed 22892, Pr(1)=0.05)

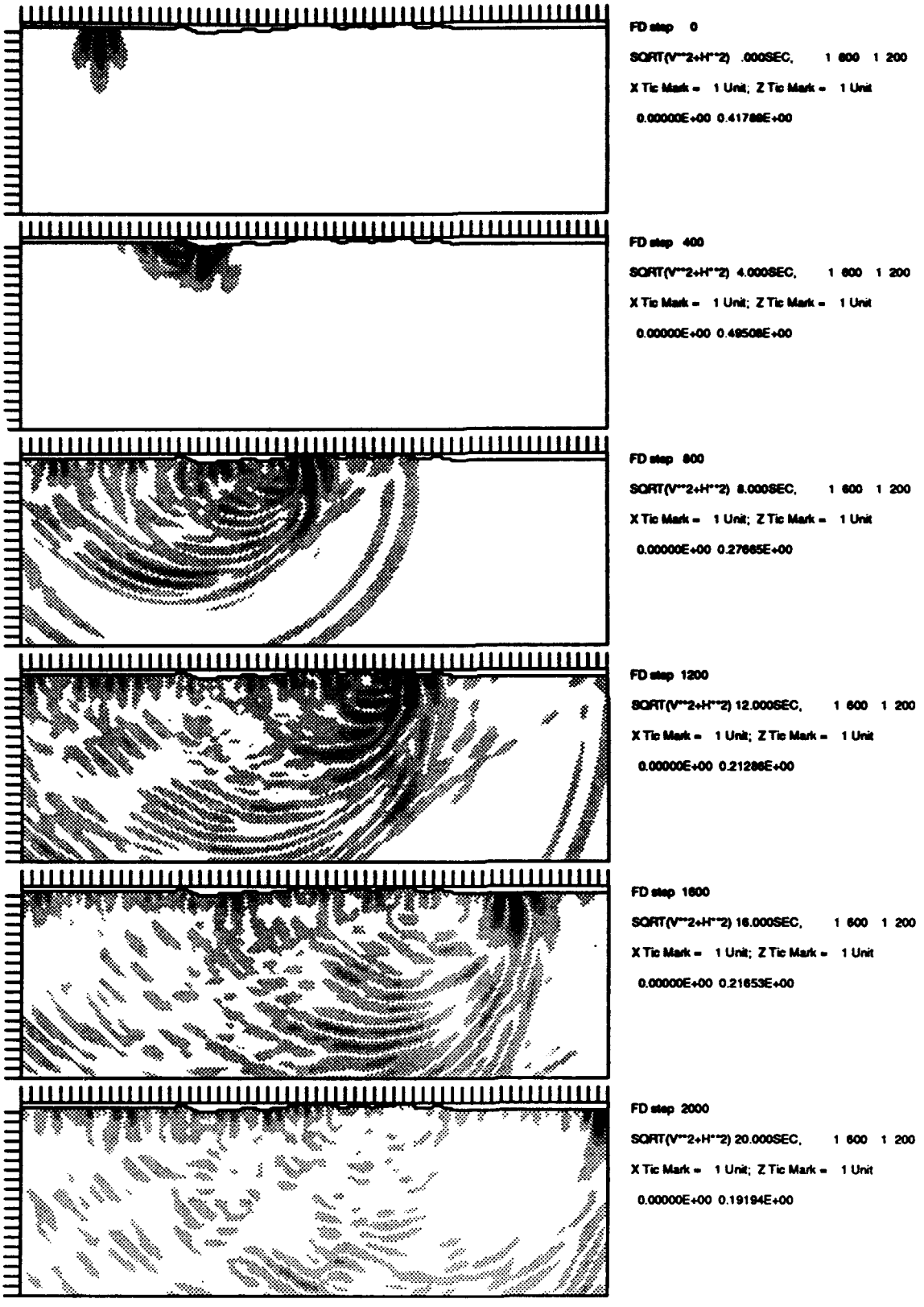
**Figure 13**




Rg (1Hz:2.665km); Grid 600*500 [dx=0.1km,dt=10ms]

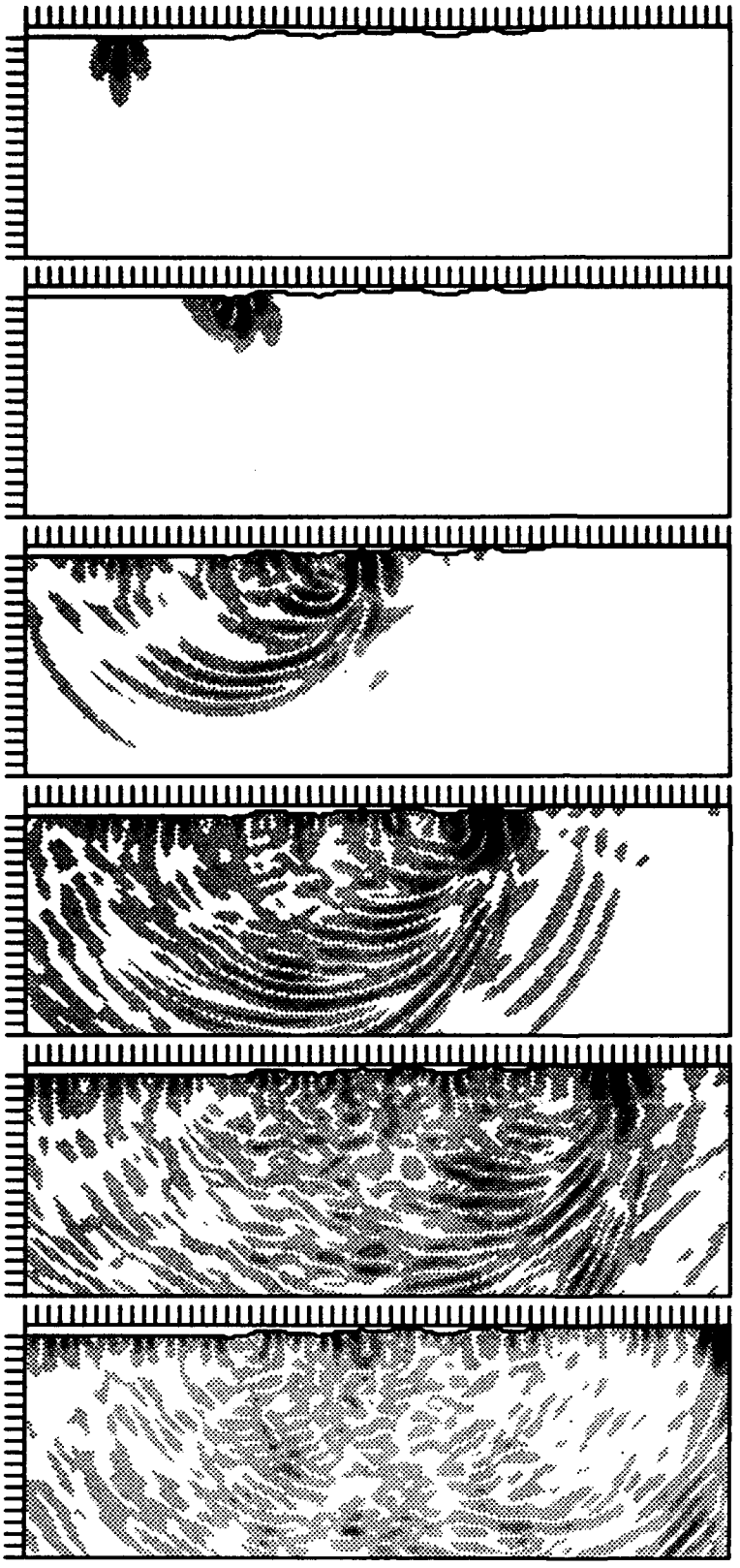
Profile 13 (seed 85995, Pr(1)=0.05)

**Figure 14**



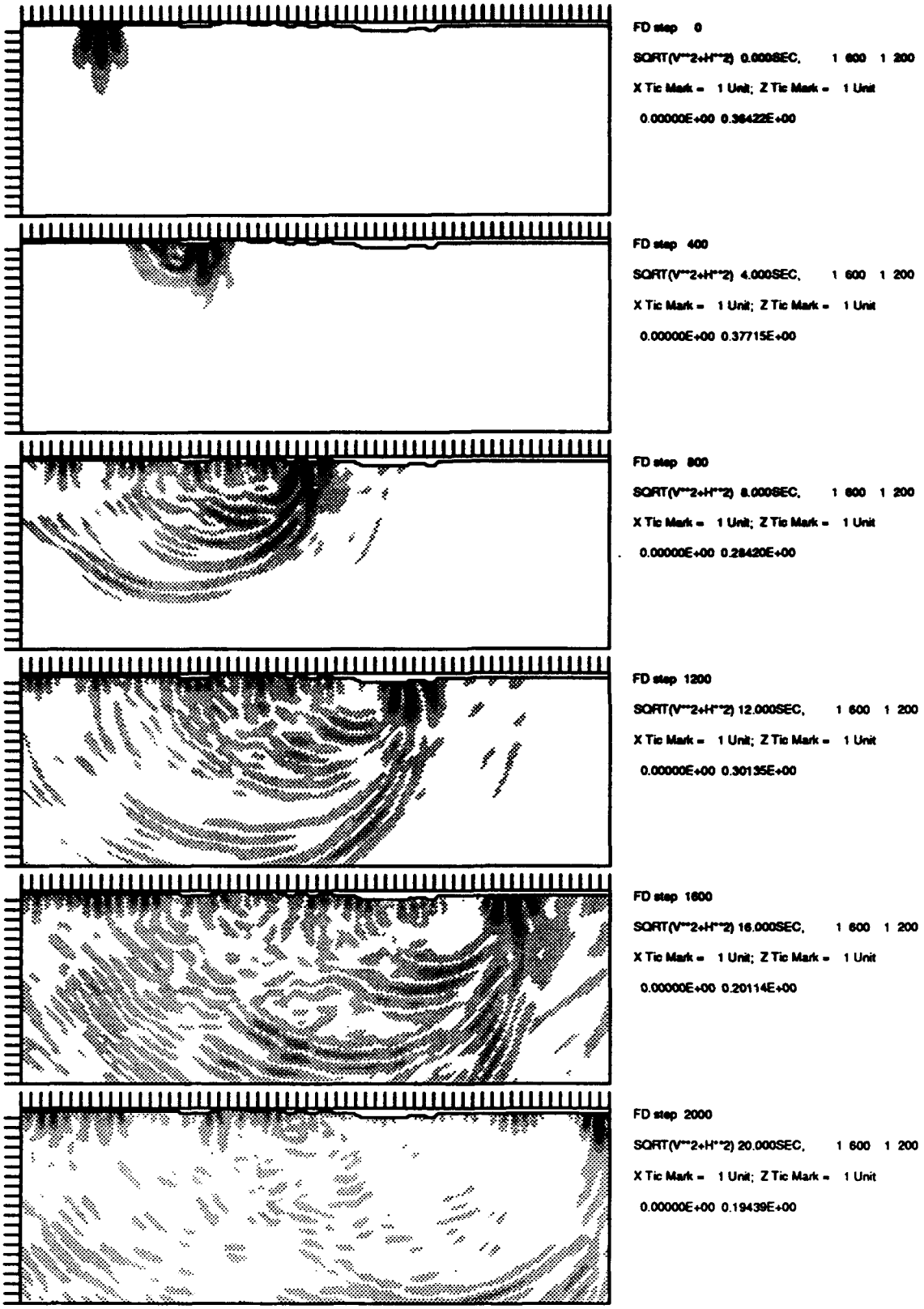

Rg (1Hz:2.665km); Grid 600*500 [dx=0.1km,dt=10ms]
Profile 14 (seed 91333, Pr(1)=0.07)

Figure 15



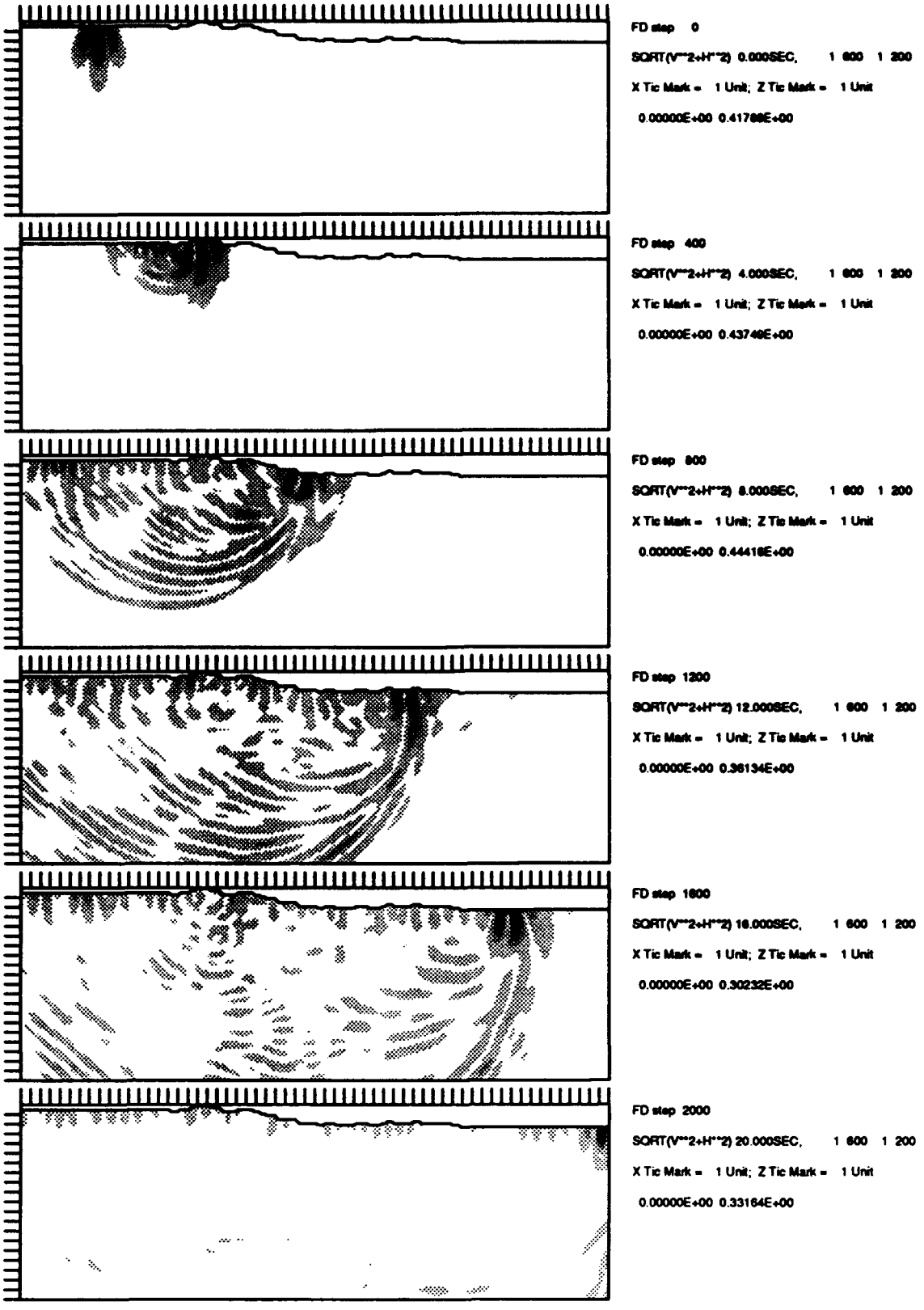

Rg (1Hz:2.665km); Grid 600*500 [dx=0.1km,dt=10ms]
Profile 15 (seed 91350, Pr(1)=0.07)

**Figure 16**



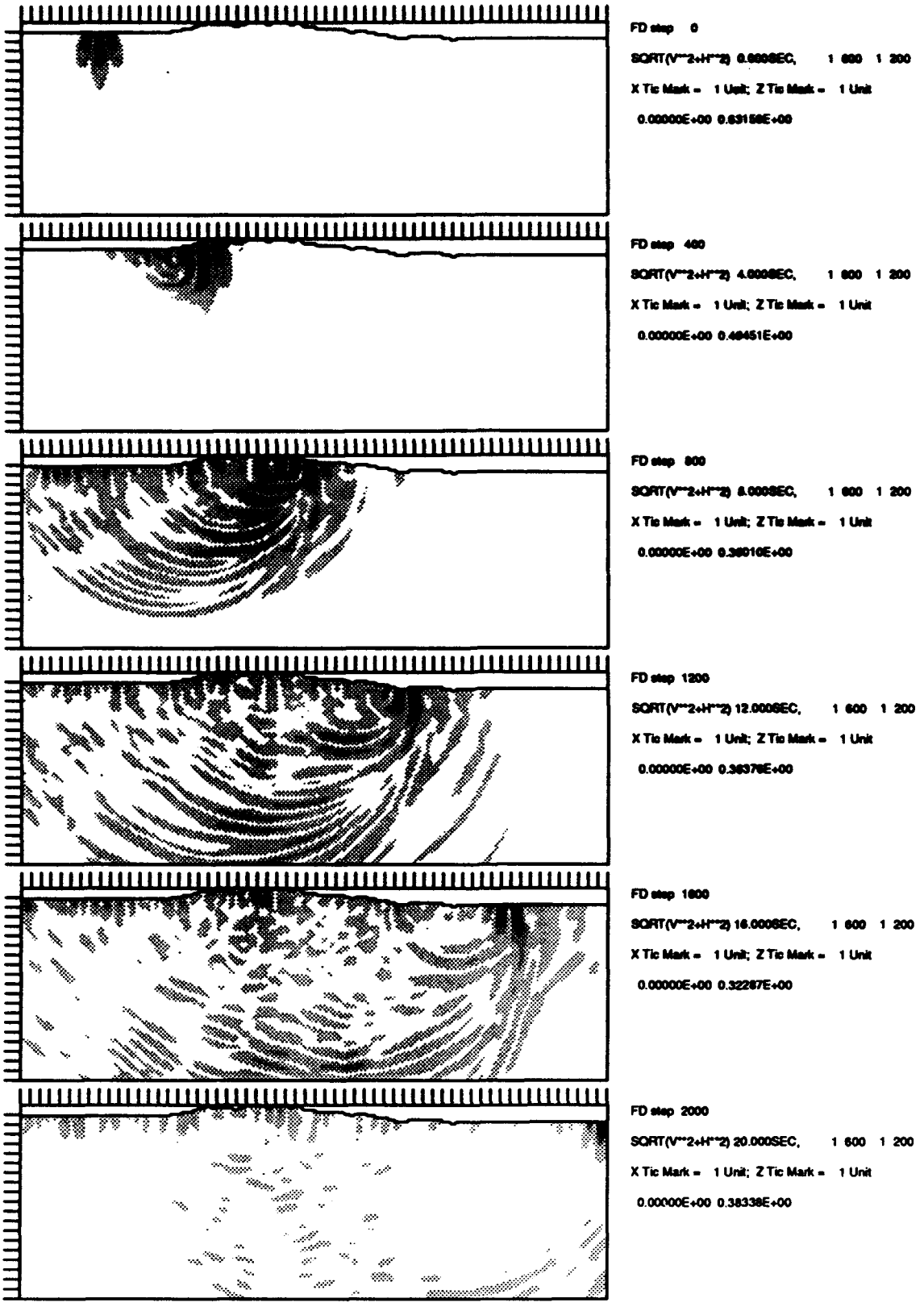

Rg (1Hz:2.665km); Grid 600*500 [dx=0.1km,dt=10ms]
Profile 16 (seed 91285, Pr(1)=0.07)

Figure 17



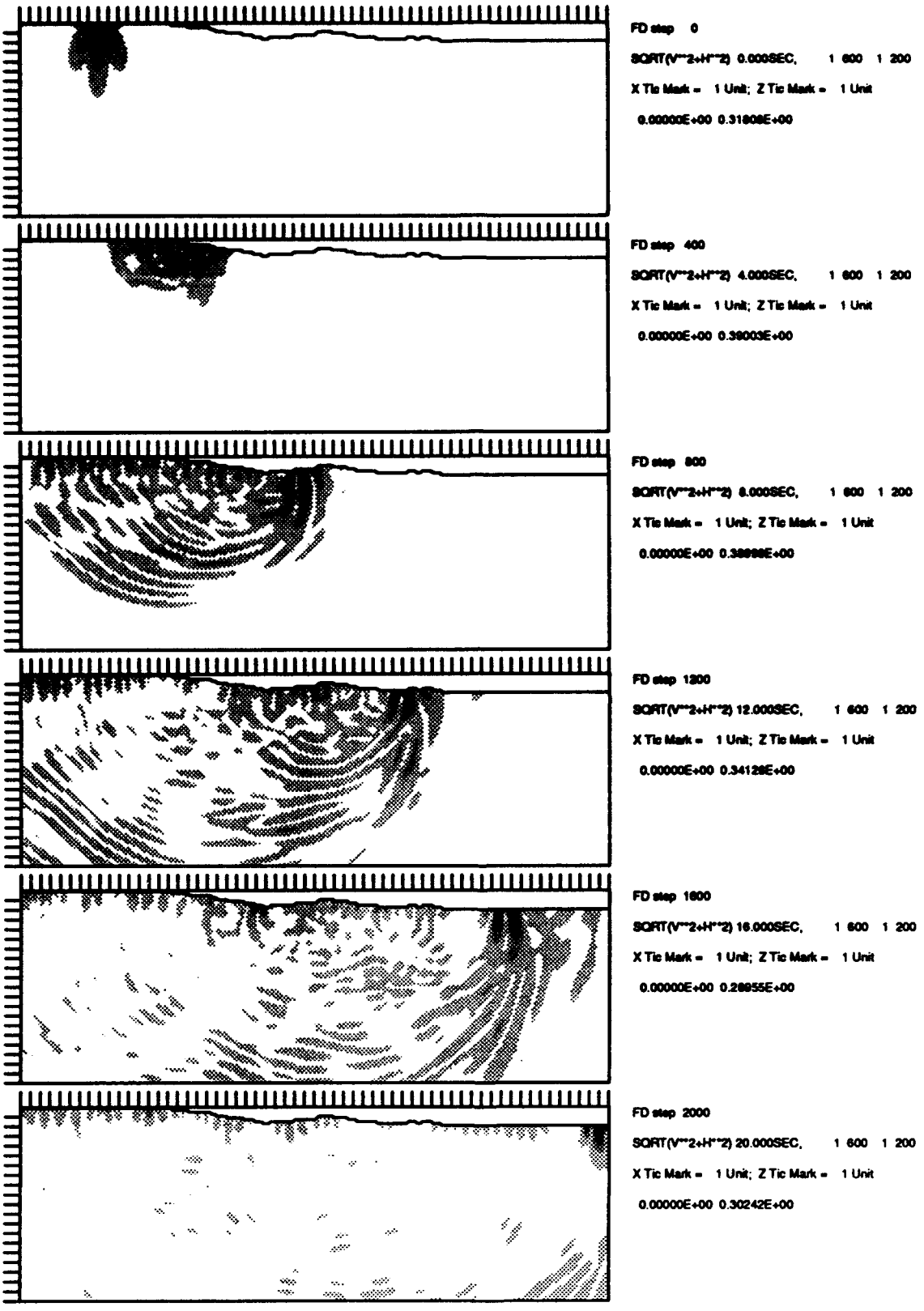

Rg (1Hz:2.665km); Grid 600*500 [dx=0.1km,dt=10ms]
Profile 21 (seed 93337, Pr(1)=0.10)

**Figure 18**



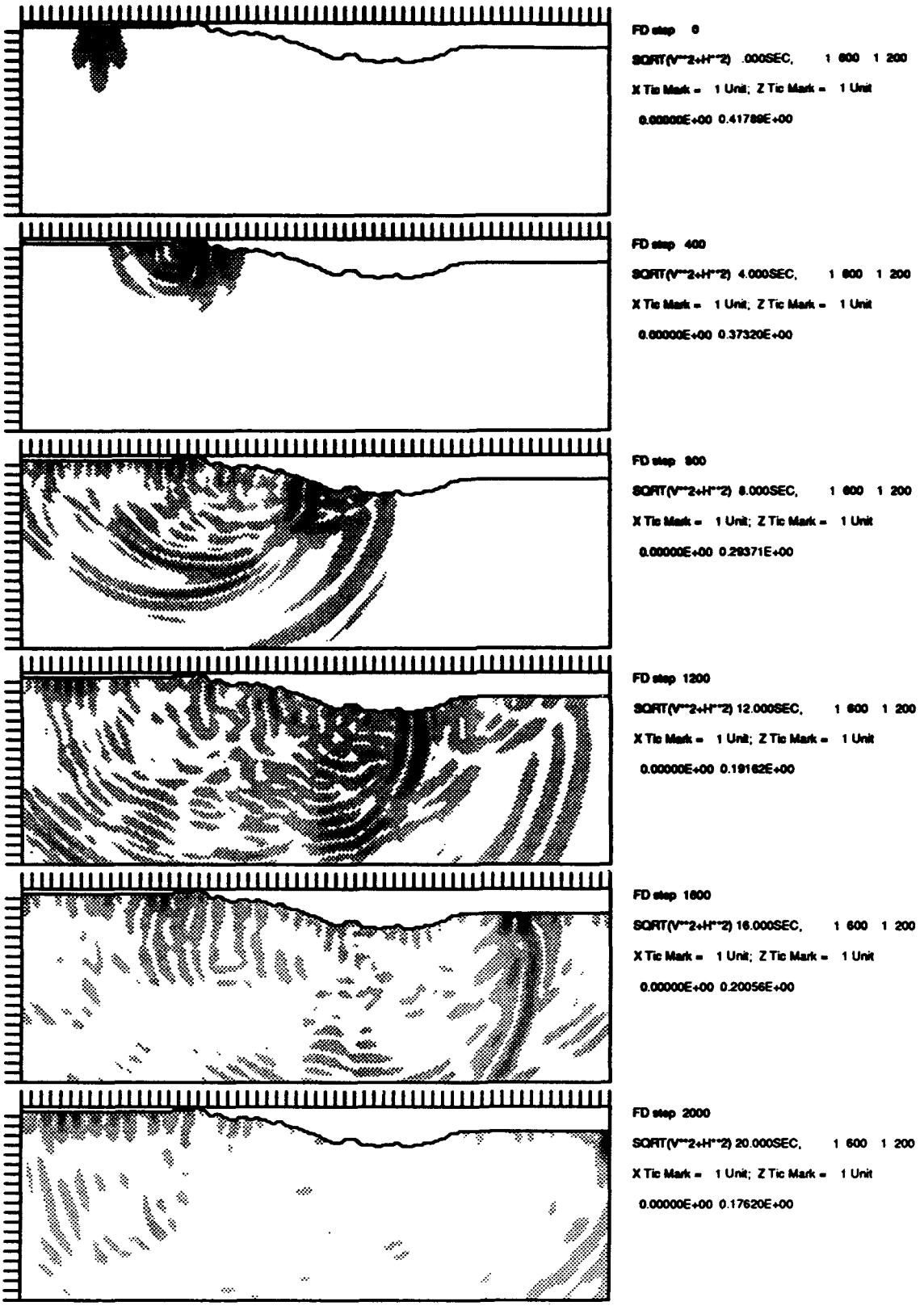

Rg (1Hz:2.665km); Grid 600*500 [dx=0.1km,dt=10ms]
Profile 22 (seed 93347, Pr(1)=0.10)

**Figure 19**



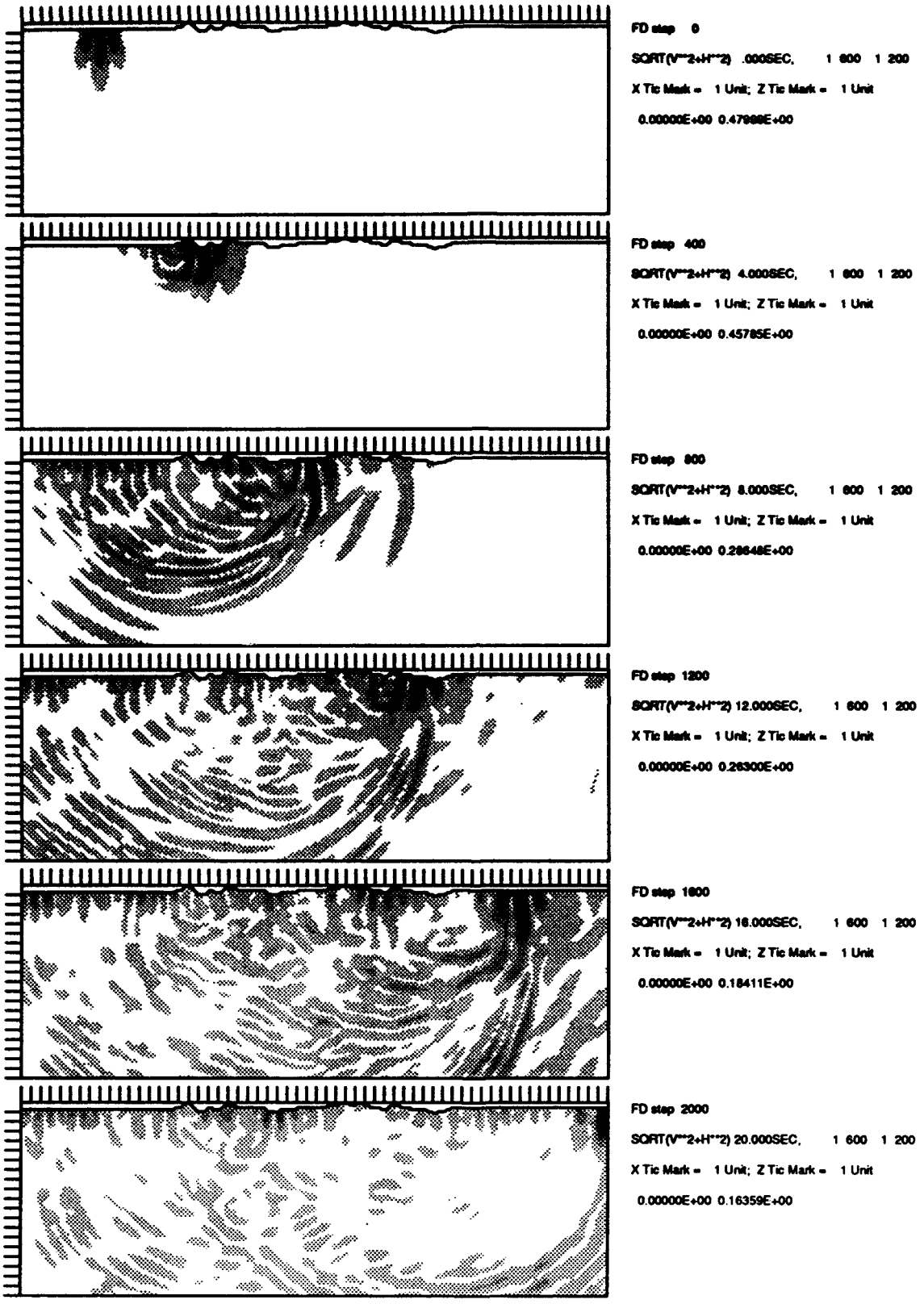

Rg (1Hz:2.665km); Grid 600*500 [dx=0.1km,dt=10ms]
Profile 23 (seed 93356, Pr(1)=0.10)

**Figure 20**



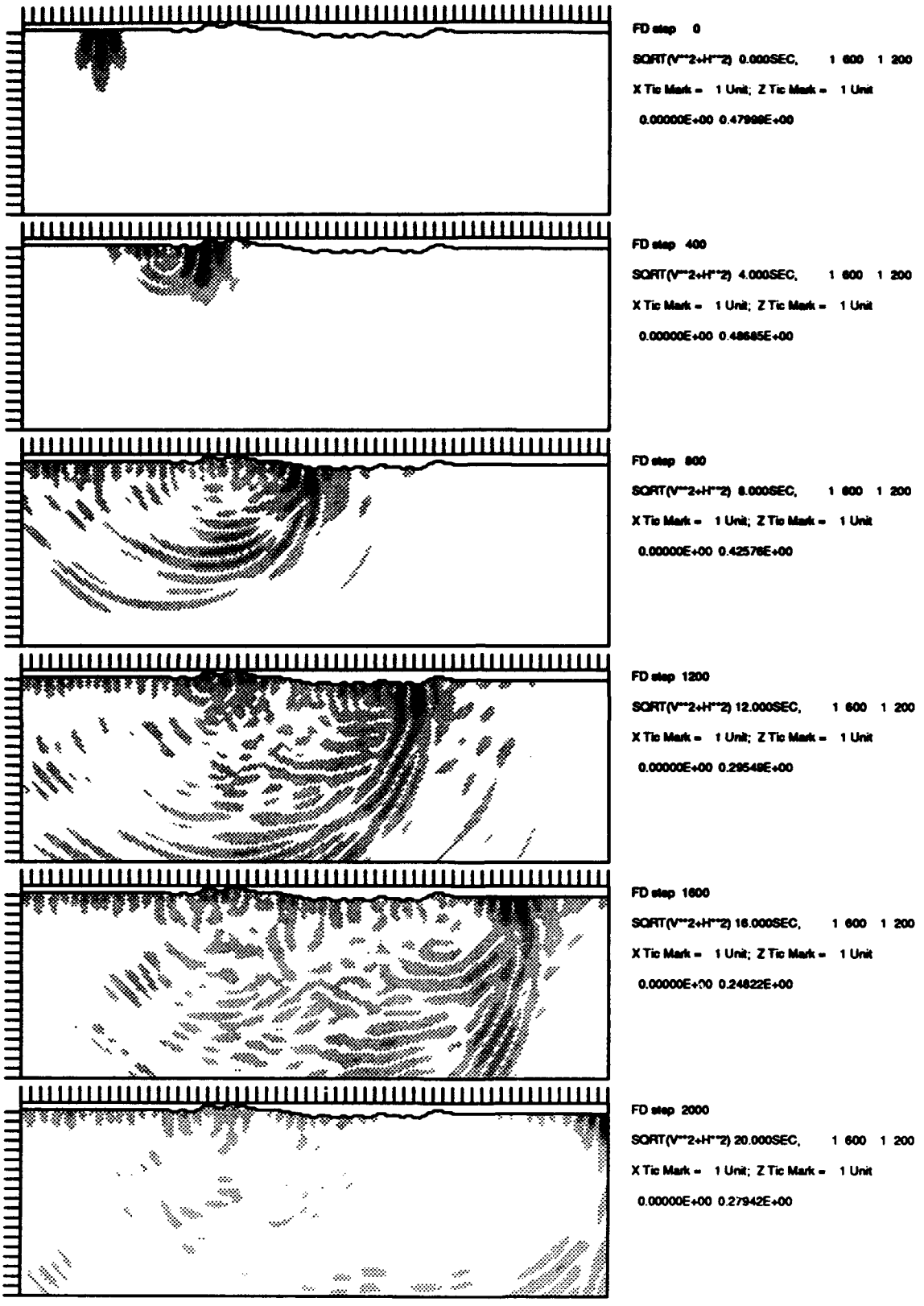

Rg (1Hz:2.665km); Grid 600*500 [dx=0.1km,dt=10ms]
Profile 31 (seed 748546615, Pr(1)=0.15)

**Figure 21**



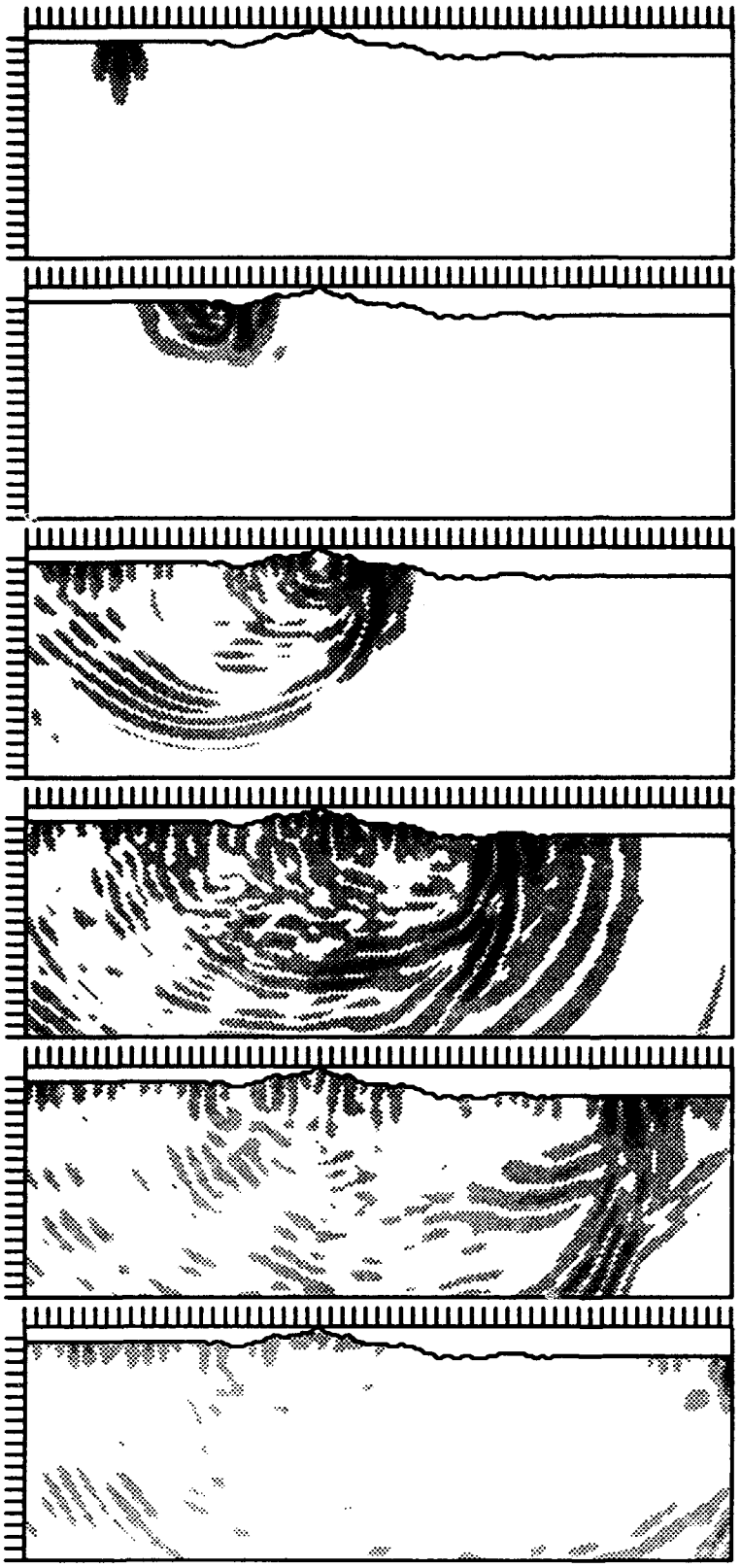

Rg (1Hz:2.665km); Grid 600*500 [dx=0.1km,dt=10ms]
Profile 32 (seed 20333, Pr(1)=0.15)

**Figure 22**



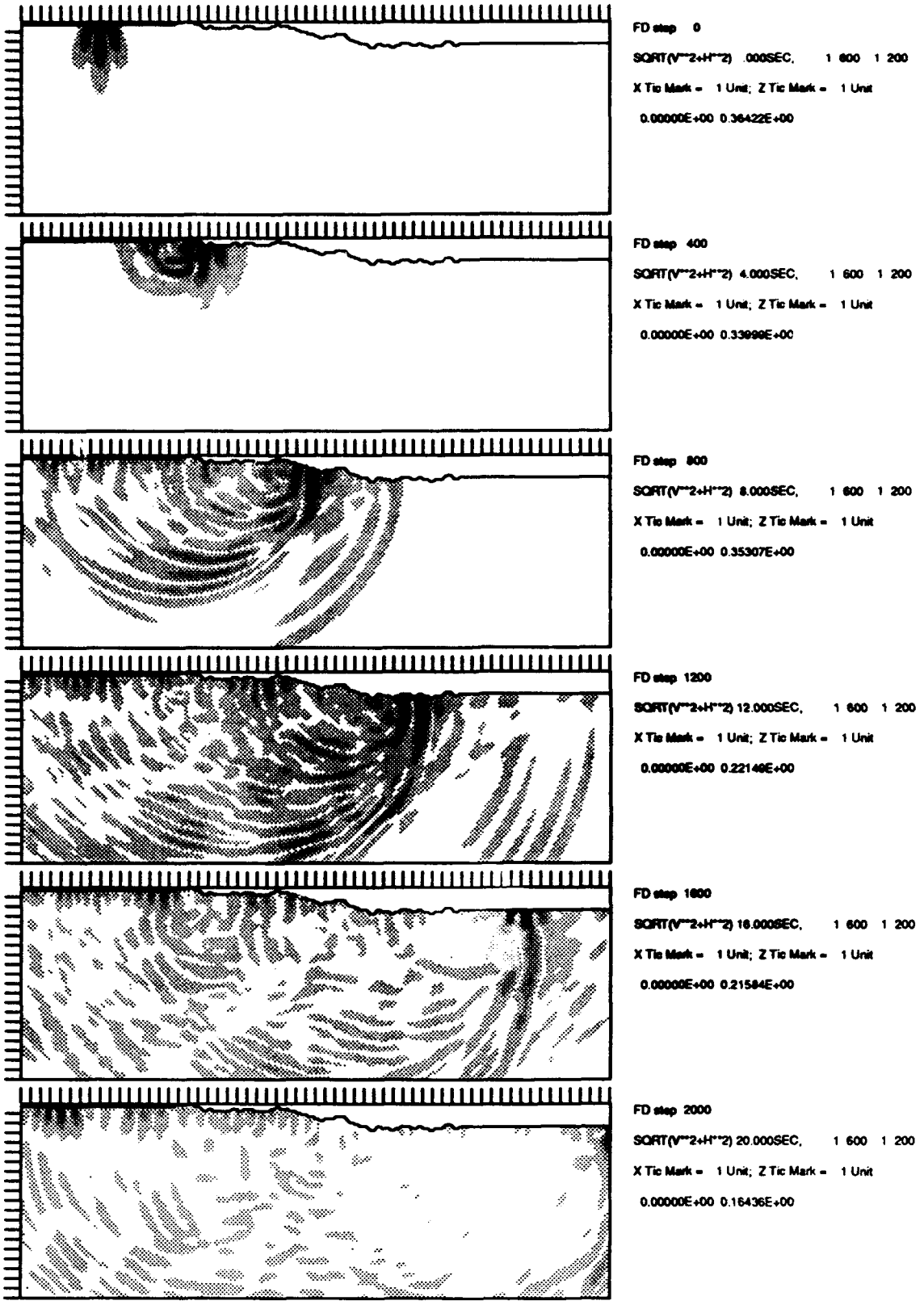

Rg (1Hz:2.665km); Grid 600*500 [dx=0.1km,dt=10ms]
Profile 33 (seed 86016, Pr(1)=0.15)

**Figure 23**



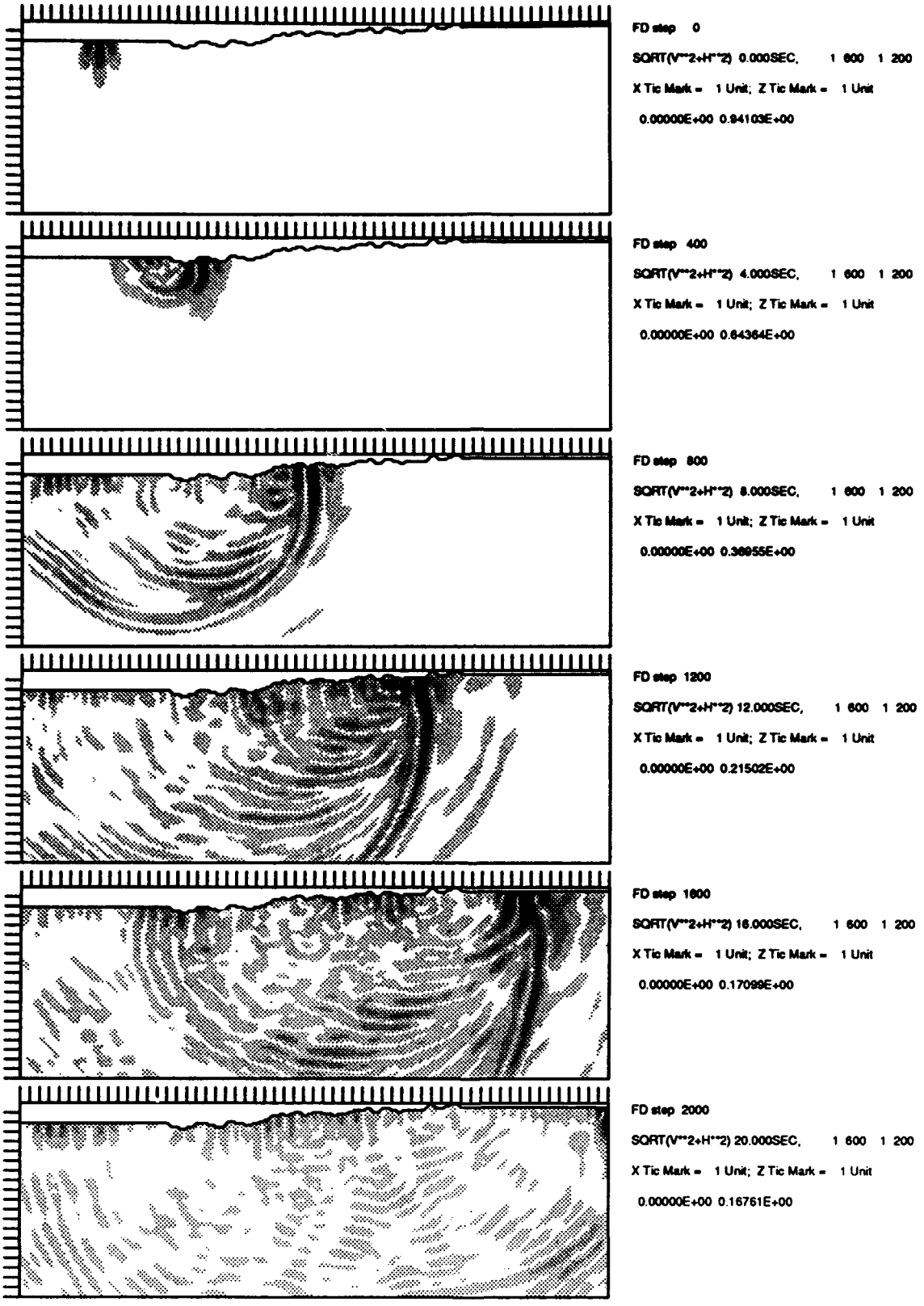

Rg (1Hz:2.665km); Grid 600*500 [dx=0.1km,dt=10ms]
Profile 41 (seed 93397, Pr(1)=0.20)

Figure 24



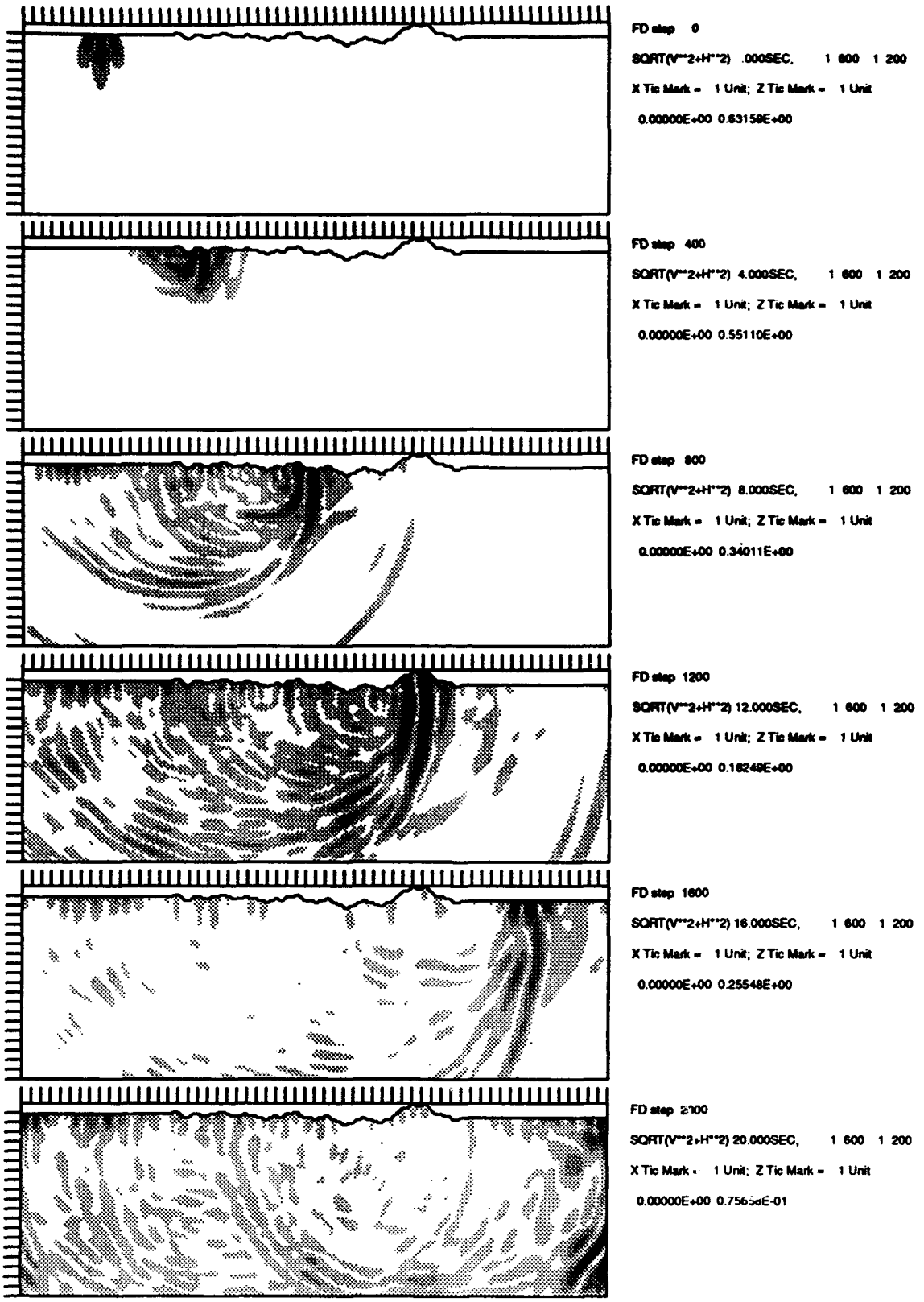

Rg (1Hz:2.665km); Grid 600*500 [dx=0.1km,dt=10ms]
Profile 42 (seed 93407, Pr(1)=0.20)

Figure 25



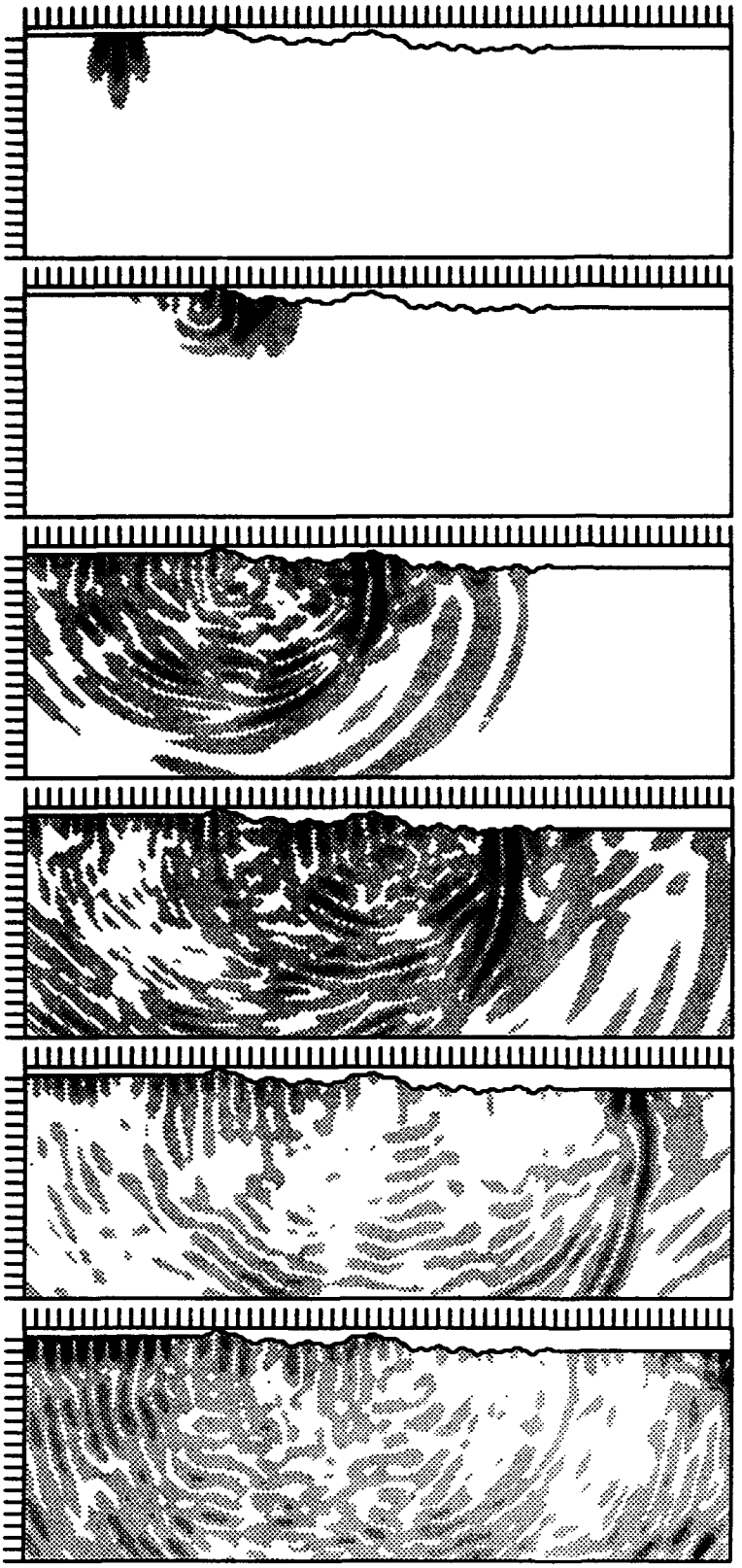

Rg (1Hz:2.665km); Grid 600*500 [dx=0.1km,dt=10ms]
Profile 43 (seed 12345, Pr(1)=0.20)

Figure 26



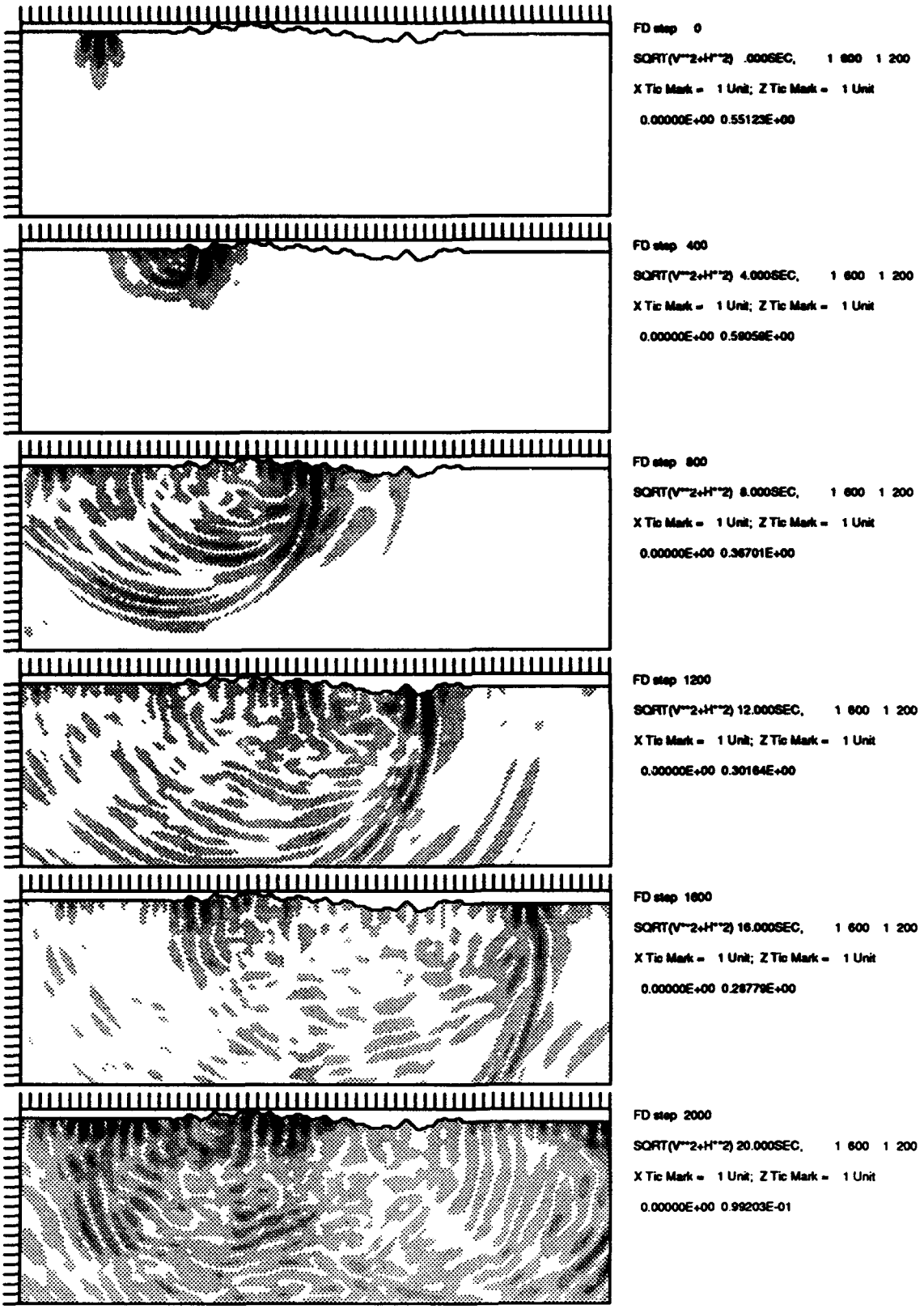

Rg (1Hz:2.665km); Grid 600*500 [dx=0.1km,dt=10ms]
Profile 51 (seed 21691, Pr(1)=0.25)

Figure 27




Rg (1Hz:2.665km); Grid 600*500 [dx=0.1km,dt=10ms]
Profile 52 (seed 21696, Pr(1)=0.25)

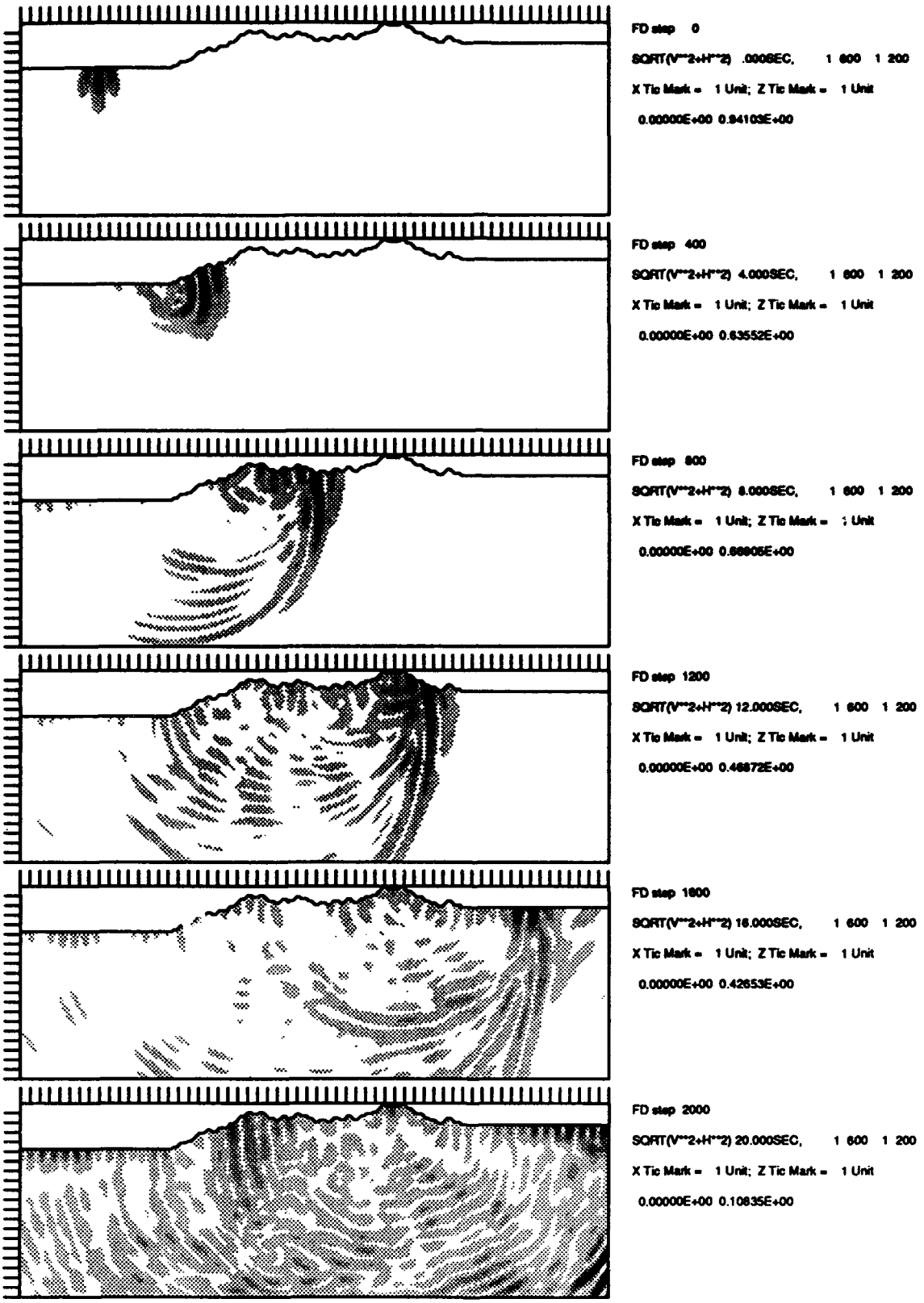
**Figure 28**




Rg (1Hz:2.665km); Grid 600*500 [dx=0.1km,dt=10ms]

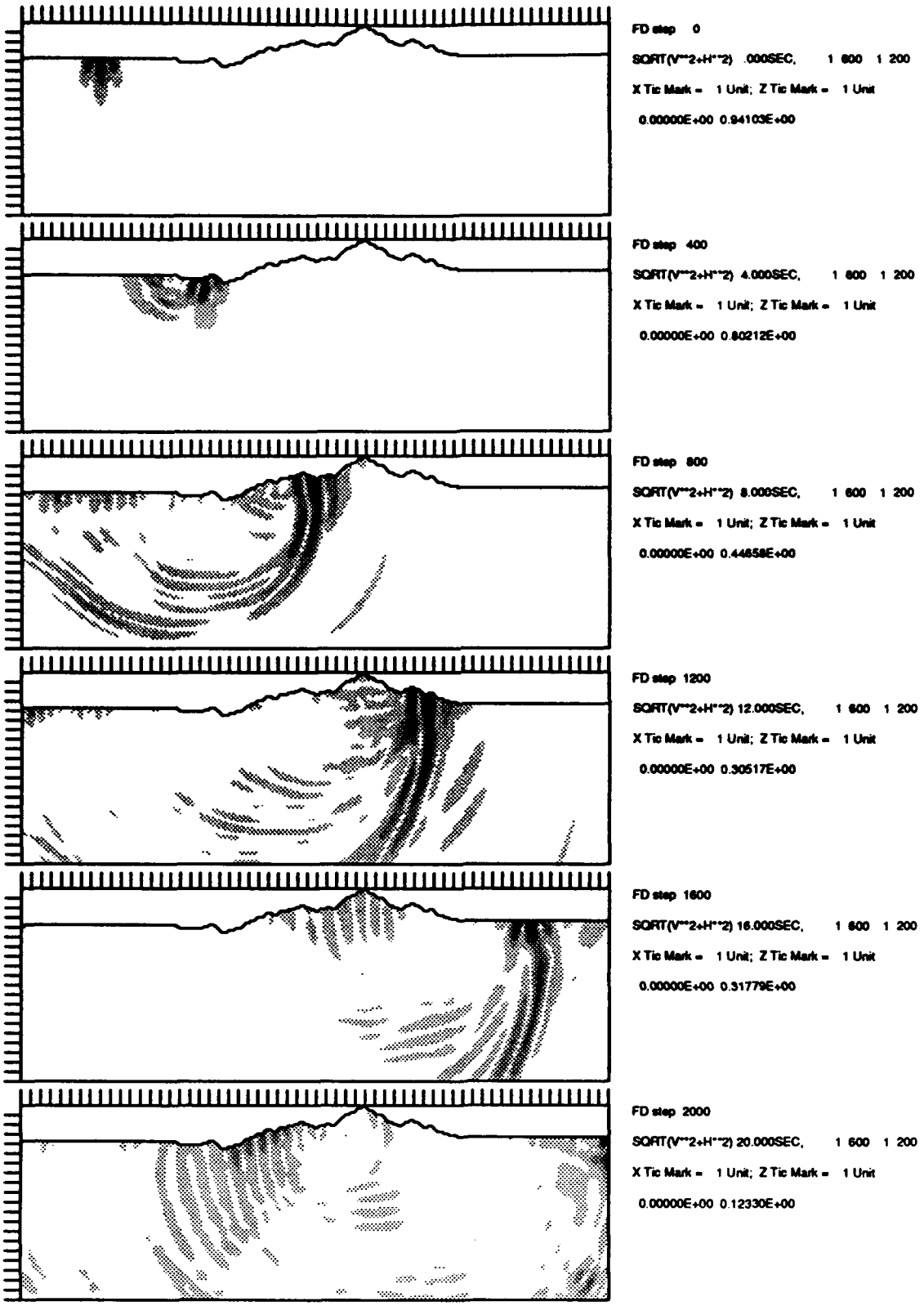
Profile 53 (seed 86037, Pr(1)=0.25)

Figure 29



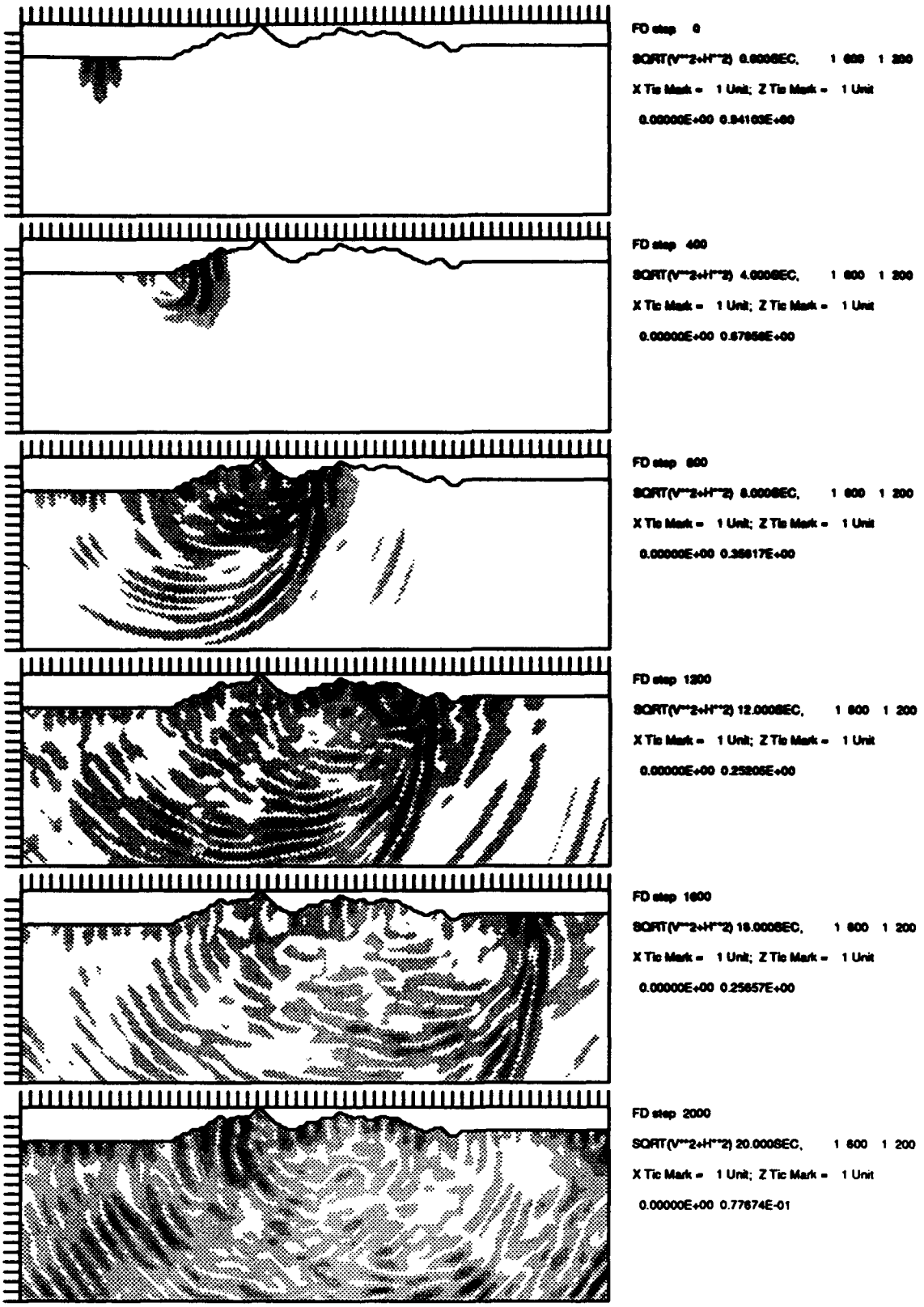

Rg (1Hz:2.665km); Grid 600*500 [dx=0.1km,dt=10ms]
Profile 61 (seed 93459, Pr(1)=0.30)

**Figure 30**



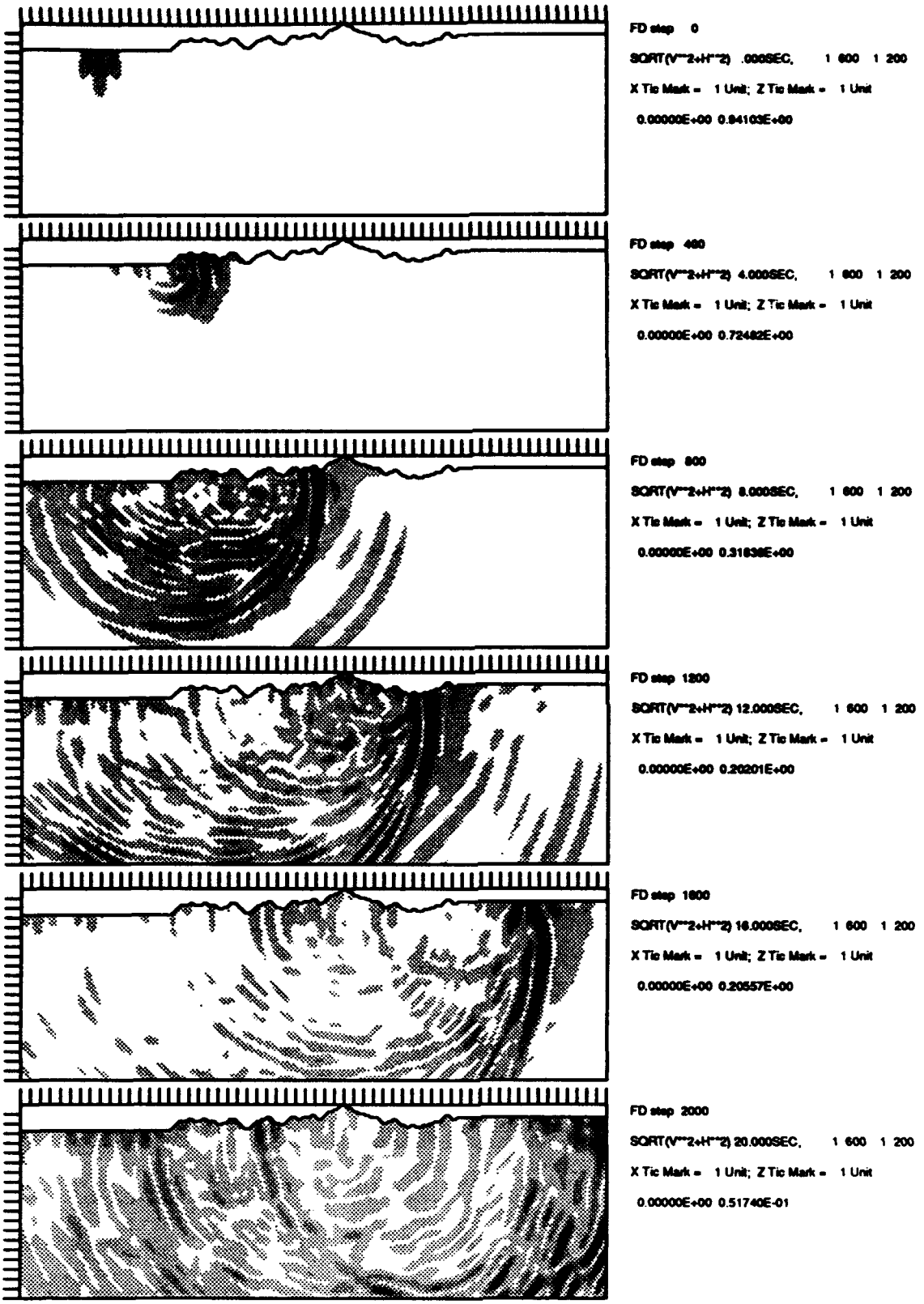

Rg (1Hz:2.665km); Grid 600*500 [dx=0.1km,dt=10ms]
Profile 62 (seed 93468, Pr(1)=0.30)

**Figure 31**



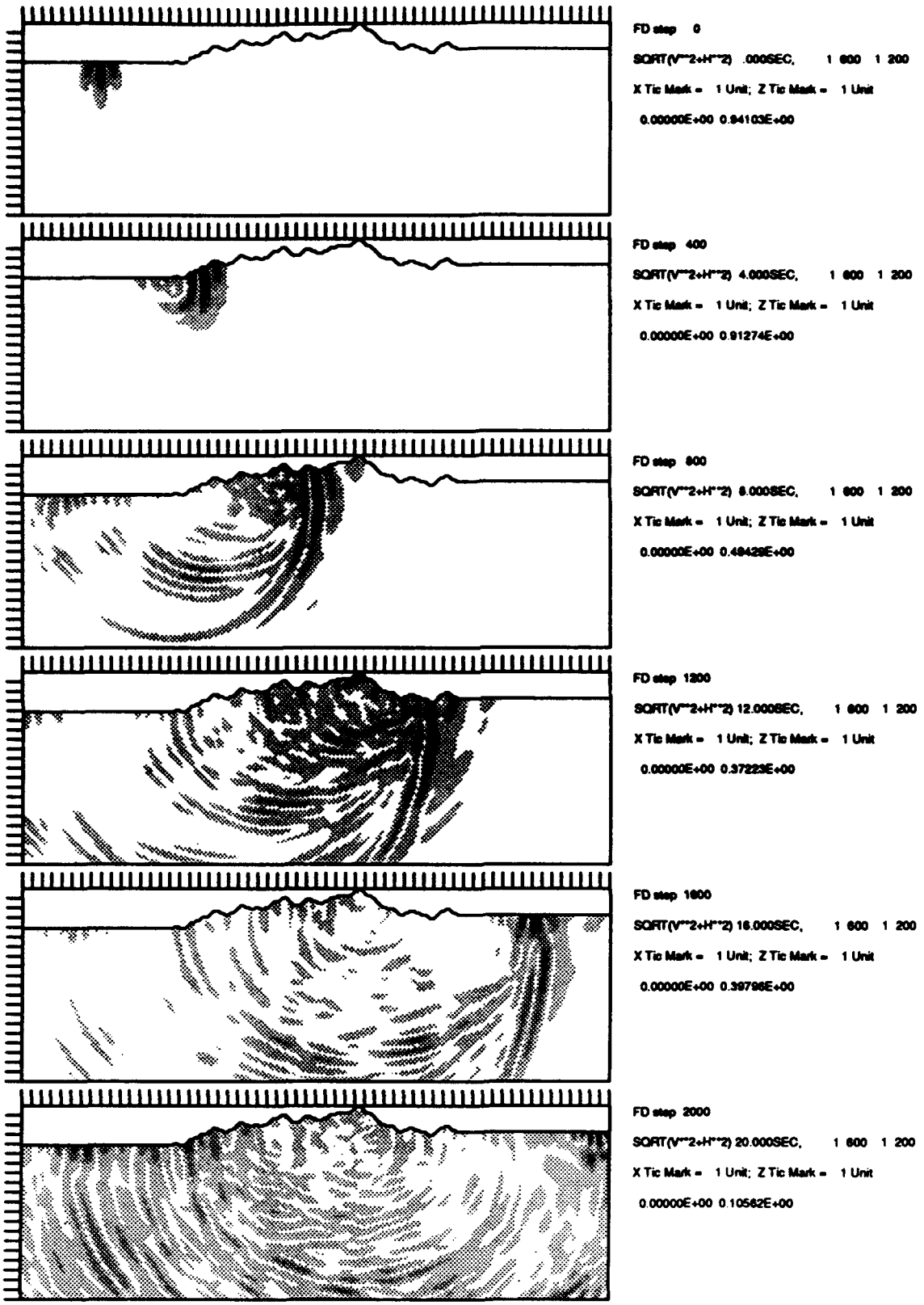

Rg (1Hz:2.665km); Grid 600*500 [dx=0.1km,dt=10ms]
Profile 63 (seed 93479, Pr(1)=0.30)

Figure 32



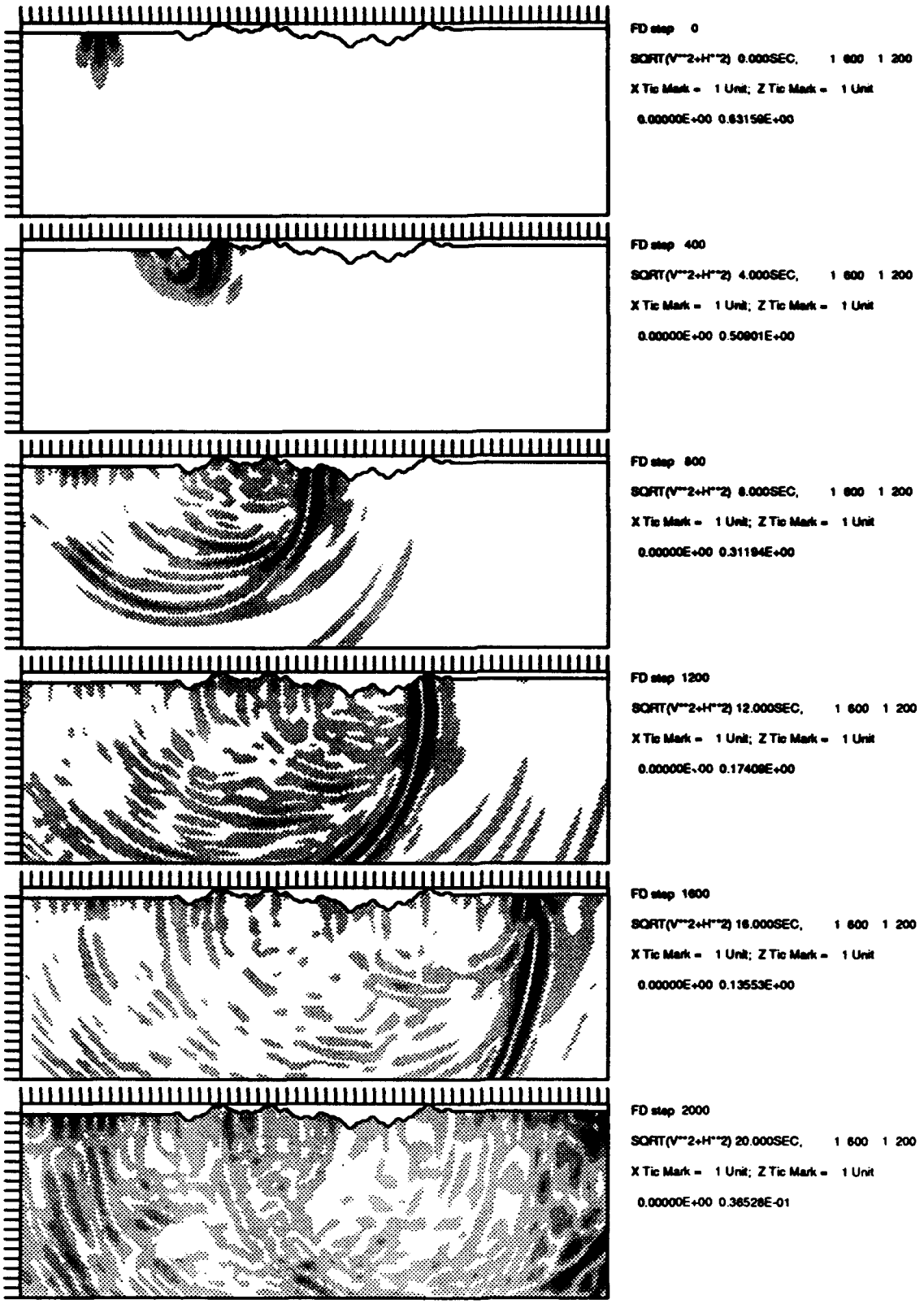

Rg (1Hz:2.665km); Grid 600*500 [dx=0.1km,dt=10ms]
Profile 64 (seed 55473, Pr(1)=0.32)

**Figure 33**



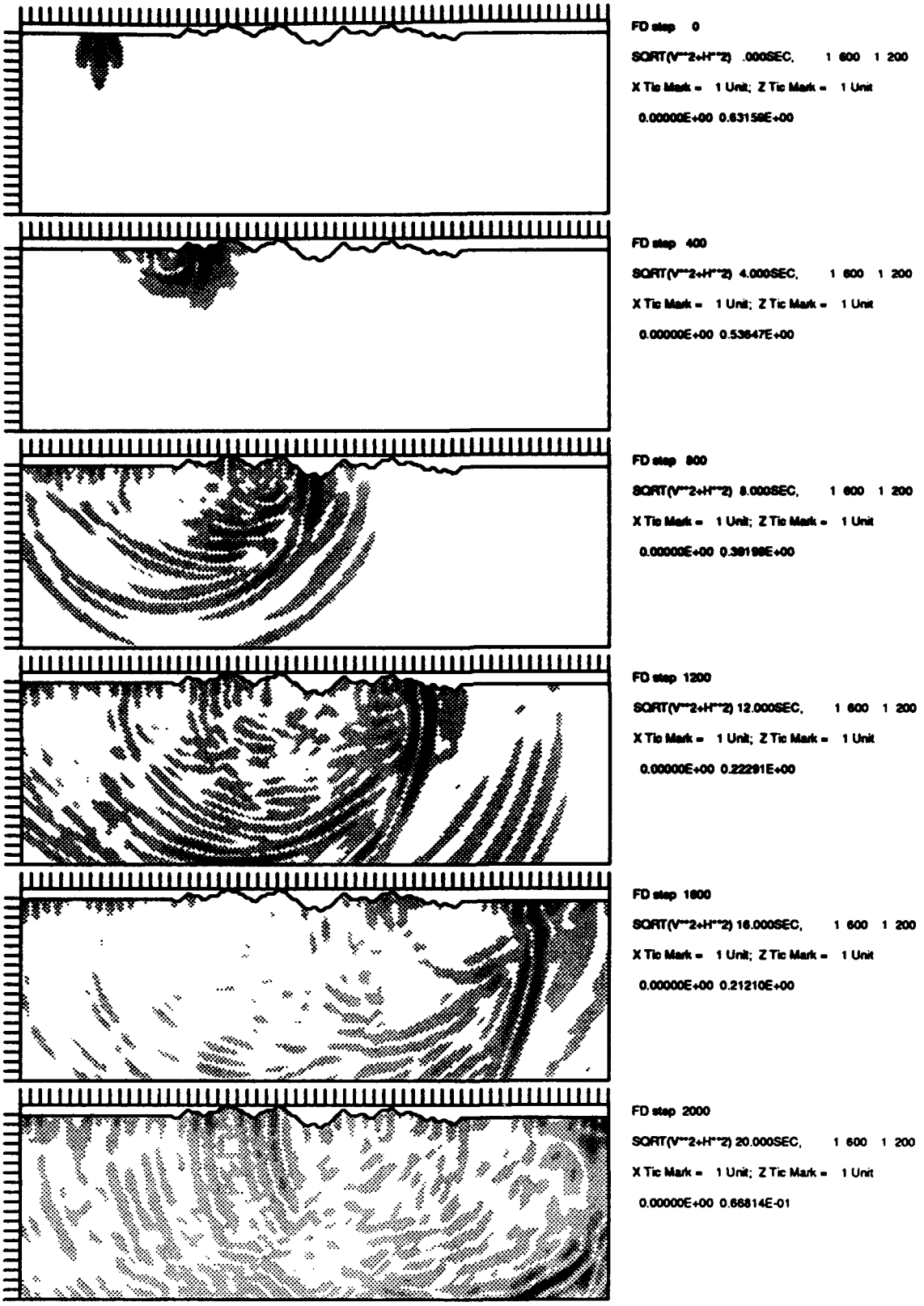

Rg (1Hz:2.665km); Grid 600*500 [dx=0.1km,dt=10ms]
Profile 65 (seed 55499, Pr(1)=0.32)

**Figure 34**




Rg (1Hz:2.665km); Grid 600*500 [dx=0.1km,dt=10ms]
Profile 66 (seed 55446, Pr(1)=0.32)

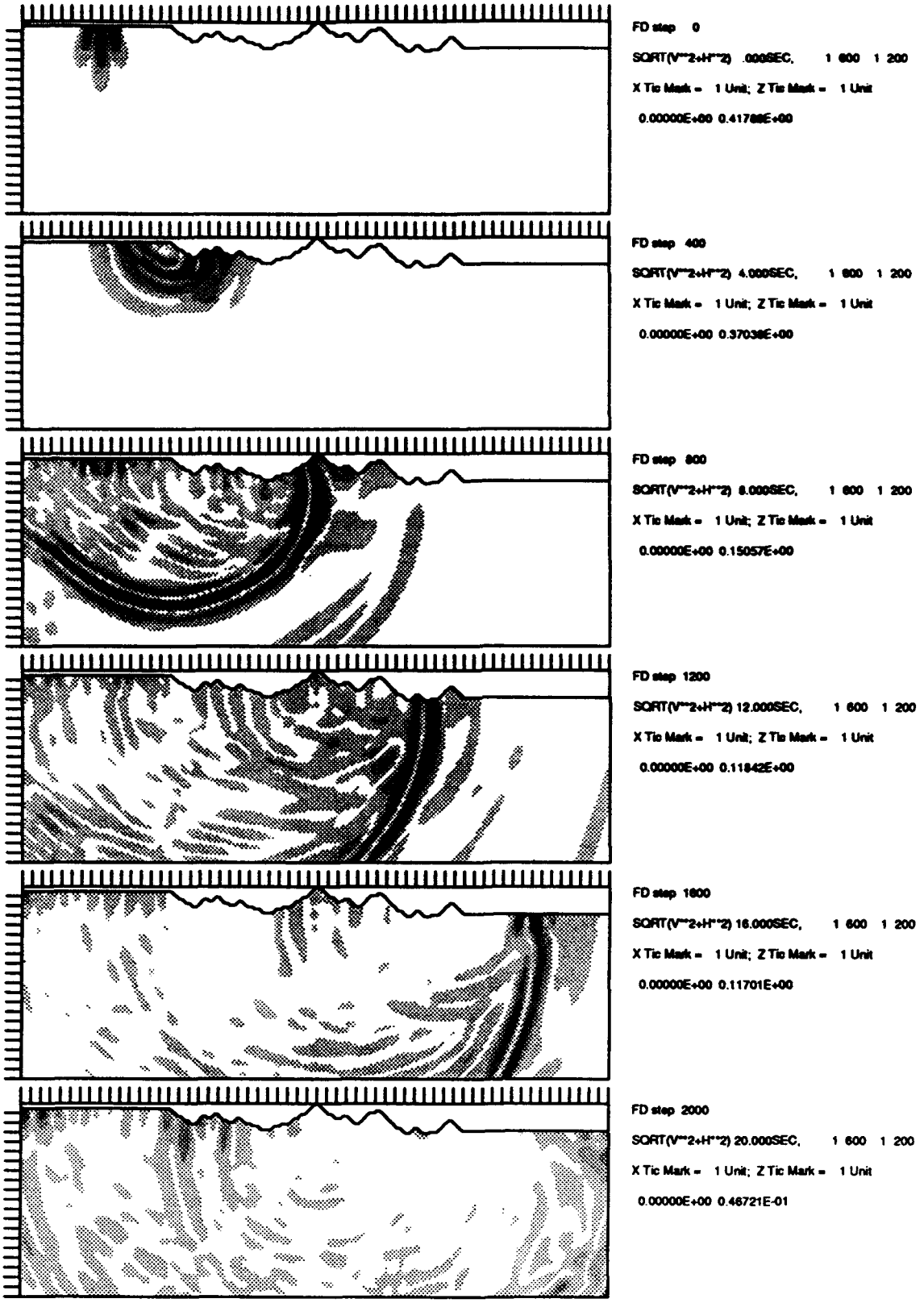
**Figure 35**




Rg (1Hz:2.665km); Grid 600*500 [dx=0.1km,dt=10ms]

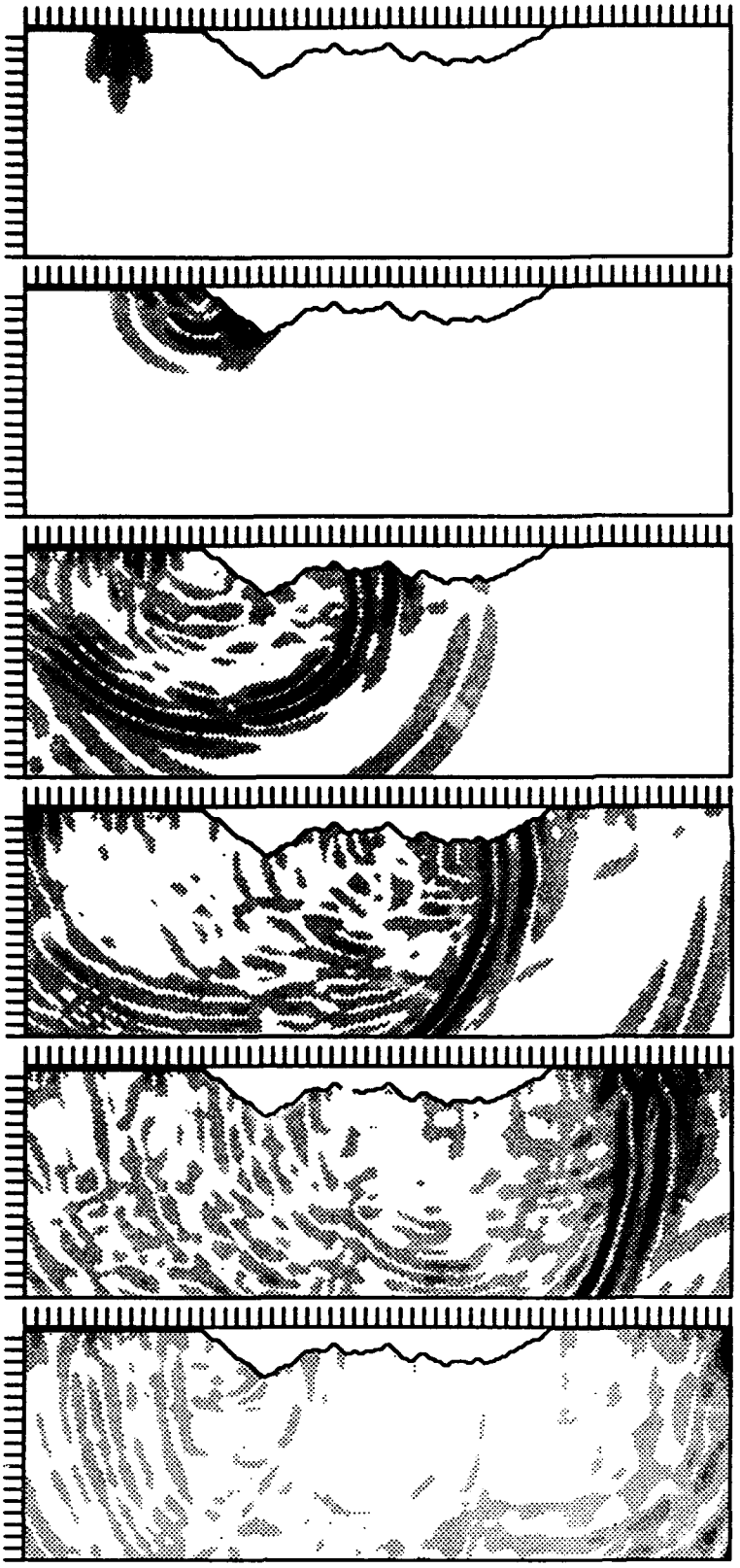
Profile 71 (seed 22192, Pr(1)=0.35)

**Figure 36**



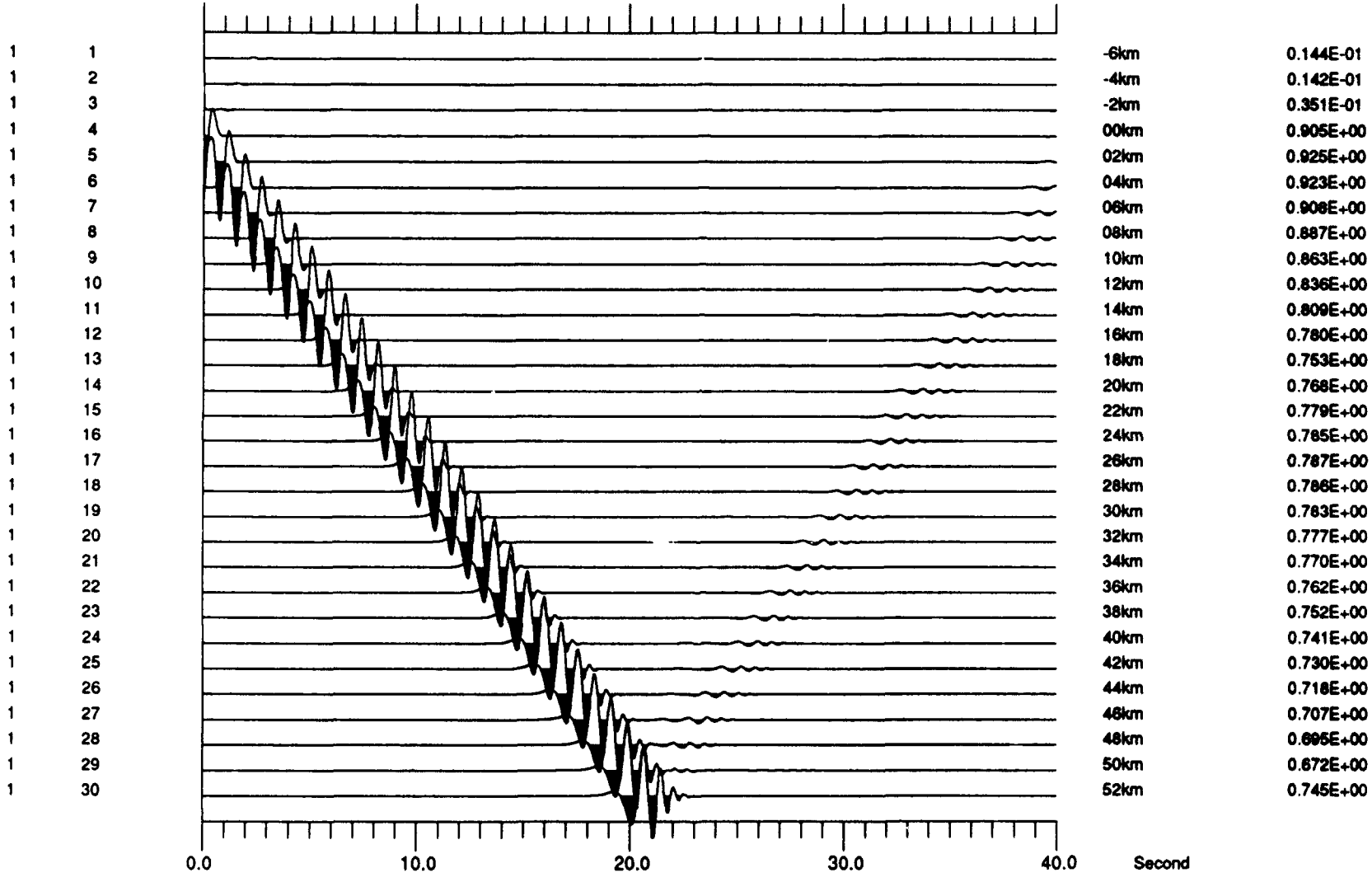

Rg (1Hz:2.665km); Grid 600*500 [dx=0.1km,dt=10ms]
Profile 72 (seed 31087, Pr(1)=0.35)

Figure 37




Rg (1Hz:2.665km); Grid 600*500 [dx=0.1km,dt=10ms]
Profile 73 (seed 86061, Pr(1)=0.35)

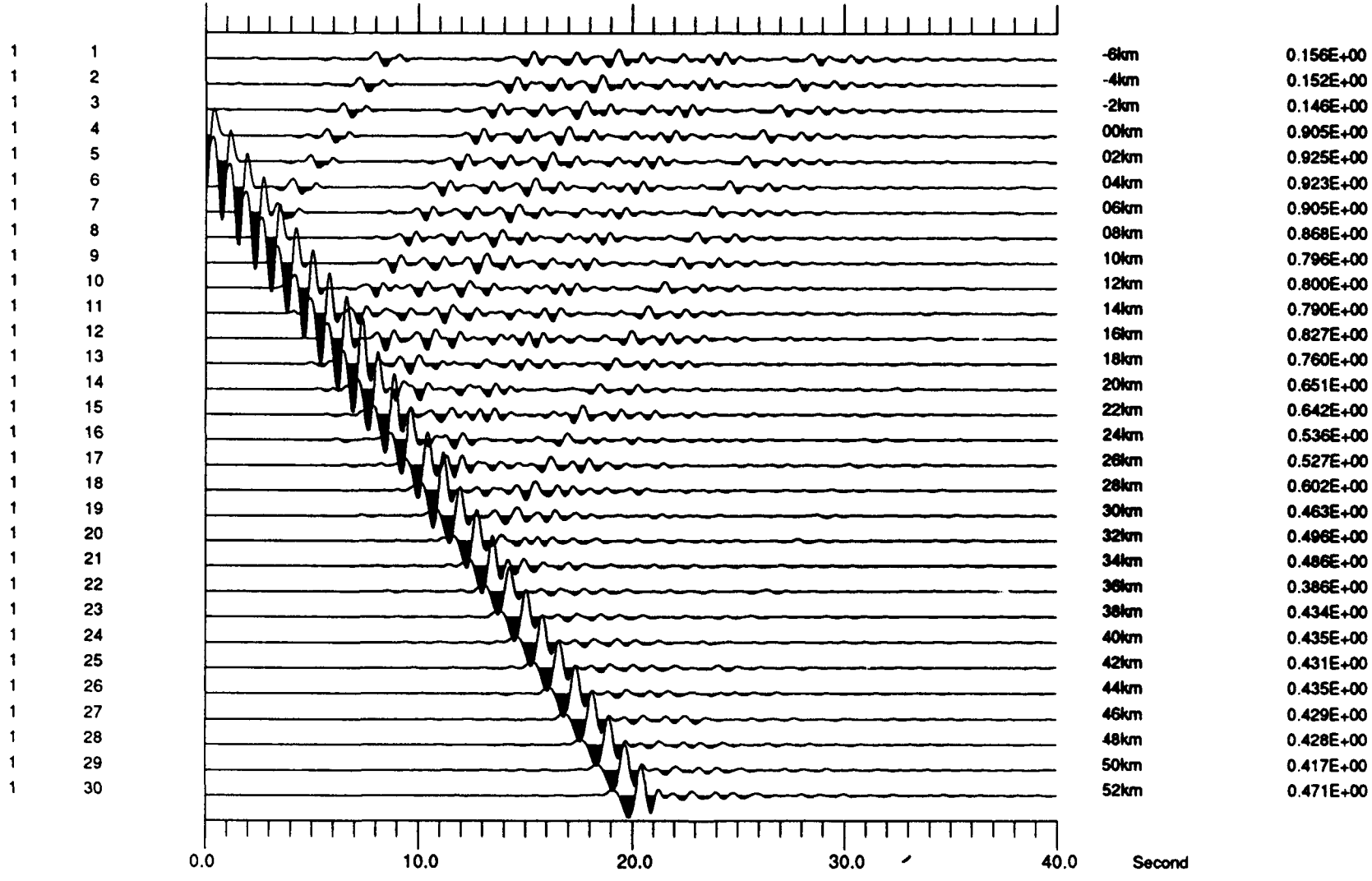
**Figure 38**




Profile 00(seed 00, Pr(1)=00), Surface Sensors

VERT, same scale, decimated by 4

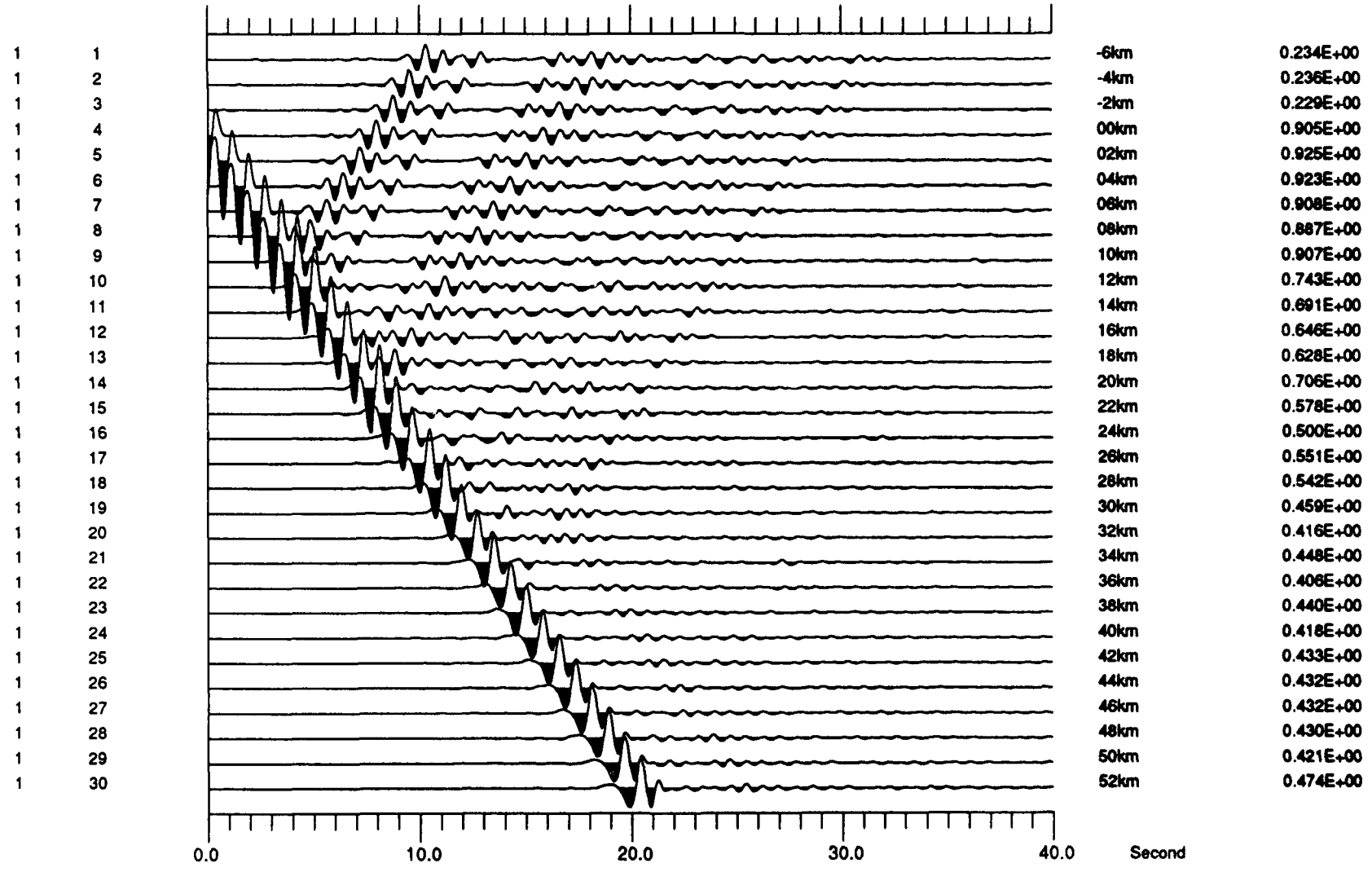
**Figure 39**




Profile 11(seed 22887, Pr(1)=0.05), Surface Sensors

VERT, same scale, decimated by 5

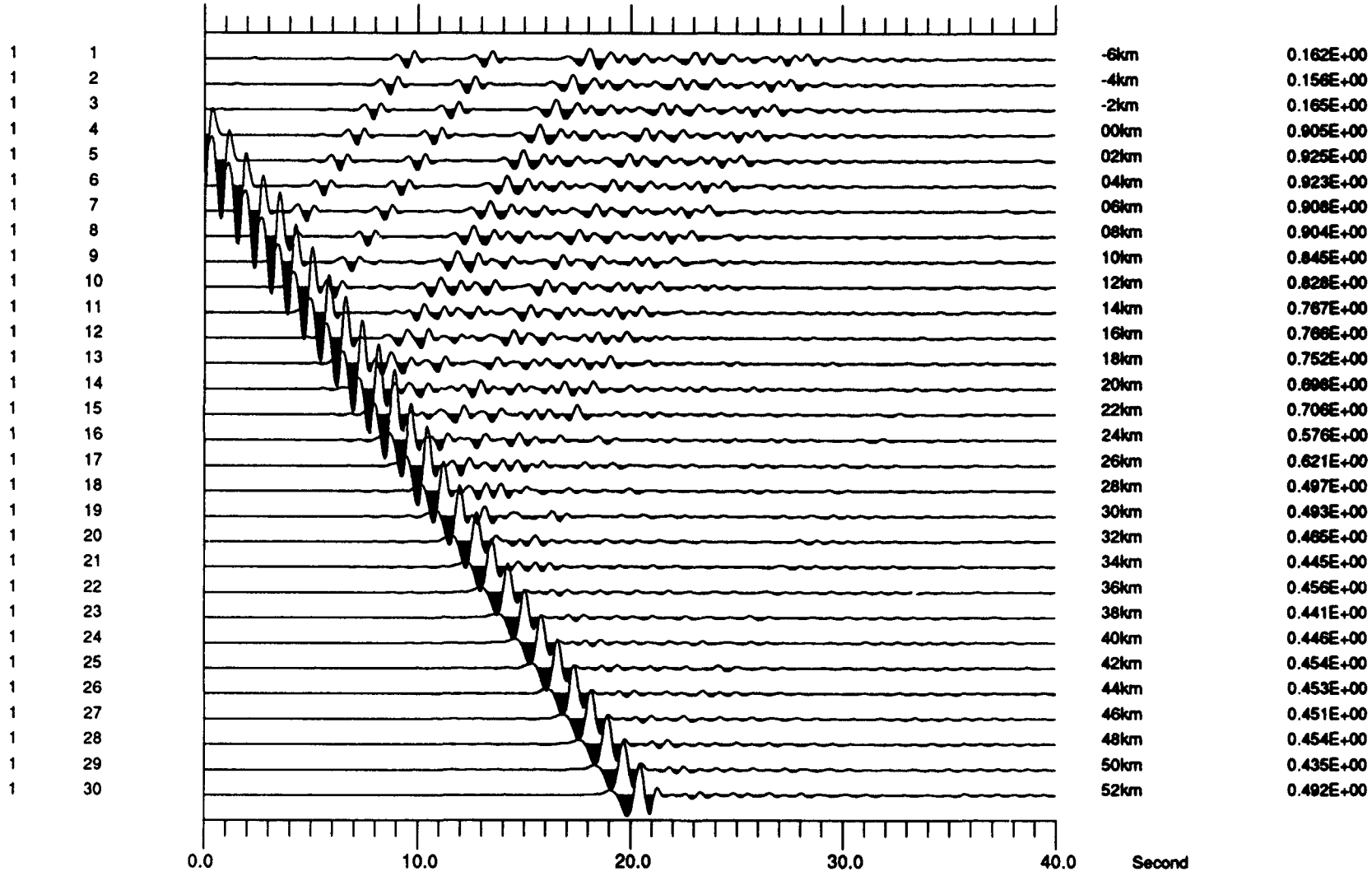
**Figure 40**




Profile 12(seed 22892, Pr(1)=0.05), Surface Sensors

VERT, same scale, decimated by 5

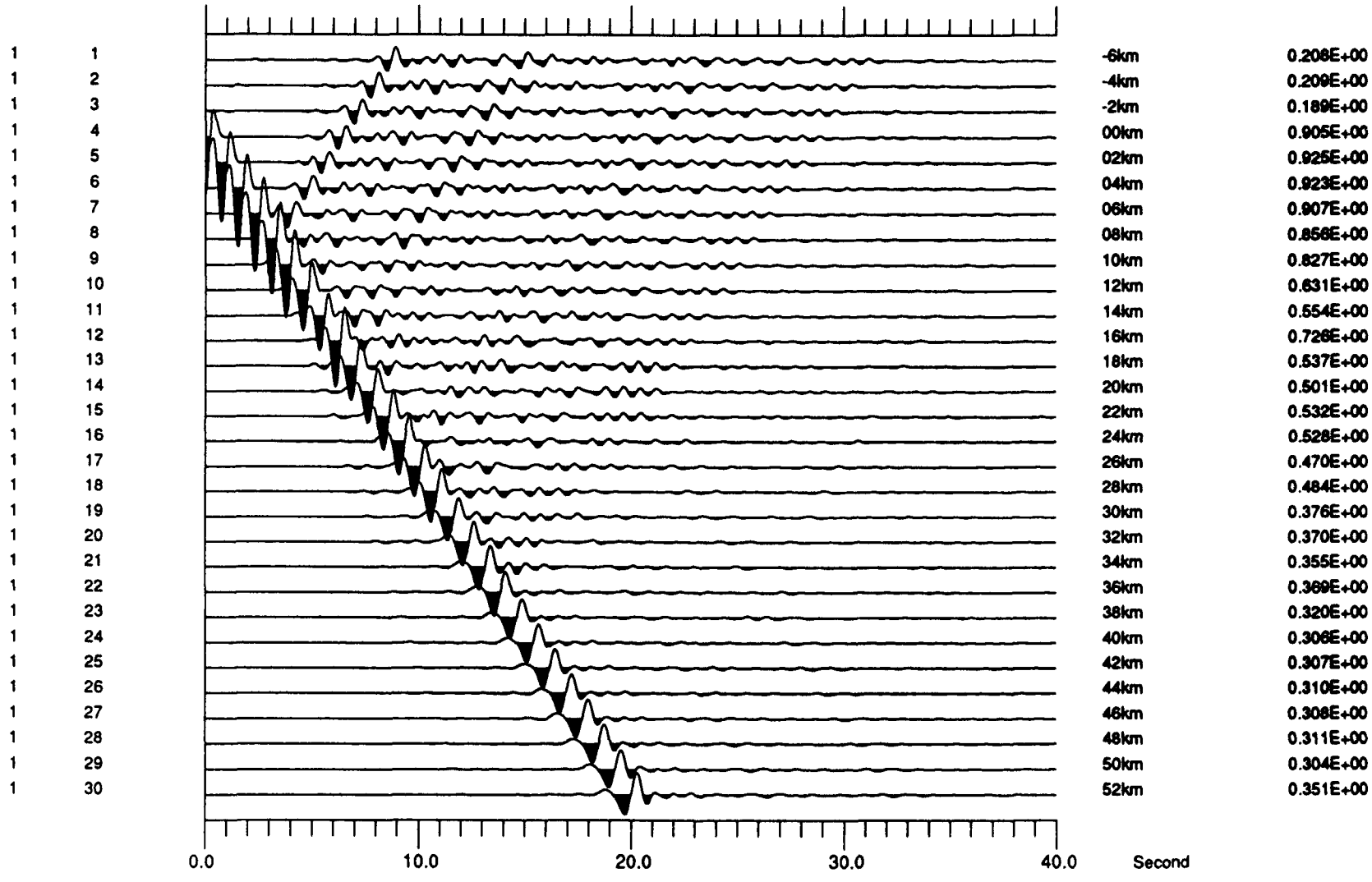
**Figure 41**




Profile 13(seed 85995, Pr(1)=0.05), Surface Sensors

VERT, same scale, decimated by 5

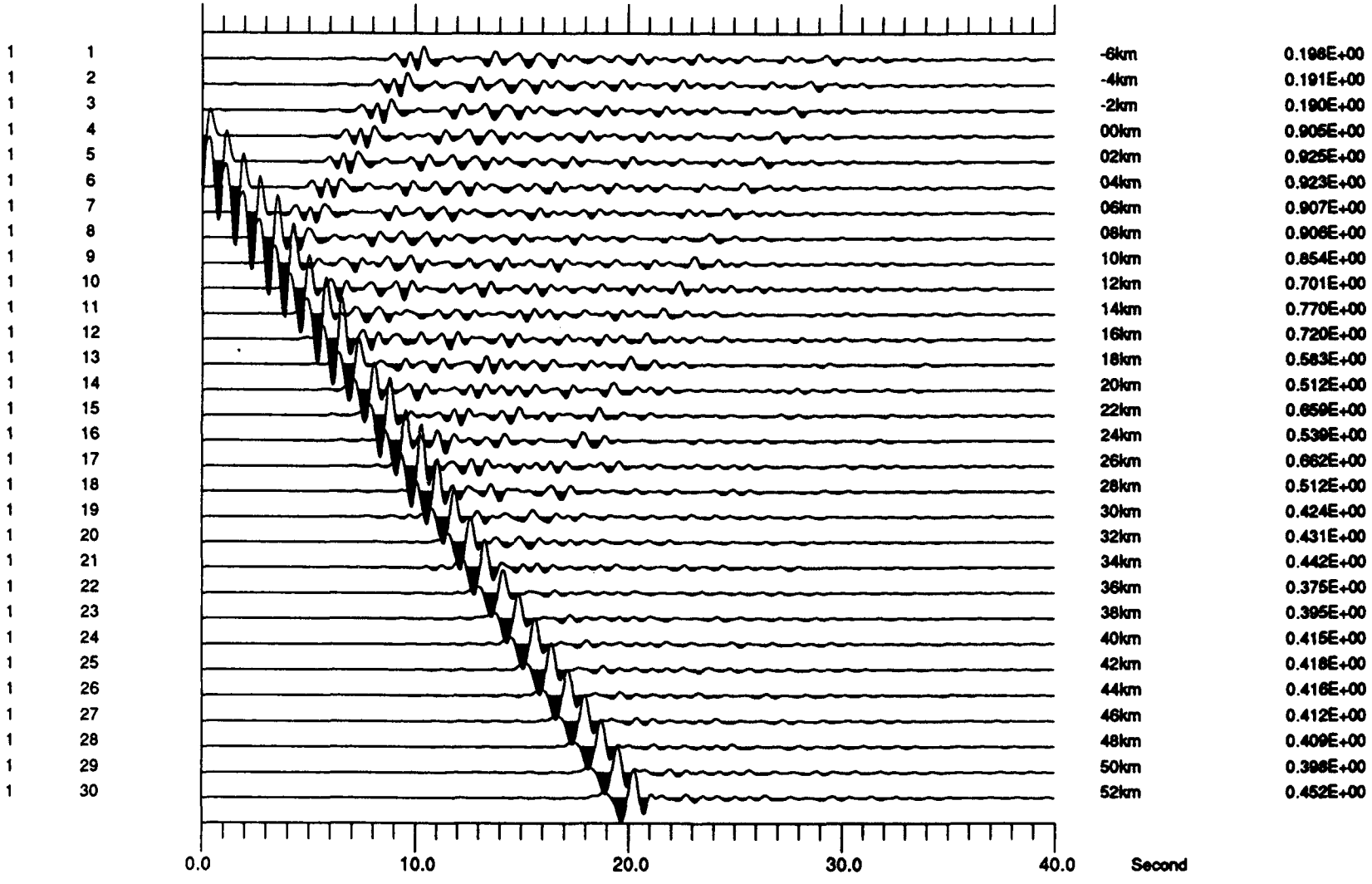
**Figure 42**




Profile 14(seed 91333, Pr(1)=0.07), Surface Sensors

VERT, same scale, decimated by 5

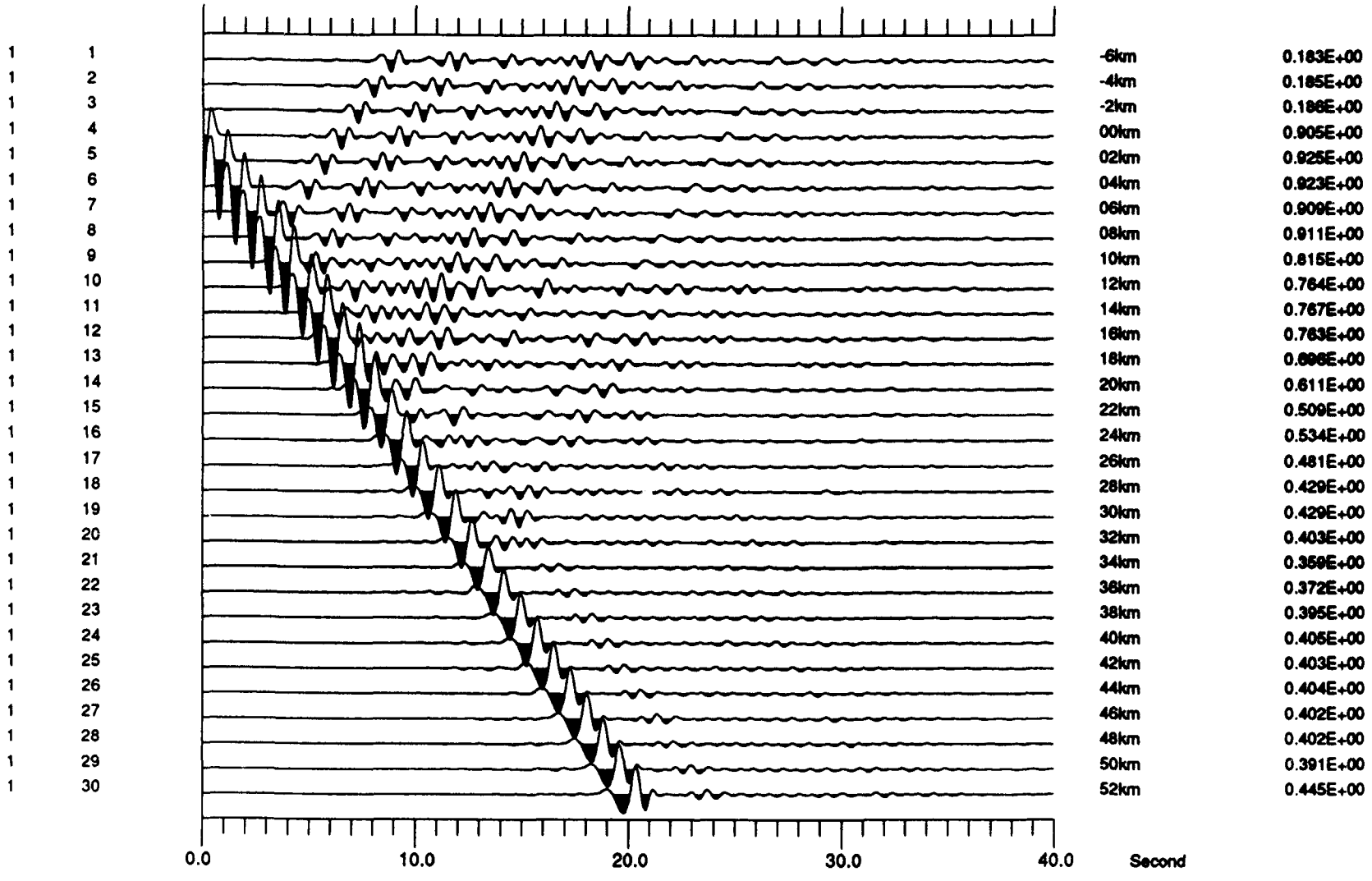
**Figure 43**




Profile 15(seed 91350, Pr(1)=0.07), Surface Sensors

VERT, same scale, decimated by 5

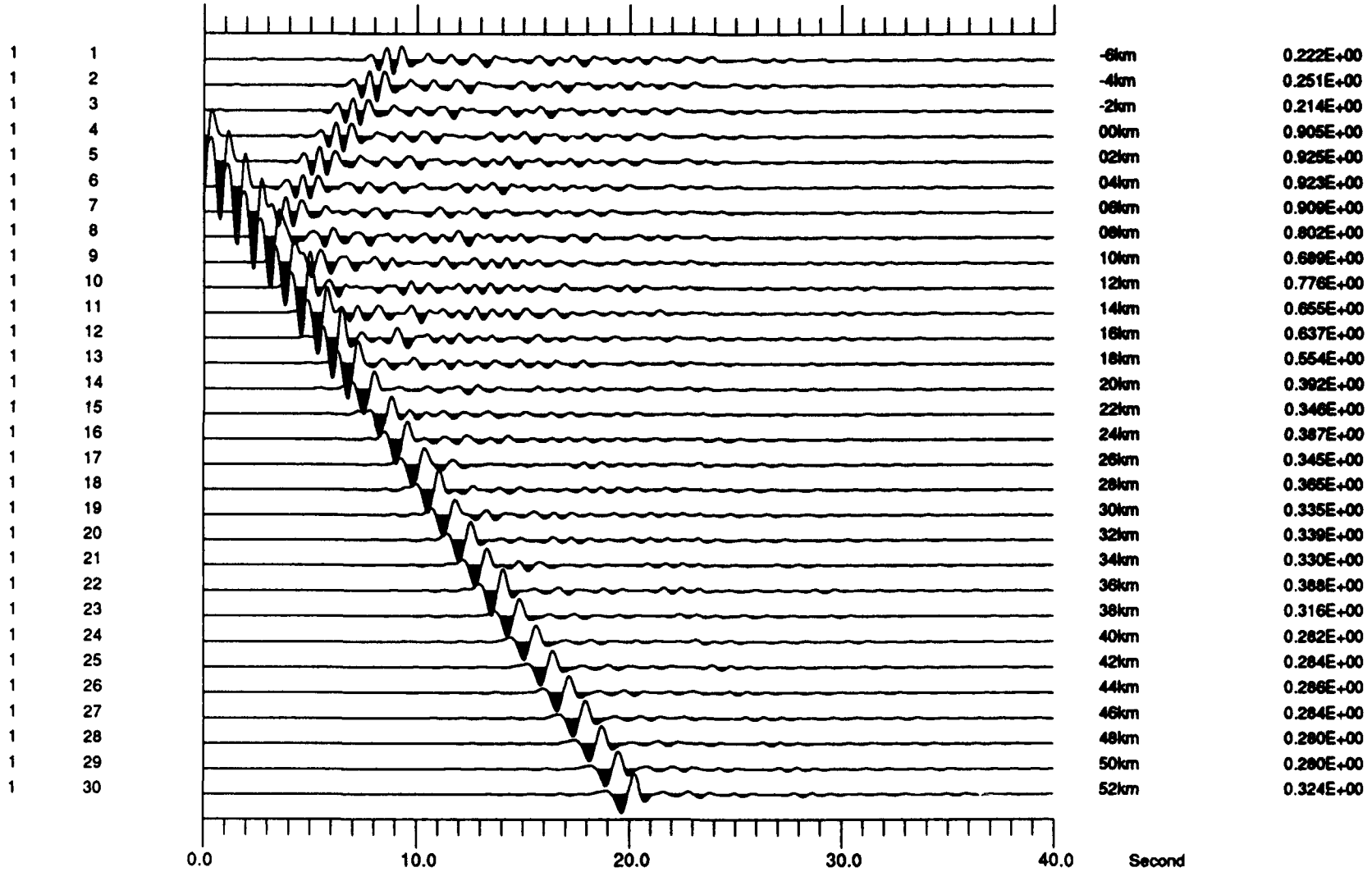
**Figure 44**




Profile 16(seed 91285, Pr(1)=0.07), Surface Sensors

VERT, same scale, decimated by 5

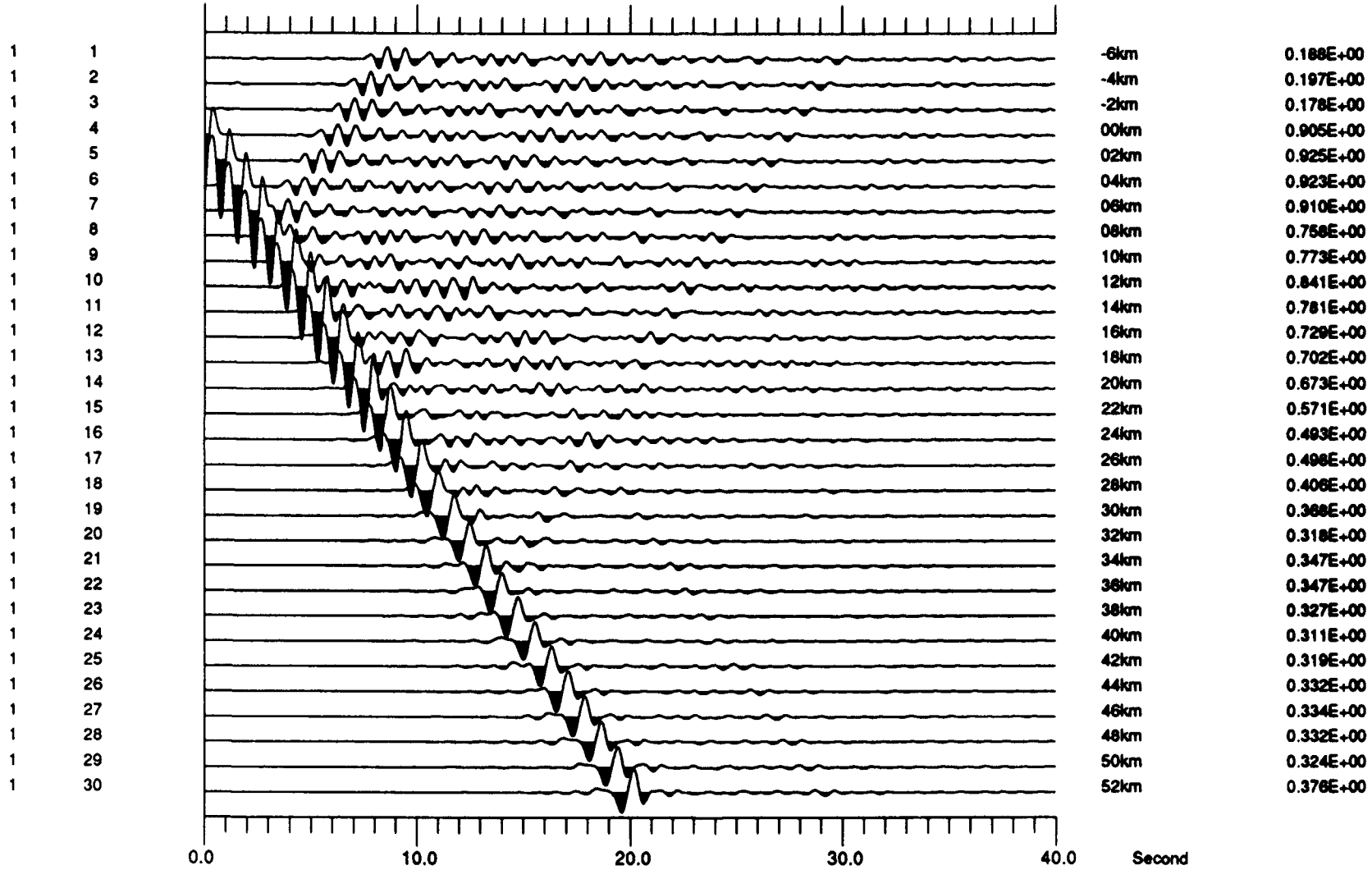
**Figure 45**




Profile 21(seed 93337, Pr(1)=0.10), Surface Sensors

VERT, same scale, decimated by 5

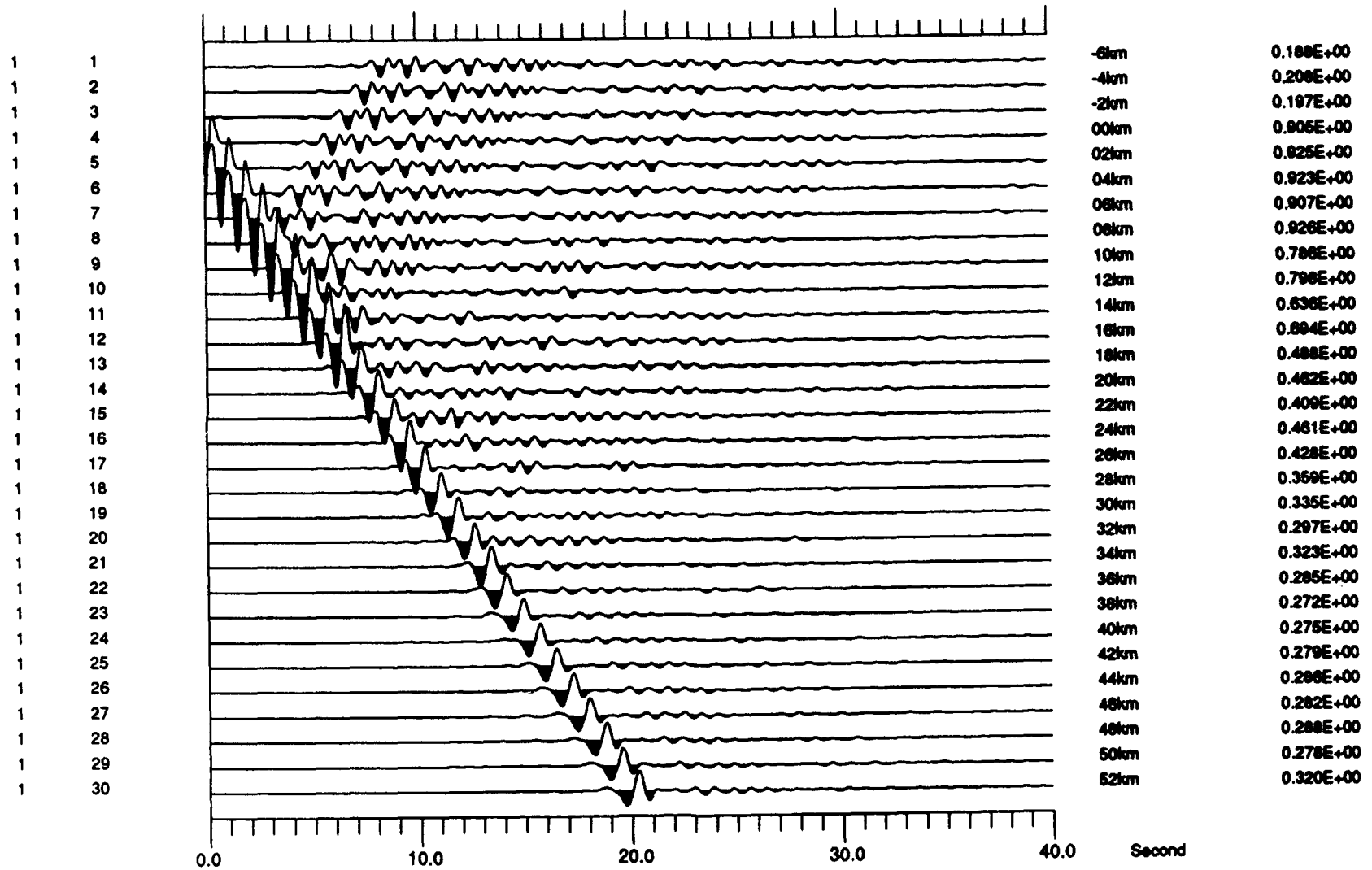
**Figure 46**




Profile 22(seed 93347, Pr(1)=0.10), Surface Sensors

VERT, same scale, decimated by 5

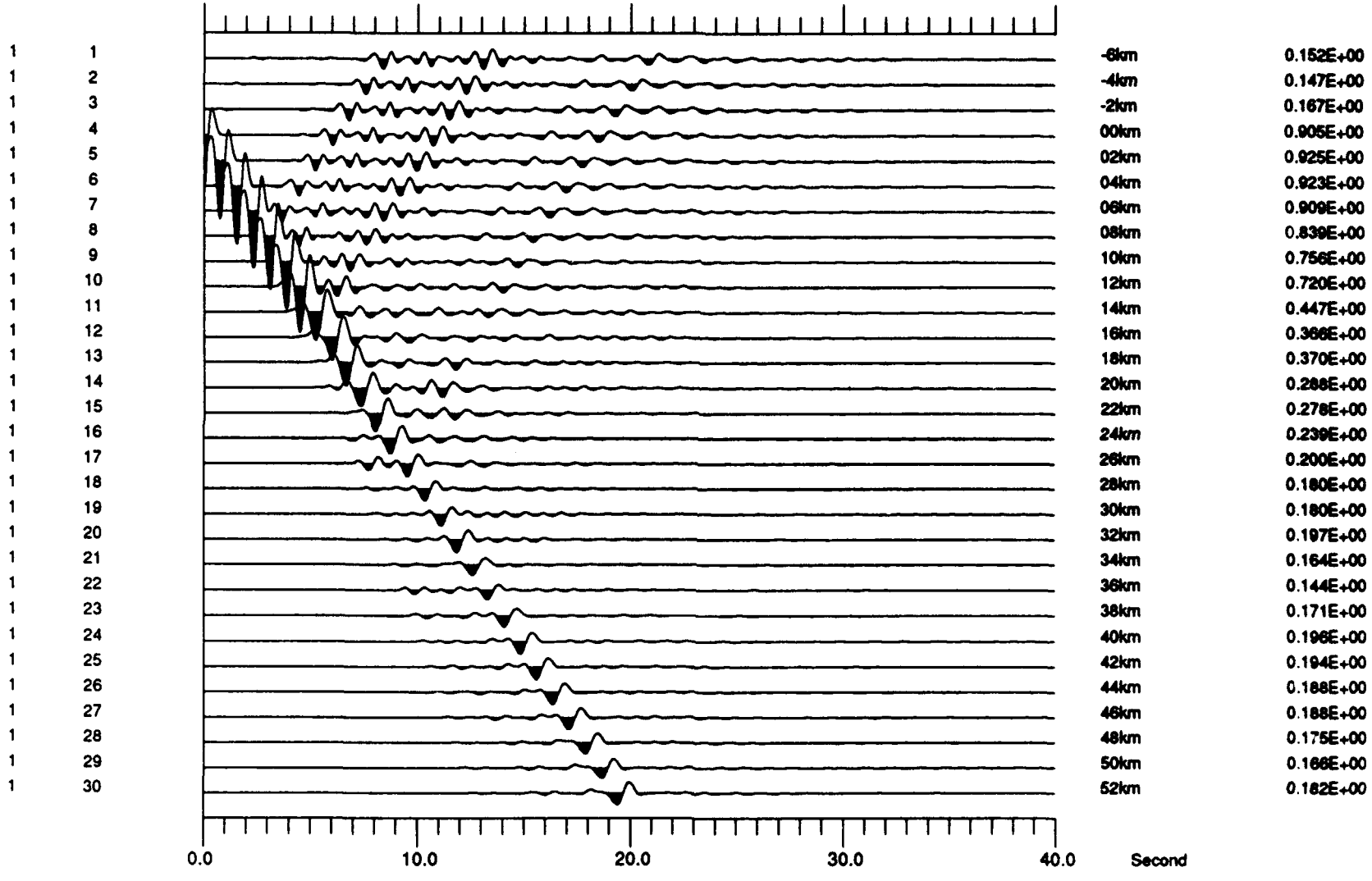
**Figure 47**




Profile 23(seed 93356, Pr(1)=0.10), Surface Sensors

VERT, same scale, decimated by 5

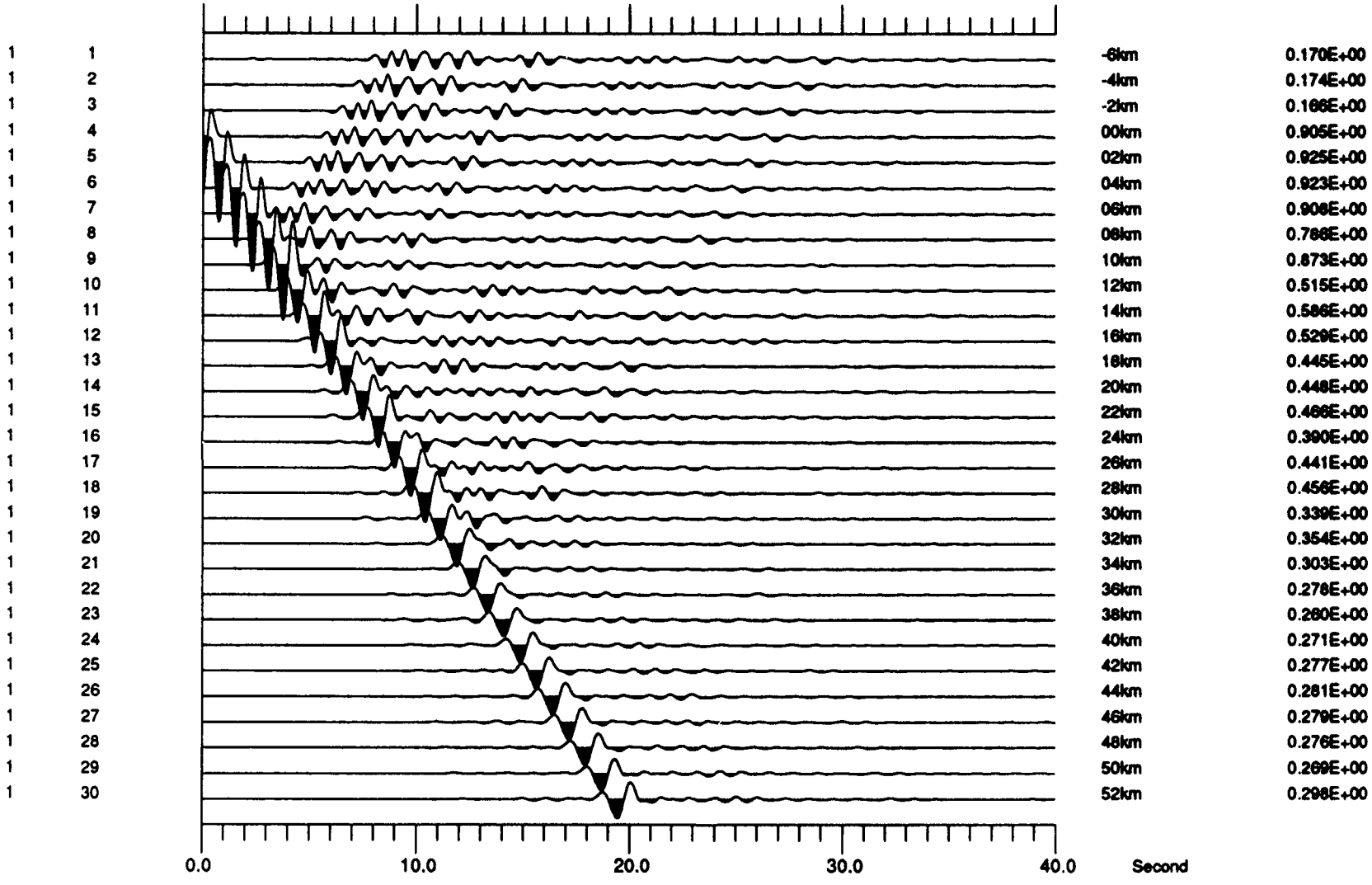
**Figure 48**




Profile 31(seed 748546615, Pr(1)=0.15), Surface Sensors

VERT, same scale, decimated by 5

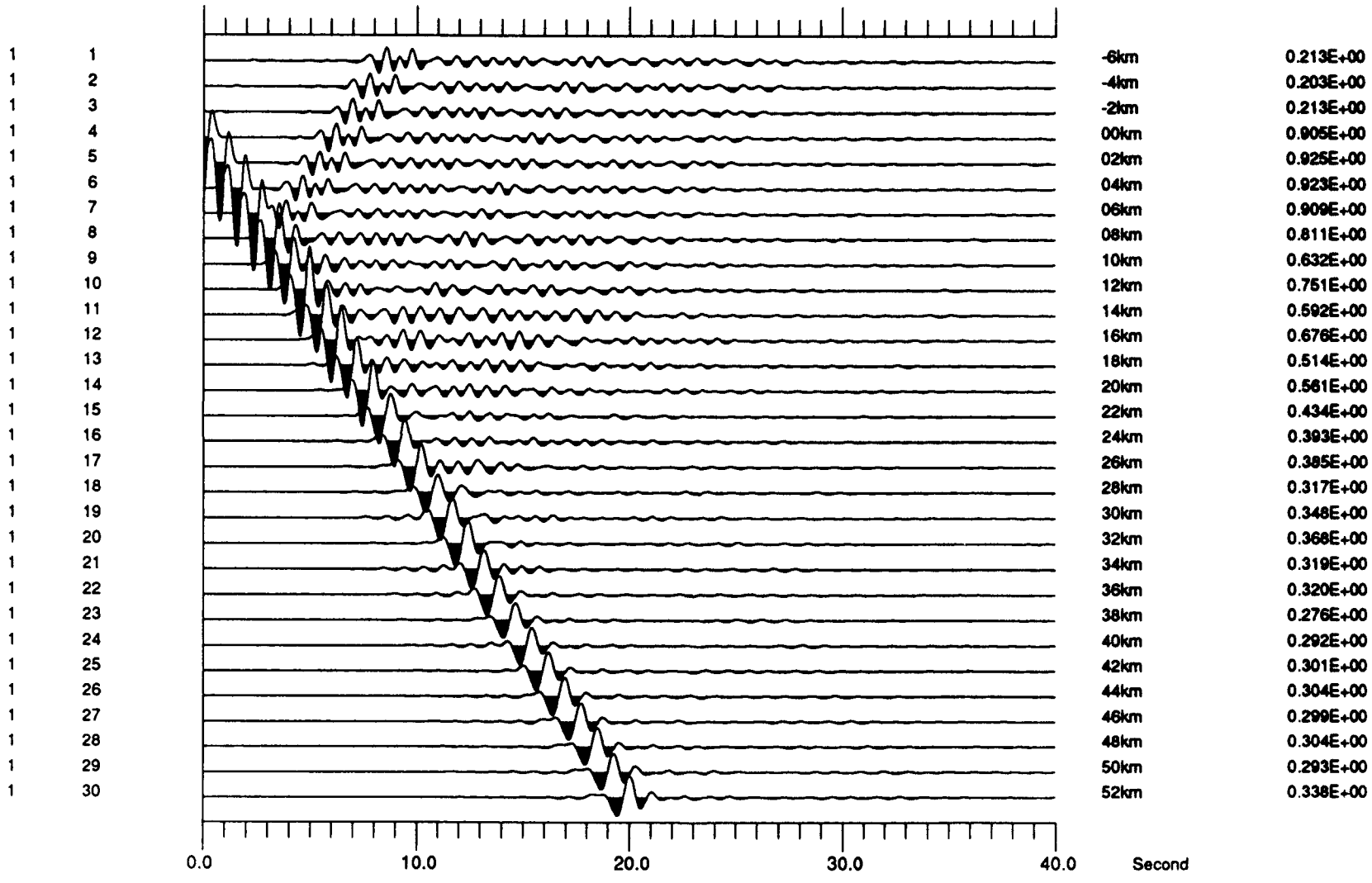
**Figure 49**




Profile 32(seed 20333, Pr(1)=0.15), Surface Sensors

VERT, same scale, decimated by 5

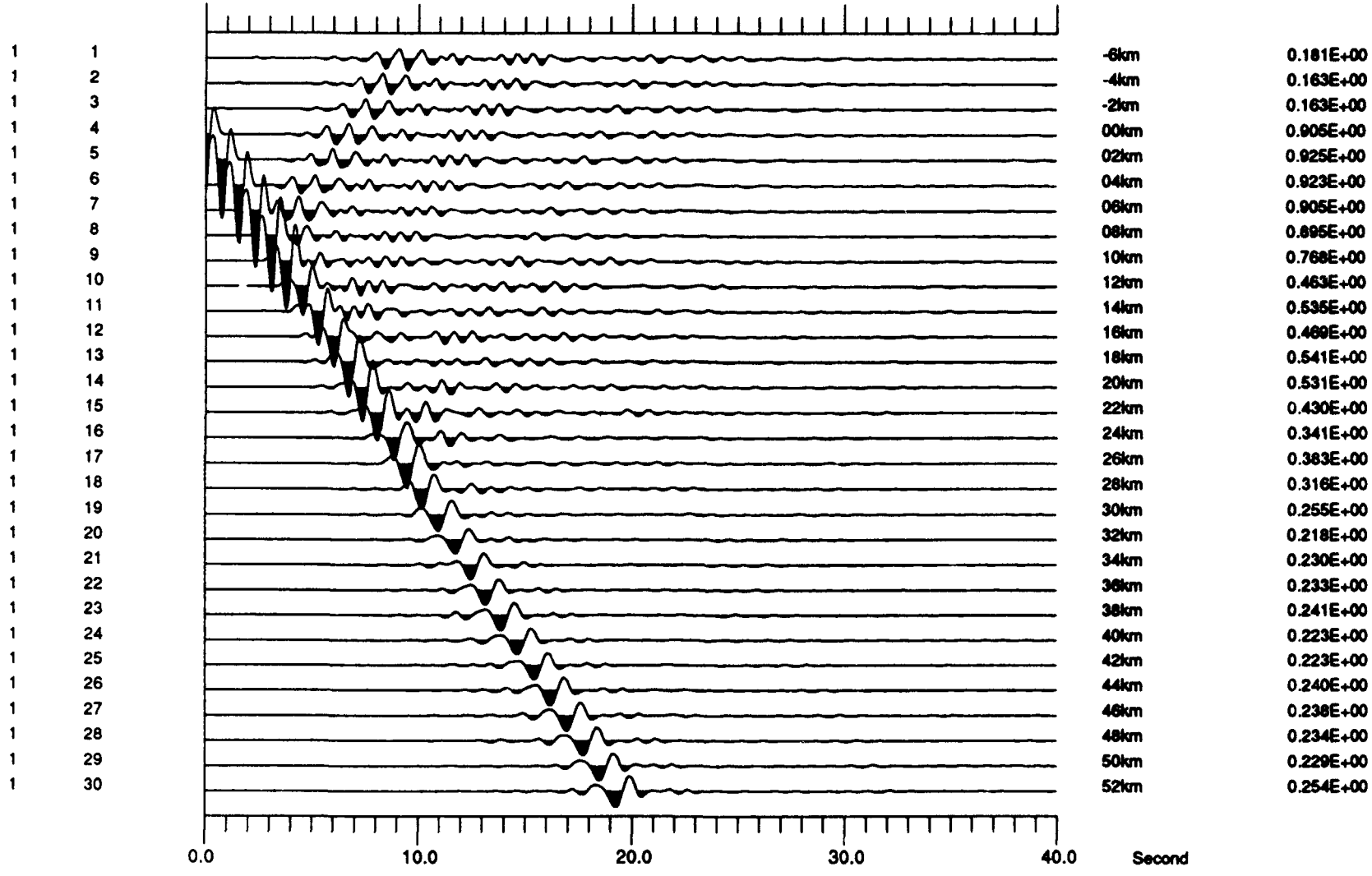
**Figure 50**




Profile 33(seed 86016, Pr(1)=0.15), Surface Sensors

VERT, same scale, decimated by 5

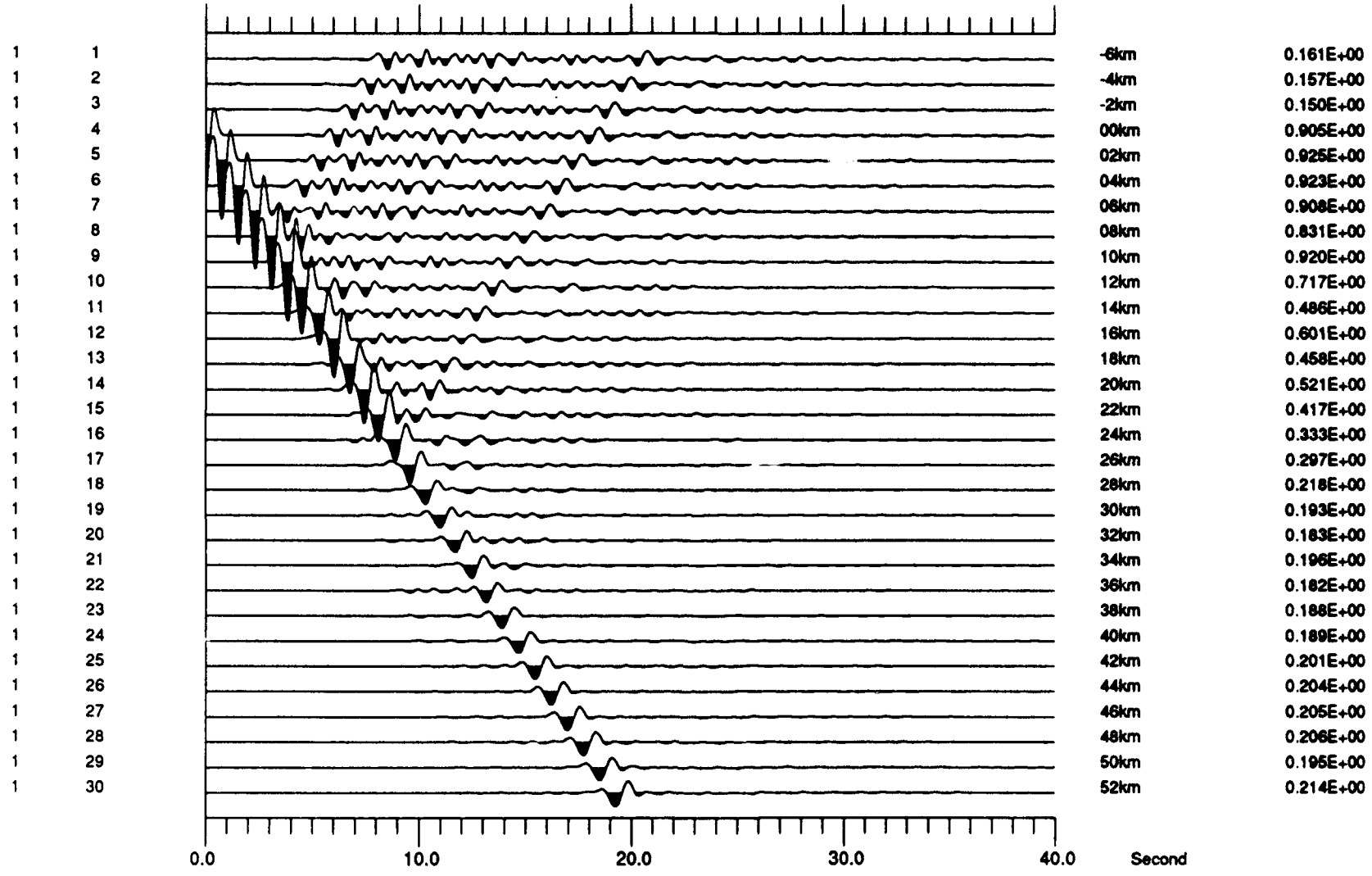
**Figure 51**




Profile 41(seed 93397, Pr(1)=0.20), Surface Sensors

VERT, same scale, decimated by 5

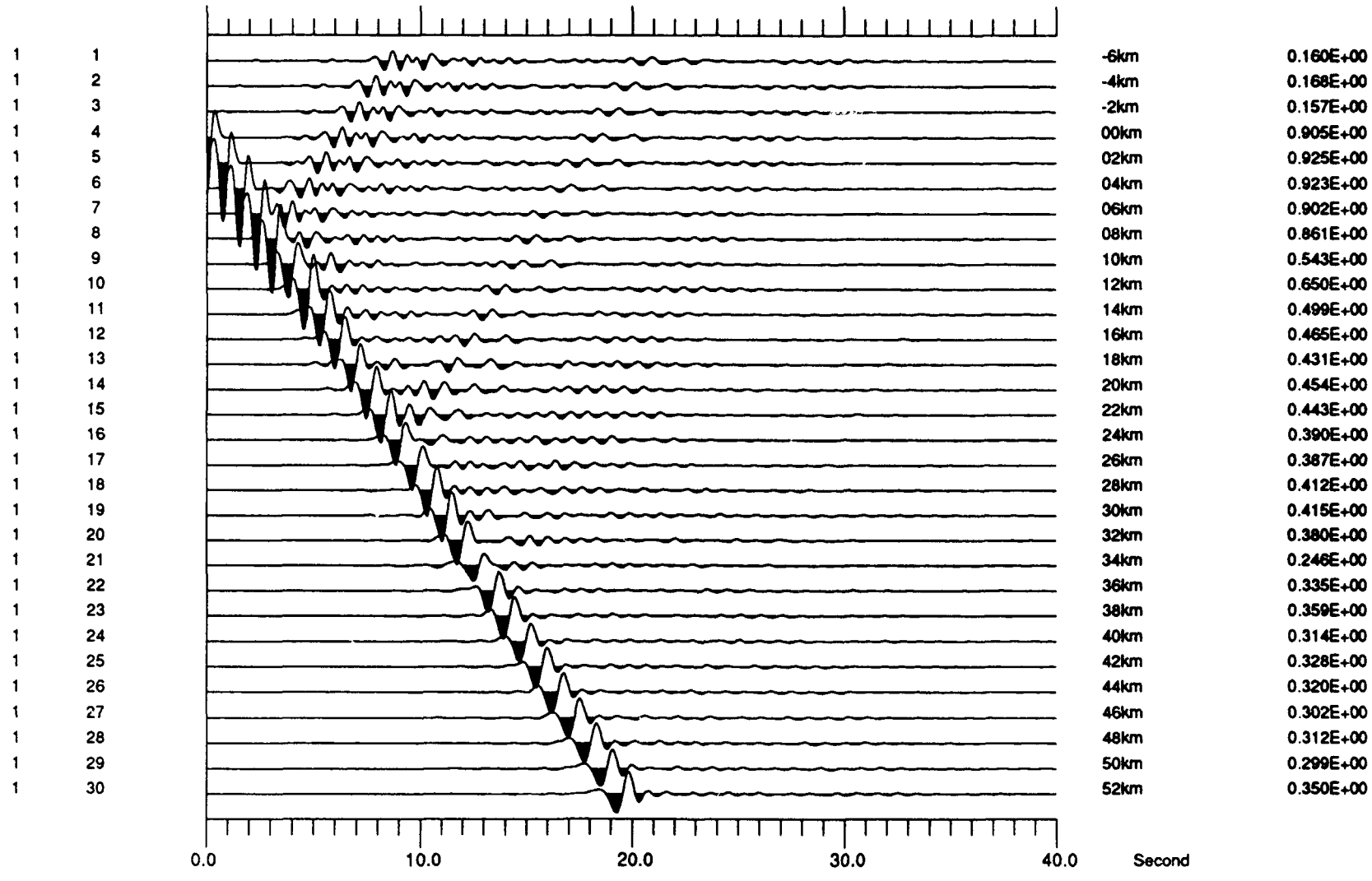
**Figure 52**




Profile 42(seed 93407, Pr(1)=0.20), Surface Sensors

VERT, same scale, decimated by 5

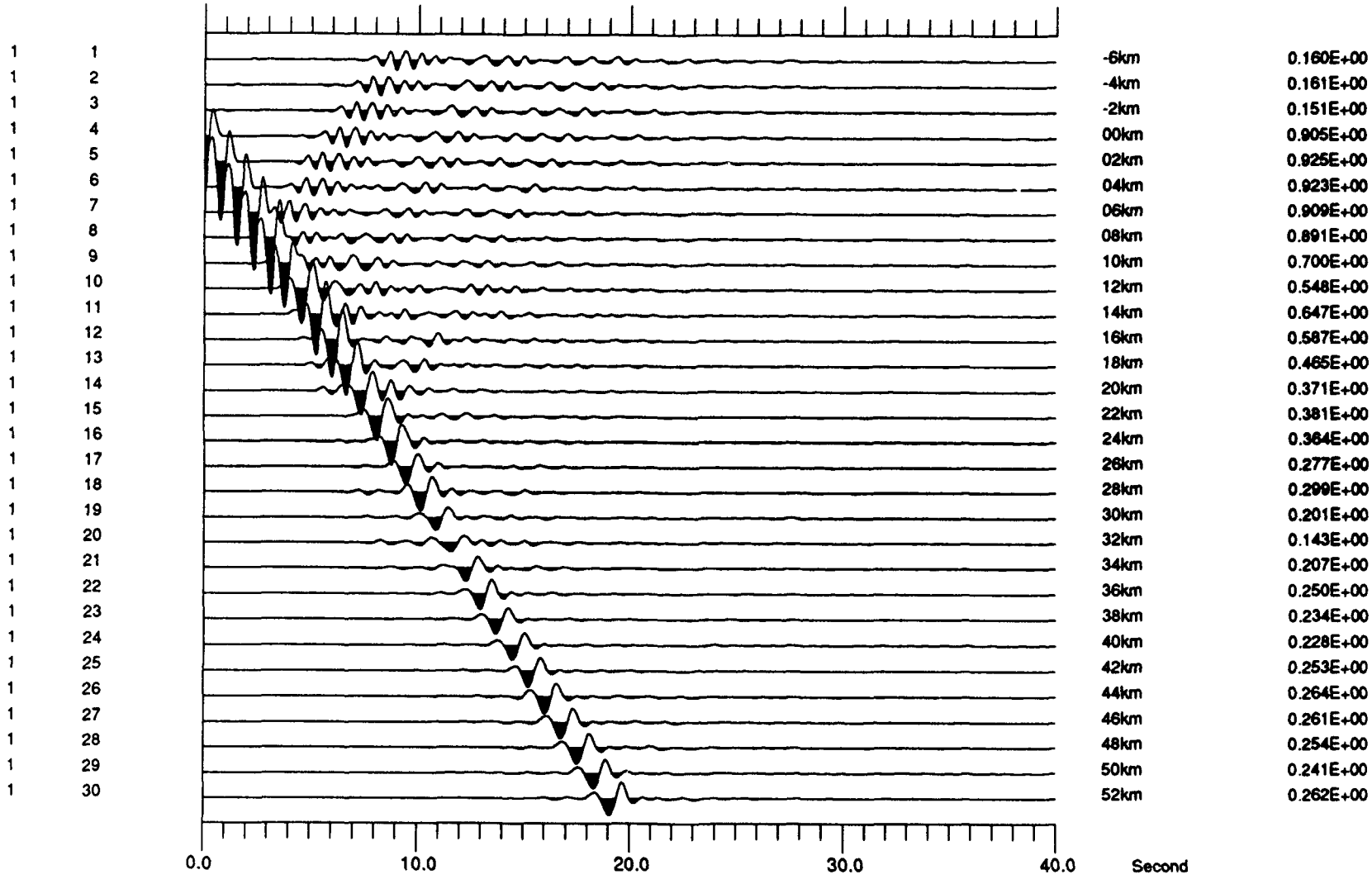
**Figure 53**




Profile 43(seed 12345, Pr(1)=0.20), Surface Sensors

VERT, samo scale, docimated by 5

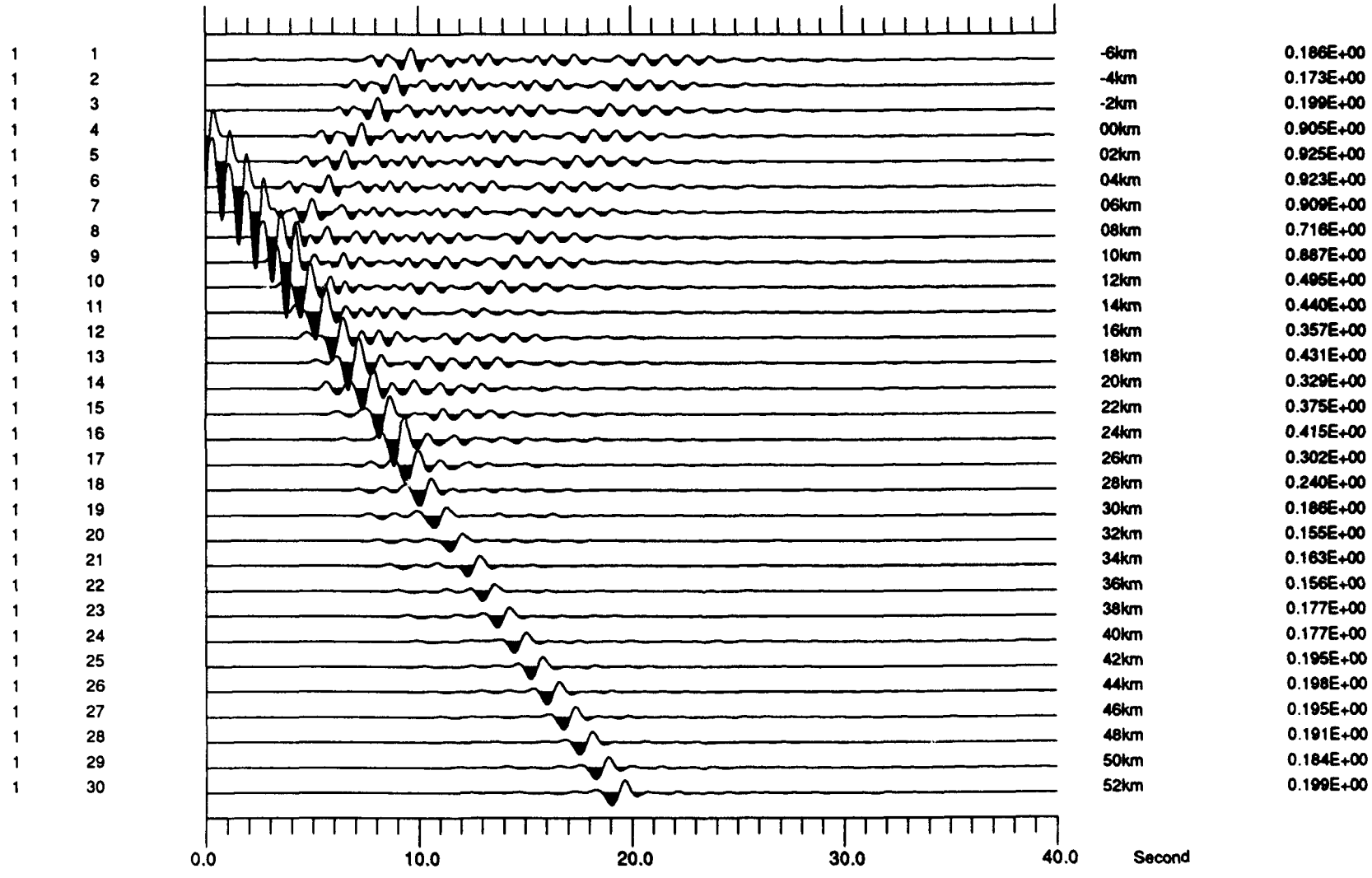
**Figure 54**




Profile 51(seed 21691, Pr(1)=0.25), Surface Sensors

VERT, same scale, decimated by 5

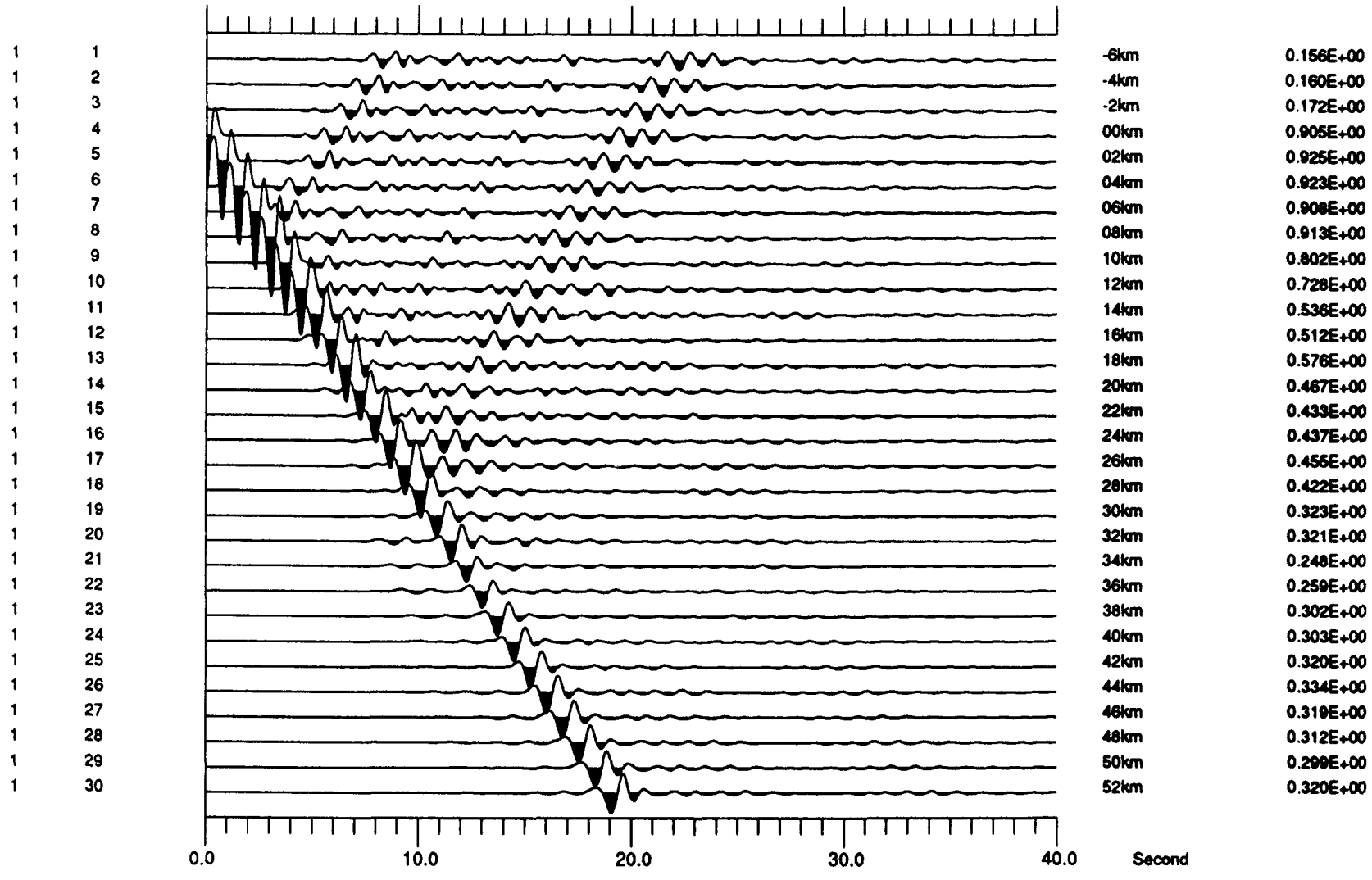
**Figure 55**




Profile 52(seed 21696, Pr(1)=0.25), Surface Sensors

VERT, same scale, decimated by 5

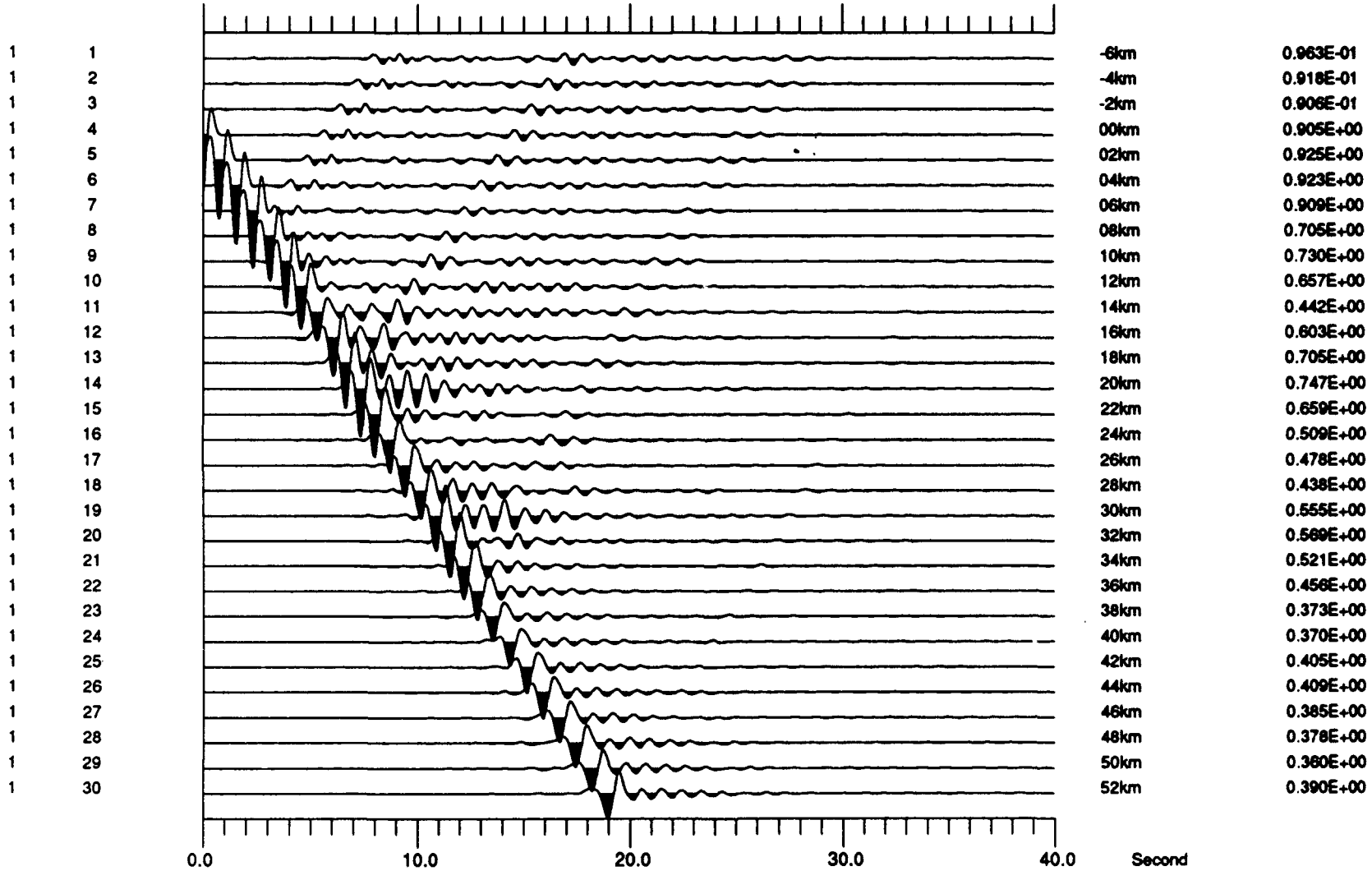
**Figure 56**




Profile 53(seed 86037, Pr(1)=0.25), Surface Sensors

VERT, same scale, decimated by 5

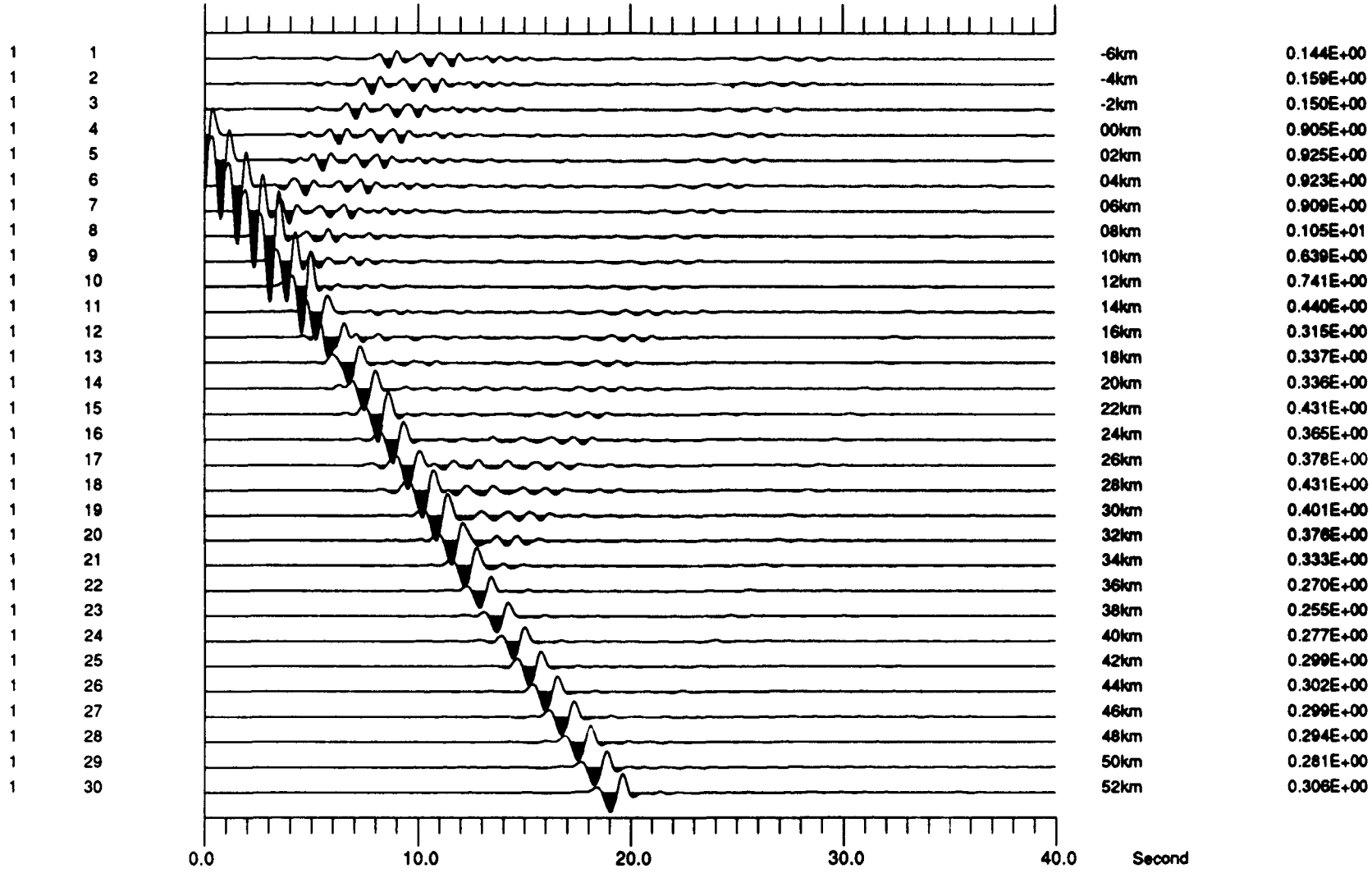
**Figure 57**




Profile 61(seed 93459, Pr(1)=0.30), Surface Sensors

VERT, same scale, decimated by 5

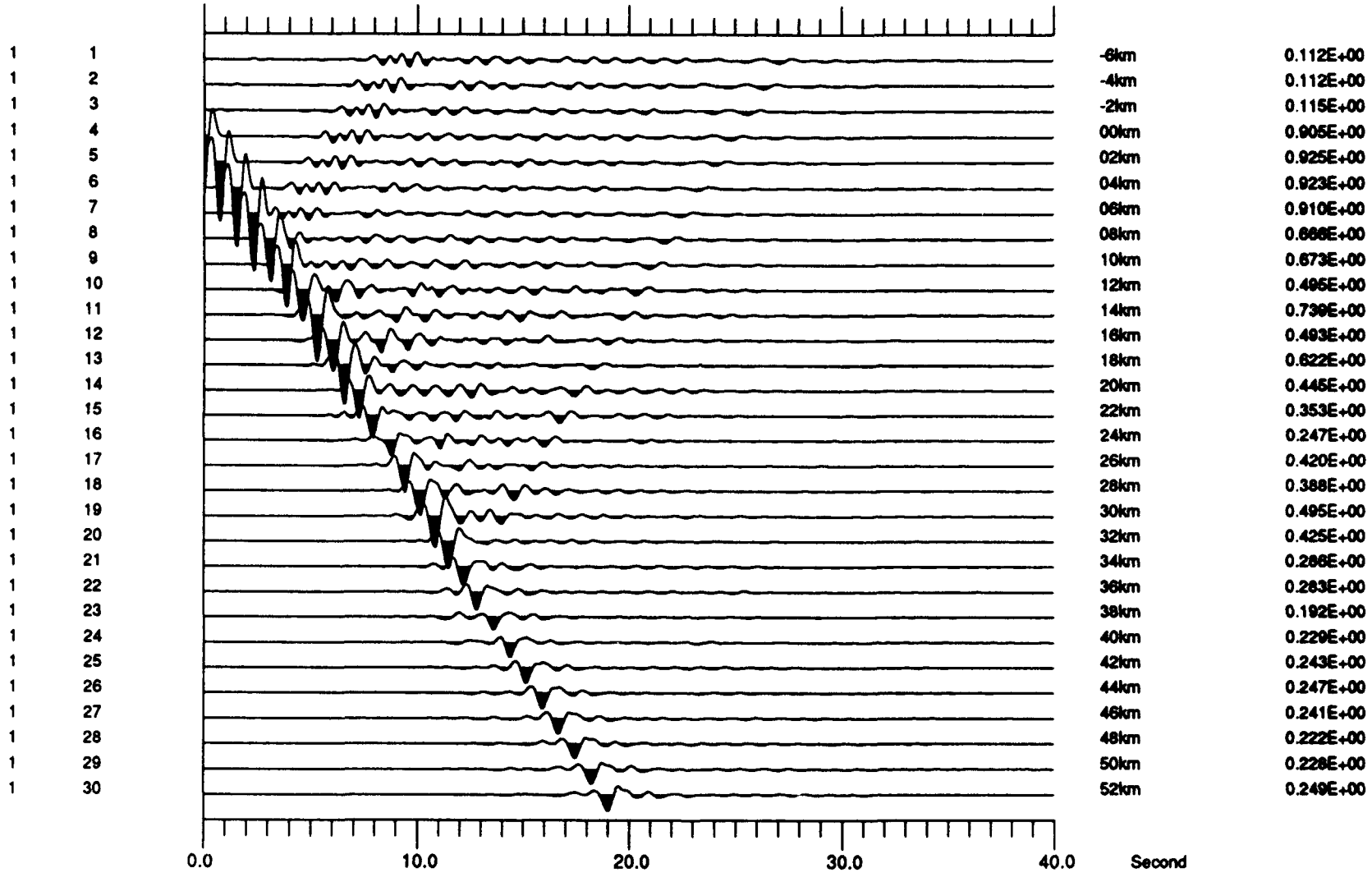
**Figure 58**




Profile 62(seed 93468, Pr(1)=0.30), Surface Sensors

VERT, same scale, decimated by 5

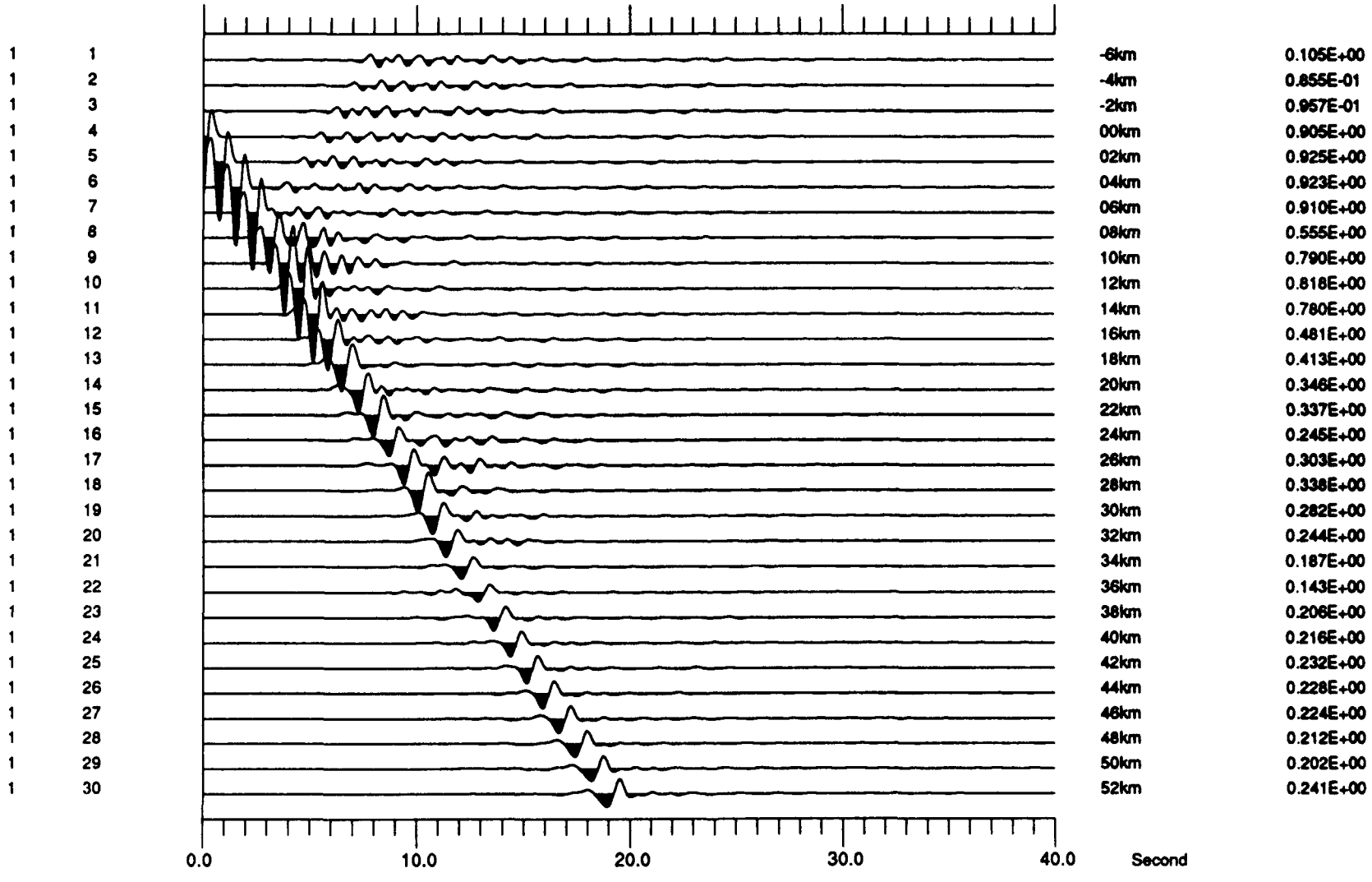
Figure 59




Profile 63(seed 93479, Pr(1)=0.30), Surface Sensors

VERT, same scale, decimated by 5

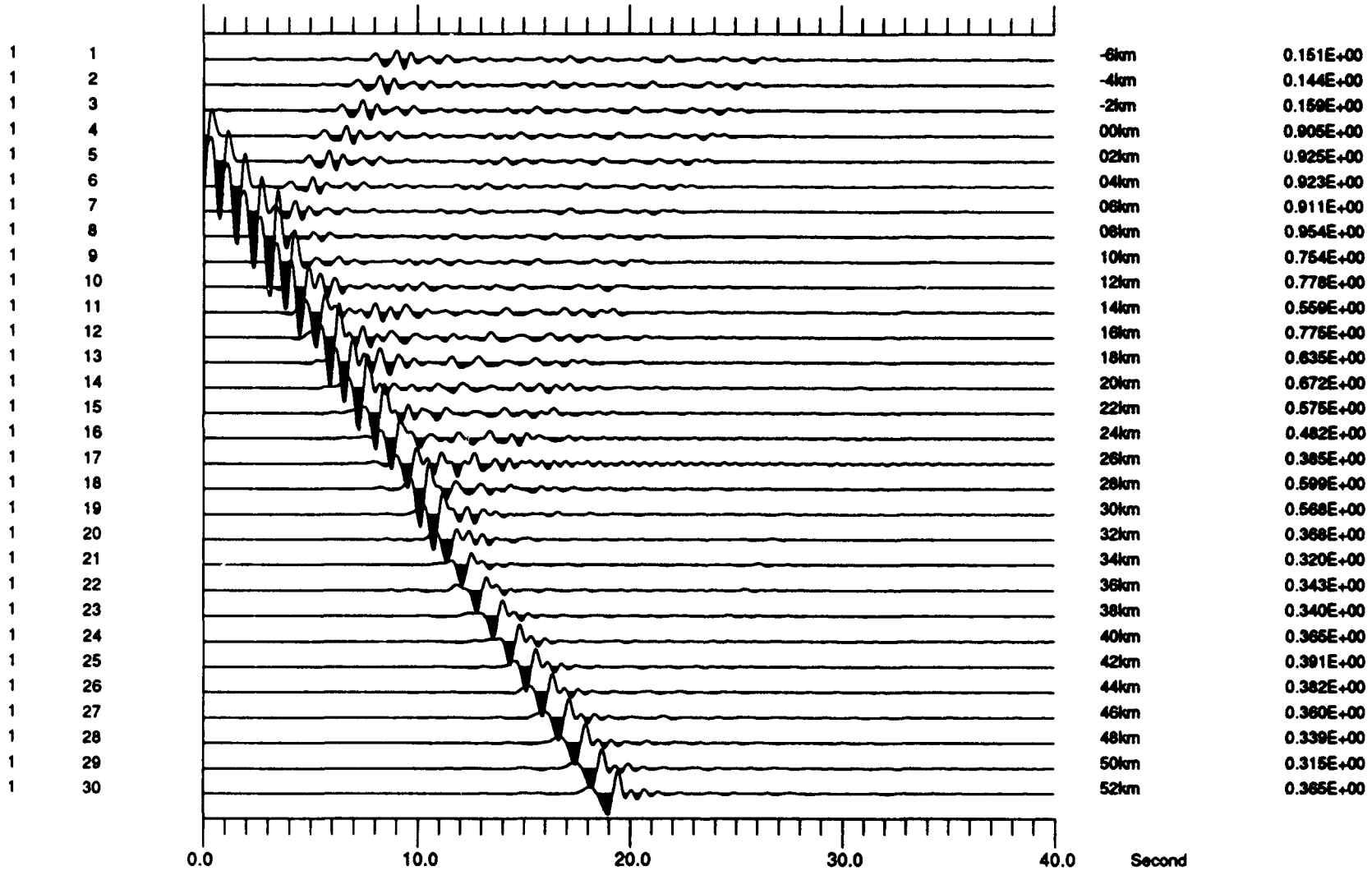
**Figure 60**




Profile 64(seed 55473, Pr(1)=0.32), Surface Sensors

VERT, same scale, decimated by 5

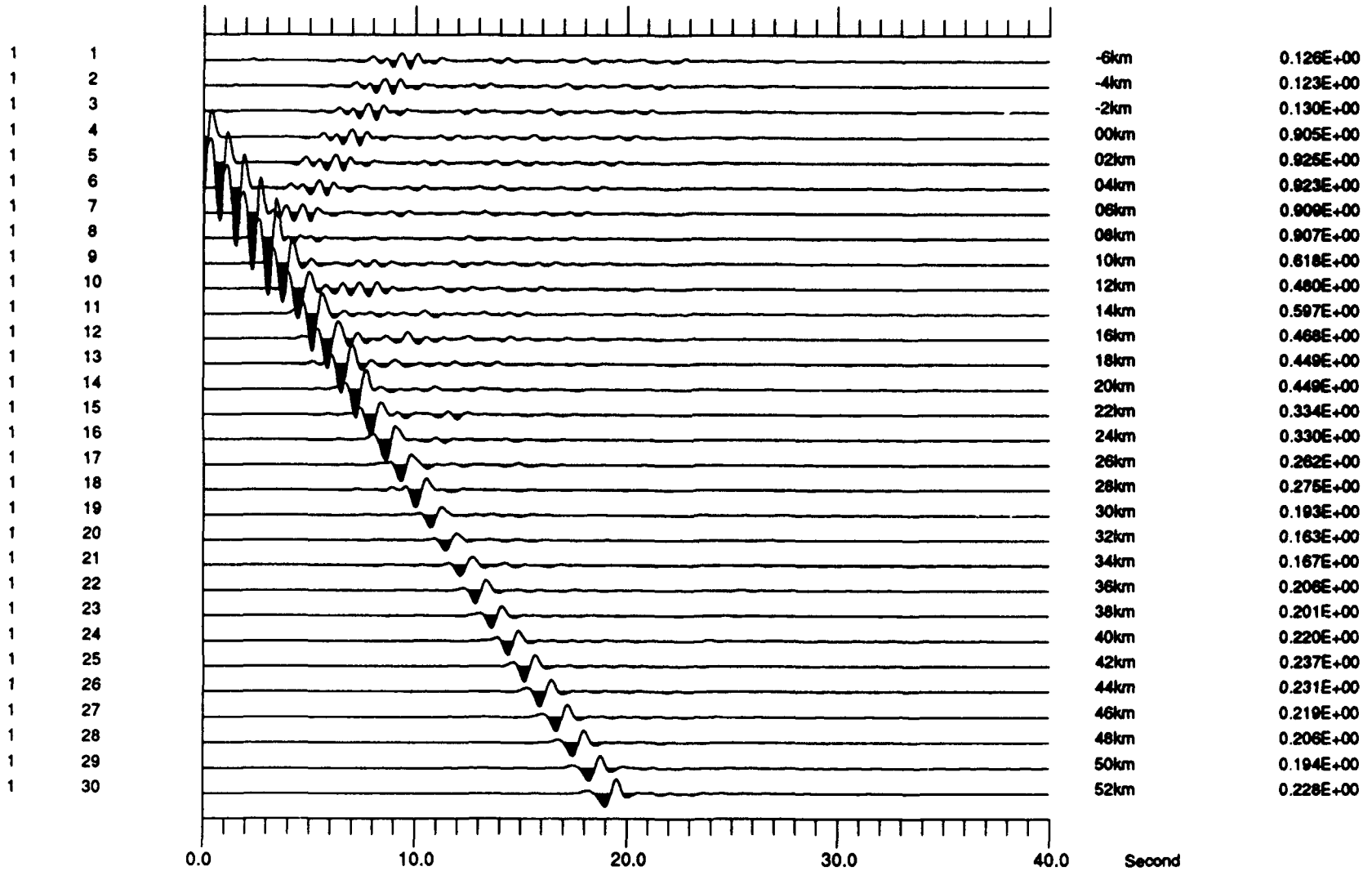
**Figure 61**




Profile 65(seed 55499, Pr(1)=0.32), Surface Sensors

VERT, same scale, decimated by 5

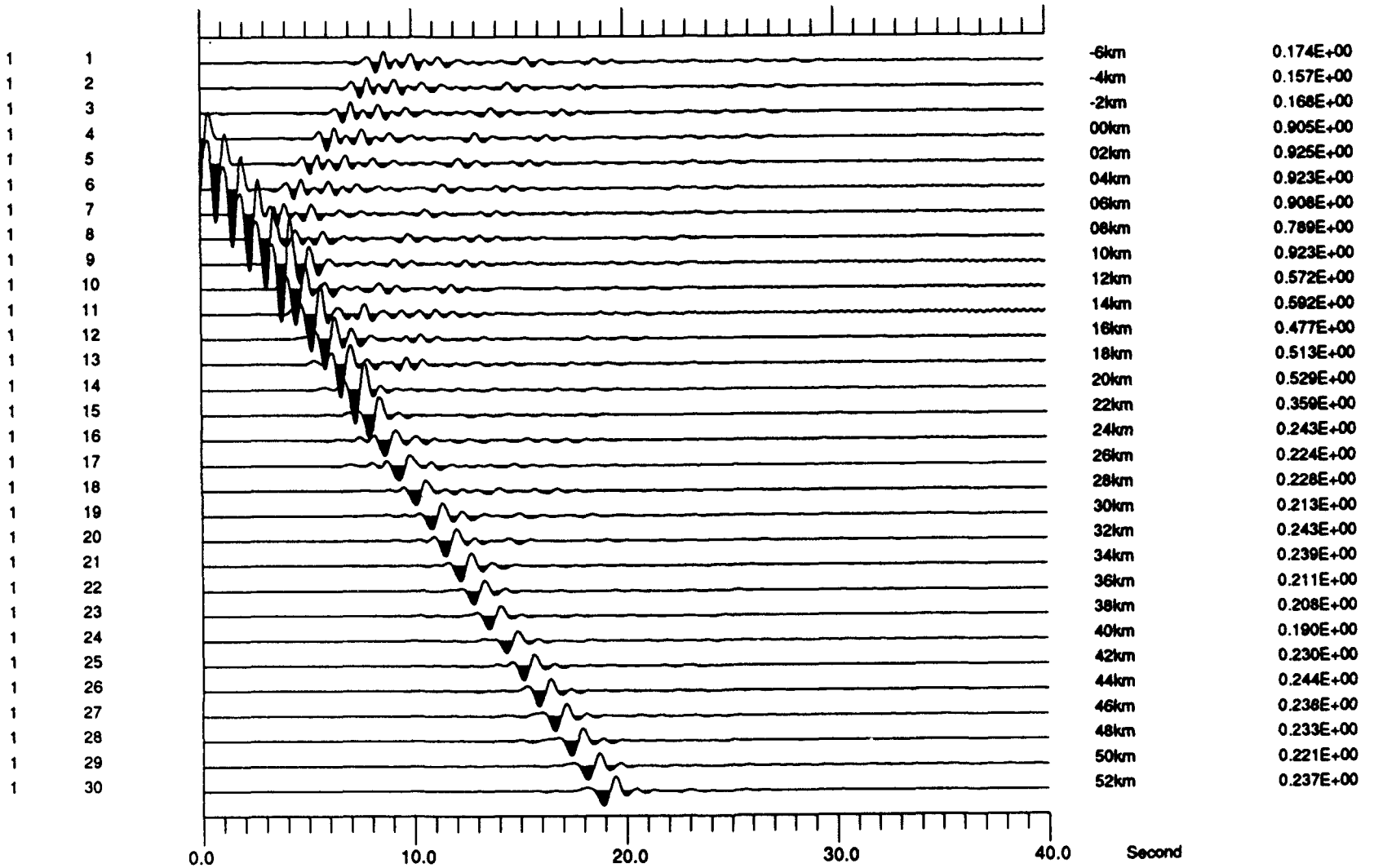
**Figure 62**




Profile 66(seed 55446, Pr(1)=0.32), Surface Sensors

VERT, same scale, decimated by 5

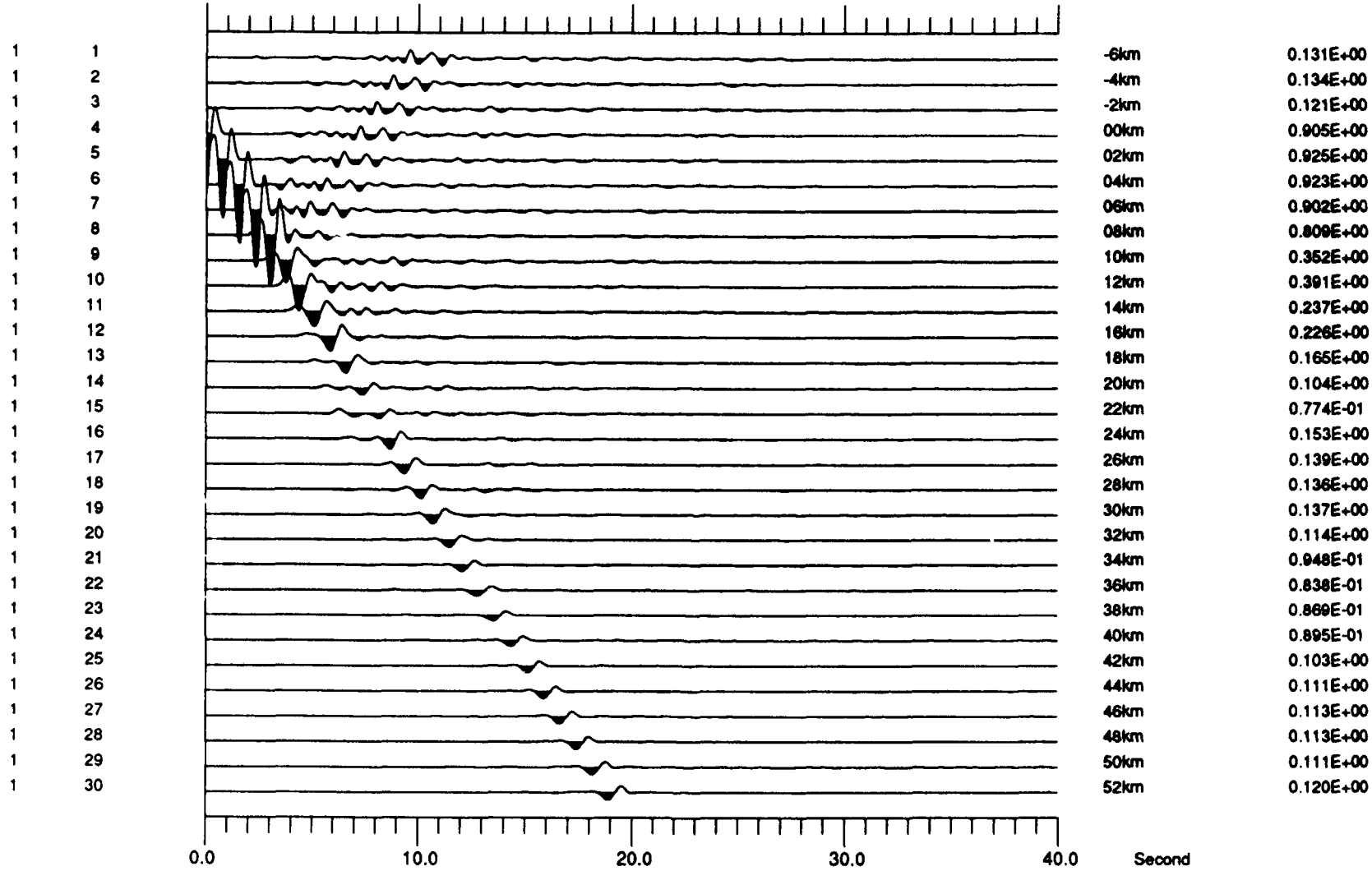
**Figure 63**




Profile 71(seed 22192, Pr(1)=0.35), Surface Sensors

VERT, same scale, decimated by 5

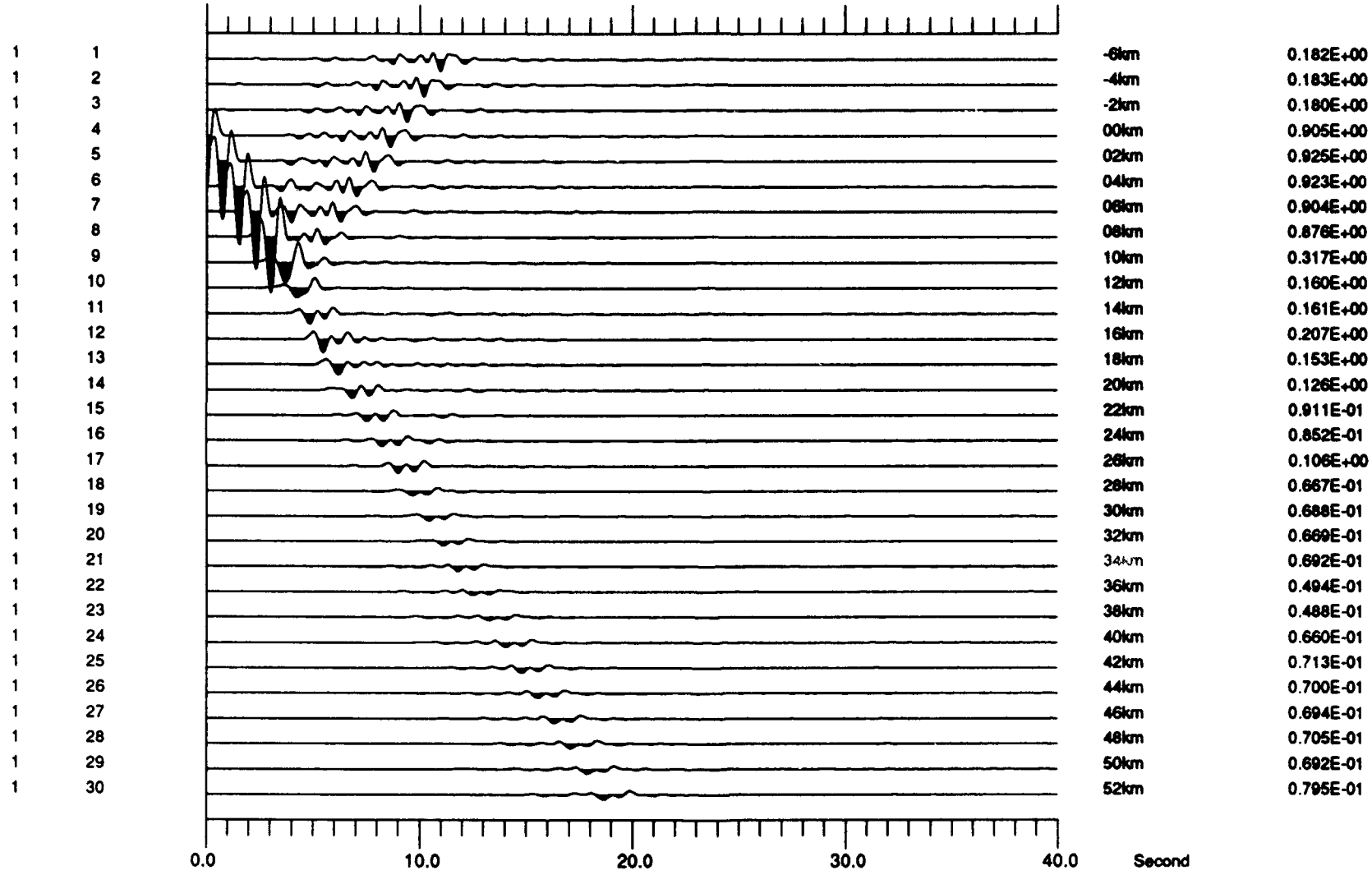
**Figure 64**




Profile 72(seed 31087, Pr(1)=0.35), Surface Sensors

VERT, same scale, decimated by 5

**Figure 65**




Profile 73(seed 86061, Pr(1)=0.35), Surface Sensors

VERT, same scale, decimated by 5

**Figure 66**

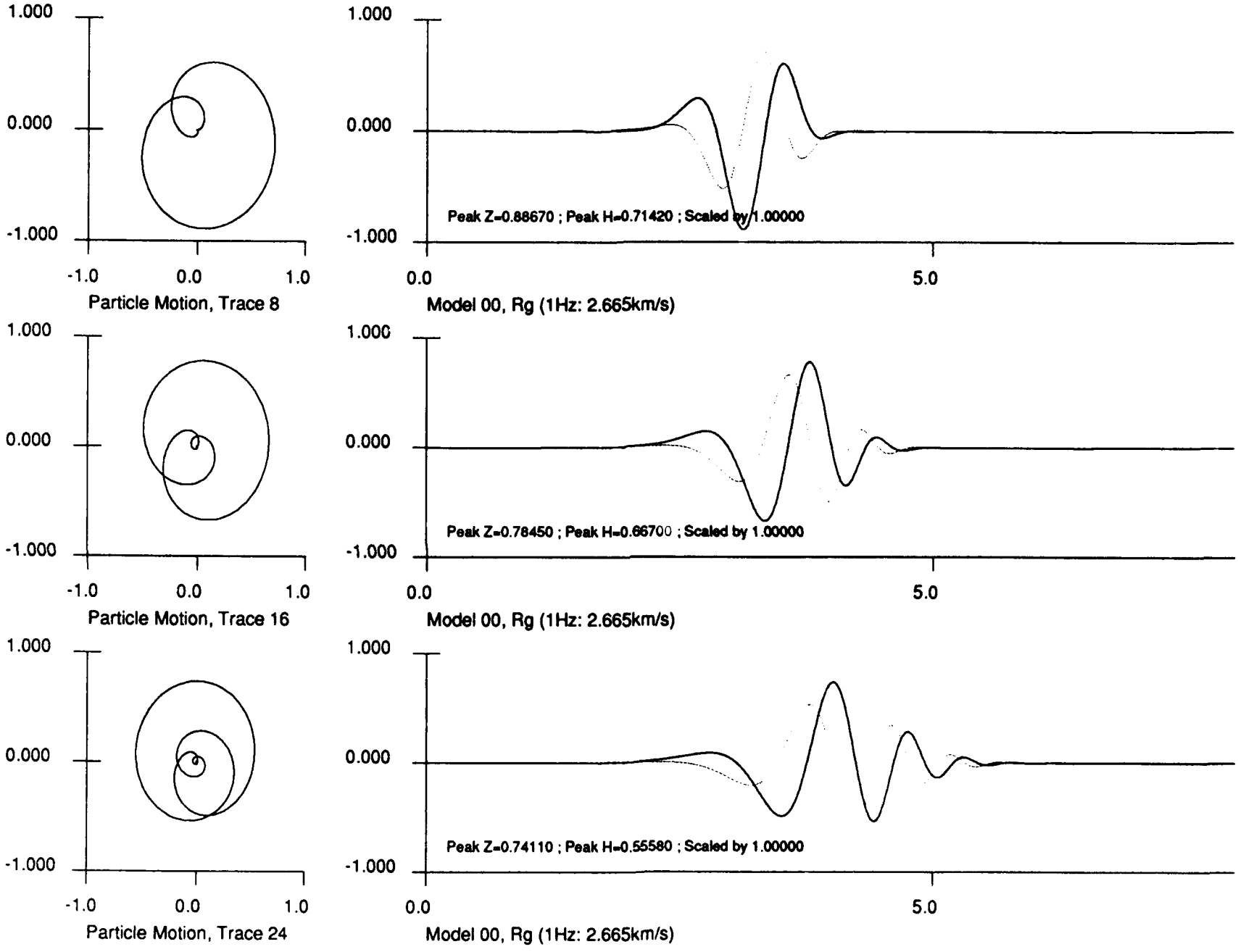

1.000
0.000
-1.000
-1.0
0.0
1.0
Particle Motion, Trace 8
Peak Z=0.88670 ; Peak H=0.71420 ; Scaled by 1.00000
0.0
5.0
Model 00, Rg (1Hz: 2.665km/s)
Particle Motion, Trace 16
Peak Z=0.78450 ; Peak H=0.66700 ; Scaled by 1.00000
Model 00, Rg (1Hz: 2.665km/s)
Particle Motion, Trace 24
Peak Z=0.74110 ; Peak H=0.55580 ; Scaled by 1.00000
Model 00, Rg (1Hz: 2.665km/s)

**Figure 67**

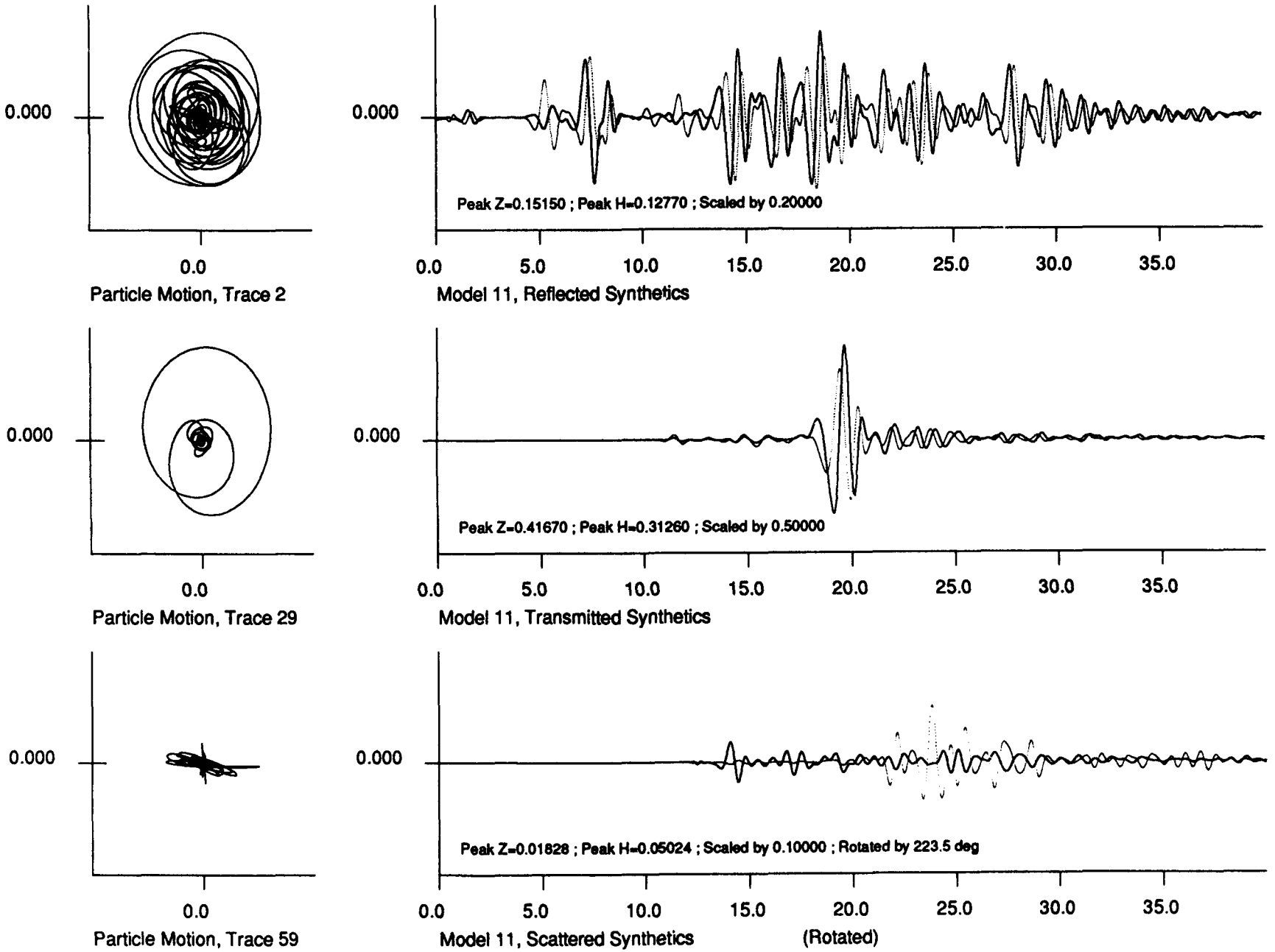

0.000
0.0
Particle Motion, Trace 2
0.000
Peak Z=0.15150 ; Peak H=0.12770 ; Scaled by 0.20000
0.0
5.0
10.0
15.0
20.0
25.0
30.0
35.0
Model 11, Reflected Synthetics
0.000
0.0
Particle Motion, Trace 29
0.000
Peak Z=0.41670 ; Peak H=0.31260 ; Scaled by 0.50000
0.0
5.0
10.0
15.0
20.0
25.0
30.0
35.0
Model 11, Transmitted Synthetics
0.000
0.0
Particle Motion, Trace 59
0.000
Peak Z=0.01828 ; Peak H=0.05024 ; Scaled by 0.10000 ; Rotated by 223.5 deg
0.0
5.0
10.0
15.0
20.0
25.0
30.0
35.0
Model 11, Scattered Synthetics
(Rotated)

**Figure 68**

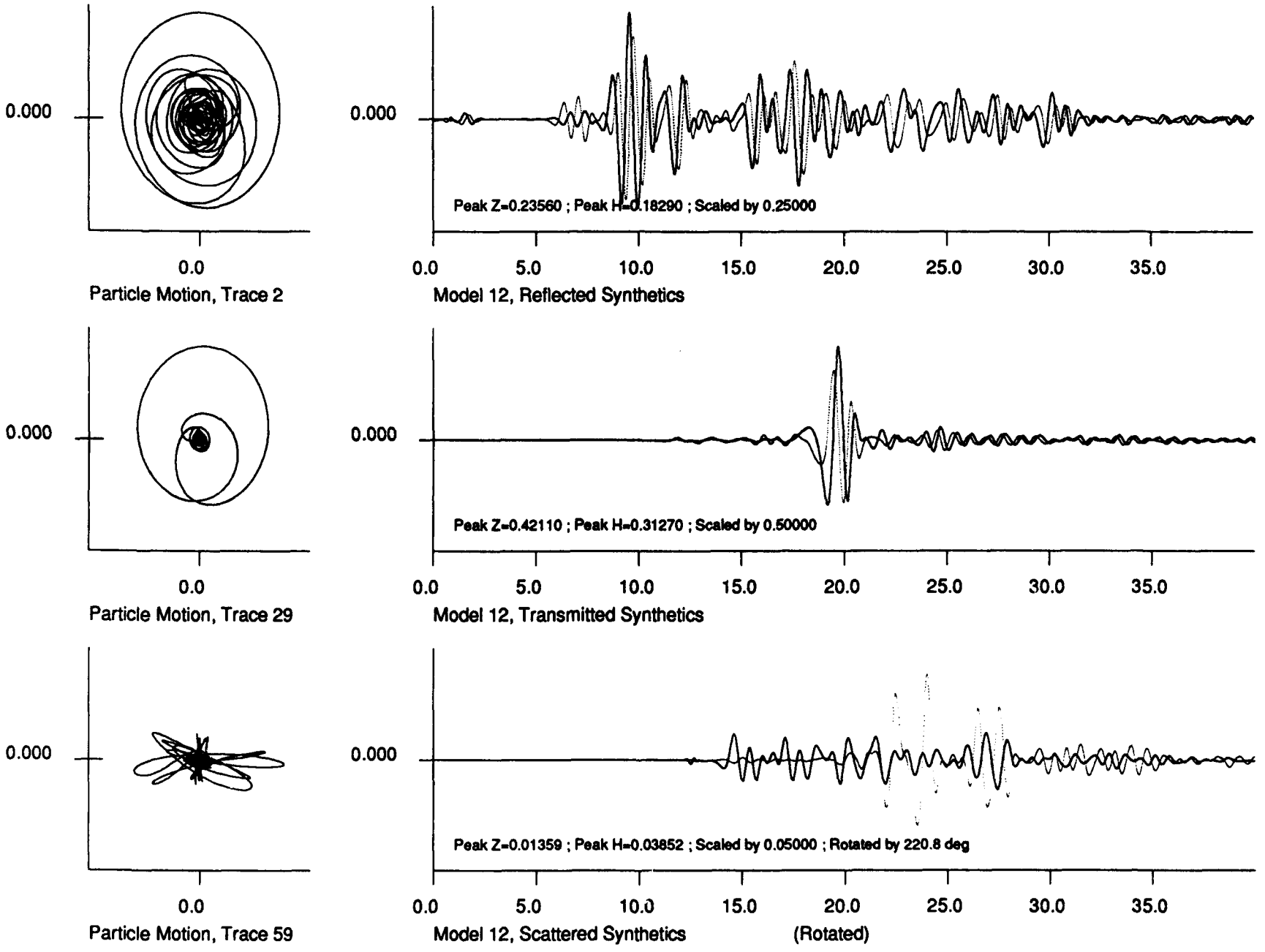

0.000
0.0
Particle Motion, Trace 2
0.000
Peak Z=0.23560 ; Peak H=0.18290 ; Scaled by 0.25000
0.0 5.0 10.0 15.0 20.0 25.0 30.0 35.0
Model 12, Reflected Synthetics
0.000
0.0
Particle Motion, Trace 29
0.000
Peak Z=0.42110 ; Peak H=0.31270 ; Scaled by 0.50000
0.0 5.0 10.0 15.0 20.0 25.0 30.0 35.0
Model 12, Transmitted Synthetics
0.000
0.0
Particle Motion, Trace 59
0.000
Peak Z=0.01359 ; Peak H=0.03852 ; Scaled by 0.05000 ; Rotated by 220.8 deg
0.0 5.0 10.0 15.0 20.0 25.0 30.0 35.0
Model 12, Scattered Synthetics (Rotated)

**Figure 69**

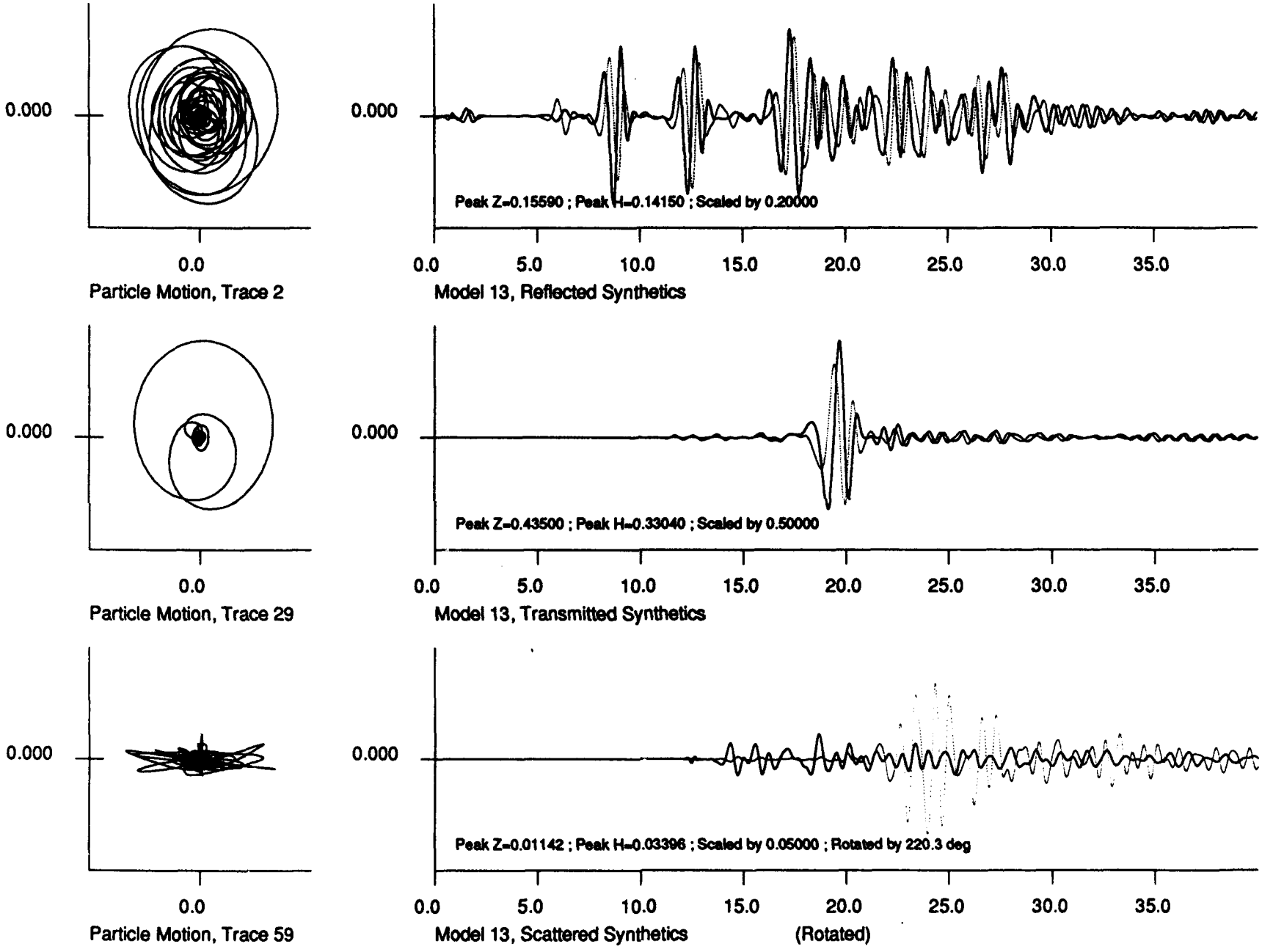

0.000
0.0
Particle Motion, Trace 2
0.000
Peak Z=0.15590 ; Peak H=0.14150 ; Scaled by 0.20000
0.0 5.0 10.0 15.0 20.0 25.0 30.0 35.0
Model 13, Reflected Synthetics
0.000
0.0
Particle Motion, Trace 29
0.000
Peak Z=0.43500 ; Peak H=0.33040 ; Scaled by 0.50000
0.0 5.0 10.0 15.0 20.0 25.0 30.0 35.0
Model 13, Transmitted Synthetics
0.000
0.0
Particle Motion, Trace 59
0.000
Peak Z=0.01142 ; Peak H=0.03396 ; Scaled by 0.05000 ; Rotated by 220.3 deg
0.0 5.0 10.0 15.0 20.0 25.0 30.0 35.0
Model 13, Scattered Synthetics (Rotated)

**Figure 70**

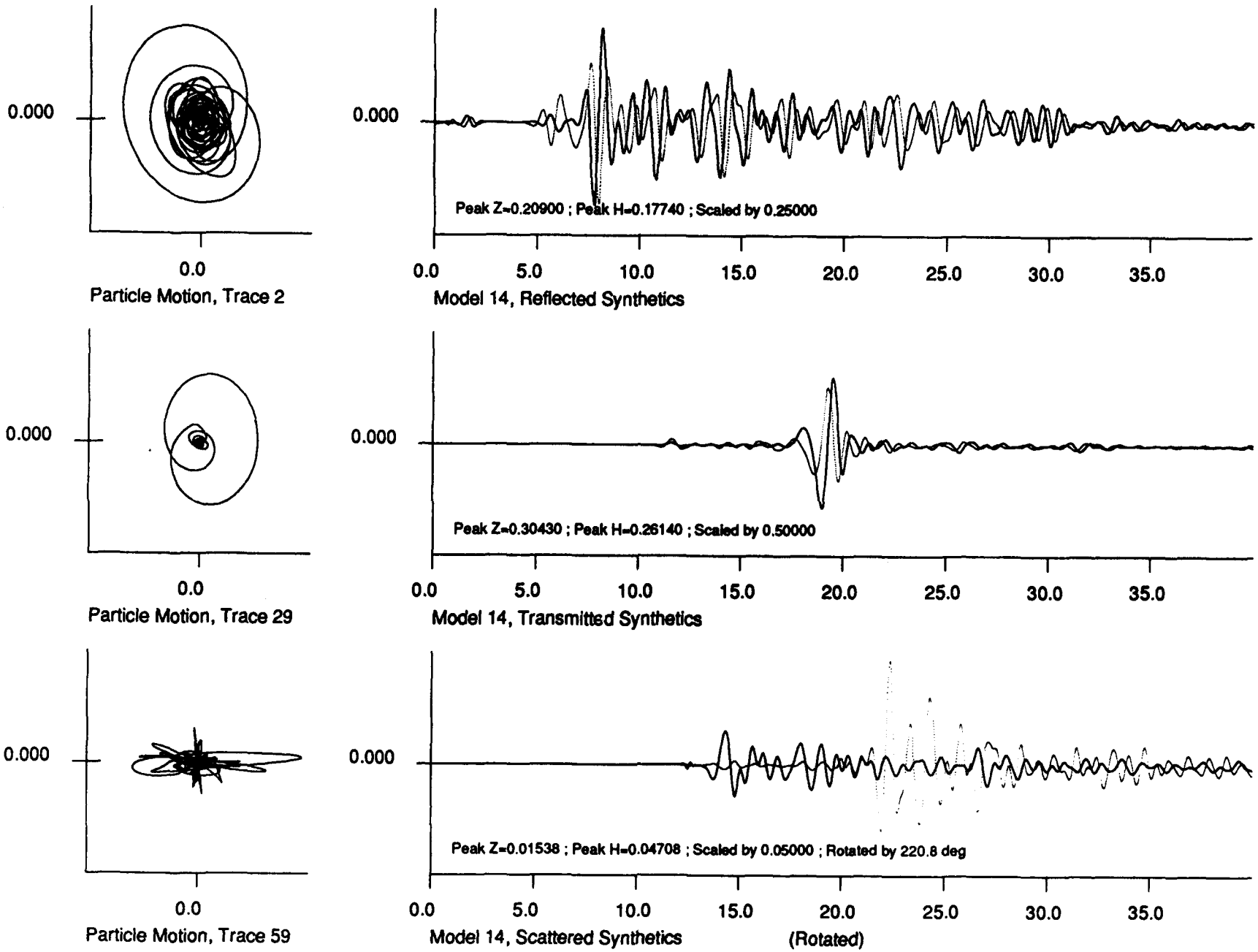

0.000
0.0
Particle Motion, Trace 2
0.000
Peak Z=0.20900 ; Peak H=0.17740 ; Scaled by 0.25000
0.0
5.0
10.0
15.0
20.0
25.0
30.0
35.0
Model 14, Reflected Synthetics
0.000
0.0
Particle Motion, Trace 29
0.000
Peak Z=0.30430 ; Peak H=0.26140 ; Scaled by 0.50000
0.0
5.0
10.0
15.0
20.0
25.0
30.0
35.0
Model 14, Transmitted Synthetics
0.000
0.0
Particle Motion, Trace 59
0.000
Peak Z=0.01538 ; Peak H=0.04708 ; Scaled by 0.05000 ; Rotated by 220.8 deg
0.0
5.0
10.0
15.0
20.0
25.0
30.0
35.0
Model 14, Scattered Synthetics
(Rotated)

**Figure 71**

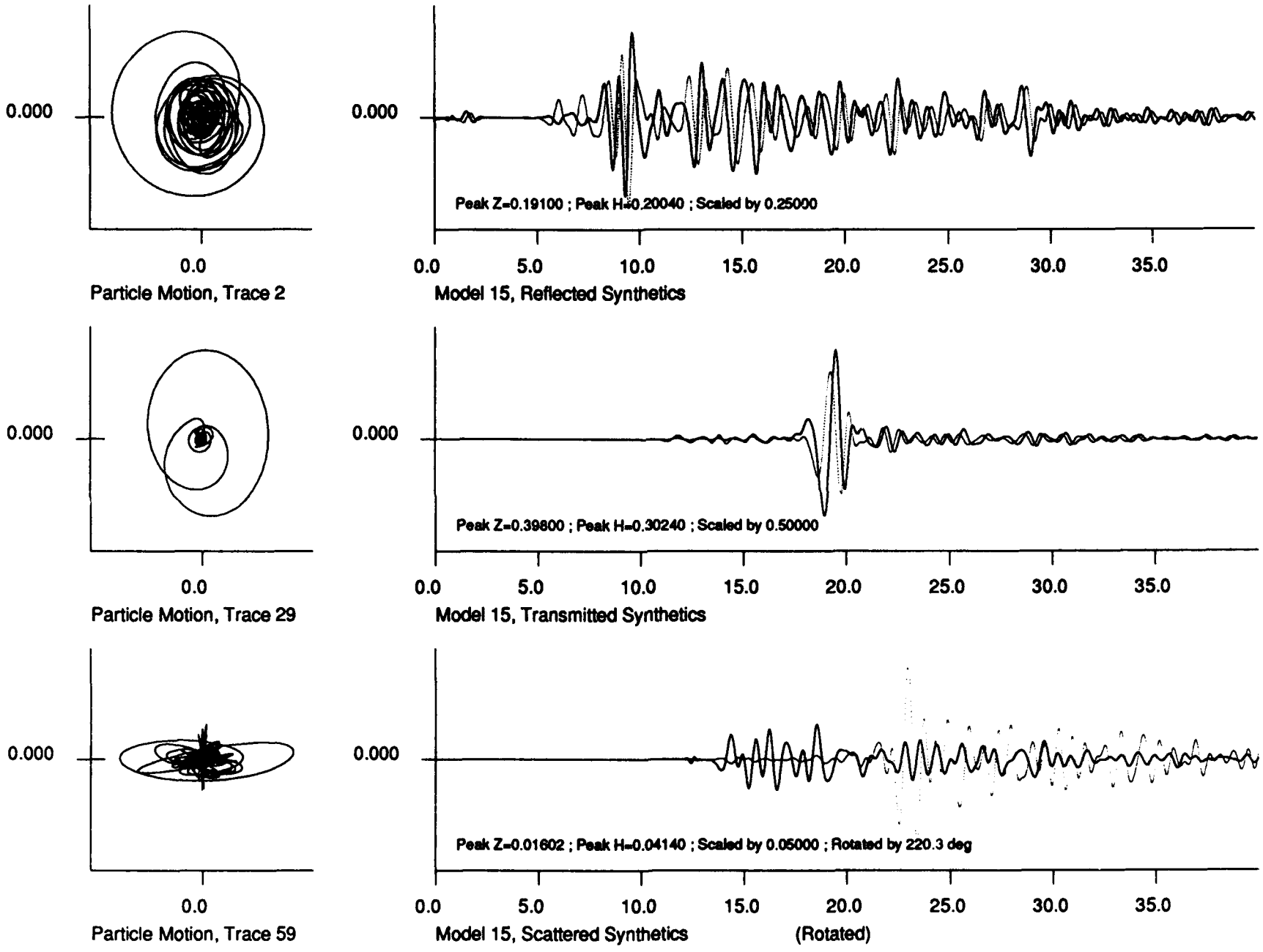

0.000
0.0
Particle Motion, Trace 2
0.000
Peak Z=0.19100 ; Peak H=0.20040 ; Scaled by 0.25000
0.0 5.0 10.0 15.0 20.0 25.0 30.0 35.0
Model 15, Reflected Synthetics
0.000
0.0
Particle Motion, Trace 29
0.000
Peak Z=0.39800 ; Peak H=0.30240 ; Scaled by 0.50000
0.0 5.0 10.0 15.0 20.0 25.0 30.0 35.0
Model 15, Transmitted Synthetics
0.000
0.0
Particle Motion, Trace 59
0.000
Peak Z=0.01602 ; Peak H=0.04140 ; Scaled by 0.05000 ; Rotated by 220.3 deg
0.0 5.0 10.0 15.0 20.0 25.0 30.0 35.0
Model 15, Scattered Synthetics (Rotated)

**Figure 72**

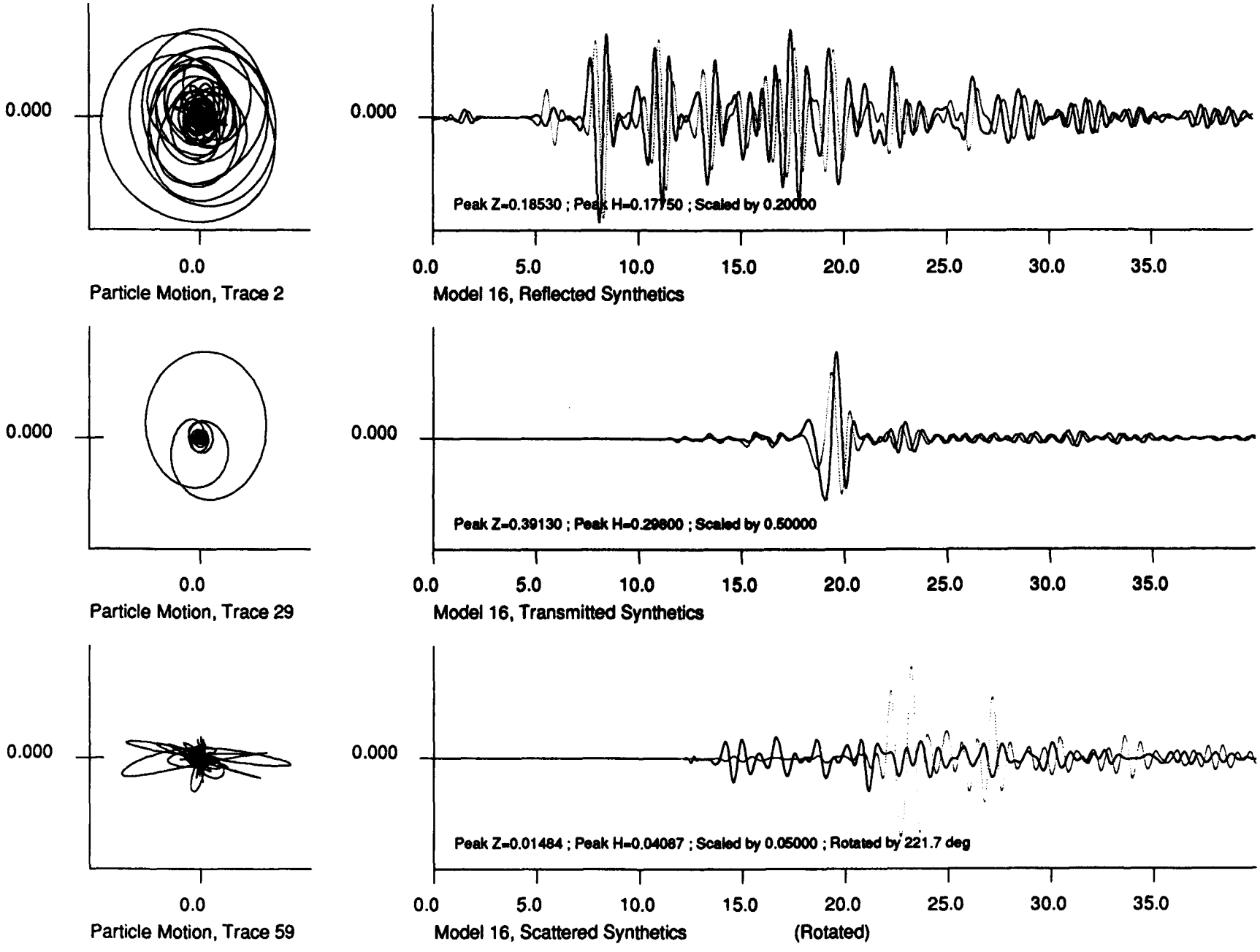

0.000
0.0
Particle Motion, Trace 2
0.000
Peak Z=0.18530 ; Peak H=0.17750 ; Scaled by 0.20000
0.0 5.0 10.0 15.0 20.0 25.0 30.0 35.0
Model 16, Reflected Synthetics
0.000
0.0
Particle Motion, Trace 29
0.000
Peak Z=0.39130 ; Peak H=0.29600 ; Scaled by 0.50000
0.0 5.0 10.0 15.0 20.0 25.0 30.0 35.0
Model 16, Transmitted Synthetics
0.000
0.0
Particle Motion, Trace 59
0.000
Peak Z=0.01484 ; Peak H=0.04087 ; Scaled by 0.05000 ; Rotated by 221.7 deg
0.0 5.0 10.0 15.0 20.0 25.0 30.0 35.0
Model 16, Scattered Synthetics (Rotated)

**Figure 73**

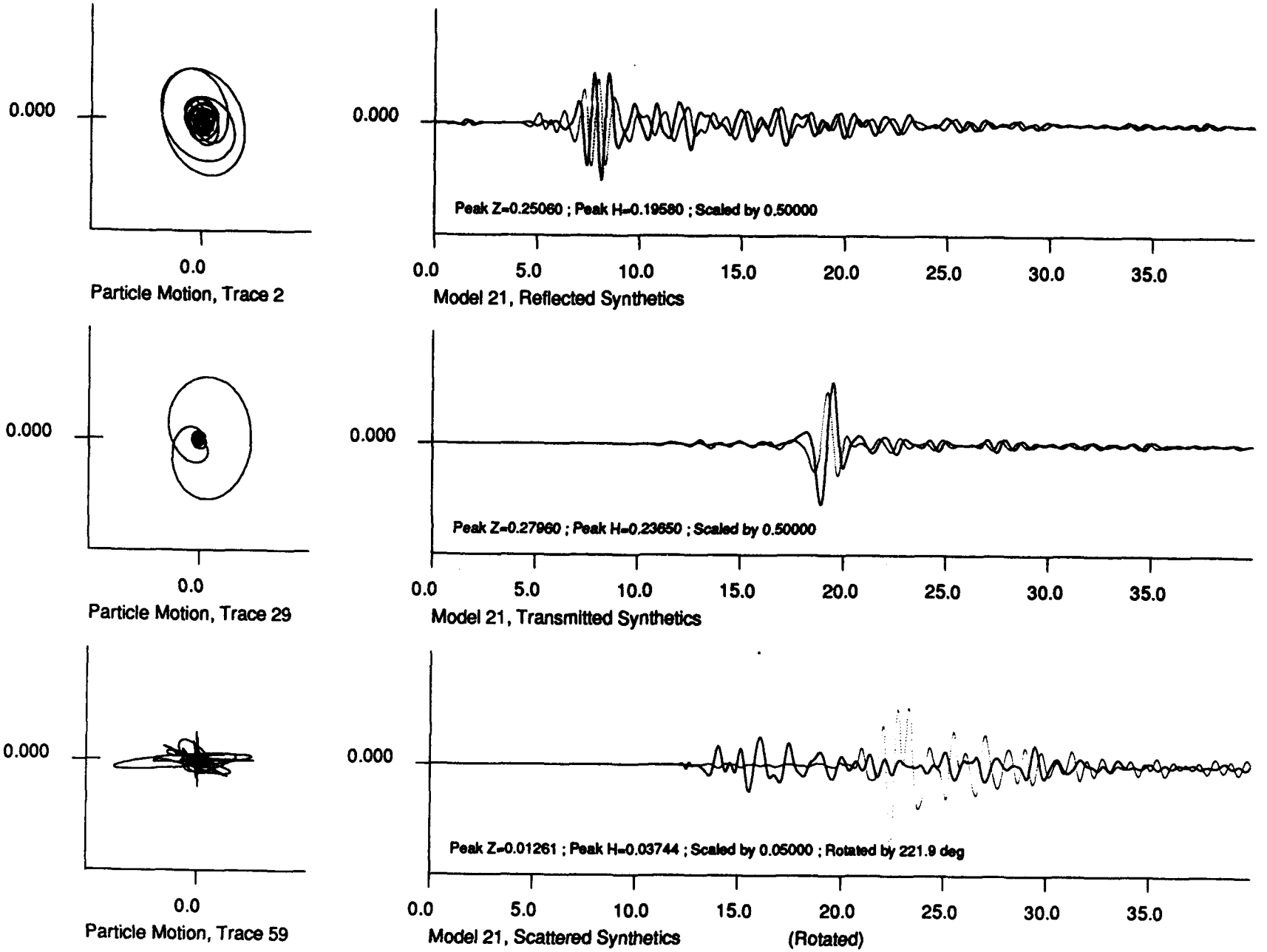

0.000
0.0
Particle Motion, Trace 2
0.000
Peak Z=0.25060 ; Peak H=0.19580 ; Scaled by 0.50000
0.0 5.0 10.0 15.0 20.0 25.0 30.0 35.0
Model 21, Reflected Synthetics
0.000
0.0
Particle Motion, Trace 29
0.000
Peak Z=0.27960 ; Peak H=0.23650 ; Scaled by 0.50000
0.0 5.0 10.0 15.0 20.0 25.0 30.0 35.0
Model 21, Transmitted Synthetics
0.000
0.0
Particle Motion, Trace 59
0.000
Peak Z=0.01261 ; Peak H=0.03744 ; Scaled by 0.05000 ; Rotated by 221.9 deg
0.0 5.0 10.0 15.0 20.0 25.0 30.0 35.0
Model 21, Scattered Synthetics
(Rotated)

**Figure 74**

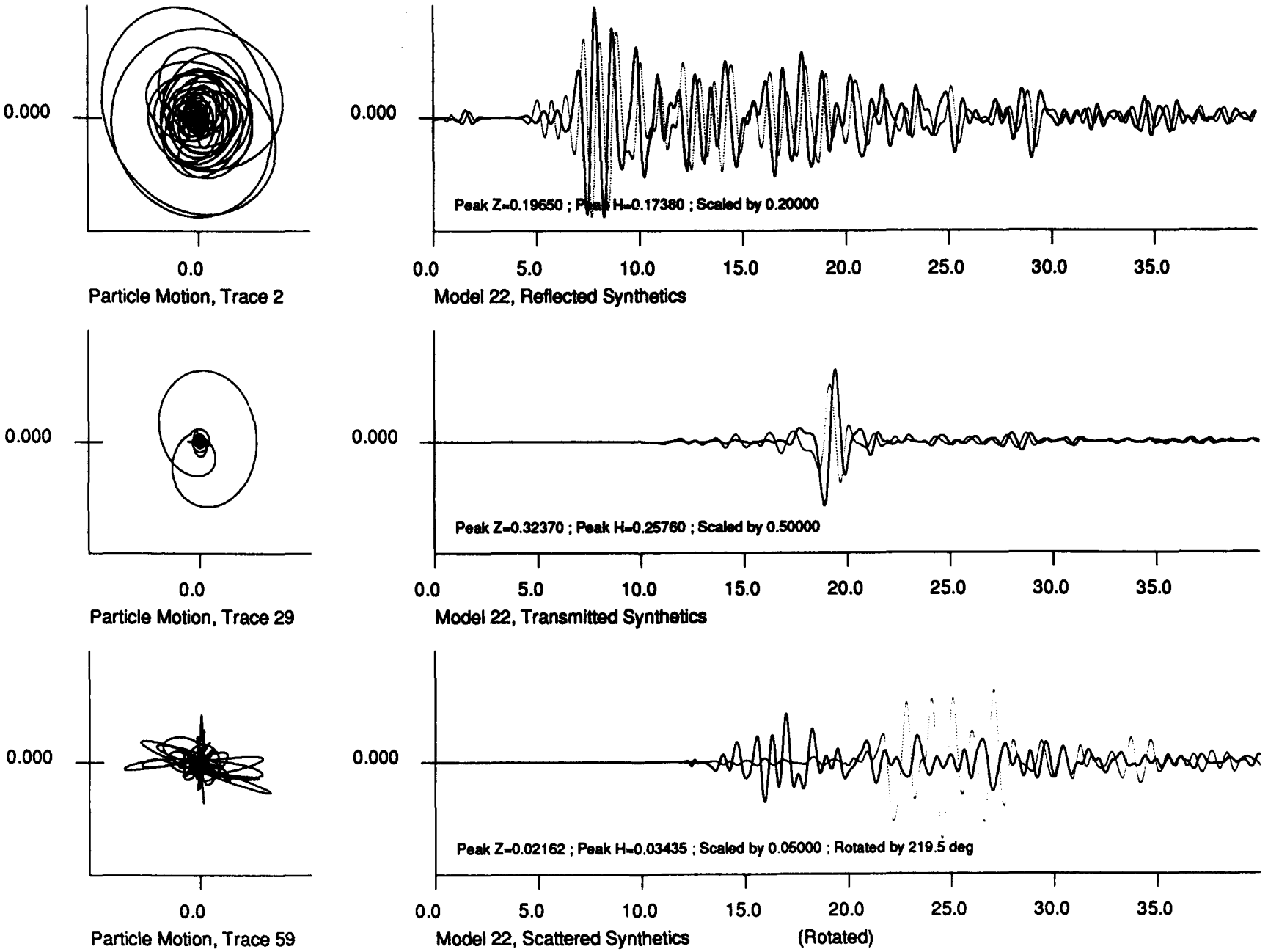

0.000
0.0
Particle Motion, Trace 2
0.000
Peak Z=0.19650 ; Peak H=0.17380 ; Scaled by 0.20000
0.0
5.0
10.0
15.0
20.0
25.0
30.0
35.0
Model 22, Reflected Synthetics
0.000
0.0
Particle Motion, Trace 29
0.000
Peak Z=0.32370 ; Peak H=0.25760 ; Scaled by 0.50000
0.0
5.0
10.0
15.0
20.0
25.0
30.0
35.0
Model 22, Transmitted Synthetics
0.000
0.0
Particle Motion, Trace 59
0.000
Peak Z=0.02162 ; Peak H=0.03435 ; Scaled by 0.05000 ; Rotated by 219.5 deg
0.0
5.0
10.0
15.0
20.0
25.0
30.0
35.0
Model 22, Scattered Synthetics
(Rotated)

**Figure 75**

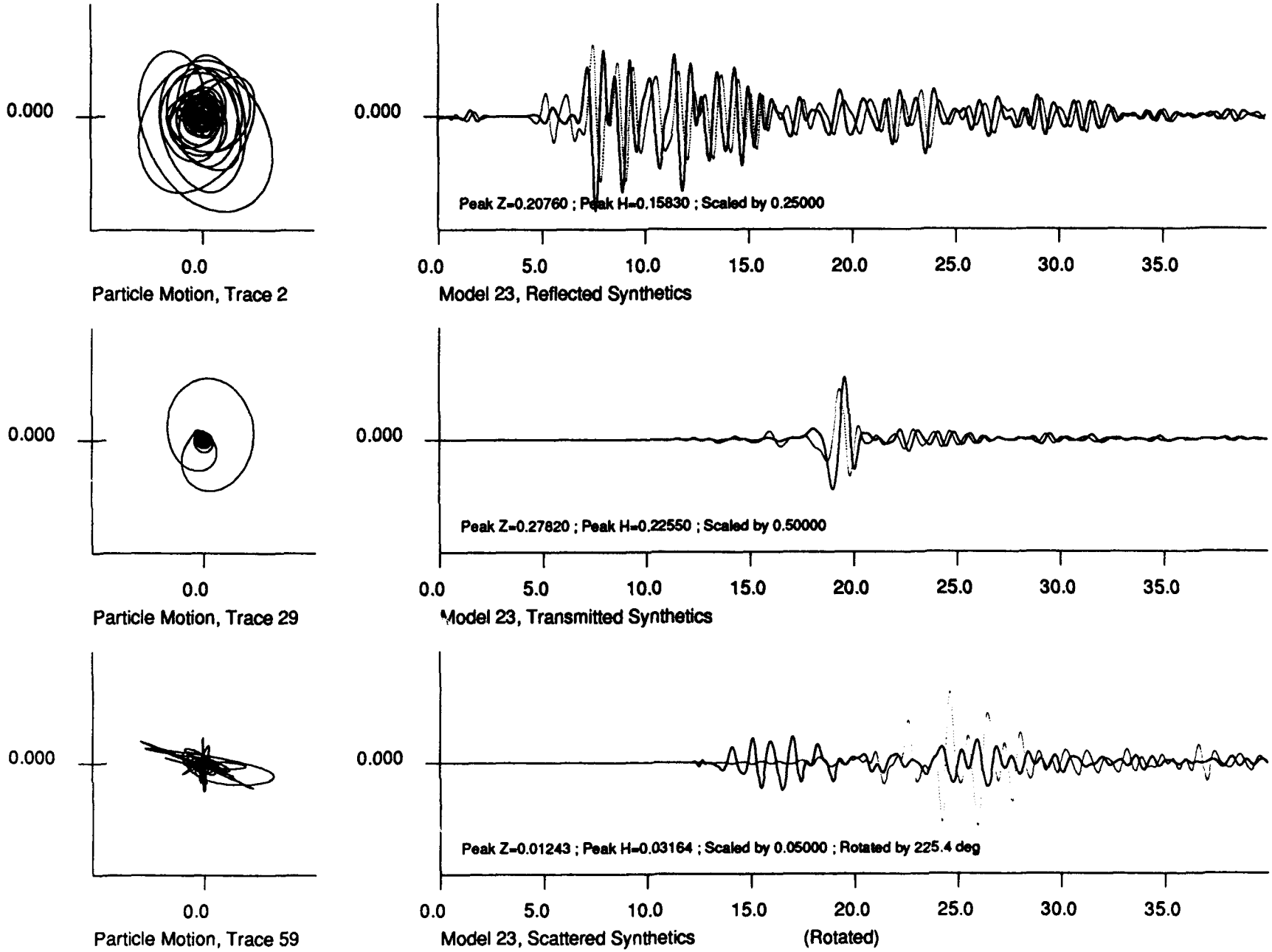

0.000
0.0
Particle Motion, Trace 2
0.000
Peak Z=0.20760 ; Peak H=0.15830 ; Scaled by 0.25000
0.0 5.0 10.0 15.0 20.0 25.0 30.0 35.0
Model 23, Reflected Synthetics
0.000
0.0
Particle Motion, Trace 29
0.000
Peak Z=0.27820 ; Peak H=0.22550 ; Scaled by 0.50000
0.0 5.0 10.0 15.0 20.0 25.0 30.0 35.0
Model 23, Transmitted Synthetics
0.000
0.0
Particle Motion, Trace 59
0.000
Peak Z=0.01243 ; Peak H=0.03164 ; Scaled by 0.05000 ; Rotated by 225.4 deg
0.0 5.0 10.0 15.0 20.0 25.0 30.0 35.0
Model 23, Scattered Synthetics (Rotated)

**Figure 76**

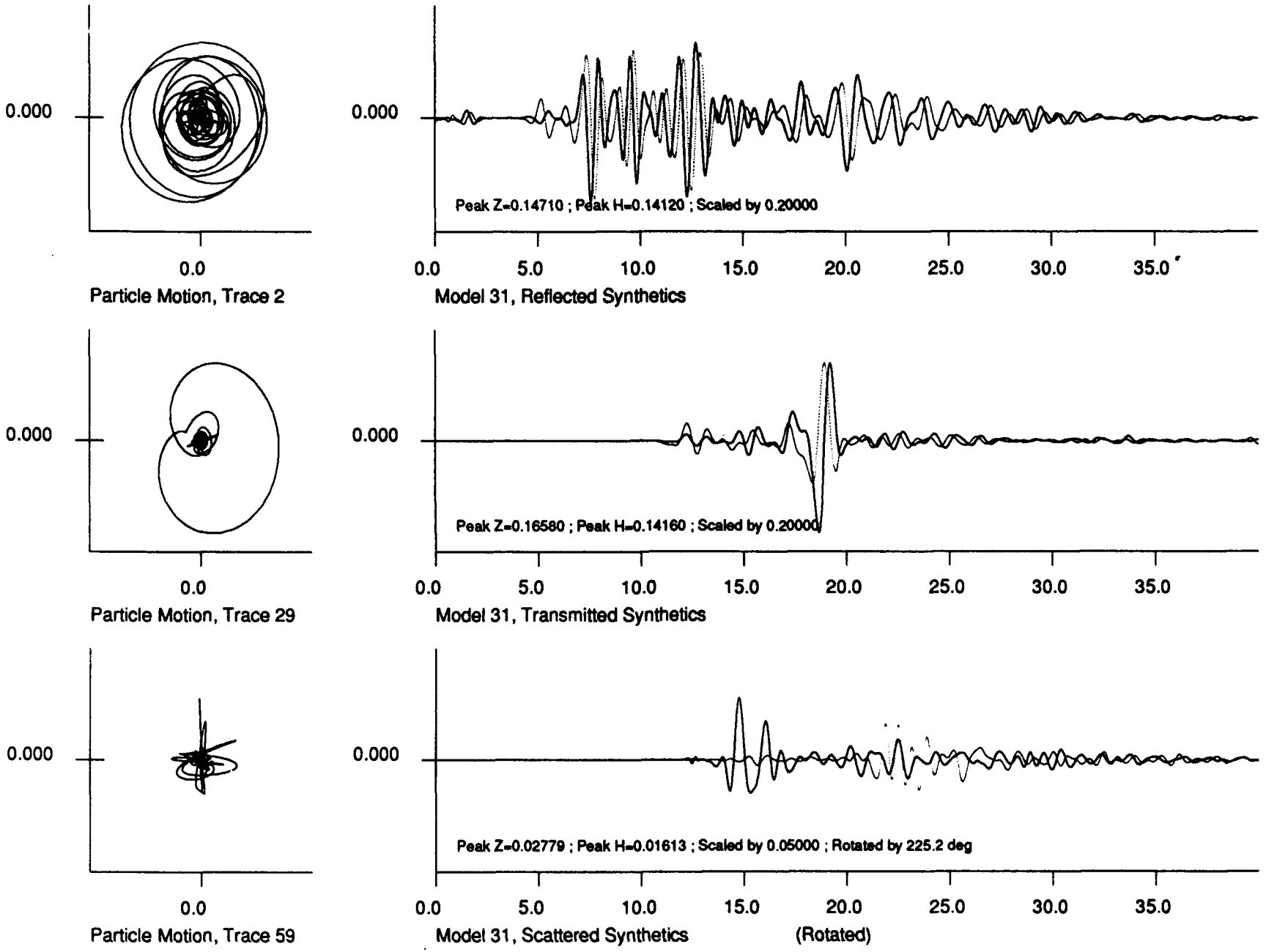

0.000
0.0
Particle Motion, Trace 2
0.000
Peak Z=0.14710 ; Peak H=0.14120 ; Scaled by 0.20000
0.0 5.0 10.0 15.0 20.0 25.0 30.0 35.0
Model 31, Reflected Synthetics
0.000
0.0
Particle Motion, Trace 29
0.000
Peak Z=0.16580 ; Peak H=0.14160 ; Scaled by 0.20000
0.0 5.0 10.0 15.0 20.0 25.0 30.0 35.0
Model 31, Transmitted Synthetics
0.000
0.0
Particle Motion, Trace 59
0.000
Peak Z=0.02779 ; Peak H=0.01613 ; Scaled by 0.05000 ; Rotated by 225.2 deg
0.0 5.0 10.0 15.0 20.0 25.0 30.0 35.0
Model 31, Scattered Synthetics (Rotated)

**Figure 77**

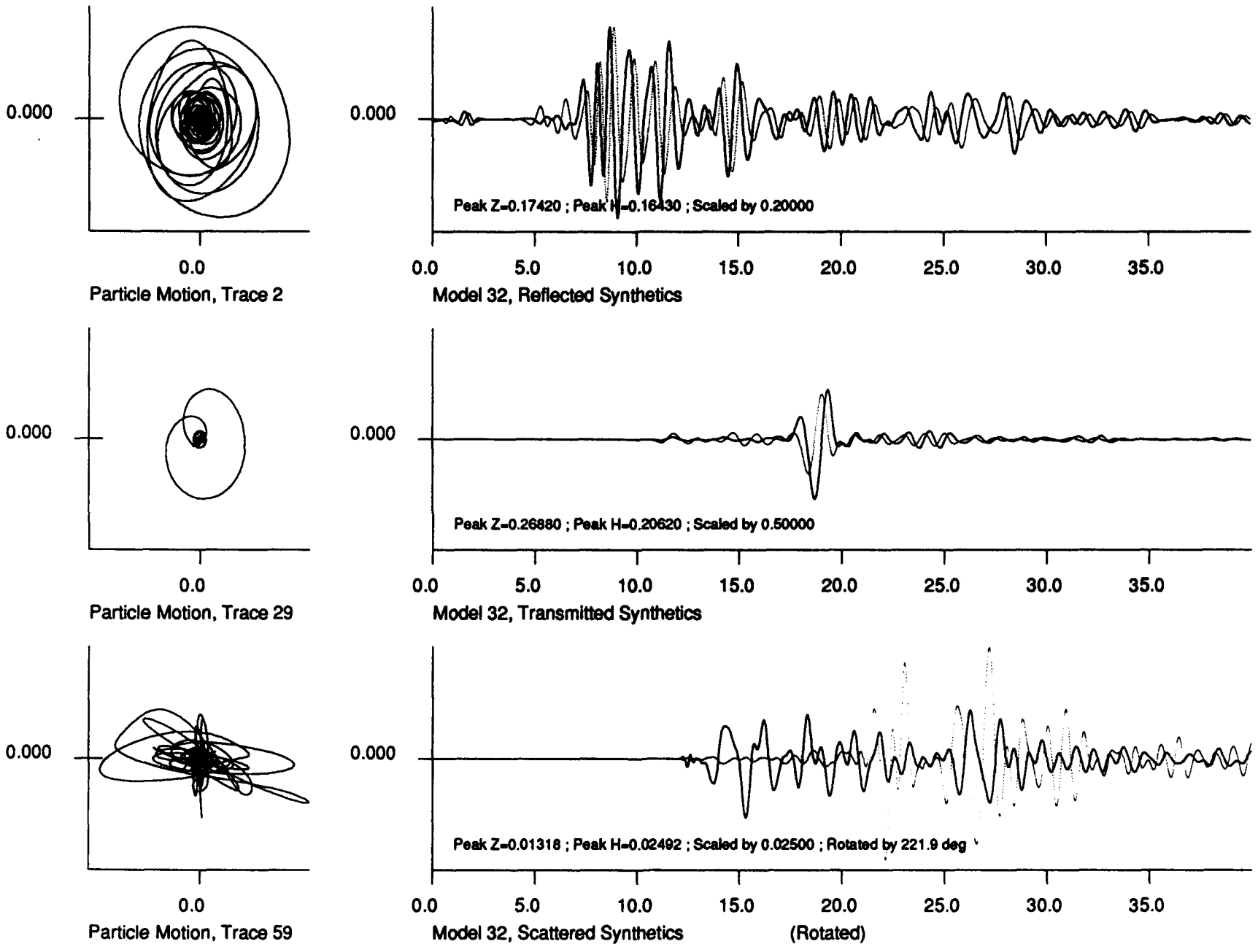

0.000
0.0
Particle Motion, Trace 2
0.000
Peak Z=0.17420 ; Peak H=0.16430 ; Scaled by 0.20000
0.0 5.0 10.0 15.0 20.0 25.0 30.0 35.0
Model 32, Reflected Synthetics
0.000
0.0
Particle Motion, Trace 29
0.000
Peak Z=0.26880 ; Peak H=0.20620 ; Scaled by 0.50000
0.0 5.0 10.0 15.0 20.0 25.0 30.0 35.0
Model 32, Transmitted Synthetics
0.000
0.0
Particle Motion, Trace 59
0.000
Peak Z=0.01318 ; Peak H=0.02492 ; Scaled by 0.02500 ; Rotated by 221.9 deg
0.0 5.0 10.0 15.0 20.0 25.0 30.0 35.0
Model 32, Scattered Synthetics (Rotated)

Figure 78

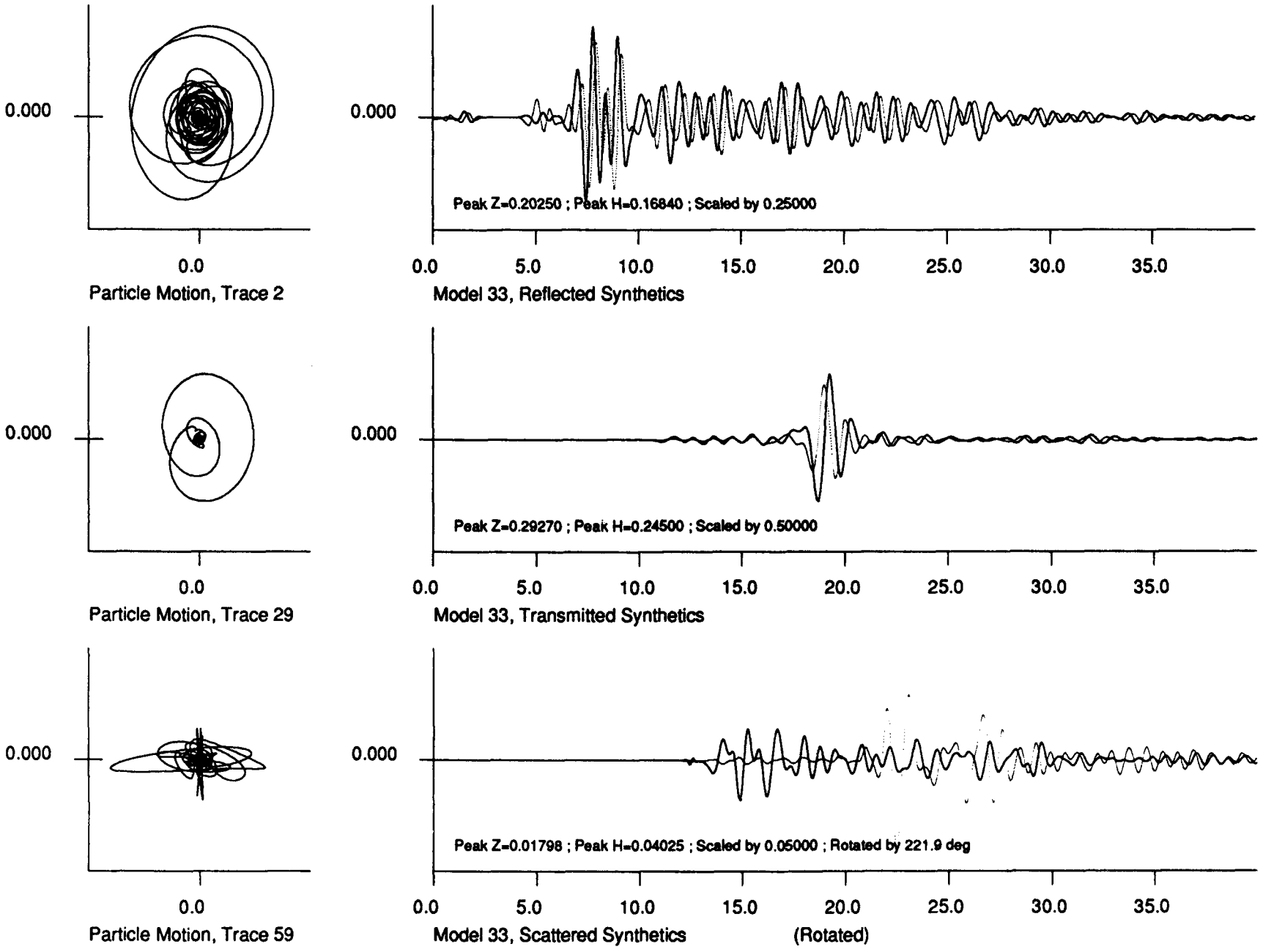

0.000
0.0
Particle Motion, Trace 2
0.000
Peak Z=0.20250 ; Peak H=0.16840 ; Scaled by 0.25000
0.0 5.0 10.0 15.0 20.0 25.0 30.0 35.0
Model 33, Reflected Synthetics
0.000
0.0
Particle Motion, Trace 29
0.000
Peak Z=0.29270 ; Peak H=0.24500 ; Scaled by 0.50000
0.0 5.0 10.0 15.0 20.0 25.0 30.0 35.0
Model 33, Transmitted Synthetics
0.000
0.0
Particle Motion, Trace 59
0.000
Peak Z=0.01798 ; Peak H=0.04025 ; Scaled by 0.05000 ; Rotated by 221.9 deg
0.0 5.0 10.0 15.0 20.0 25.0 30.0 35.0
Model 33, Scattered Synthetics (Rotated)

Figure 79

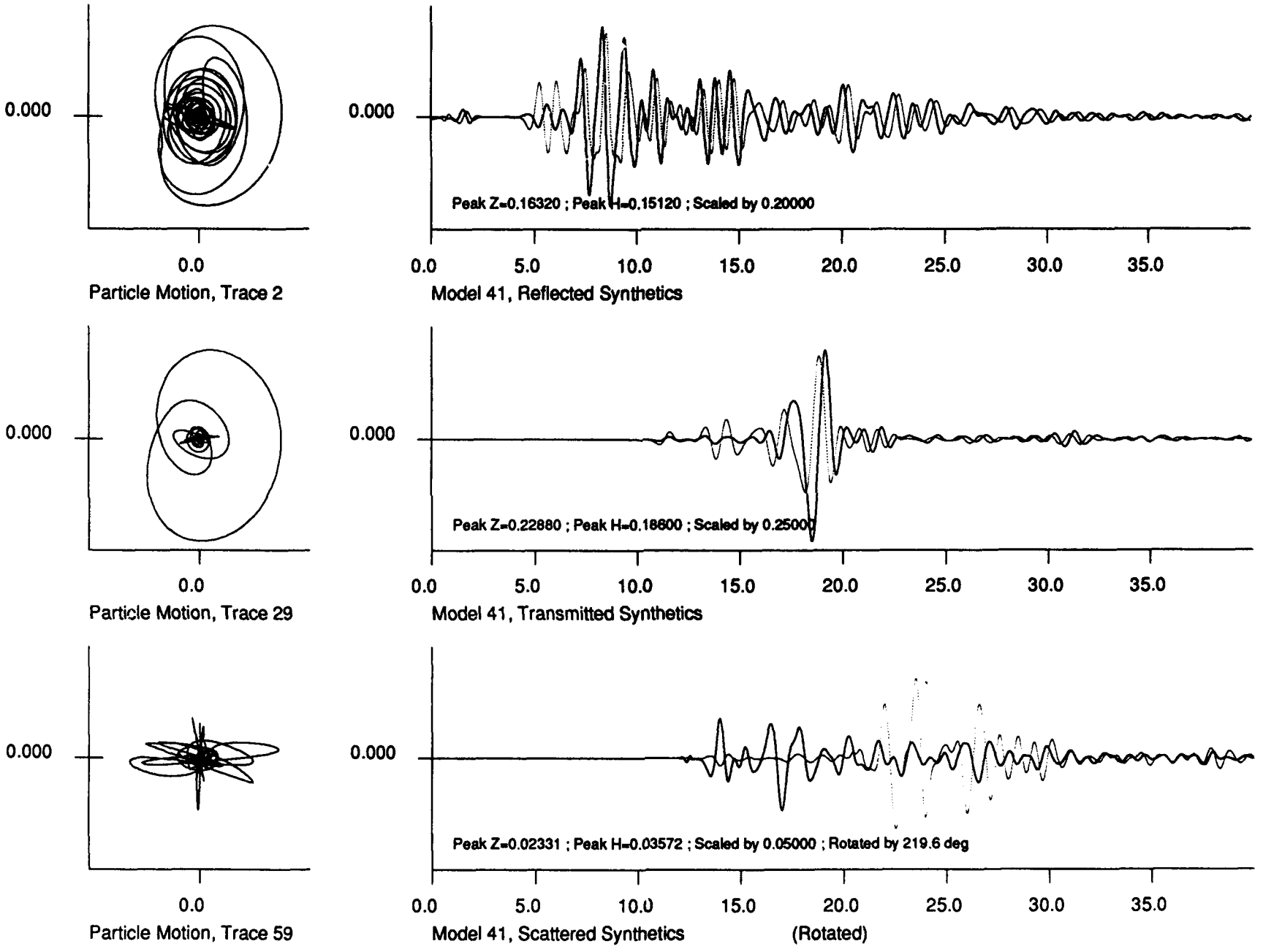

0.000
0.0
Particle Motion, Trace 2
0.000
Peak Z=0.16320 ; Peak H=0.15120 ; Scaled by 0.20000
0.0 5.0 10.0 15.0 20.0 25.0 30.0 35.0
Model 41, Reflected Synthetics
0.000
0.0
Particle Motion, Trace 29
0.000
Peak Z=0.22880 ; Peak H=0.18600 ; Scaled by 0.25000
0.0 5.0 10.0 15.0 20.0 25.0 30.0 35.0
Model 41, Transmitted Synthetics
0.000
0.0
Particle Motion, Trace 59
0.000
Peak Z=0.02331 ; Peak H=0.03572 ; Scaled by 0.05000 ; Rotated by 219.6 deg
0.0 5.0 10.0 15.0 20.0 25.0 30.0 35.0
Model 41, Scattered Synthetics (Rotated)

**Figure 80**

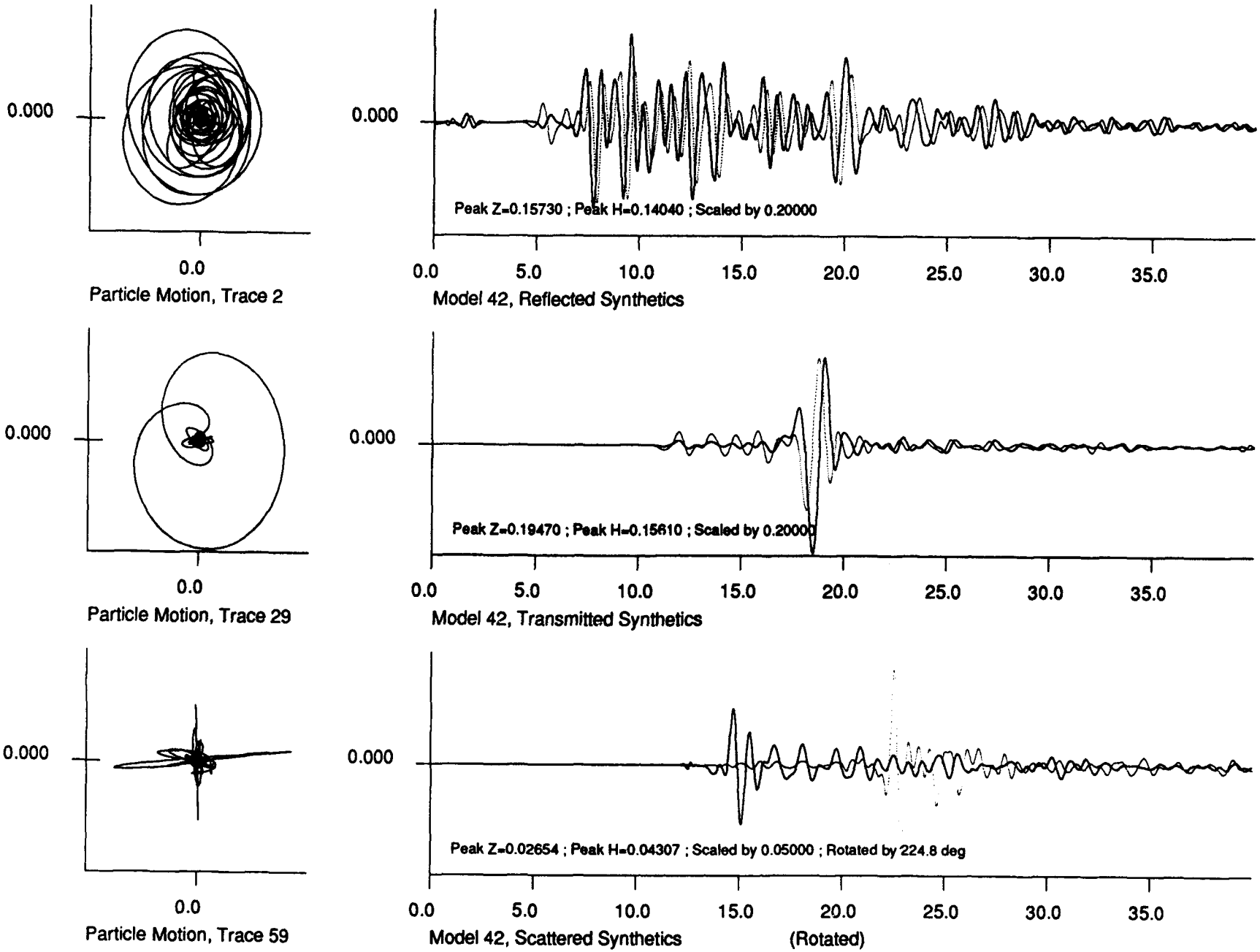

0.000
0.0
Particle Motion, Trace 2
0.000
Peak Z=0.15730 ; Peak H=0.14040 ; Scaled by 0.20000
0.0
5.0
10.0
15.0
20.0
25.0
30.0
35.0
Model 42, Reflected Synthetics
0.000
0.0
Particle Motion, Trace 29
0.000
Peak Z=0.19470 ; Peak H=0.15610 ; Scaled by 0.20000
0.0
5.0
10.0
15.0
20.0
25.0
30.0
35.0
Model 42, Transmitted Synthetics
0.000
0.0
Particle Motion, Trace 59
0.000
Peak Z=0.02654 ; Peak H=0.04307 ; Scaled by 0.05000 ; Rotated by 224.8 deg
0.0
5.0
10.0
15.0
20.0
25.0
30.0
35.0
Model 42, Scattered Synthetics
(Rotated)

**Figure 81**

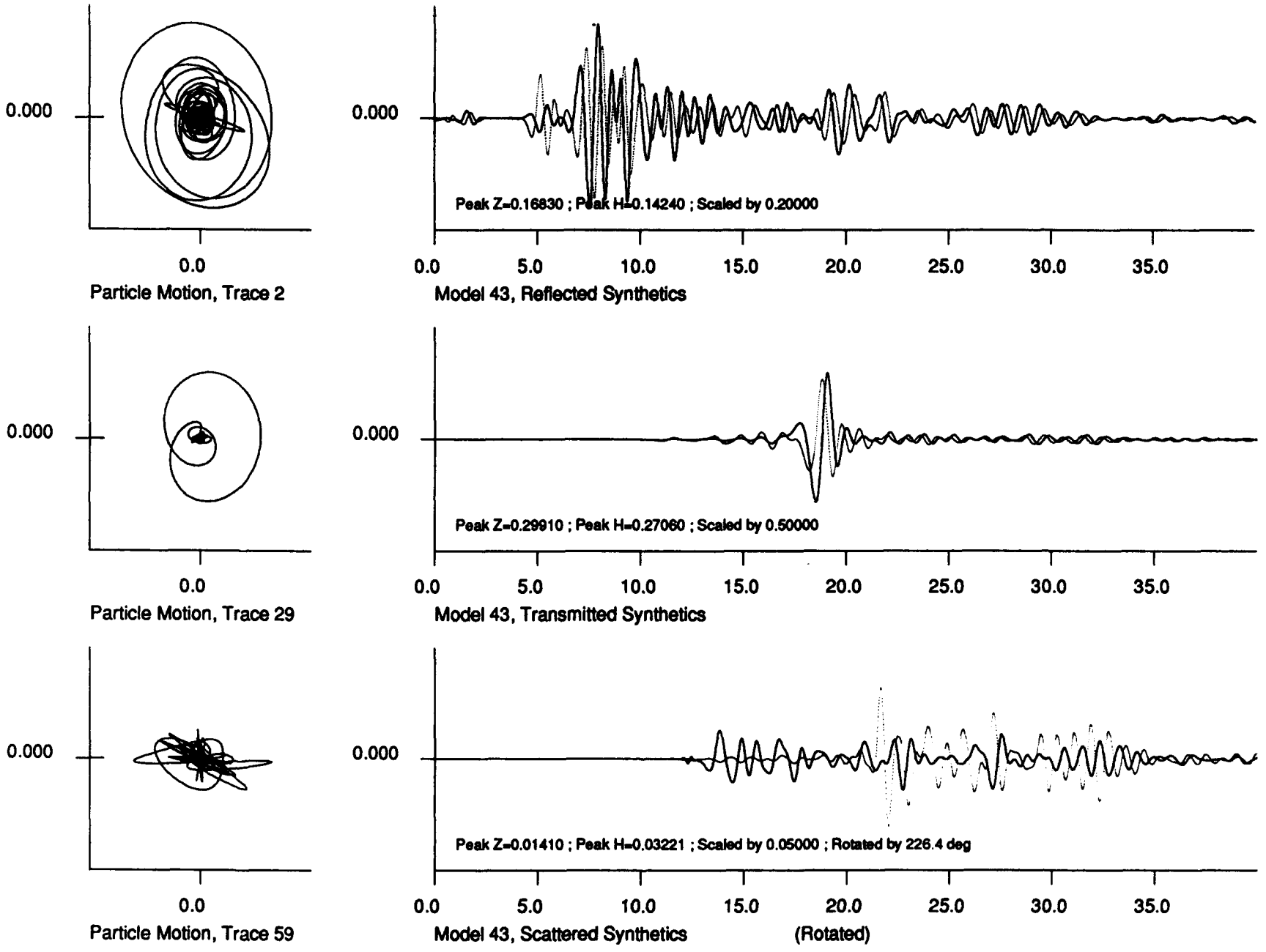

0.000
0.0
Particle Motion, Trace 2
0.000
Peak Z=0.16830 ; Peak H=0.14240 ; Scaled by 0.20000
0.0 5.0 10.0 15.0 20.0 25.0 30.0 35.0
Model 43, Reflected Synthetics
0.000
0.0
Particle Motion, Trace 29
0.000
Peak Z=0.29910 ; Peak H=0.27060 ; Scaled by 0.50000
0.0 5.0 10.0 15.0 20.0 25.0 30.0 35.0
Model 43, Transmitted Synthetics
0.000
0.0
Particle Motion, Trace 59
0.000
Peak Z=0.01410 ; Peak H=0.03221 ; Scaled by 0.05000 ; Rotated by 226.4 deg
0.0 5.0 10.0 15.0 20.0 25.0 30.0 35.0
Model 43, Scattered Synthetics (Rotated)

**Figure 82**

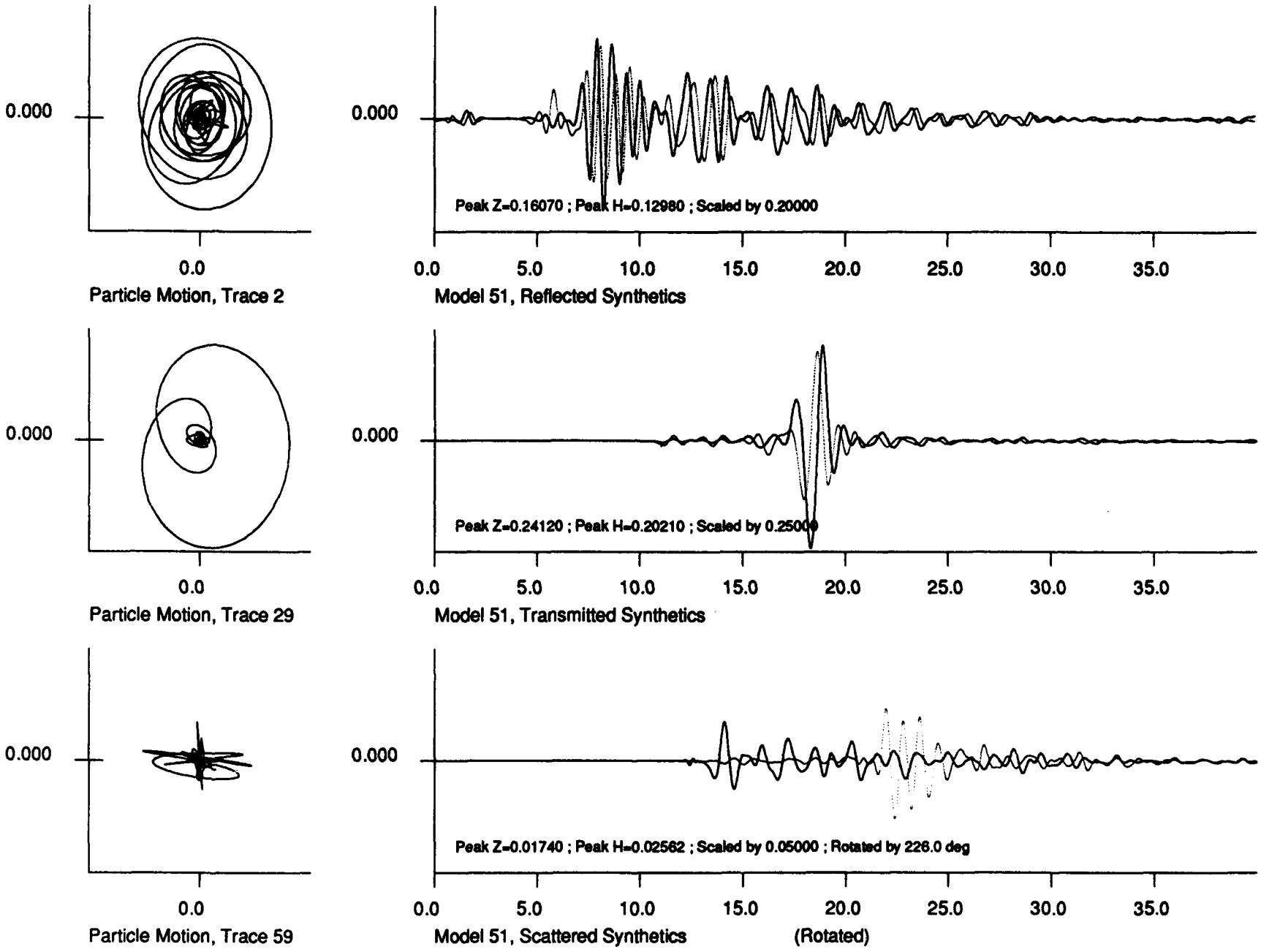

0.000
0.0
Particle Motion, Trace 2
0.000
Peak Z=0.16070 ; Peak H=0.12980 ; Scaled by 0.20000
0.0 5.0 10.0 15.0 20.0 25.0 30.0 35.0
Model 51, Reflected Synthetics
0.000
0.0
Particle Motion, Trace 29
0.000
Peak Z=0.24120 ; Peak H=0.20210 ; Scaled by 0.25000
0.0 5.0 10.0 15.0 20.0 25.0 30.0 35.0
Model 51, Transmitted Synthetics
0.000
0.0
Particle Motion, Trace 59
0.000
Peak Z=0.01740 ; Peak H=0.02562 ; Scaled by 0.05000 ; Rotated by 226.0 deg
0.0 5.0 10.0 15.0 20.0 25.0 30.0 35.0
Model 51, Scattered Synthetics (Rotated)

Figure 83

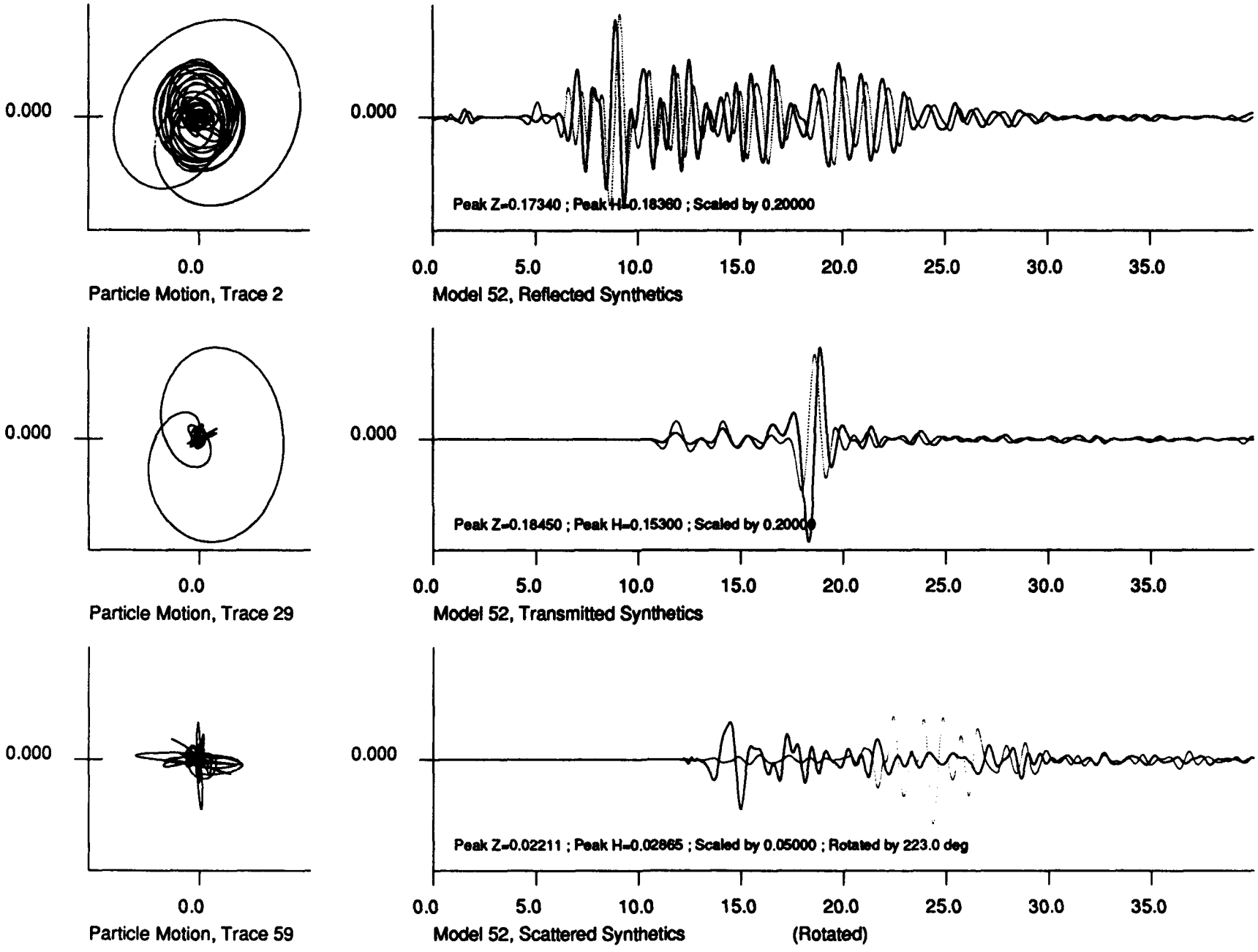

0.000
0.0
Particle Motion, Trace 2
0.000
Peak Z=0.17340 ; Peak H=0.18380 ; Scaled by 0.20000
0.0
5.0
10.0
15.0
20.0
25.0
30.0
35.0
Model 52, Reflected Synthetics
0.000
0.0
Particle Motion, Trace 29
0.000
Peak Z=0.18450 ; Peak H=0.15300 ; Scaled by 0.20000
0.0
5.0
10.0
15.0
20.0
25.0
30.0
35.0
Model 52, Transmitted Synthetics
0.000
0.0
Particle Motion, Trace 59
0.000
Peak Z=0.02211 ; Peak H=0.02865 ; Scaled by 0.05000 ; Rotated by 223.0 deg
0.0
5.0
10.0
15.0
20.0
25.0
30.0
35.0
Model 52, Scattered Synthetics
(Rotated)

**Figure 84**

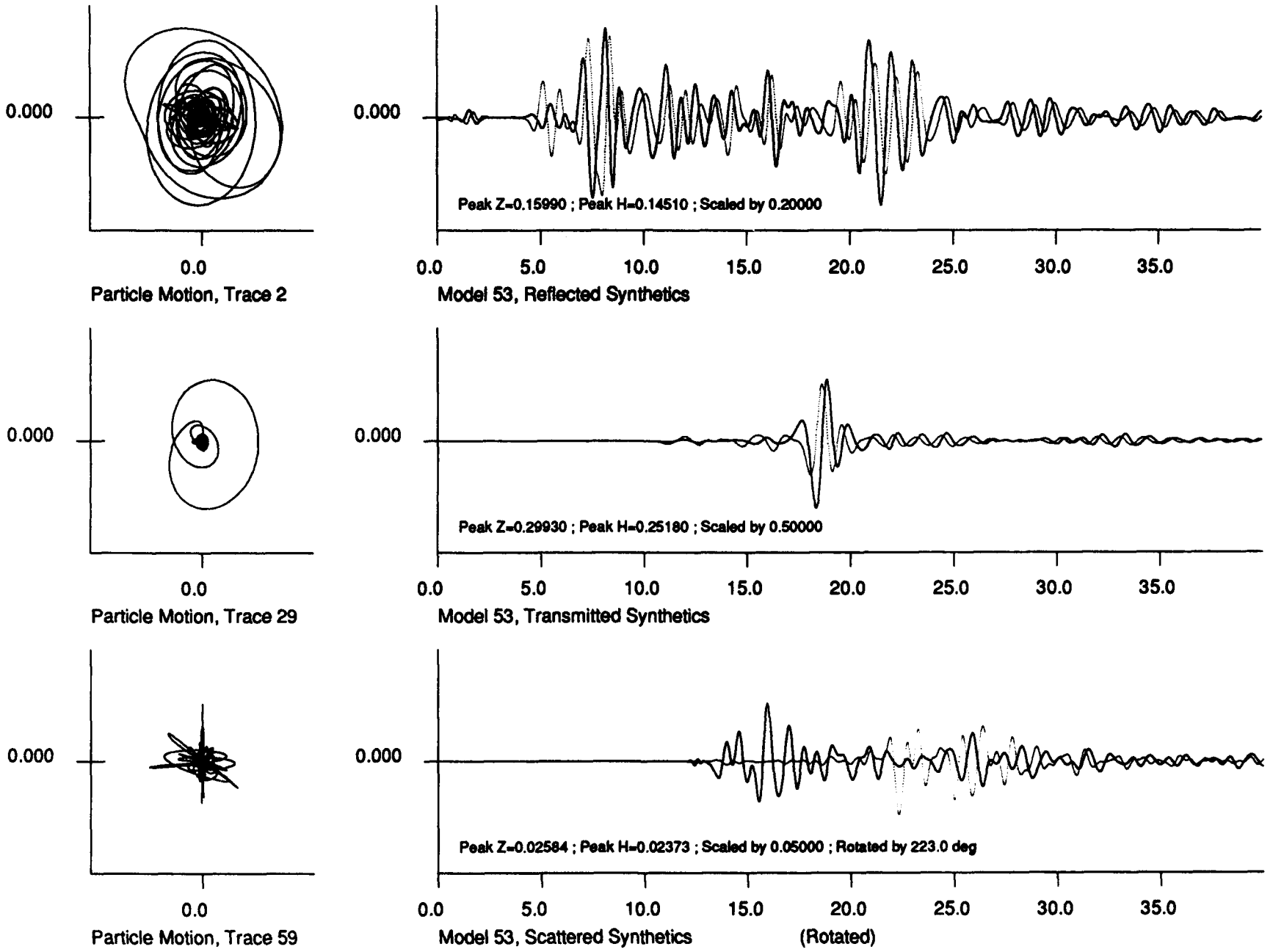

0.000
0.0
Particle Motion, Trace 2
0.000
Peak Z=0.15990 ; Peak H=0.14510 ; Scaled by 0.20000
0.0
5.0
10.0
15.0
20.0
25.0
30.0
35.0
Model 53, Reflected Synthetics
0.000
0.0
Particle Motion, Trace 29
0.000
Peak Z=0.29930 ; Peak H=0.25180 ; Scaled by 0.50000
0.0
5.0
10.0
15.0
20.0
25.0
30.0
35.0
Model 53, Transmitted Synthetics
0.000
0.0
Particle Motion, Trace 59
0.000
Peak Z=0.02584 ; Peak H=0.02373 ; Scaled by 0.05000 ; Rotated by 223.0 deg
0.0
5.0
10.0
15.0
20.0
25.0
30.0
35.0
Model 53, Scattered Synthetics
(Rotated)

**Figure 85**

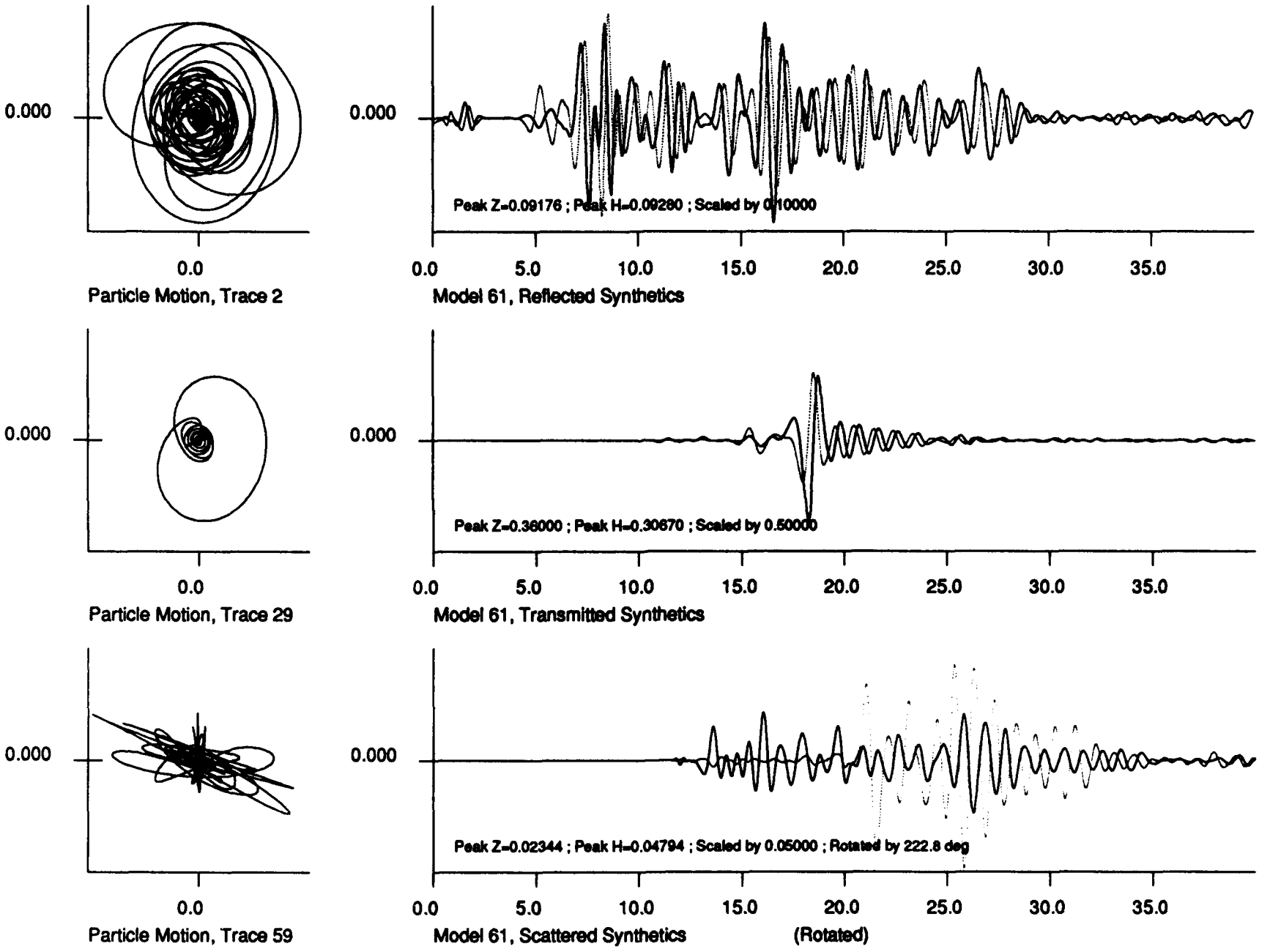

0.000
0.0
Particle Motion, Trace 2
0.000
Peak Z=0.09176 ; Peak H=0.09280 ; Scaled by 0.10000
0.0 5.0 10.0 15.0 20.0 25.0 30.0 35.0
Model 61, Reflected Synthetics
0.000
0.0
Particle Motion, Trace 29
0.000
Peak Z=0.36000 ; Peak H=0.30670 ; Scaled by 0.50000
0.0 5.0 10.0 15.0 20.0 25.0 30.0 35.0
Model 61, Transmitted Synthetics
0.000
0.0
Particle Motion, Trace 59
0.000
Peak Z=0.02344 ; Peak H=0.04794 ; Scaled by 0.05000 ; Rotated by 222.8 deg
0.0 5.0 10.0 15.0 20.0 25.0 30.0 35.0
Model 61, Scattered Synthetics (Rotated)

**Figure 86**

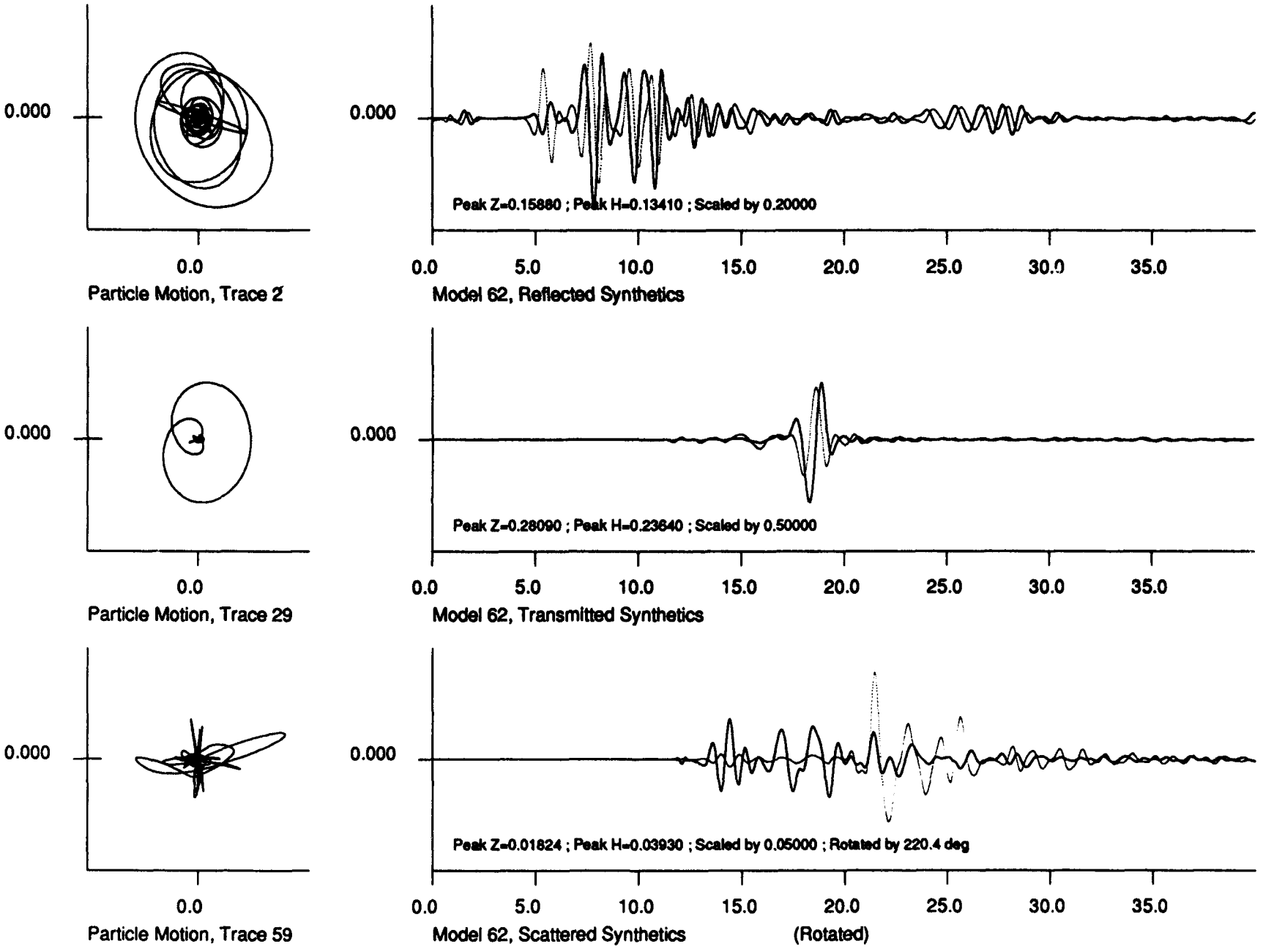

0.000
0.0
Particle Motion, Trace 2
0.000
Peak Z=0.15880 ; Peak H=0.13410 ; Scaled by 0.20000
0.0 5.0 10.0 15.0 20.0 25.0 30.0 35.0
Model 62, Reflected Synthetics
0.000
0.0
Particle Motion, Trace 29
0.000
Peak Z=0.28090 ; Peak H=0.23640 ; Scaled by 0.50000
0.0 5.0 10.0 15.0 20.0 25.0 30.0 35.0
Model 62, Transmitted Synthetics
0.000
0.0
Particle Motion, Trace 59
0.000
Peak Z=0.01824 ; Peak H=0.03930 ; Scaled by 0.05000 ; Rotated by 220.4 deg
0.0 5.0 10.0 15.0 20.0 25.0 30.0 35.0
Model 62, Scattered Synthetics (Rotated)

**Figure 87**

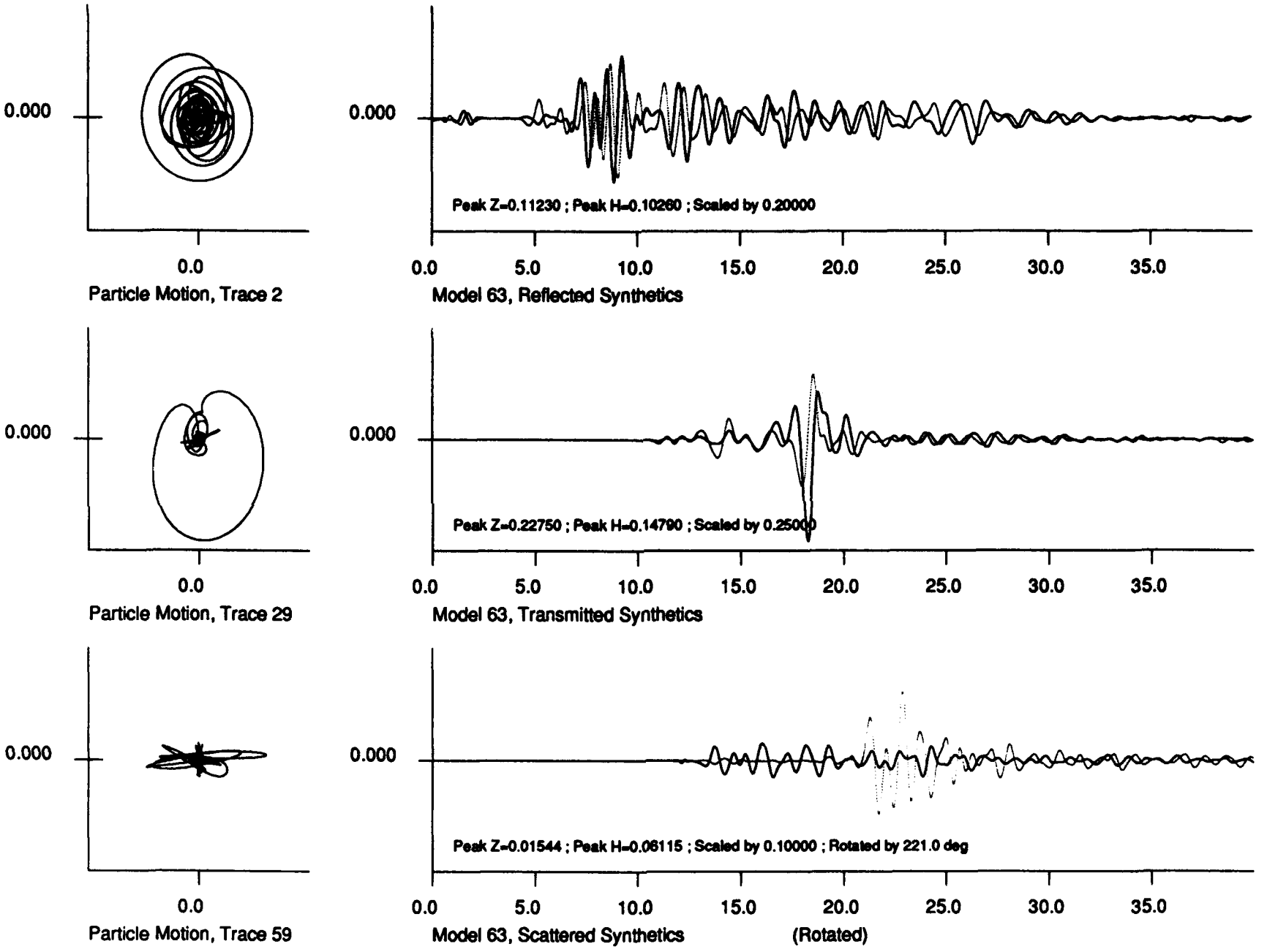

0.000
0.0
Particle Motion, Trace 2
0.000
Peak Z=0.11230 ; Peak H=0.10260 ; Scaled by 0.20000
0.0 5.0 10.0 15.0 20.0 25.0 30.0 35.0
Model 63, Reflected Synthetics
0.000
0.0
Particle Motion, Trace 29
0.000
Peak Z=0.22750 ; Peak H=0.14790 ; Scaled by 0.25000
0.0 5.0 10.0 15.0 20.0 25.0 30.0 35.0
Model 63, Transmitted Synthetics
0.000
0.0
Particle Motion, Trace 59
0.000
Peak Z=0.01544 ; Peak H=0.06115 ; Scaled by 0.10000 ; Rotated by 221.0 deg
0.0 5.0 10.0 15.0 20.0 25.0 30.0 35.0
Model 63, Scattered Synthetics (Rotated)

**Figure 88**

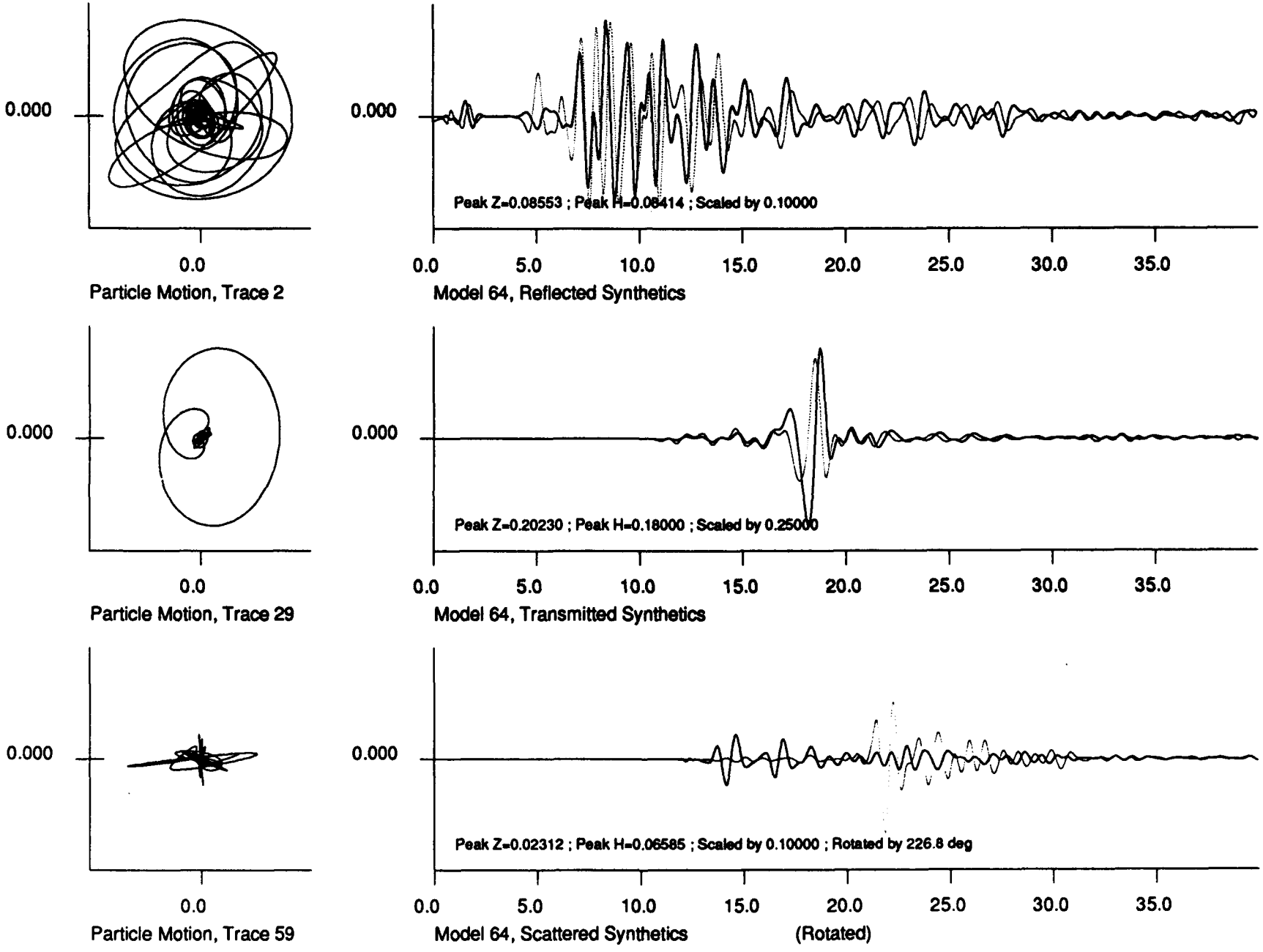

0.000
0.0
Particle Motion, Trace 2
0.000
Peak Z=0.08553 ; Peak H=0.08414 ; Scaled by 0.10000
0.0 5.0 10.0 15.0 20.0 25.0 30.0 35.0
Model 64, Reflected Synthetics
0.000
0.0
Particle Motion, Trace 29
0.000
Peak Z=0.20230 ; Peak H=0.18000 ; Scaled by 0.25000
0.0 5.0 10.0 15.0 20.0 25.0 30.0 35.0
Model 64, Transmitted Synthetics
0.000
0.0
Particle Motion, Trace 59
0.000
Peak Z=0.02312 ; Peak H=0.06585 ; Scaled by 0.10000 ; Rotated by 226.8 deg
0.0 5.0 10.0 15.0 20.0 25.0 30.0 35.0
Model 64, Scattered Synthetics (Rotated)

**Figure 89**

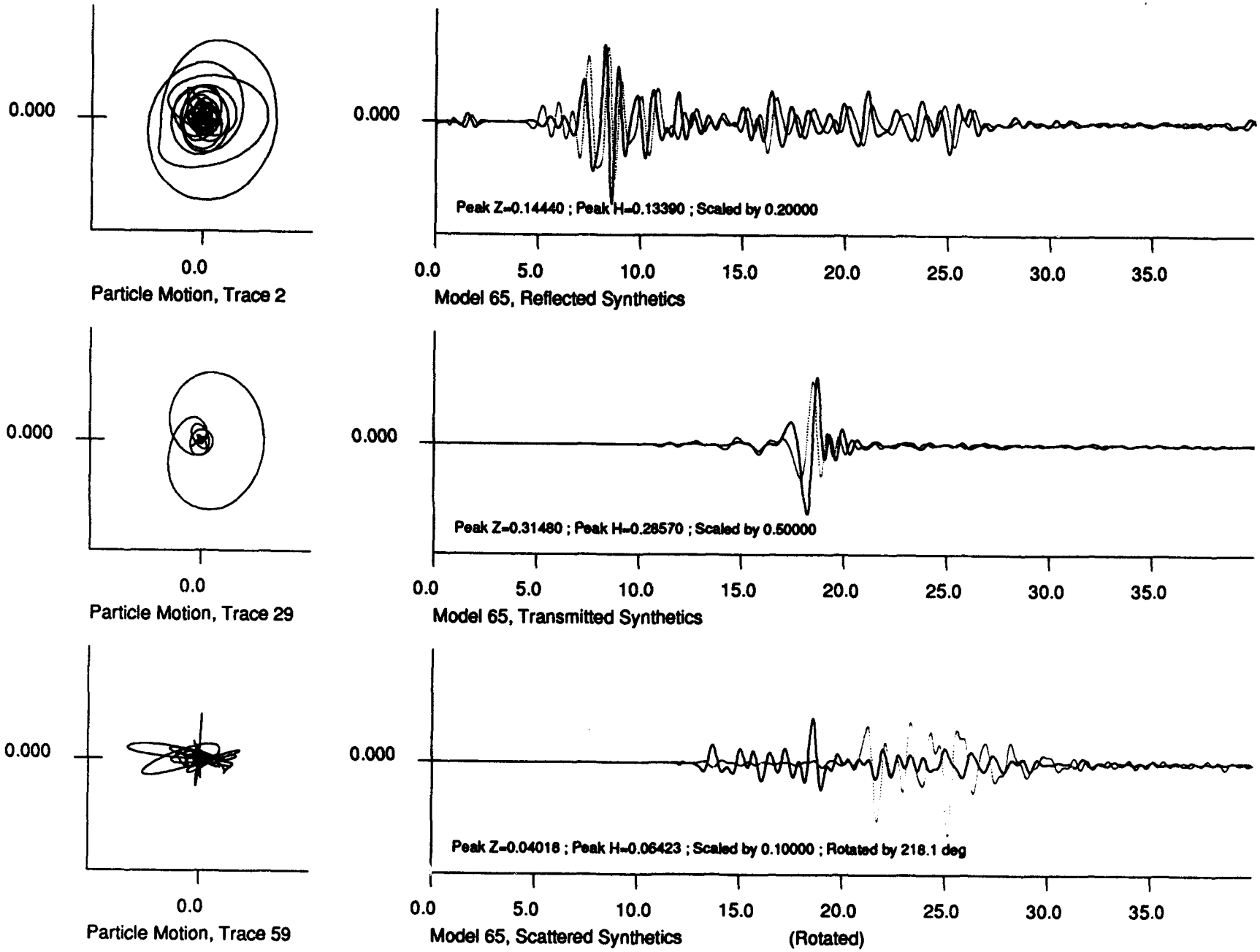

0.000
0.0
Particle Motion, Trace 2
0.000
Peak Z=0.14440 ; Peak H=0.13390 ; Scaled by 0.20000
0.0
5.0
10.0
15.0
20.0
25.0
30.0
35.0
Model 65, Reflected Synthetics
0.000
0.0
Particle Motion, Trace 29
0.000
Peak Z=0.31480 ; Peak H=0.28570 ; Scaled by 0.50000
0.0
5.0
10.0
15.0
20.0
25.0
30.0
35.0
Model 65, Transmitted Synthetics
0.000
0.0
Particle Motion, Trace 59
0.000
Peak Z=0.04018 ; Peak H=0.06423 ; Scaled by 0.10000 ; Rotated by 218.1 deg
0.0
5.0
10.0
15.0
20.0
25.0
30.0
35.0
Model 65, Scattered Synthetics
(Rotated)

**Figure 90**

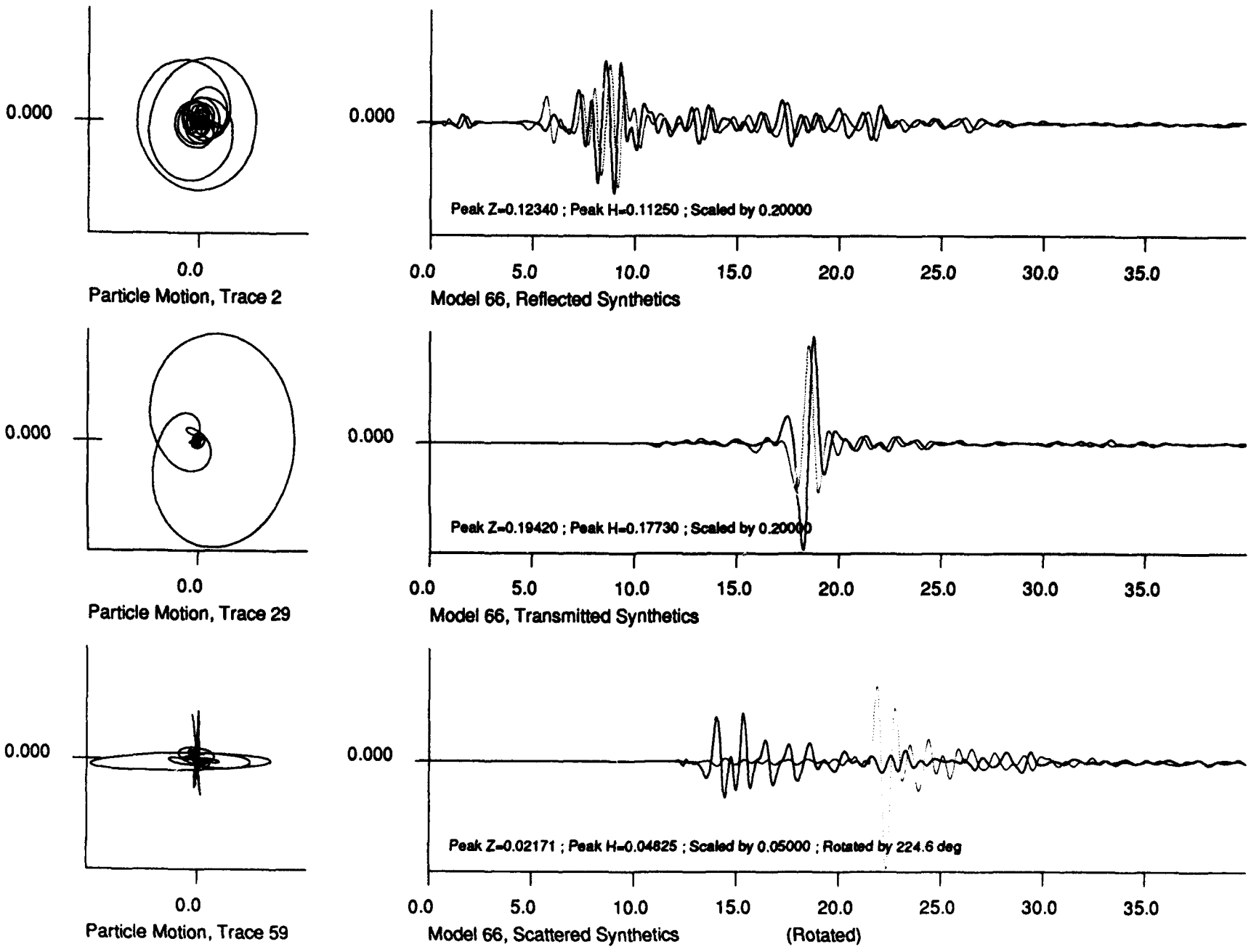

0.000
0.0
Particle Motion, Trace 2
0.000
Peak Z=0.12340 ; Peak H=0.11250 ; Scaled by 0.20000
0.0
5.0
10.0
15.0
20.0
25.0
30.0
35.0
Model 66, Reflected Synthetics
0.000
0.0
Particle Motion, Trace 29
0.000
Peak Z=0.19420 ; Peak H=0.17730 ; Scaled by 0.20000
0.0
5.0
10.0
15.0
20.0
25.0
30.0
35.0
Model 66, Transmitted Synthetics
0.000
0.0
Particle Motion, Trace 59
0.000
Peak Z=0.02171 ; Peak H=0.04825 ; Scaled by 0.05000 ; Rotated by 224.6 deg
0.0
5.0
10.0
15.0
20.0
25.0
30.0
35.0
Model 66, Scattered Synthetics
(Rotated)

**Figure 91**

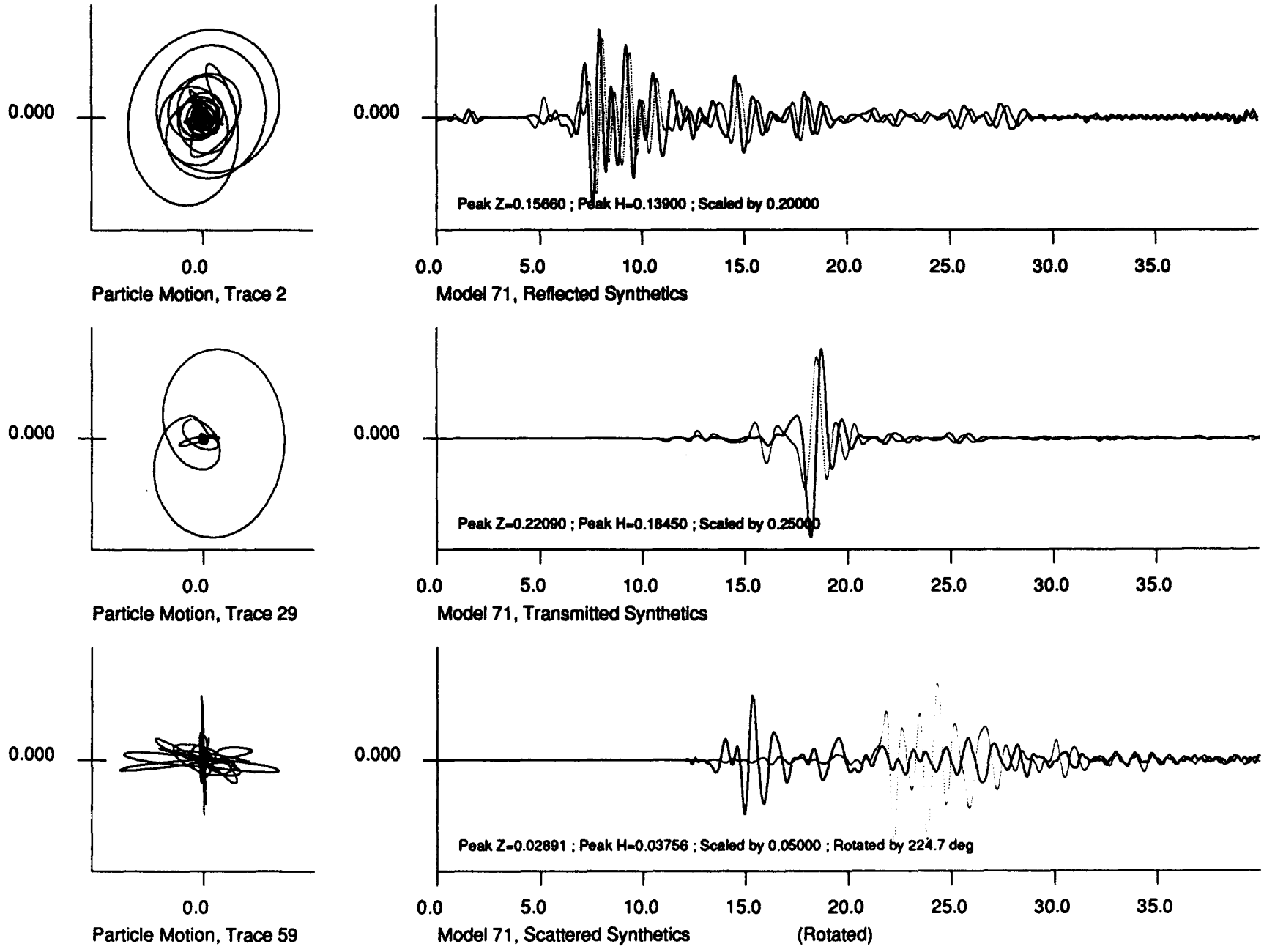

0.000
0.0
Particle Motion, Trace 2
0.000
Peak Z=0.15660 ; Peak H=0.13900 ; Scaled by 0.20000
0.0 5.0 10.0 15.0 20.0 25.0 30.0 35.0
Model 71, Reflected Synthetics
0.000
0.0
Particle Motion, Trace 29
0.000
Peak Z=0.22090 ; Peak H=0.18450 ; Scaled by 0.25000
0.0 5.0 10.0 15.0 20.0 25.0 30.0 35.0
Model 71, Transmitted Synthetics
0.000
0.0
Particle Motion, Trace 59
0.000
Peak Z=0.02891 ; Peak H=0.03756 ; Scaled by 0.05000 ; Rotated by 224.7 deg
0.0 5.0 10.0 15.0 20.0 25.0 30.0 35.0
Model 71, Scattered Synthetics (Rotated)

**Figure 92**

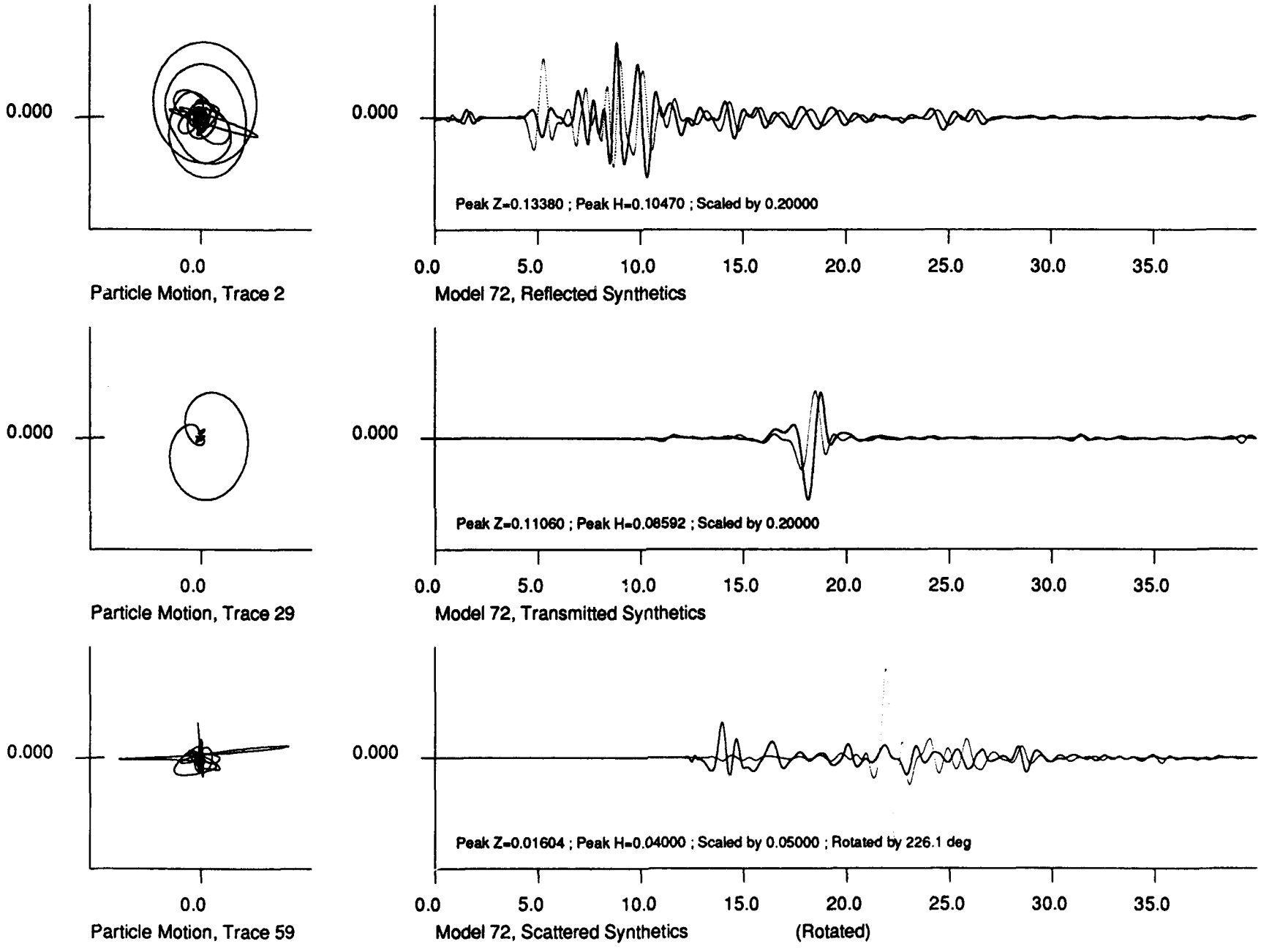

0.000
0.0
Particle Motion, Trace 2
0.000
Peak Z=0.13380 ; Peak H=0.10470 ; Scaled by 0.20000
0.0 5.0 10.0 15.0 20.0 25.0 30.0 35.0
Model 72, Reflected Synthetics
0.000
0.0
Particle Motion, Trace 29
0.000
Peak Z=0.11060 ; Peak H=0.08592 ; Scaled by 0.20000
0.0 5.0 10.0 15.0 20.0 25.0 30.0 35.0
Model 72, Transmitted Synthetics
0.000
0.0
Particle Motion, Trace 59
0.000
Peak Z=0.01604 ; Peak H=0.04000 ; Scaled by 0.05000 ; Rotated by 226.1 deg
0.0 5.0 10.0 15.0 20.0 25.0 30.0 35.0
Model 72, Scattered Synthetics (Rotated)

**Figure 93**

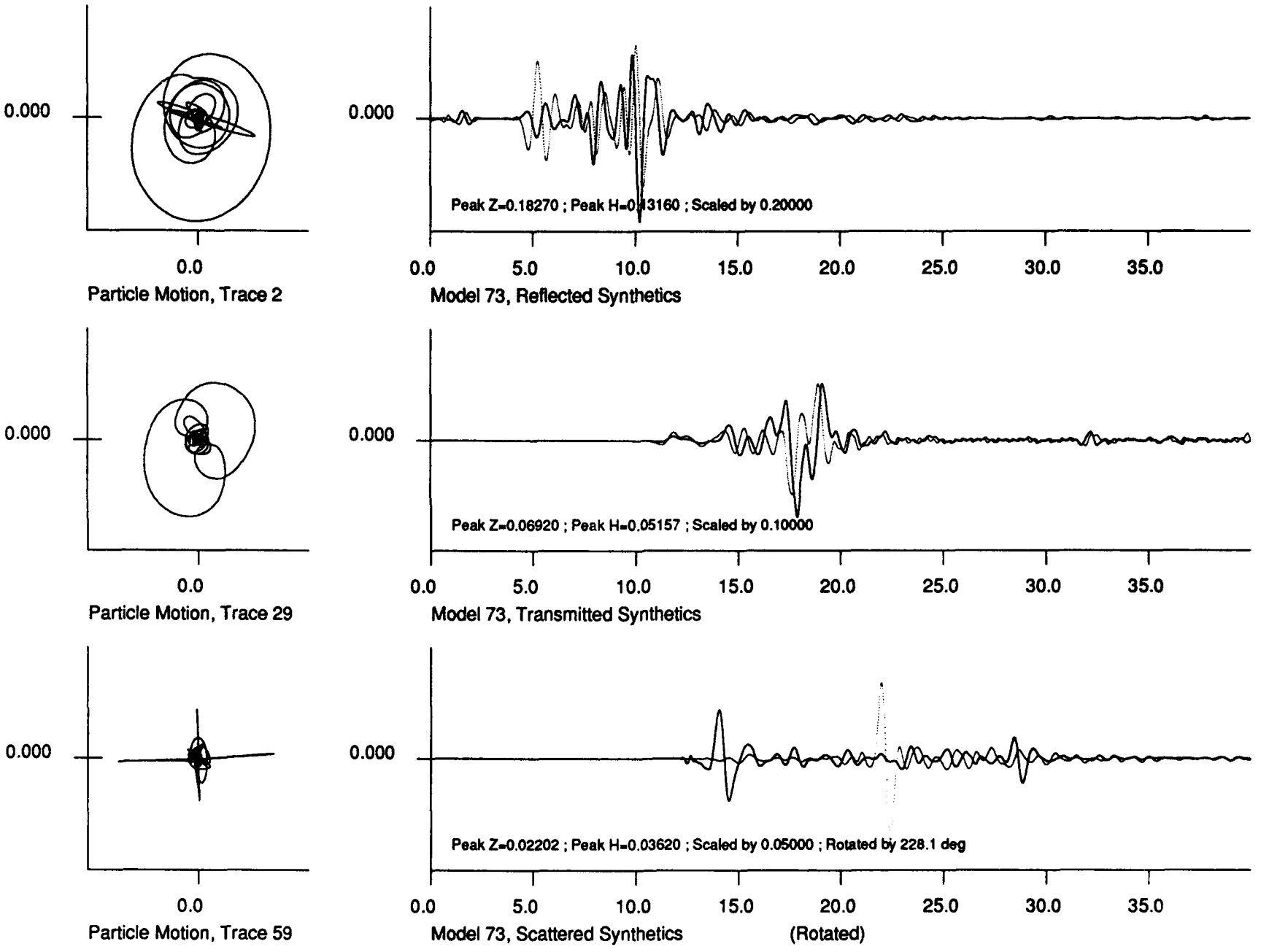
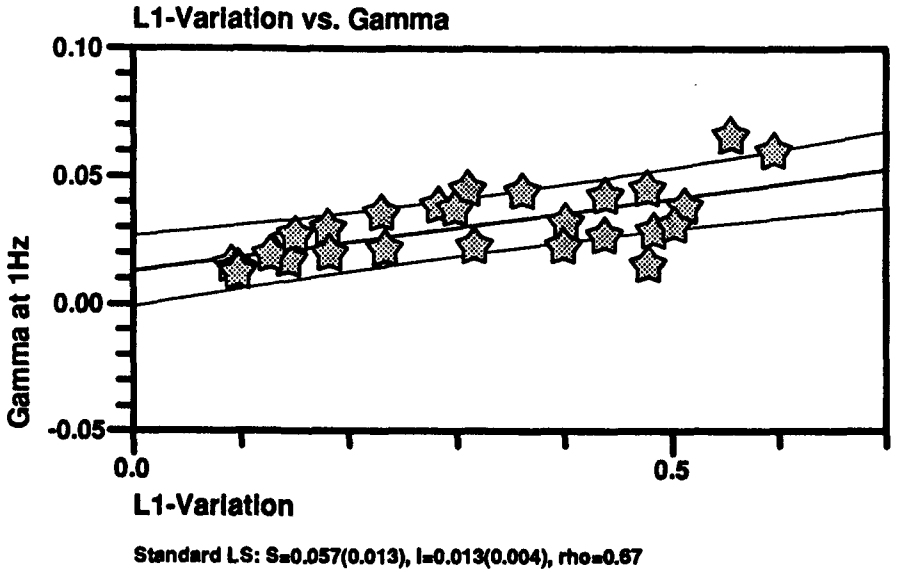
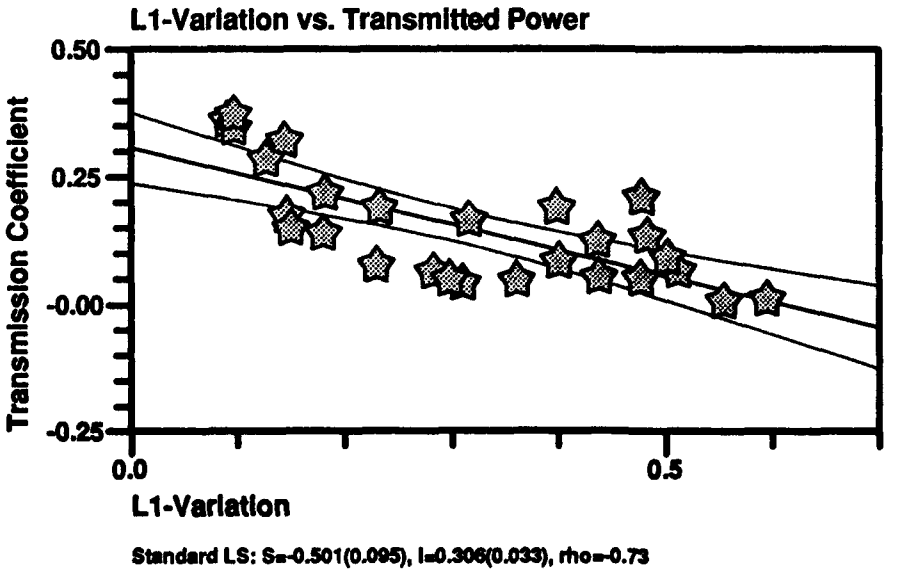
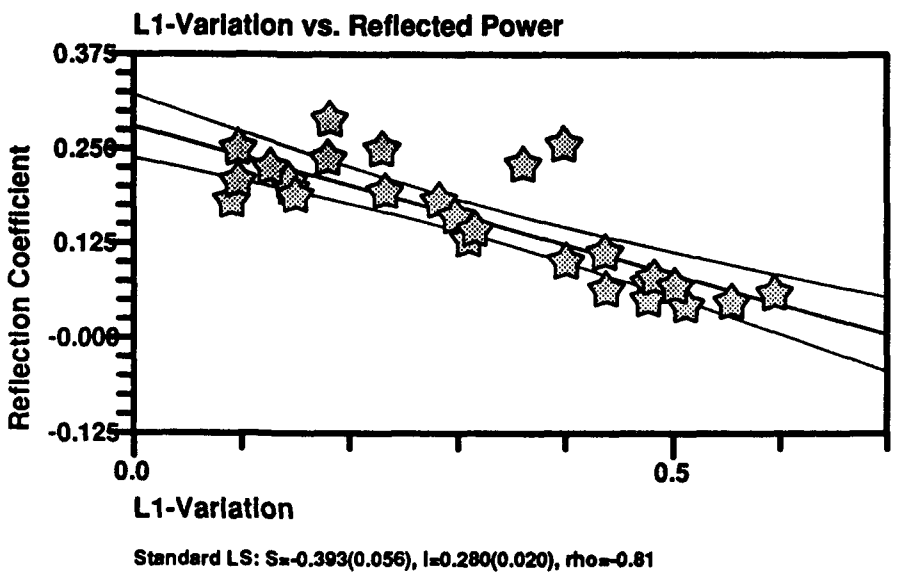

0.000
0.0
Particle Motion, Trace 2
0.000
Peak Z=0.18270 ; Peak H=0.13160 ; Scaled by 0.20000
0.0
5.0
10.0
15.0
20.0
25.0
30.0
35.0
Model 73, Reflected Synthetics
0.000
0.0
Particle Motion, Trace 29
0.000
Peak Z=0.06920 ; Peak H=0.05157 ; Scaled by 0.10000
0.0
5.0
10.0
15.0
20.0
25.0
30.0
35.0
Model 73, Transmitted Synthetics
0.000
0.0
Particle Motion, Trace 59
0.000
Peak Z=0.02202 ; Peak H=0.03620 ; Scaled by 0.05000 ; Rotated by 228.1 deg
0.0
5.0
10.0
15.0
20.0
25.0
30.0
35.0
Model 73, Scattered Synthetics
(Rotated)

**Figure 94**


L1-Variation vs. Gamma
0.10
0.05
0.00
-0.05
Gamma at 1Hz
0.0
0.5
L1-Variation
Standard LS: S=0.057(0.013), I=0.013(0.004), rho=0.67


L1-Variation vs. Transmitted Power
0.50
0.25
-0.00
-0.25
Transmission Coefficient
0.0
0.5
L1-Variation
Standard LS: S=-0.501(0.095), I=0.306(0.033), rho=-0.73


L1-Variation vs. Reflected Power
0.375
0.250
0.125
-0.000
-0.125
Reflection Coefficient
0.0
0.5
L1-Variation
Standard LS: S=-0.393(0.056), I=0.280(0.020), rho=-0.81

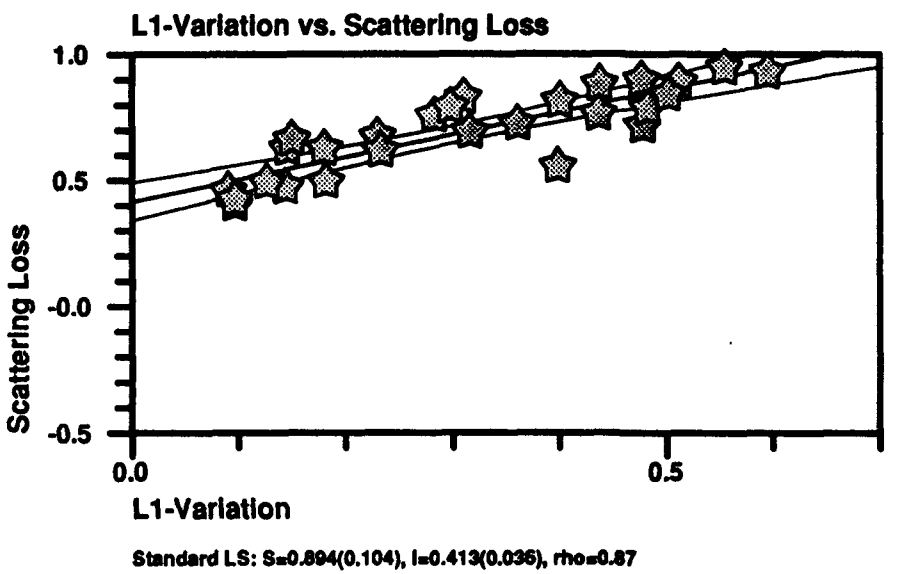
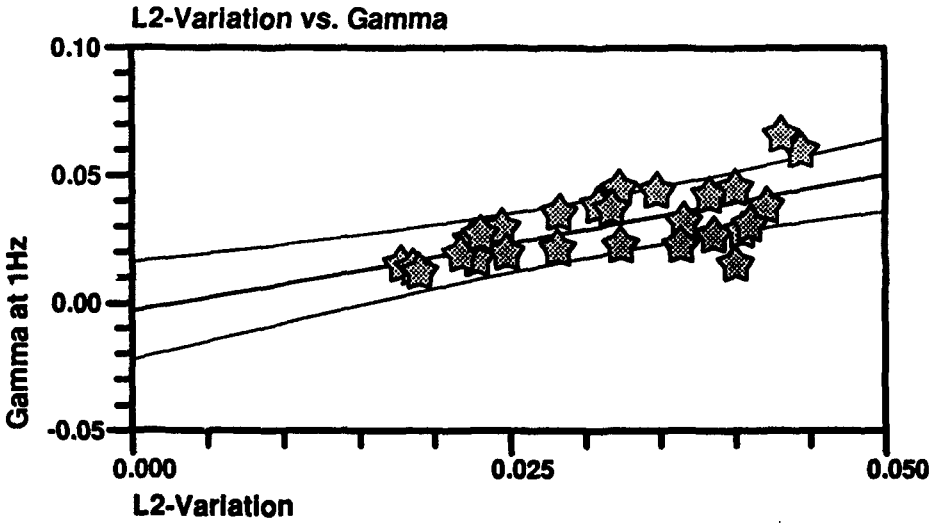
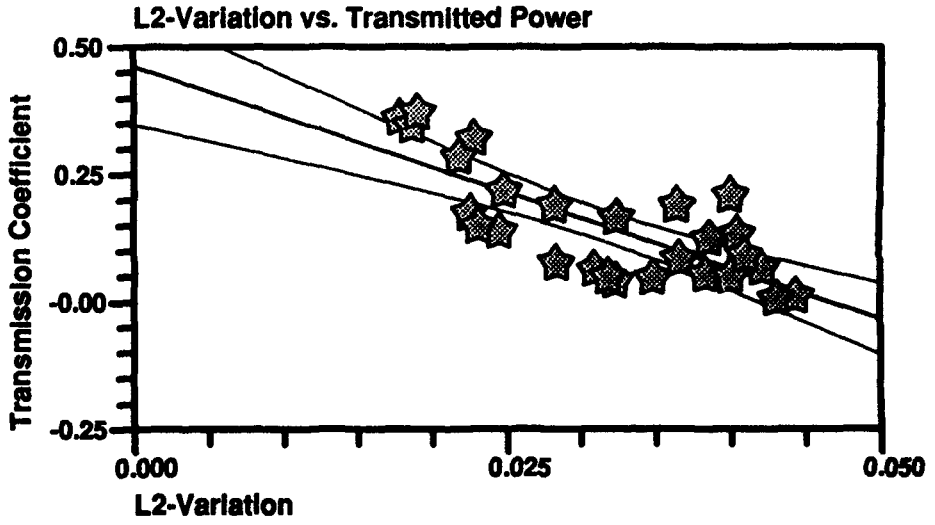
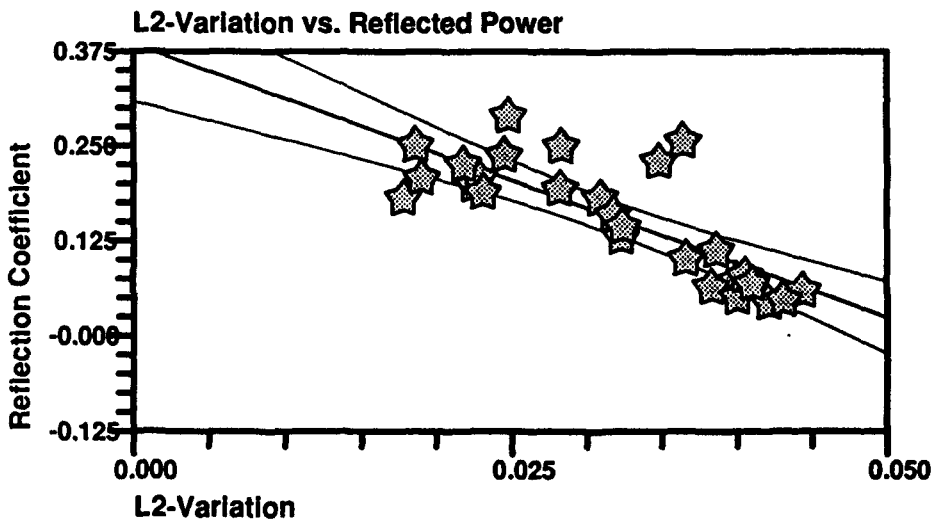

L1-Variation vs. Scattering Loss
1.0
0.5
-0.0
-0.5
Scattering Loss
0.0
0.5
L1-Variation
Standard LS: S=0.894(0.104), I=0.413(0.036), rho=0.87

Figure 95


L2-Variation vs. Gamma
Gamma at 1Hz
0.10
0.05
0.00
-0.05
0.000
0.025
0.050
L2-Variation
Standard LS: S=1.069(0.242), I=-0.003(0.008), rho=0.66


L2-Variation vs. Transmitted Power
Transmission Coefficient
0.50
0.25
-0.00
-0.25
0.000
0.025
0.050
L2-Variation
Standard LS: S=-9.913(1.687), I=0.462(0.055), rho=-0.76


L2-Variation vs. Reflected Power
Reflection Coefficient
0.375
0.250
0.125
-0.000
-0.125
0.000
0.025
0.050
L2-Variation
Standard LS: S=-7.205(1.118), I=0.384(0.037), rho=-0.79

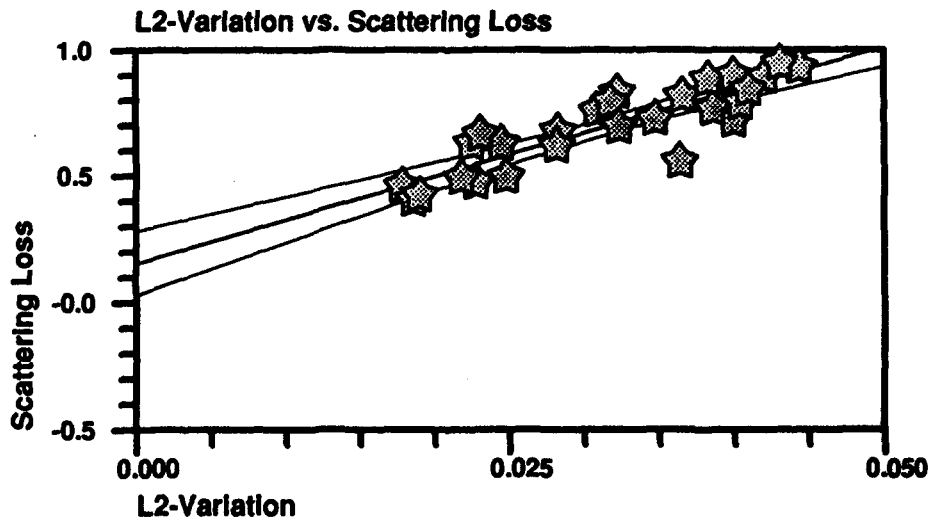
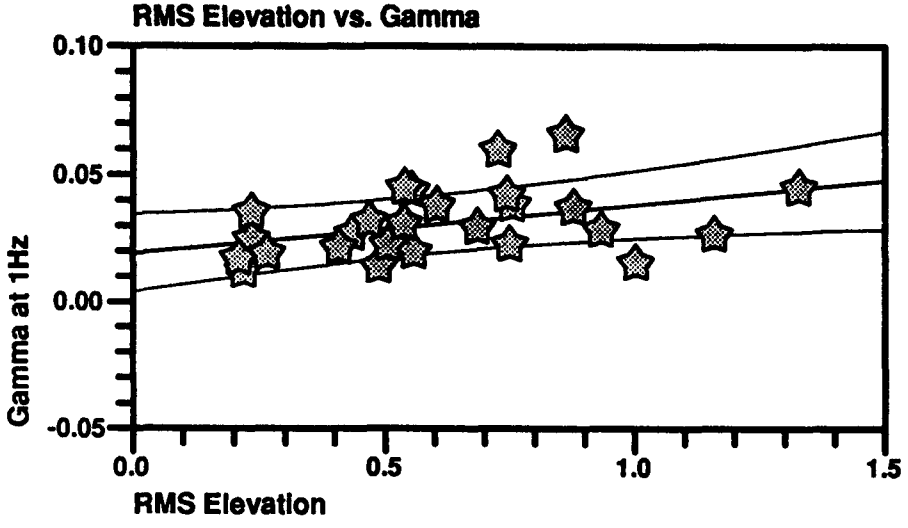
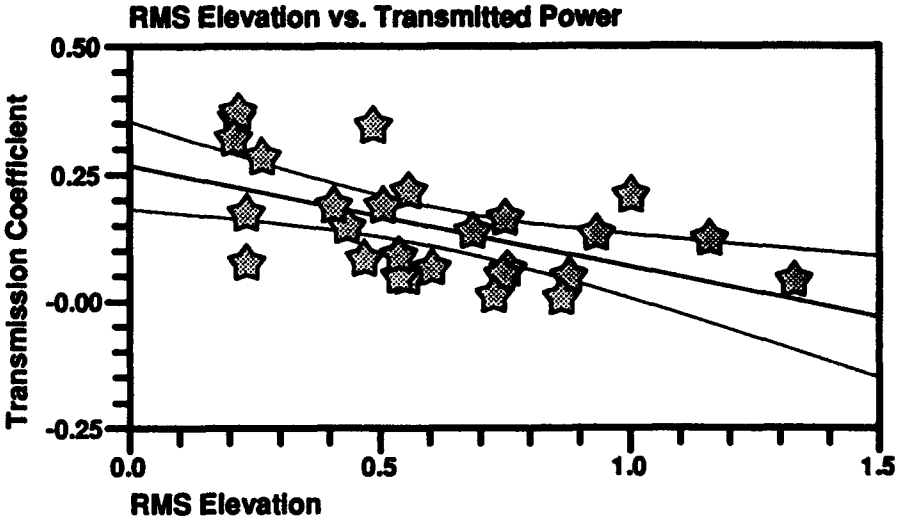
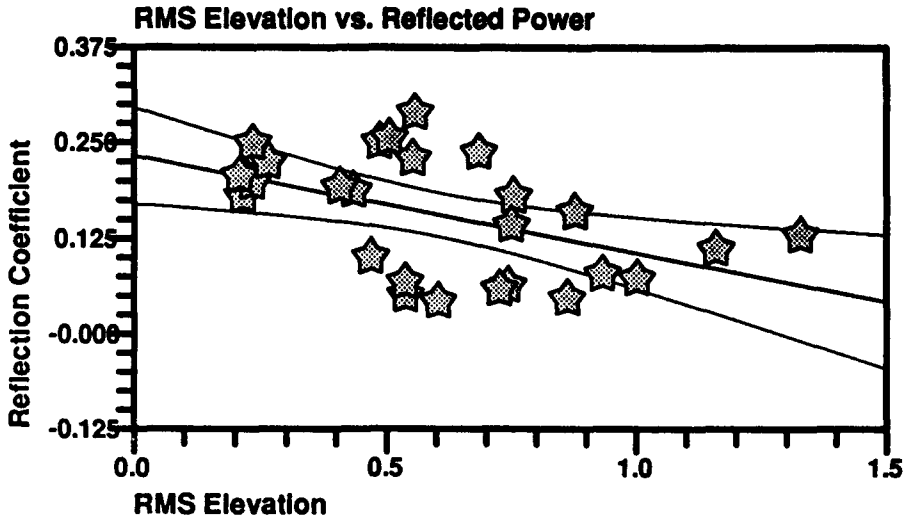

L2-Variation vs. Scattering Loss
Scattering Loss
1.0
0.5
-0.0
-0.5
0.000
0.025
0.050
L2-Variation
Standard LS: S=17.118(1.871), I=0.154(0.061), rho=0.88

Figure 96


RMS Elevation vs. Gamma
Gamma at 1Hz
0.10
0.05
0.00
-0.05
0.0
0.5
1.0
1.5
RMS Elevation
Standard LS: S=0.019(0.008), I=0.019(0.006), rho=0.42


RMS Elevation vs. Transmitted Power
Transmission Coefficient
0.50
0.25
-0.00
-0.25
0.0
0.5
1.0
1.5
RMS Elevation
Standard LS: S=-0.199(0.062), I=0.268(0.041), rho=-0.54


RMS Elevation vs. Reflected Power
Reflection Coefficient
0.375
0.250
0.125
-0.000
-0.125
0.0
0.5
1.0
1.5
RMS Elevation
Standard LS: S=-0.127(0.045), I=0.233(0.030), rho=-0.49

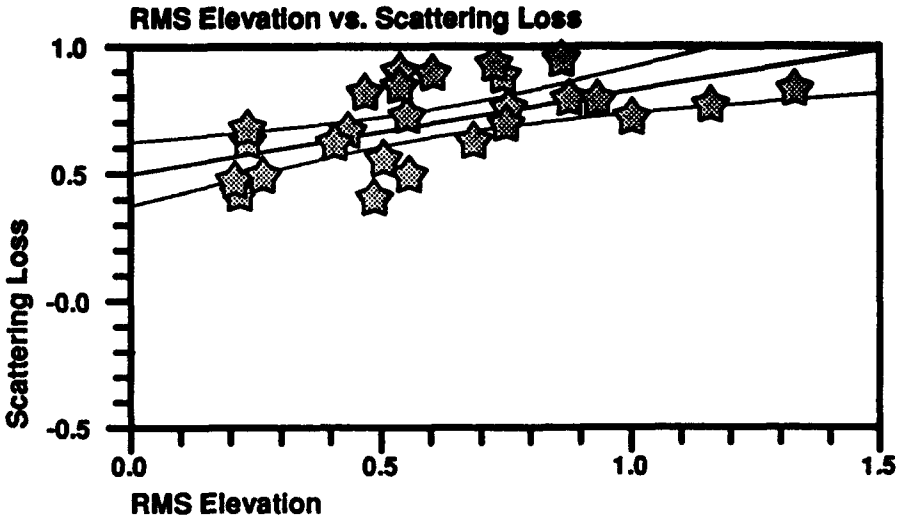
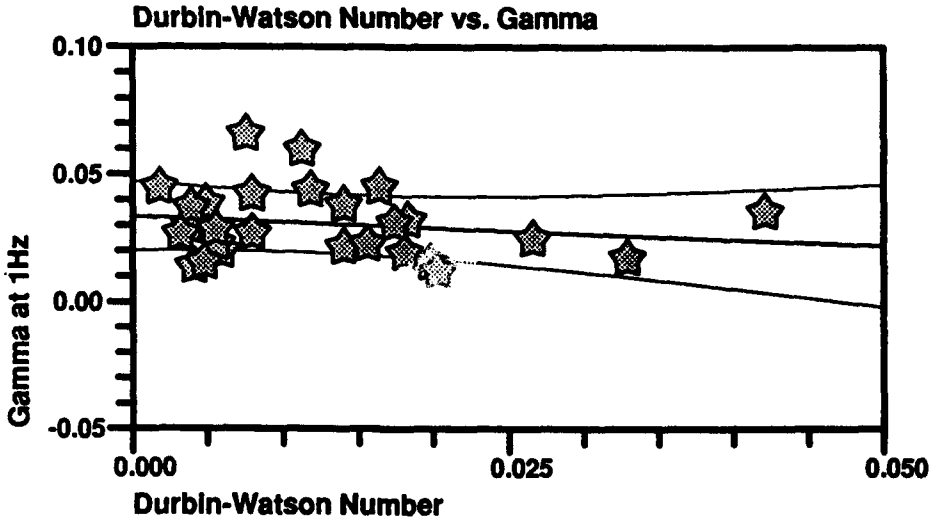
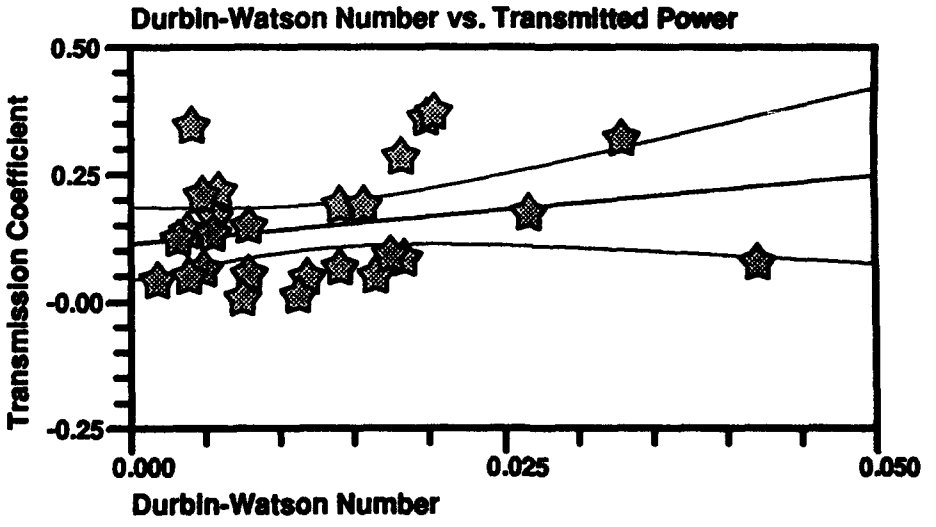
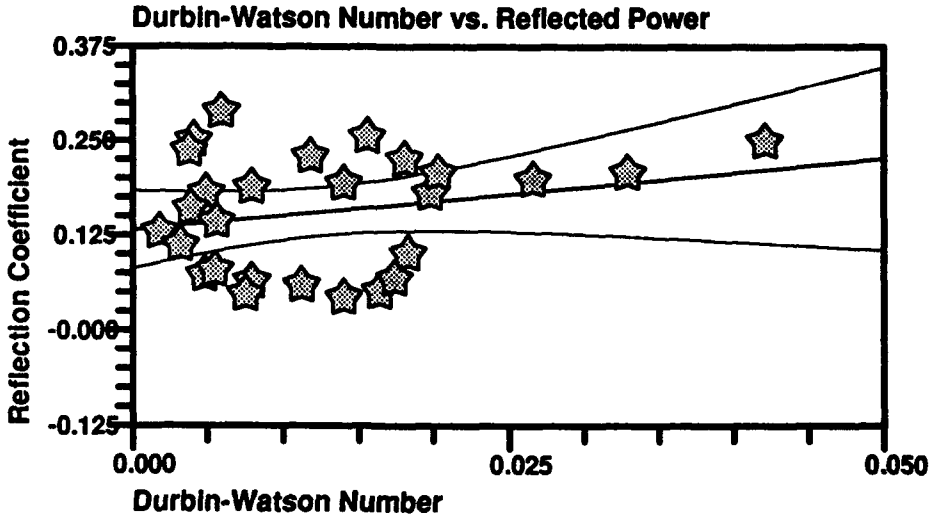

RMS Elevation vs. Scattering Loss
Scattering Loss
1.0
0.5
-0.0
-0.5
0.0
0.5
1.0
1.5
RMS Elevation
Standard LS: S=0.326(0.089), I=0.499(0.060), rho=0.59

Figure 97


Durbin-Watson Number vs. Gamma
0.10
0.05
0.00
-0.05
Gamma at 1Hz
0.000
0.025
0.050
Durbin-Watson Number
Standard LS: S=-0.234(0.274), I=0.034(0.004), rho=-0.17


Durbin-Watson Number vs. Transmitted Power
0.50
0.25
-0.00
-0.25
Transmission Coefficient
0.000
0.025
0.050
Durbin-Watson Number
Standard LS: S=2.869(2.179), I=0.114(0.035), rho=0.24


Durbin-Watson Number vs. Reflected Power
0.375
0.250
0.125
-0.000
-0.125
Reflection Coefficient
0.000
0.025
0.050
Durbin-Watson Number
Standard LS: S=1.876(1.527), I=0.132(0.024), rho=0.24

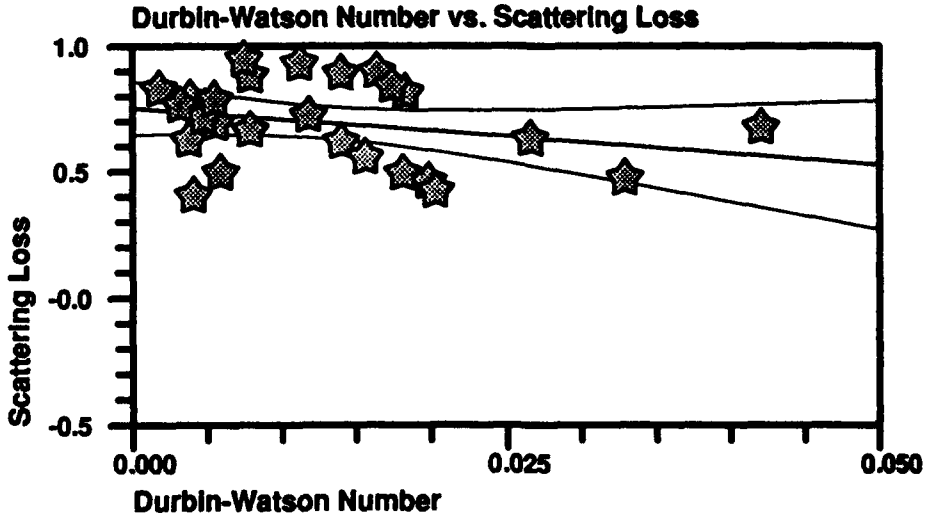
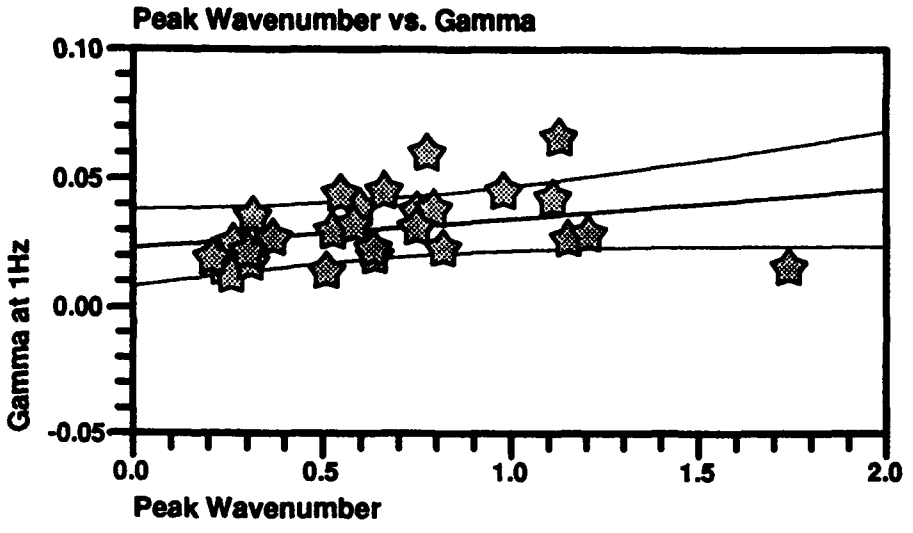
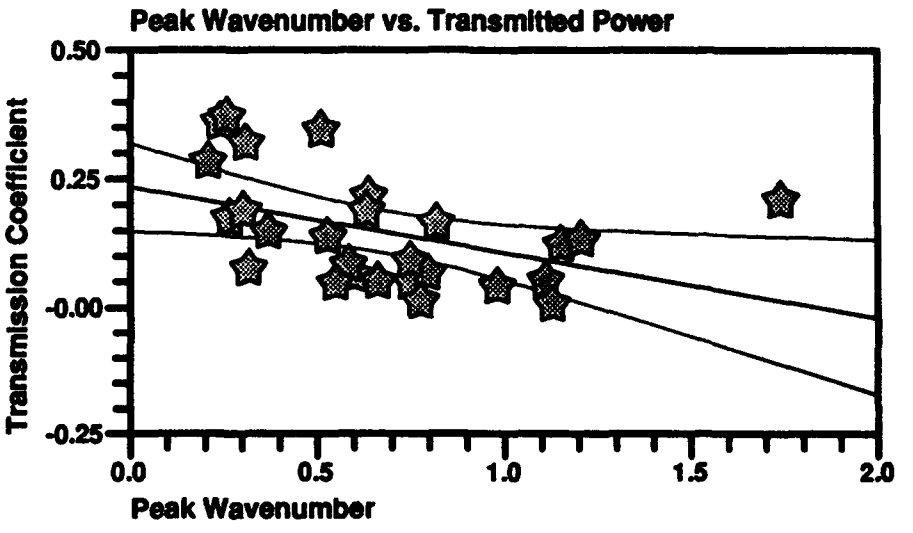
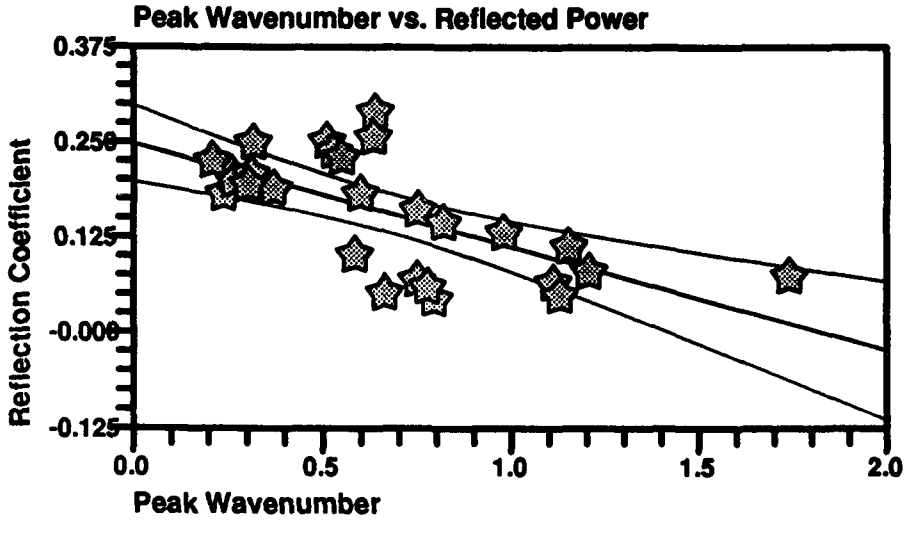

Durbin-Watson Number vs. Scattering Loss
1.0
0.5
-0.0
-0.5
Scattering Loss
0.000
0.025
0.050
Durbin-Watson Number
Standard LS: S=-4.545(3.238), I=0.754(0.052), rho=-0.27

Figure 98


Peak Wavenumber vs. Gamma
Gamma at 1Hz
0.10
0.05
0.00
-0.05
0.0
0.5
1.0
1.5
2.0
Peak Wavenumber
Standard LS: S=0.011(0.007), I=0.023(0.005), rho=0.31


Peak Wavenumber vs. Transmitted Power
Transmission Coefficient
0.50
0.25
-0.00
-0.25
0.0
0.5
1.0
1.5
2.0
Peak Wavenumber
Standard LS: S=-0.127(0.054), I=0.234(0.041), rho=-0.43


Peak Wavenumber vs. Reflected Power
Reflection Coefficient
0.375
0.250
0.125
-0.000
-0.125
0.0
0.5
1.0
1.5
2.0
Peak Wavenumber
Standard LS: S=-0.136(0.032), I=0.248(0.024), rho=-0.65

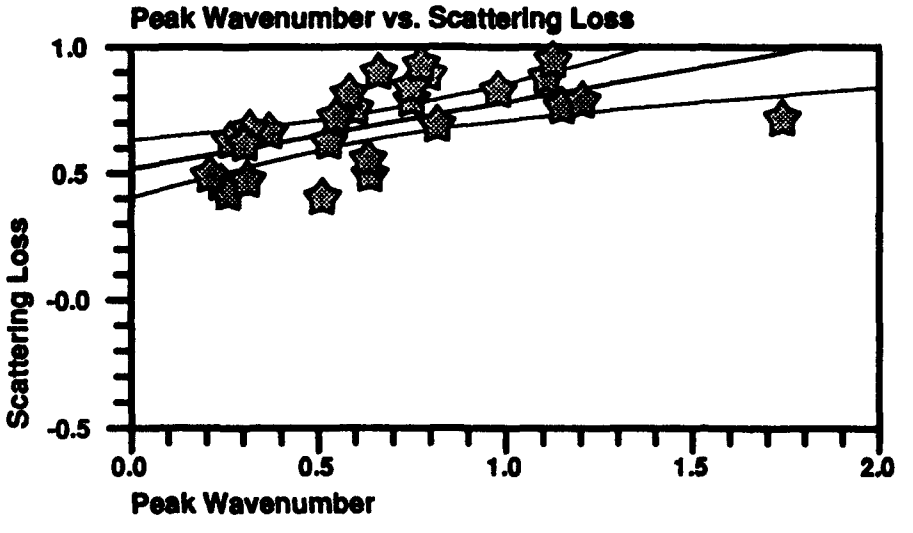
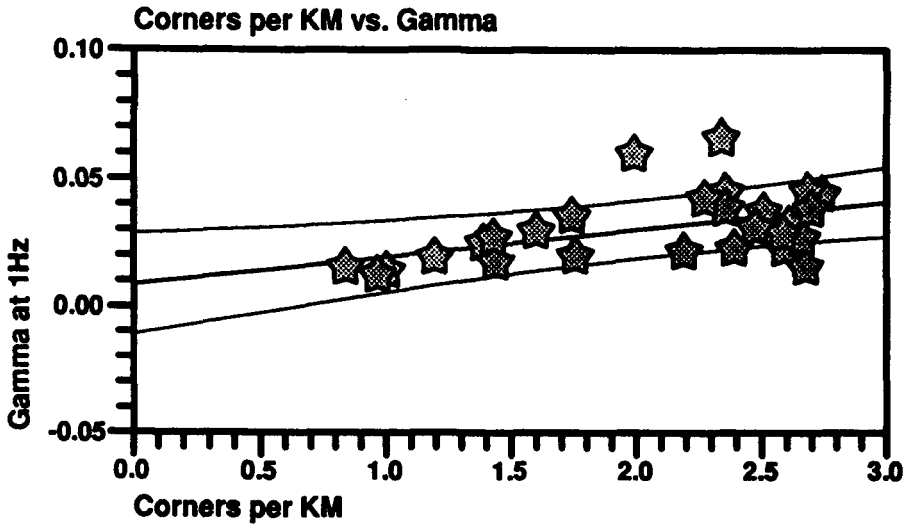
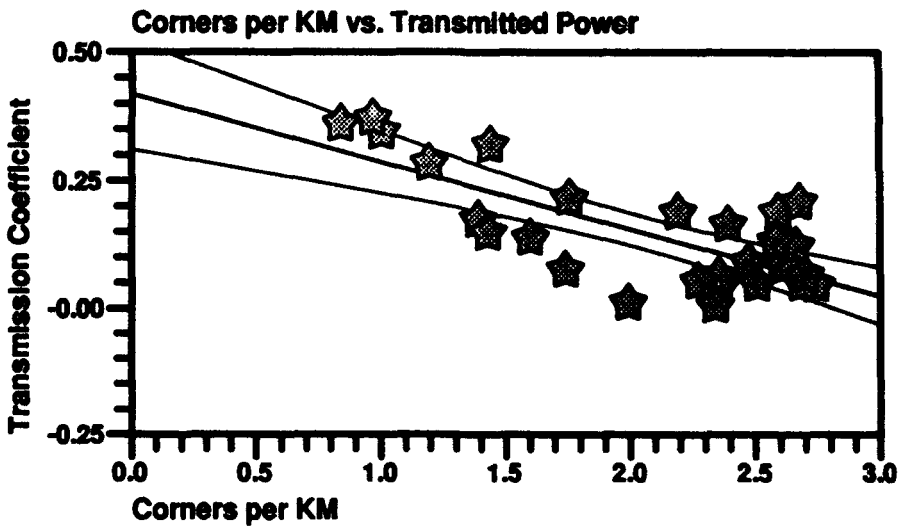
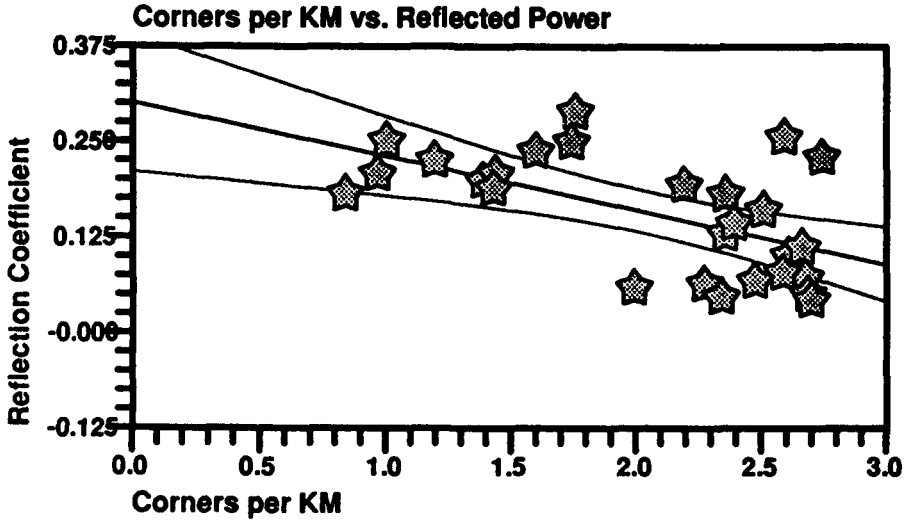

Peak Wavenumber vs. Scattering Loss
Scattering Loss
1.0
0.5
-0.0
-0.5
0.0
0.5
1.0
1.5
2.0
Peak Wavenumber
Standard LS: S=0.263(0.072), I=0.518(0.055), rho=0.59

Figure 99


Corners per KM vs. Gamma
Gamma at 1Hz
0.10
0.05
0.00
-0.05
0.0
0.5
1.0
1.5
2.0
2.5
3.0
Corners per KM
Standard LS: S=0.011(0.004), I=0.009(0.008), rho=0.49


Corners per KM vs. Transmitted Power
Transmission Coefficient
0.50
0.25
-0.00
-0.25
0.0
0.5
1.0
1.5
2.0
2.5
3.0
Corners per KM
Standard LS: S=-0.131(0.024), I=0.418(0.051), rho=-0.74


Corners per KM vs. Reflected Power
Reflection Coefficient
0.375
0.250
0.125
-0.000
-0.125
0.0
0.5
1.0
1.5
2.0
2.5
3.0
Corners per KM
Standard LS: S=-0.070(0.020), I=0.301(0.044), rho=-0.57

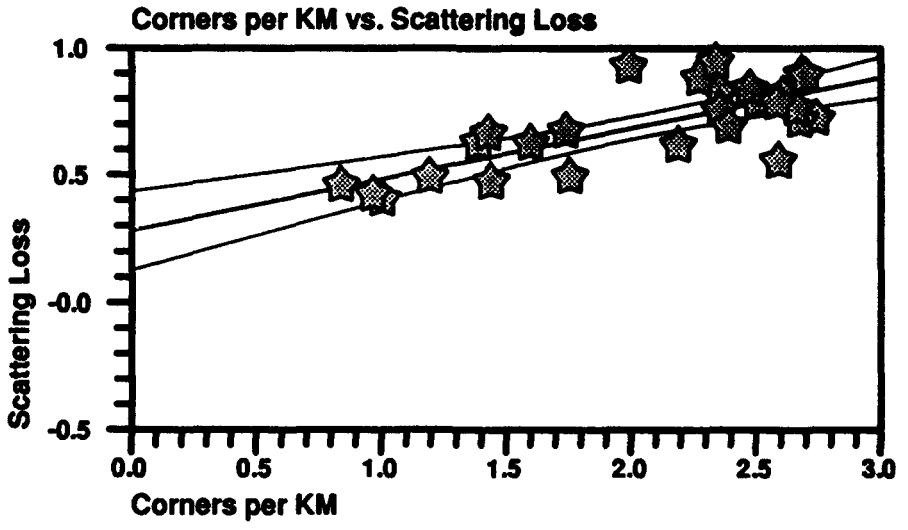
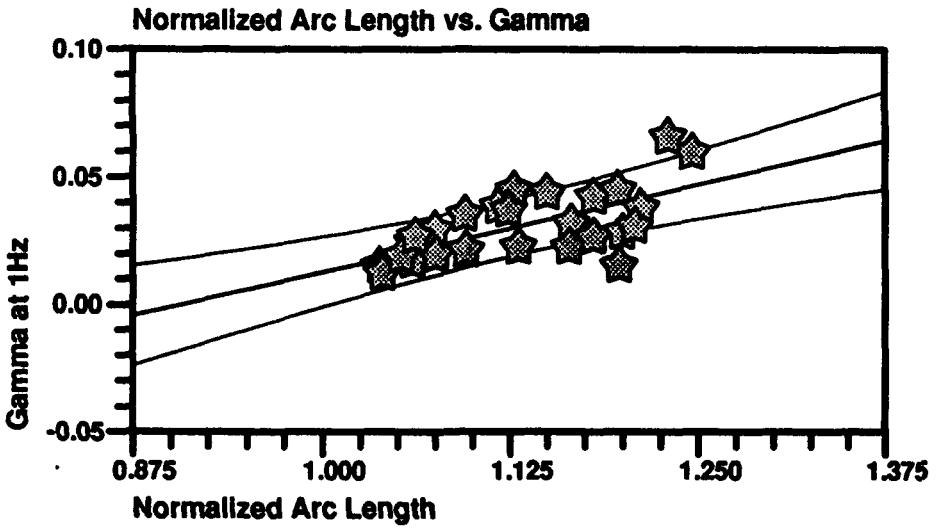
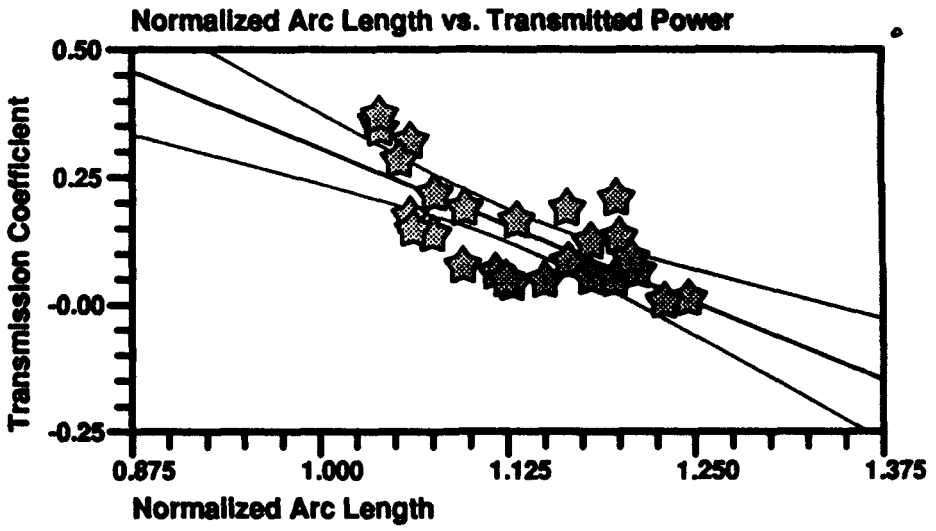
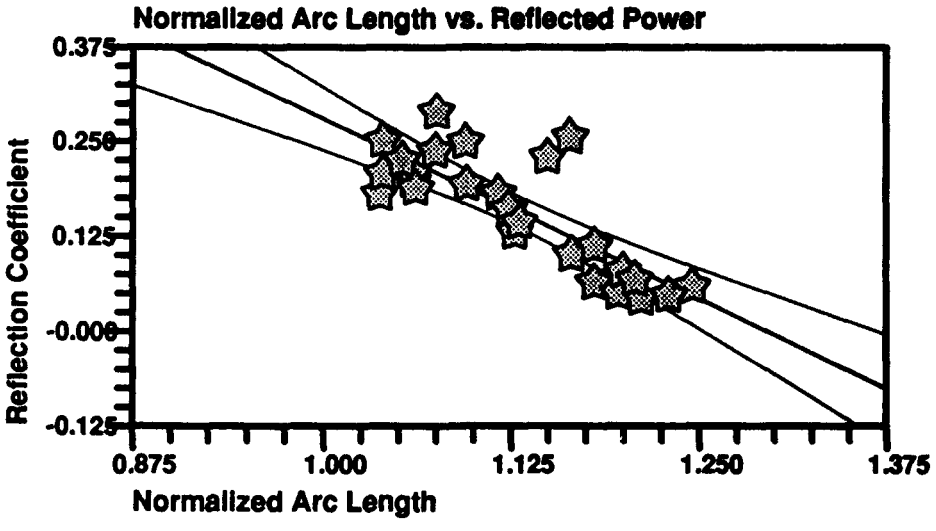

Corners per KM vs. Scattering Loss
Scattering Loss
1.0
0.5
-0.0
-0.5
0.0
0.5
1.0
1.5
2.0
2.5
3.0
Corners per KM
Standard LS: S=0.202(0.035), I=0.281(0.074), rho=0.76

Figure 100


Normalized Arc Length vs. Gamma
Gamma at 1Hz
0.10
0.05
0.00
-0.05
0.875
1.000
1.125
1.250
1.375
Normalized Arc Length
Standard LS: S=0.137(0.031), I=-0.124(0.035), rho=0.66


Normalized Arc Length vs. Transmitted Power
Transmission Coefficient
0.50
0.25
-0.00
-0.25
0.875
1.000
1.125
1.250
1.375
Normalized Arc Length
Standard LS: S=-1.210(0.229), I=1.517(0.259), rho=-0.73


Normalized Arc Length vs. Reflected Power
Reflection Coefficient
0.375
0.250
0.125
-0.000
-0.125
0.875
1.000
1.125
1.250
1.375
Normalized Arc Length
Standard LS: S=-0.949(0.136), I=1.229(0.154), rho=-0.81

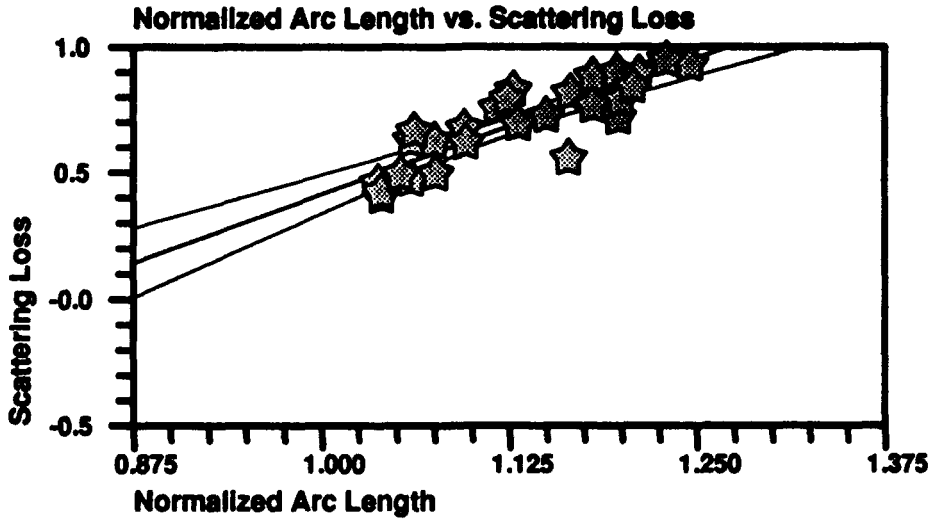
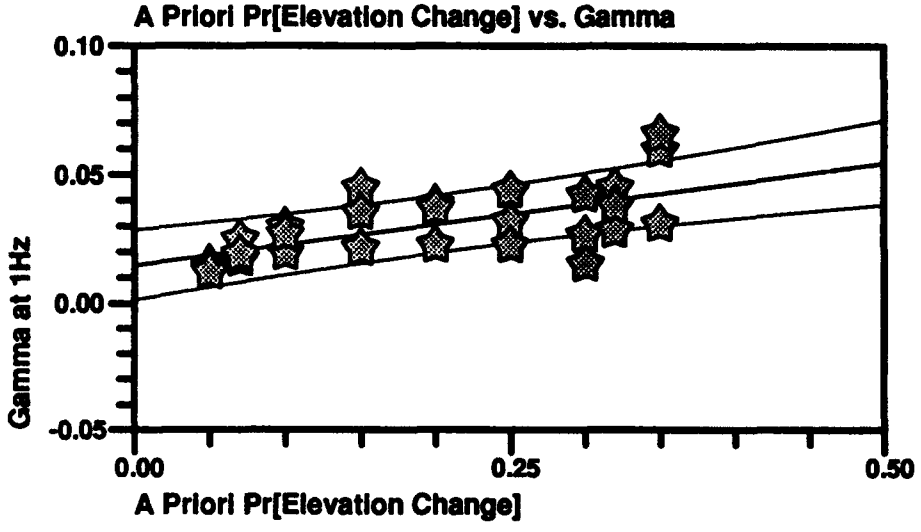
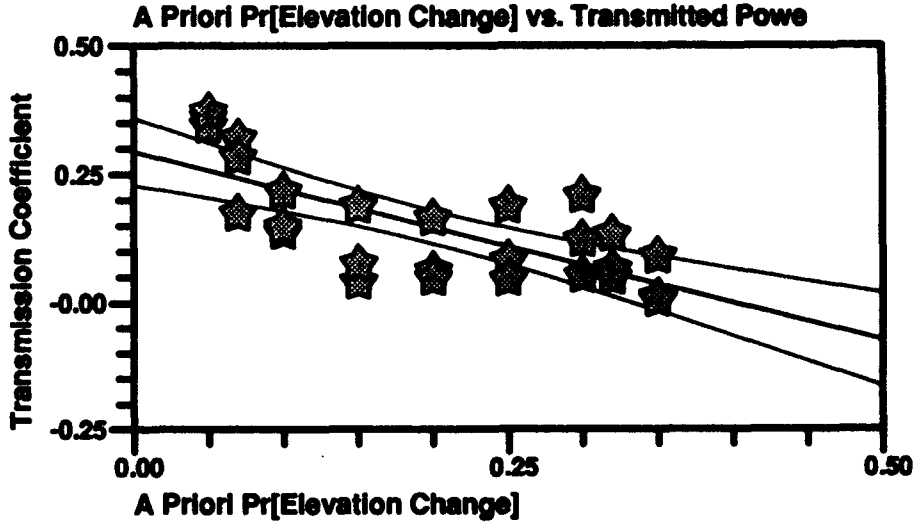
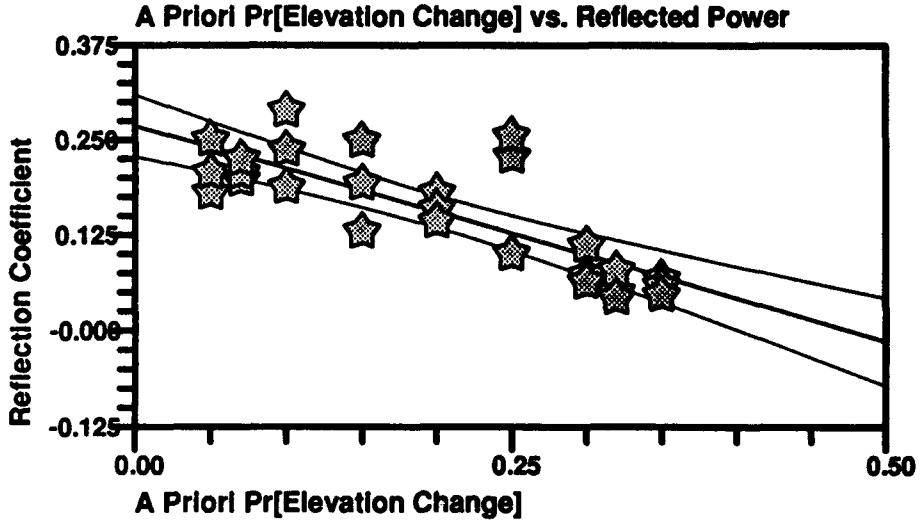

Normalized Arc Length vs. Scattering Loss
Scattering Loss
1.0
0.5
-0.0
-0.5
0.875
1.000
1.125
1.250
1.375
Normalized Arc Length
Standard LS: S=2.159(0.251), I=-1.746(0.284), rho=0.86

Figure 101


A Priori Pr[Elevation Change] vs. Gamma
Gamma at 1Hz
0.10
0.05
0.00
-0.05
0.00
0.25
0.50
A Priori Pr[Elevation Change]
Standard LS: S=0.080(0.019), I=0.015(0.004), rho=0.64


A Priori Pr[Elevation Change] vs. Transmitted Powe
Transmission Coefficient
0.50
0.25
-0.00
-0.25
0.00
0.25
0.50
A Priori Pr[Elevation Change]
Standard LS: S=-0.734(0.139), I=0.294(0.031), rho=-0.73


A Priori Pr[Elevation Change] vs. Reflected Power
Reflection Coefficient
0.375
0.250
0.125
-0.000
-0.125
0.00
0.25
0.50
A Priori Pr[Elevation Change]
Standard LS: S=-0.566(0.085), I=0.269(0.019), rho=-0.80

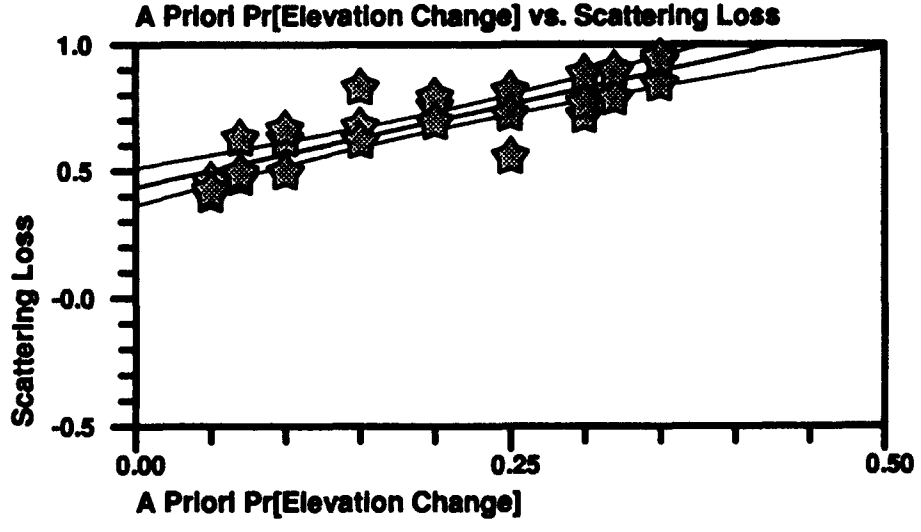
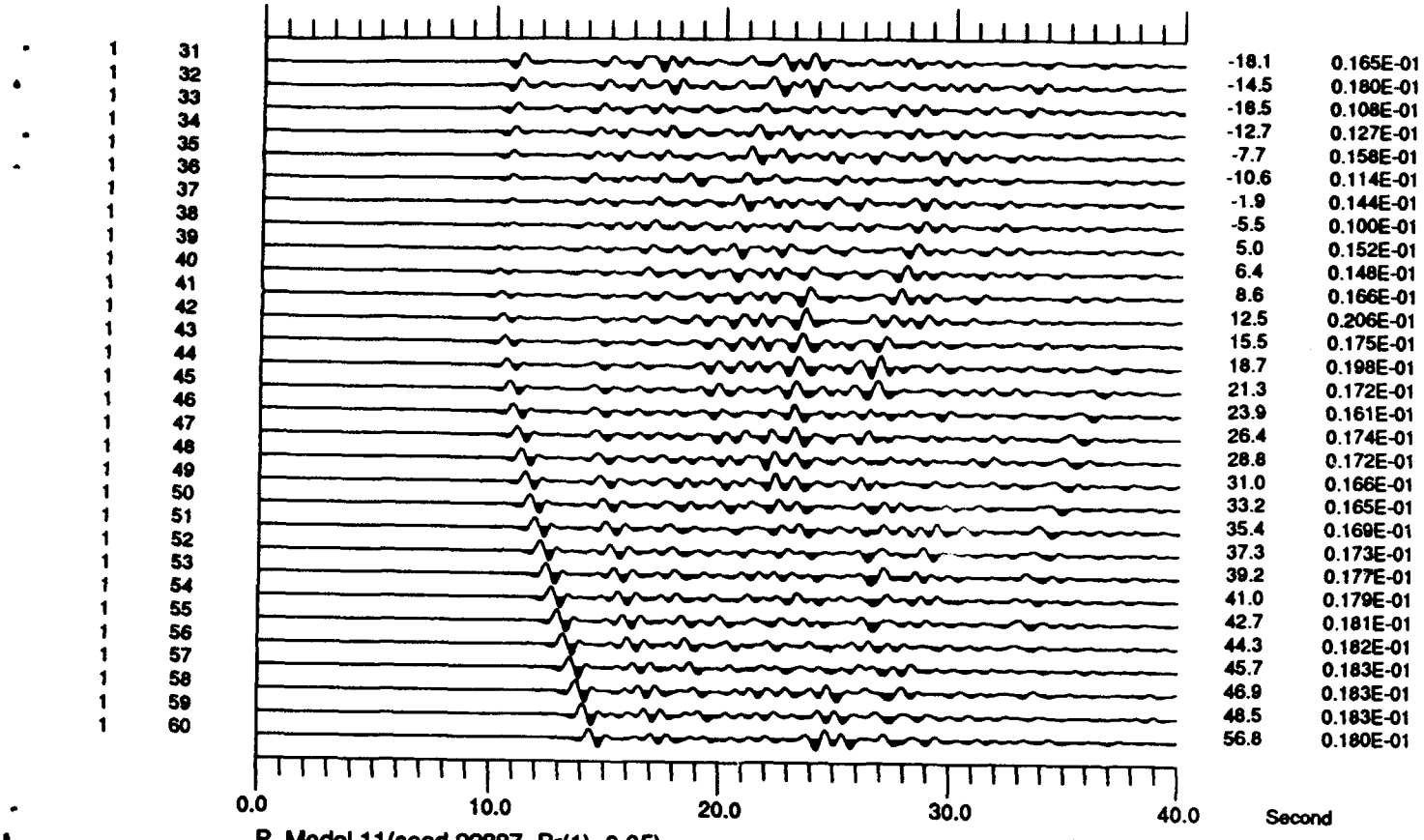
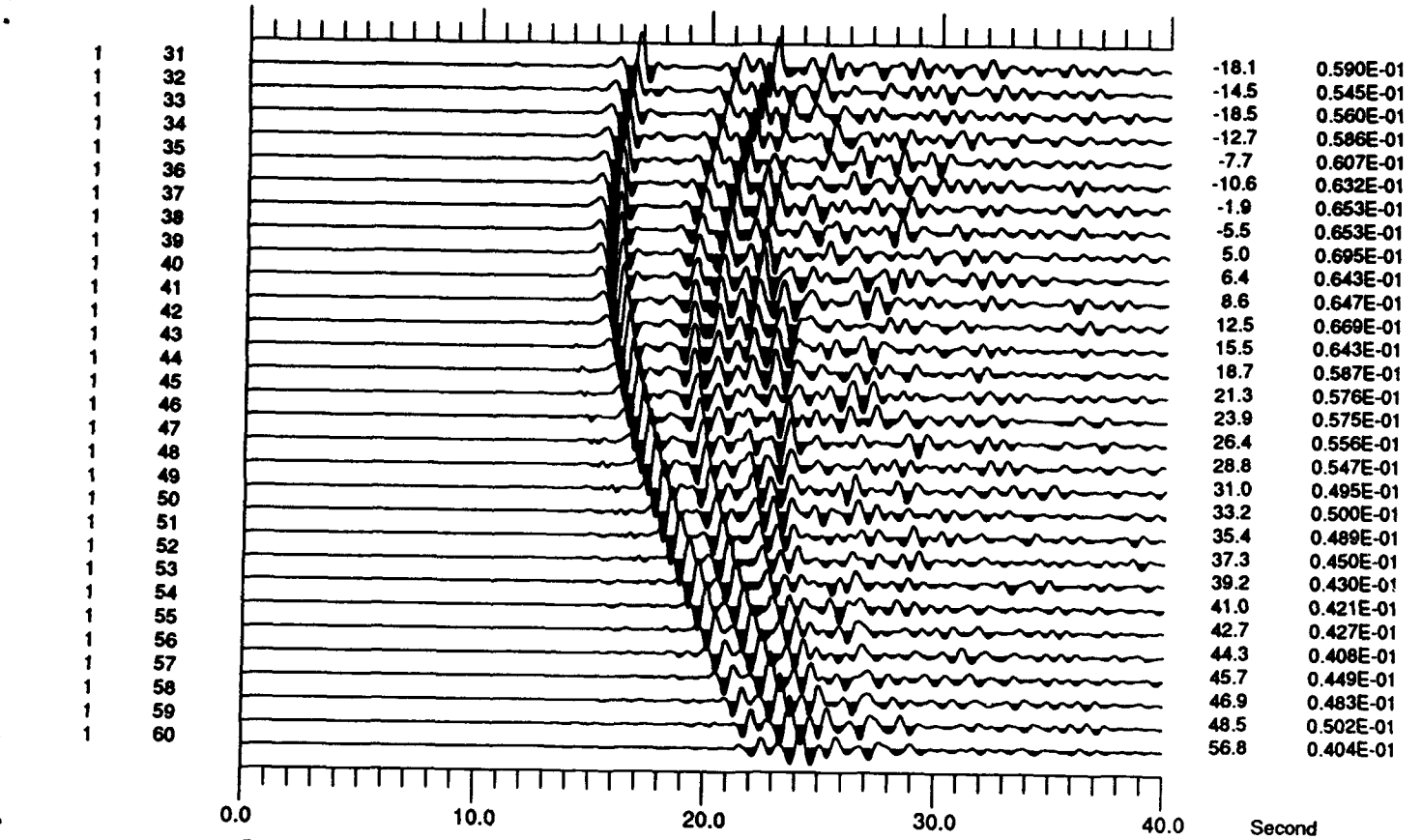

A Priori Pr[Elevation Change] vs. Scattering Loss
Scattering Loss
1.0
0.5
-0.0
-0.5
0.00
0.25
0.50
A Priori Pr[Elevation Change]
Standard LS: S=1.300(0.156), I=0.437(0.035), rho=0.86

Figure 102




P, Model 11(seed 22887, Pr(1)=0.05)

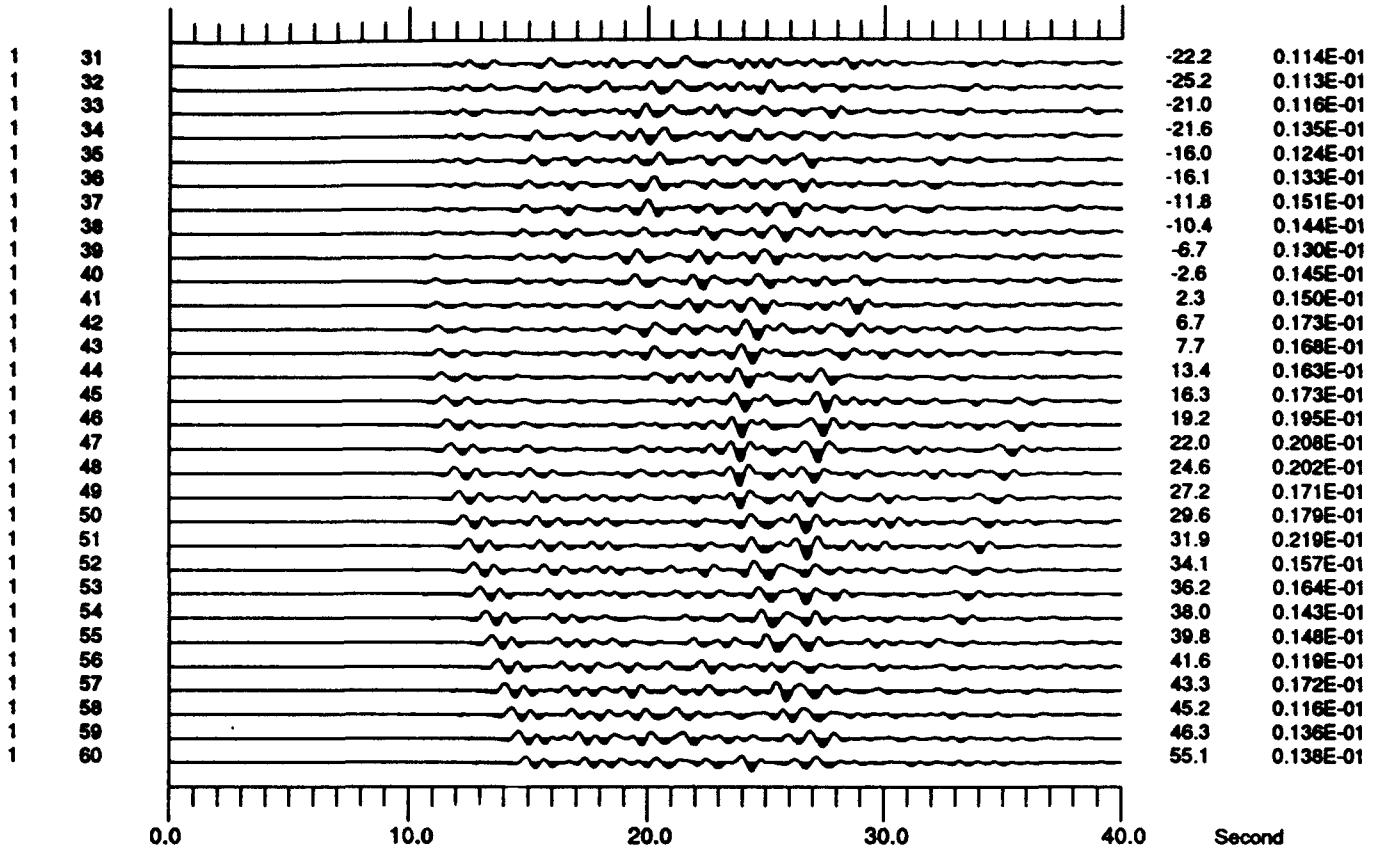
vert, same scale, decimated by 5




S, Model 11(seed 22887, Pr(1)=0.05)

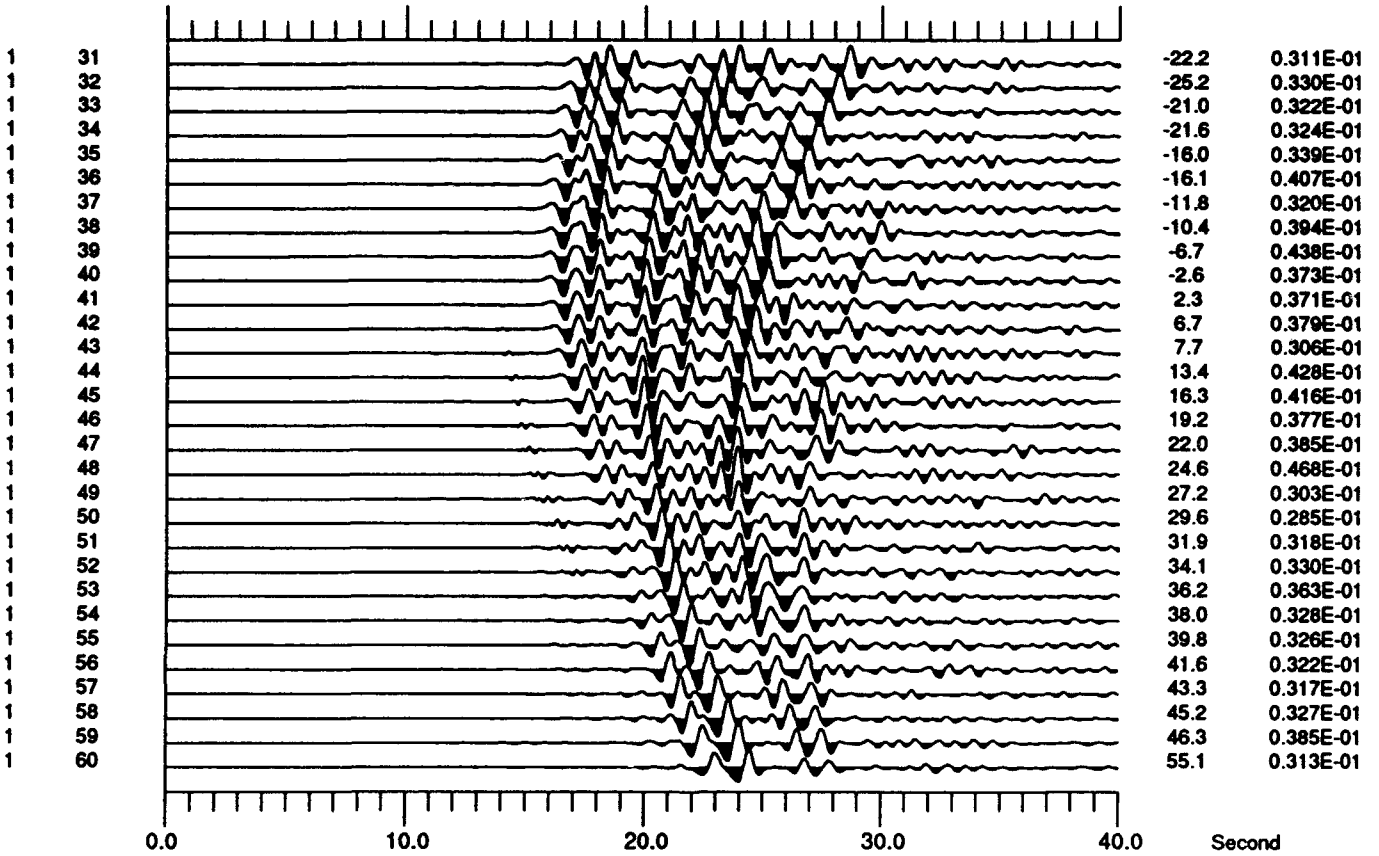
hori, same scale, decimated by 5

**Figure 103**




P, Model 12(seed 22892, Pr(1)=0.05)

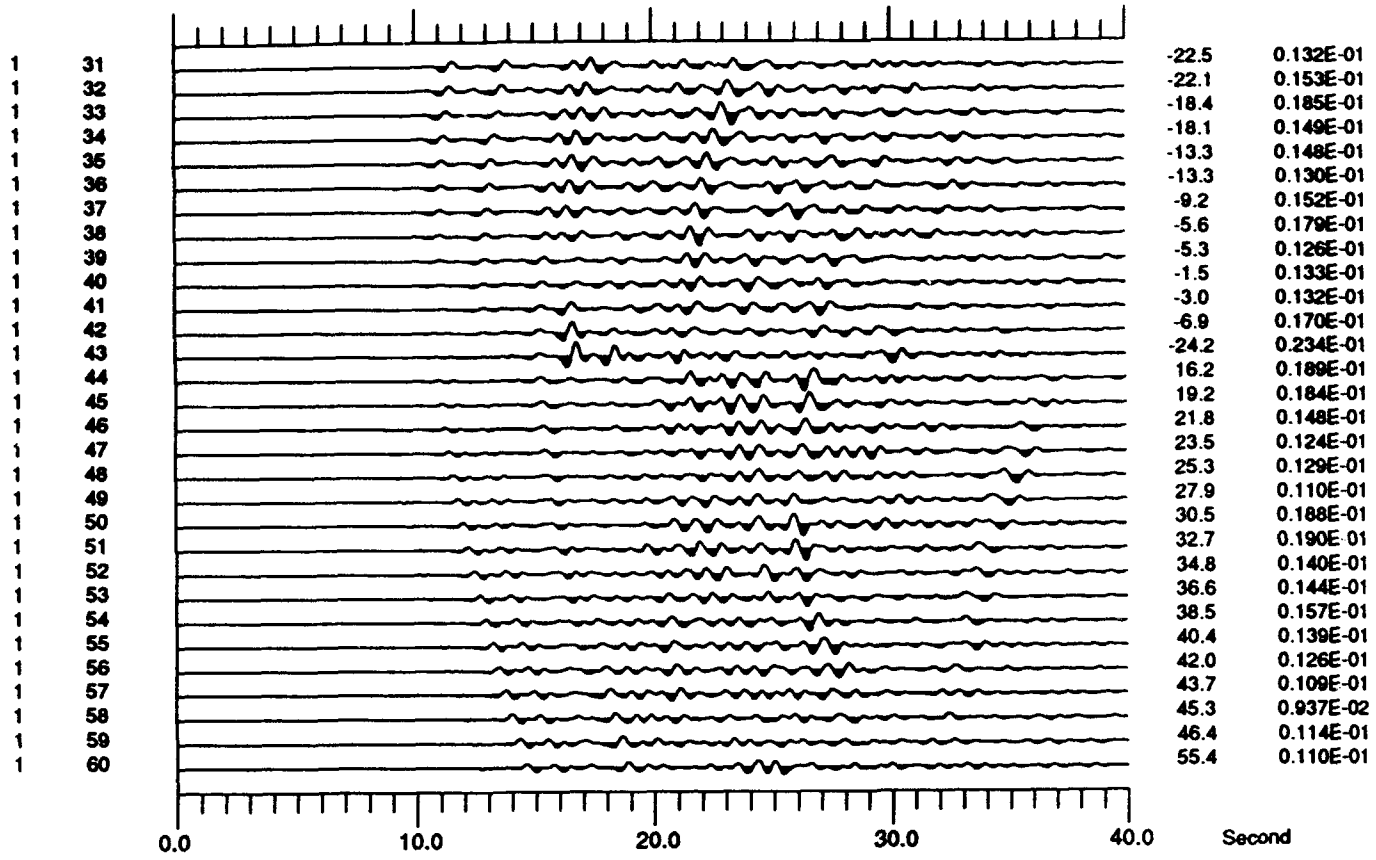
vert, same scale, decimated by 5




S, Model 12(seed 22892, Pr(1)=0.05)

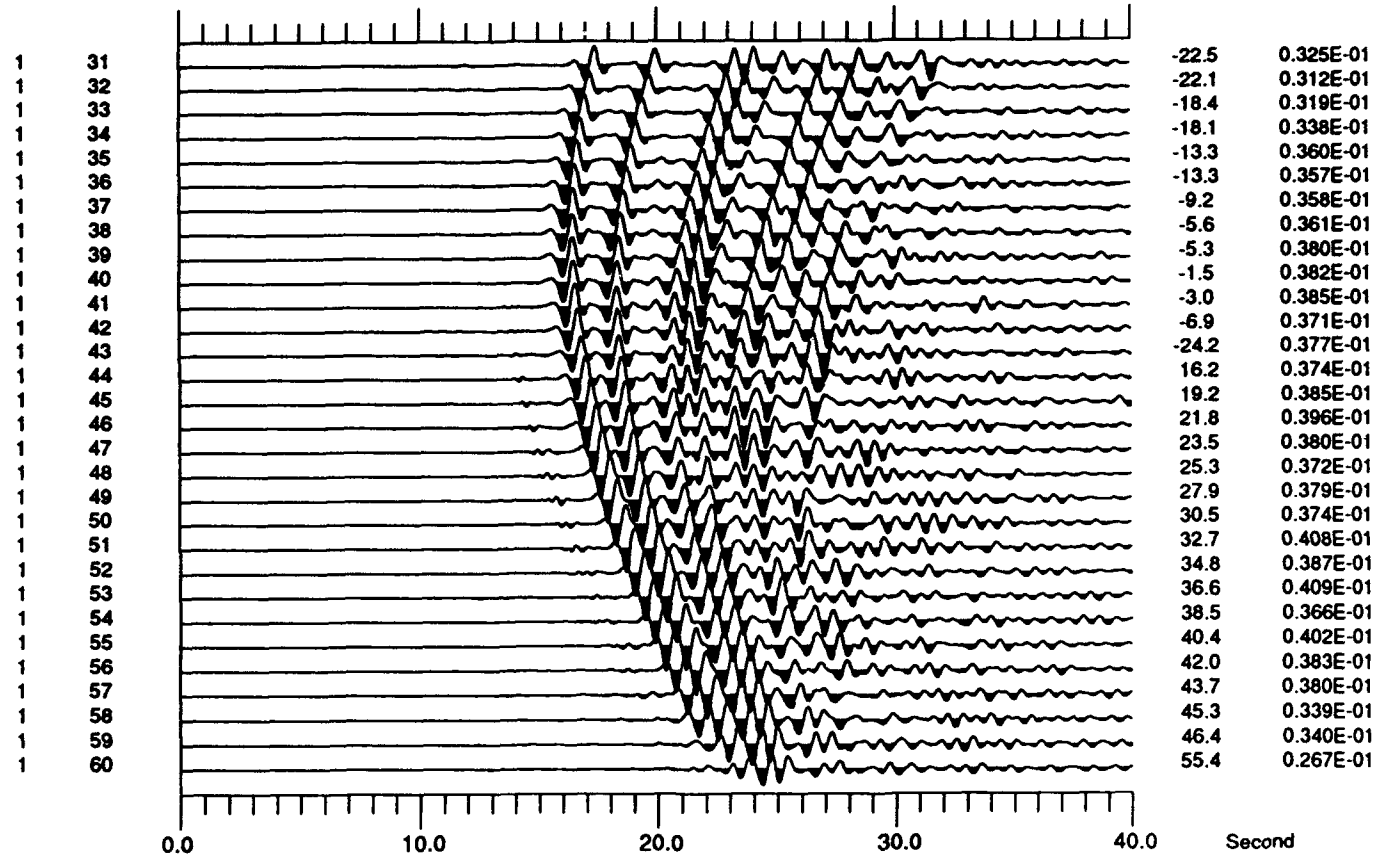
hori, same scale, decimated by 5

**Figure 104**




P, Model 13(seed 85995, Pr(1)=0.05)

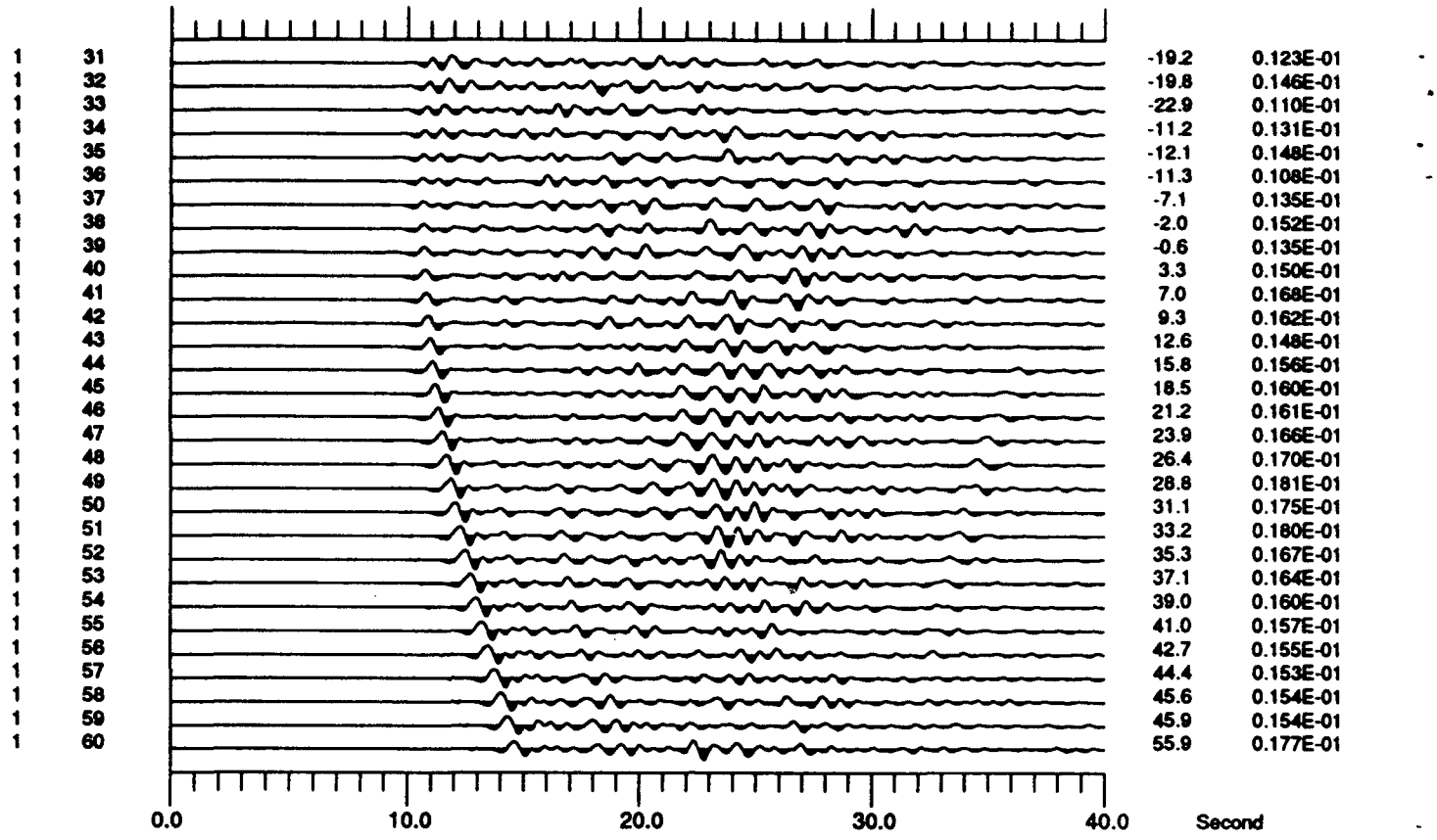
vert, same scale, decimated by 5




S, Model 13(seed 85995, Pr(1)=0.05)

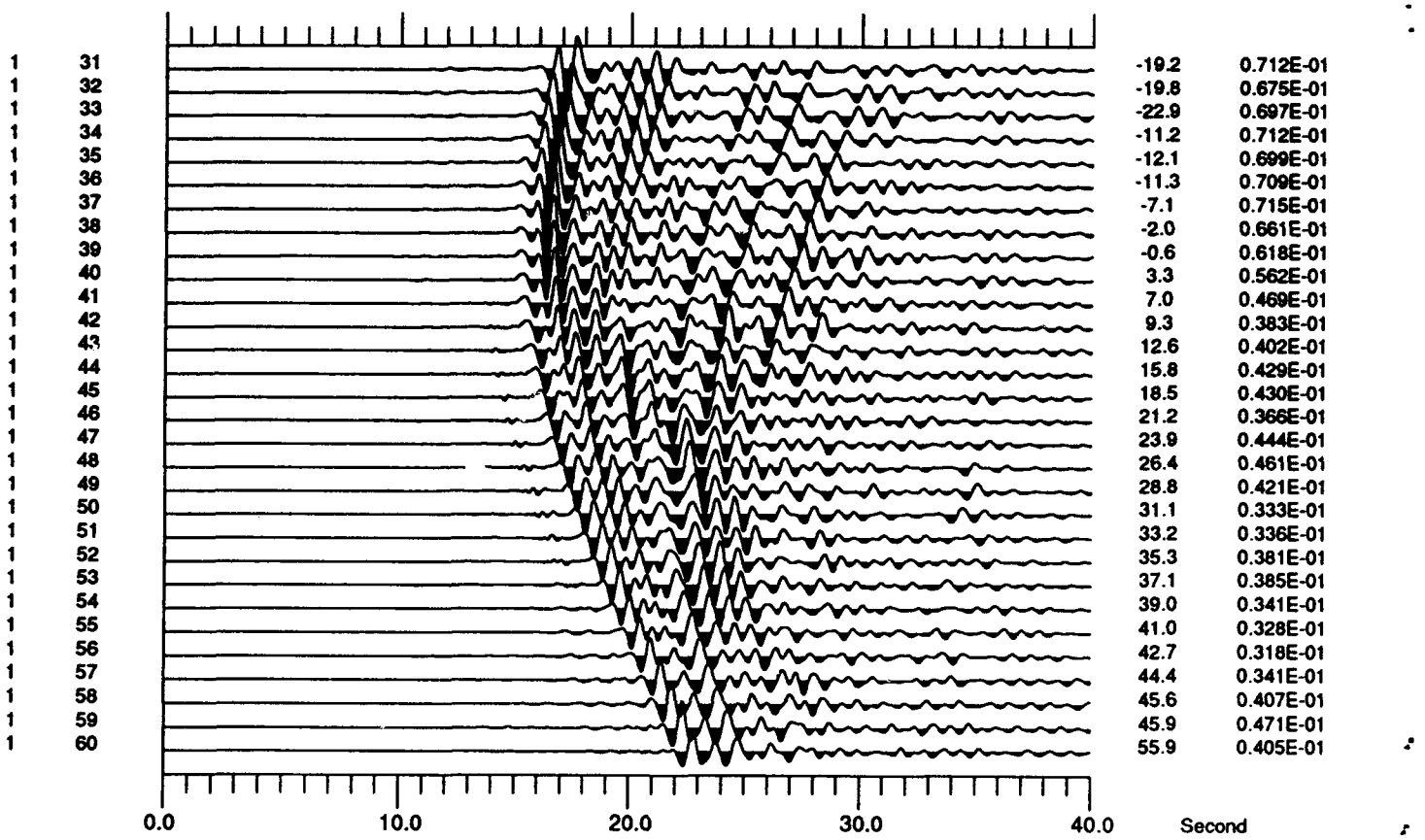
hori, same scale, decimated by 5

**Figure 105**




P, Model 14(seed 91333, Pr(1)=0.07)

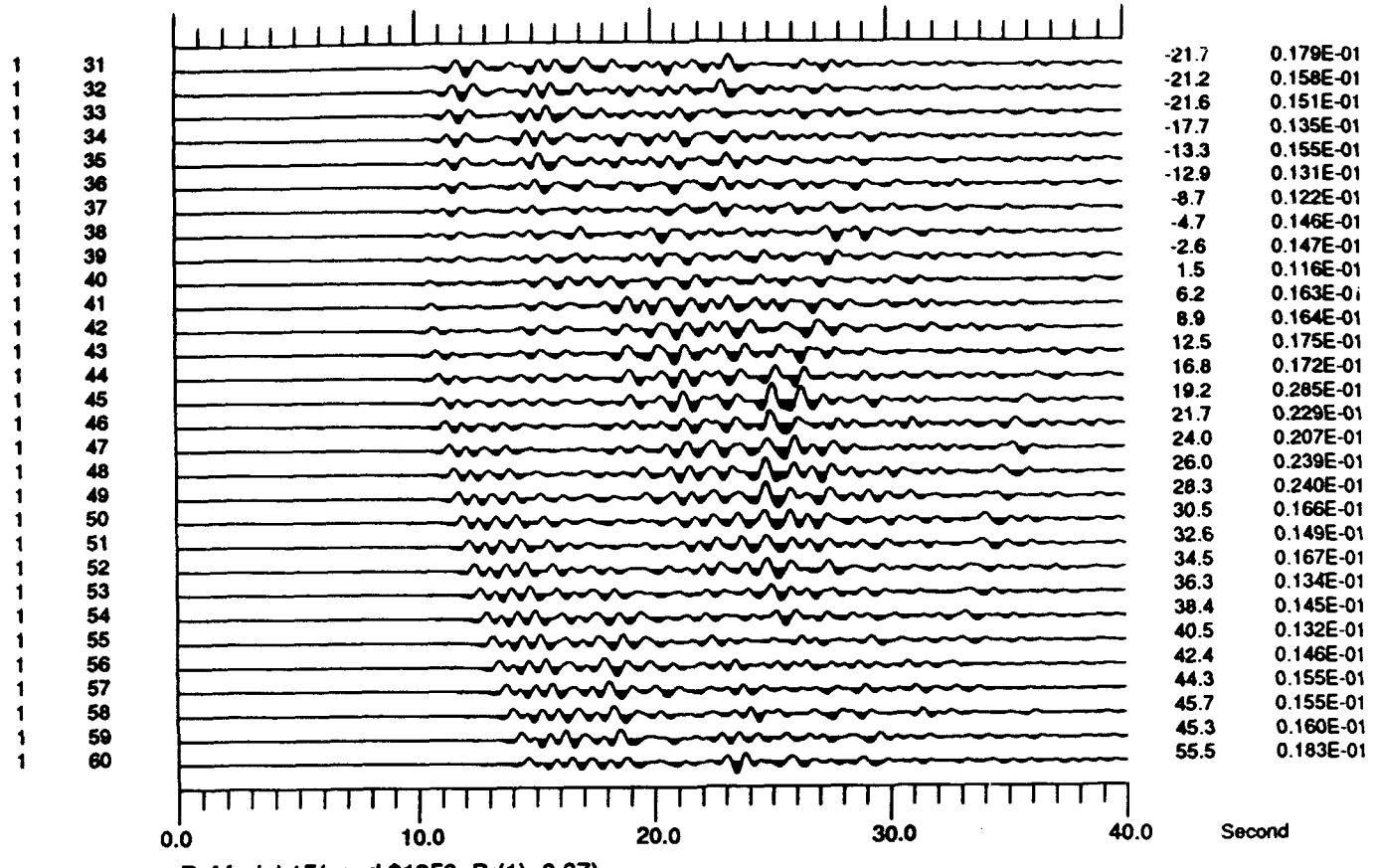
vert, same scale, decimated by 5




S, Model 14(seed 91333, Pr(1)=0.07)

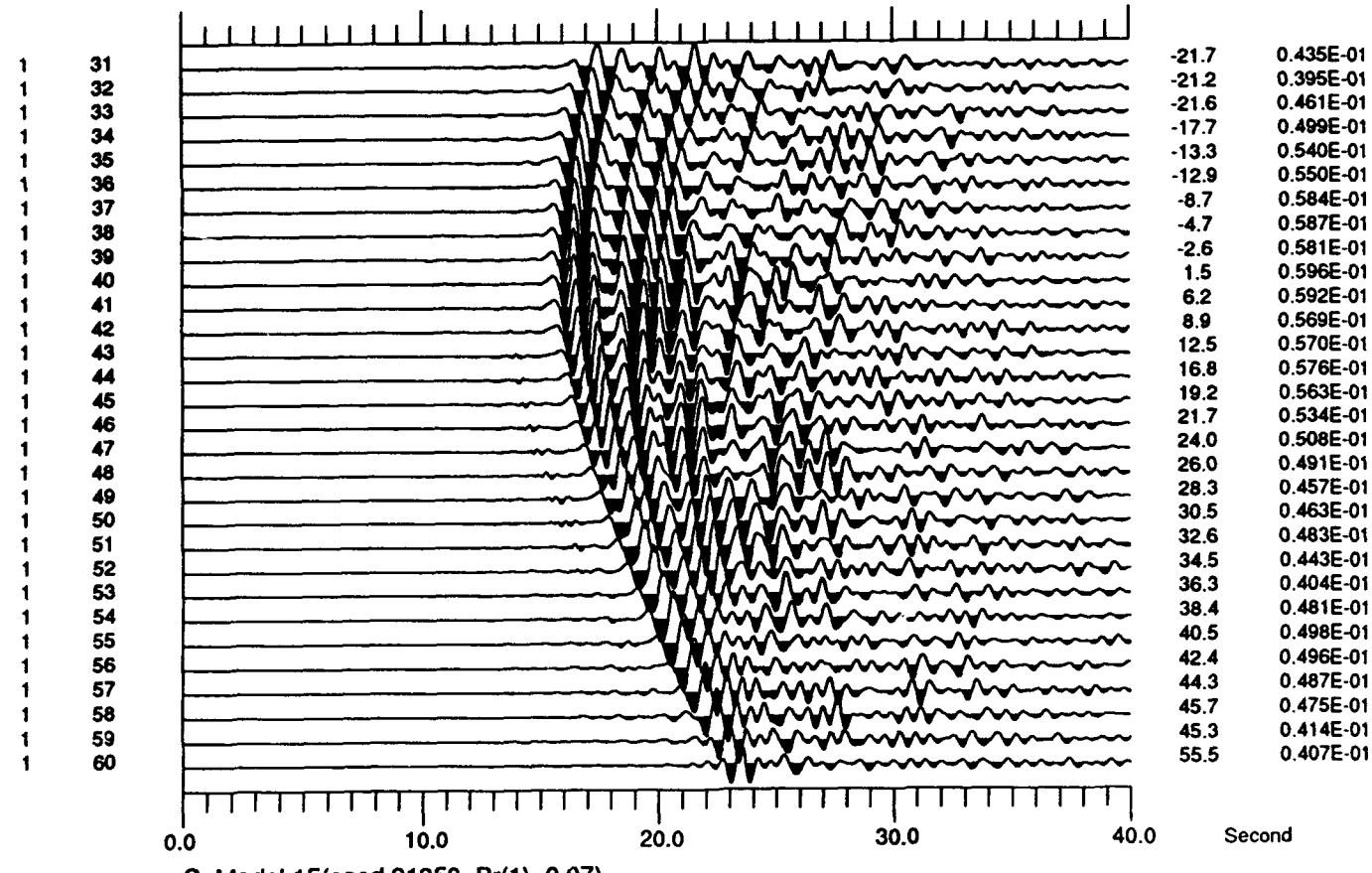
hori, same scale, decimated by 5

Figure 106




P, Model 15(seed 91350, Pr(1)=0.07)

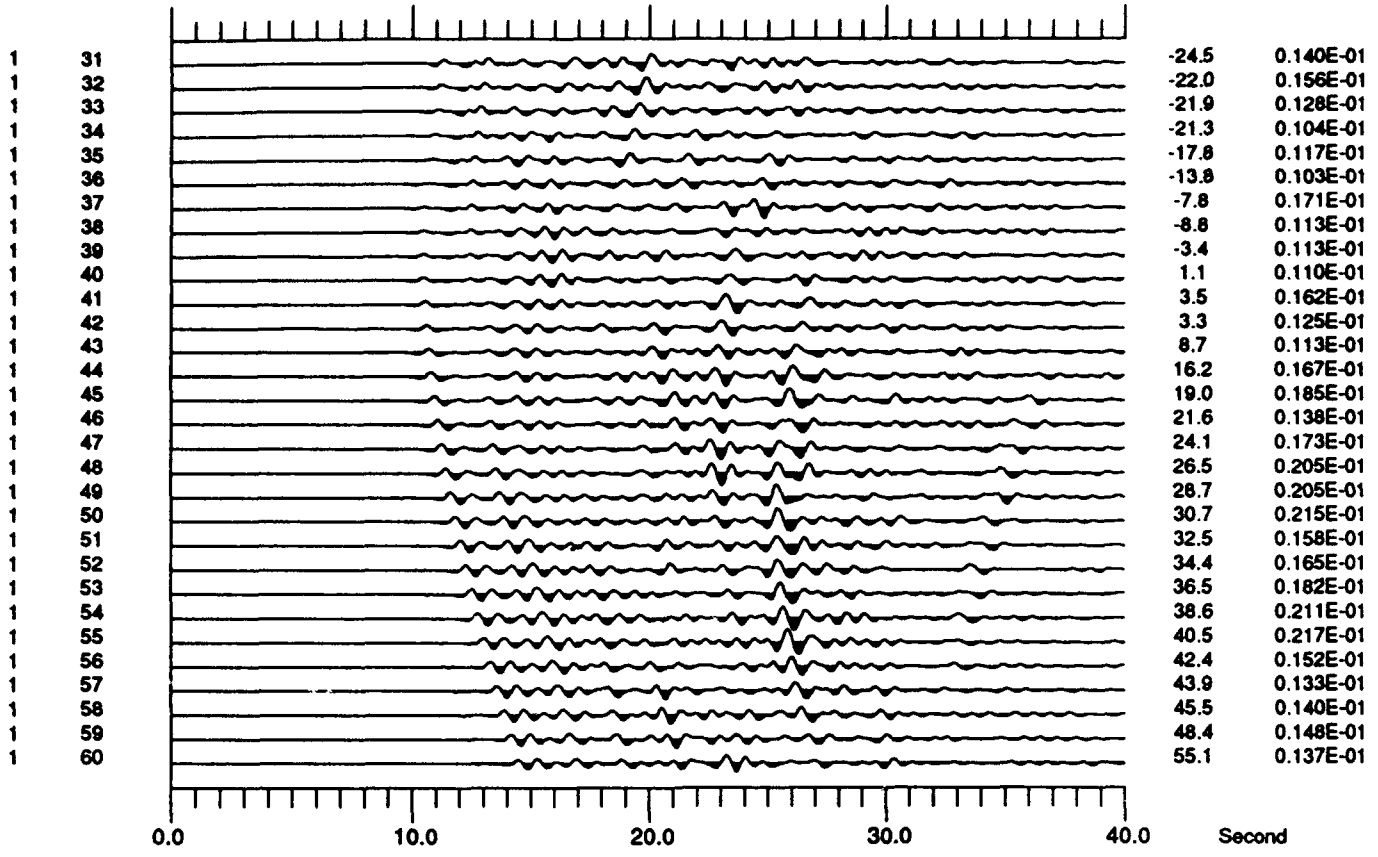
vert, same scale, decimated by 5




S, Model 15(seed 91350, Pr(1)=0.07)

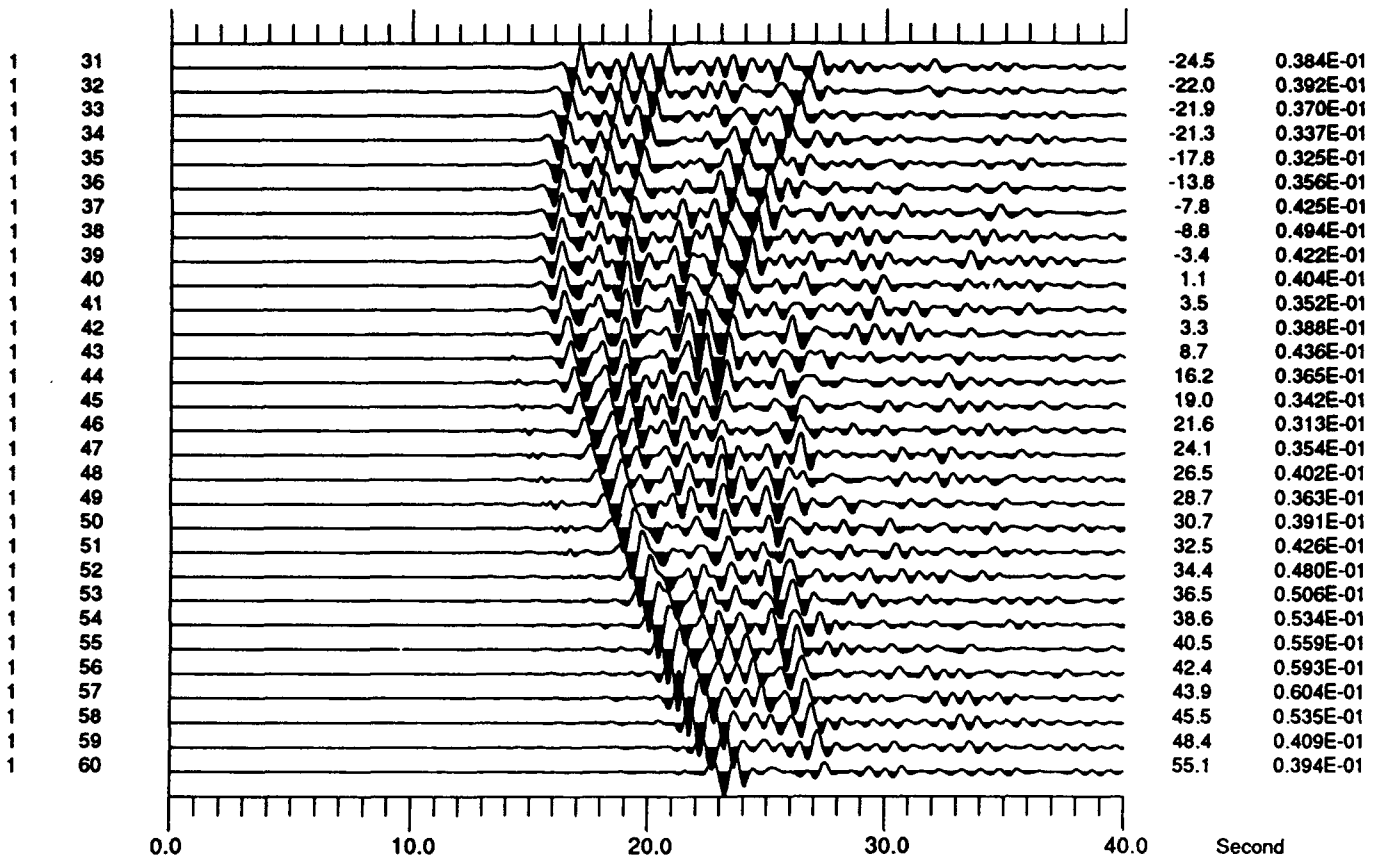
hori, same scale, decimated by 5

**Figure 107**




P, Model 16(seed 91285, Pr(1)=0.07)

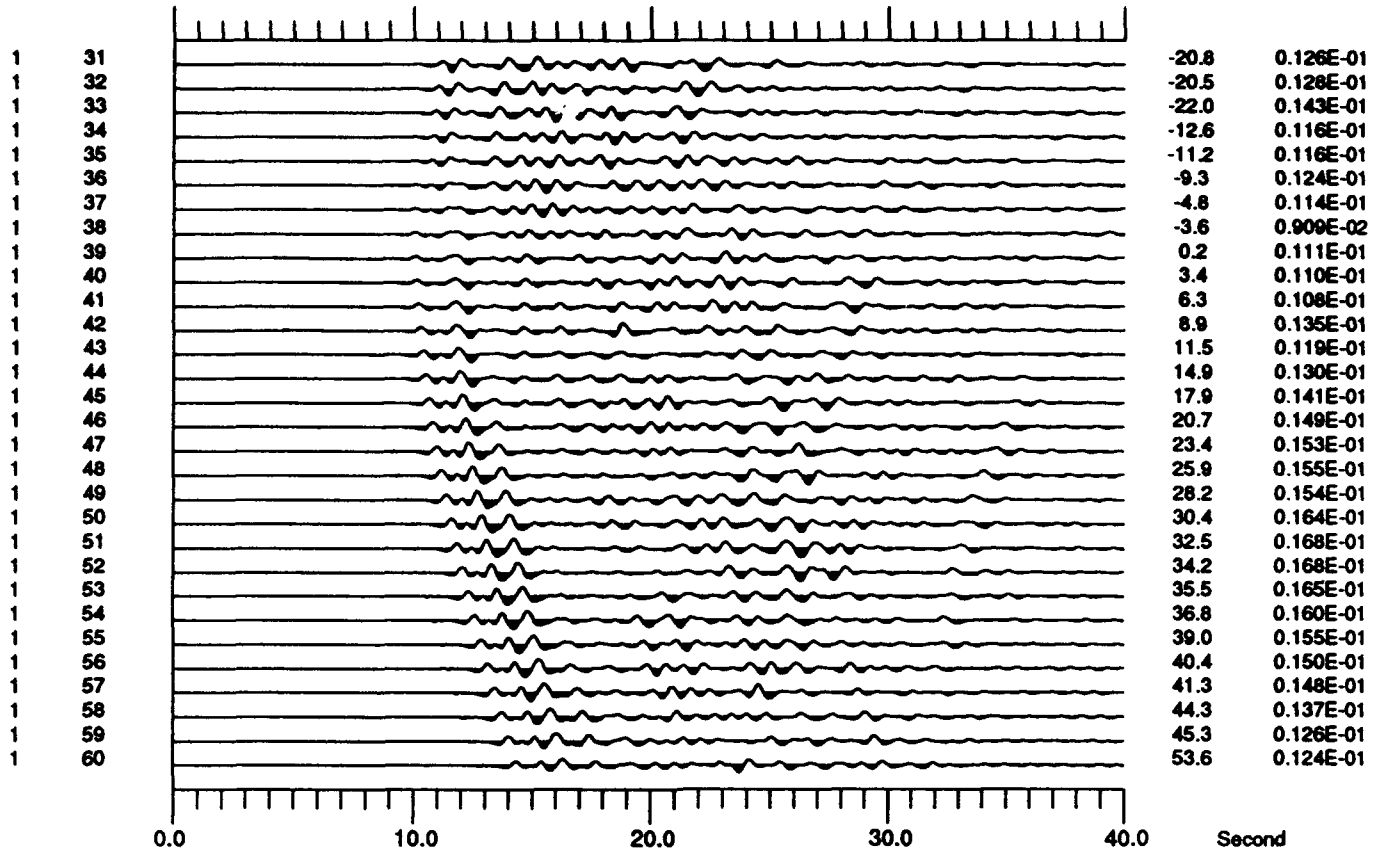
vert, same scale, decimated by 5




S, Model 16(seed 91285, Pr(1)=0.07)

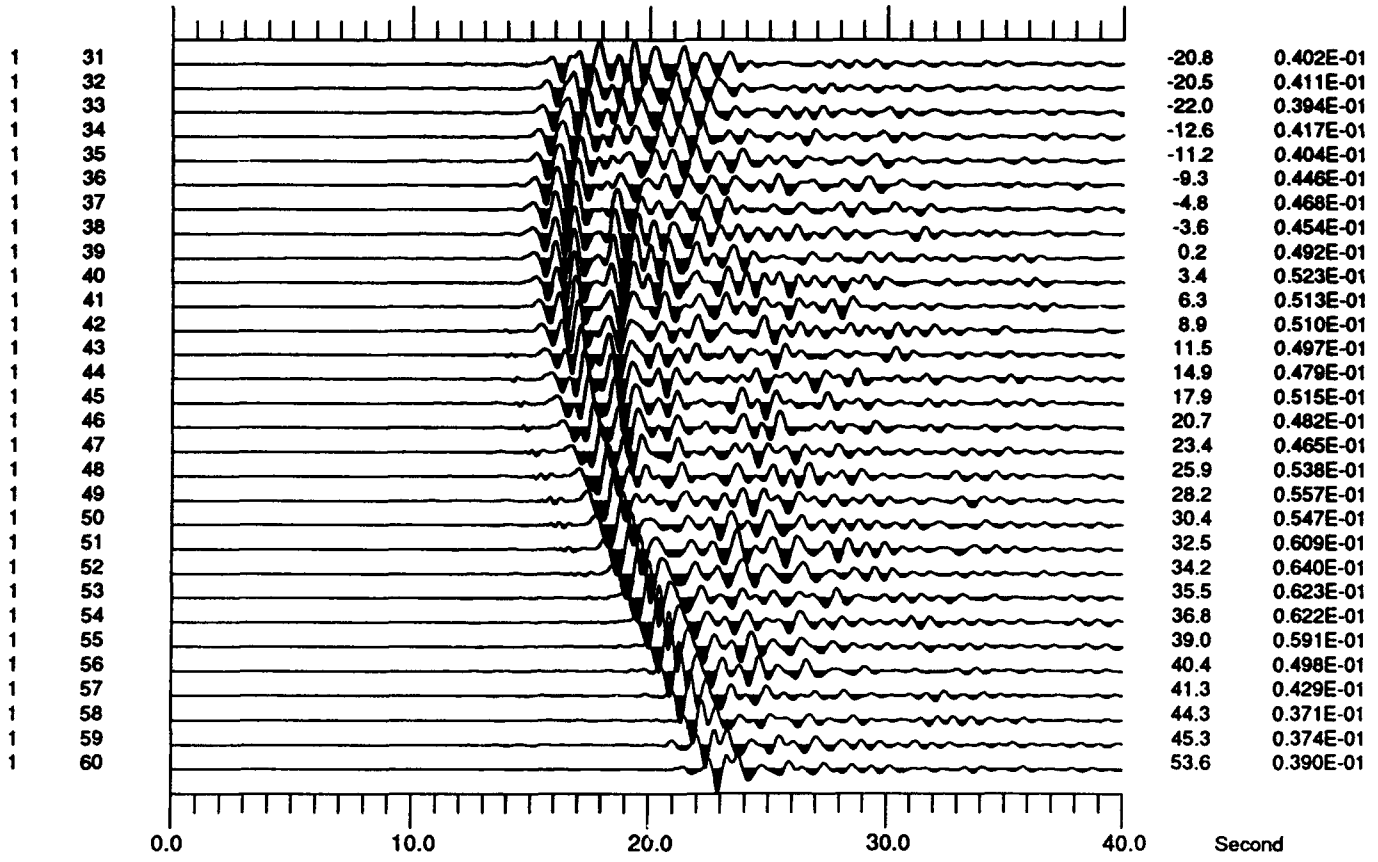
hori, same scale, decimated by 5

**Figure 108**




P, Model 21(seed 93337, Pr(1)=0.10)

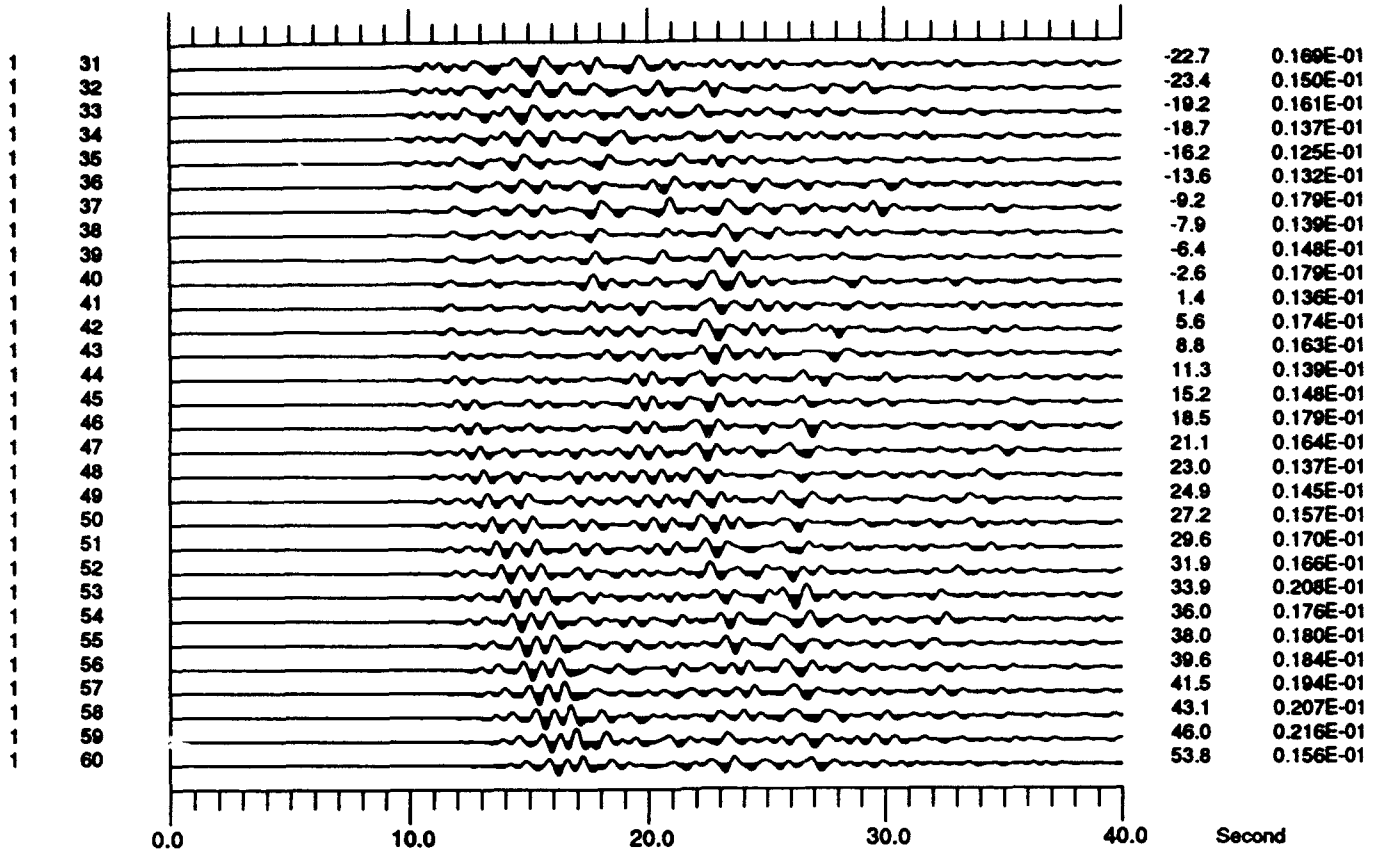
vert, same scale, decimated by 5




S, Model 21(seed 93337, Pr(1)=0.10)

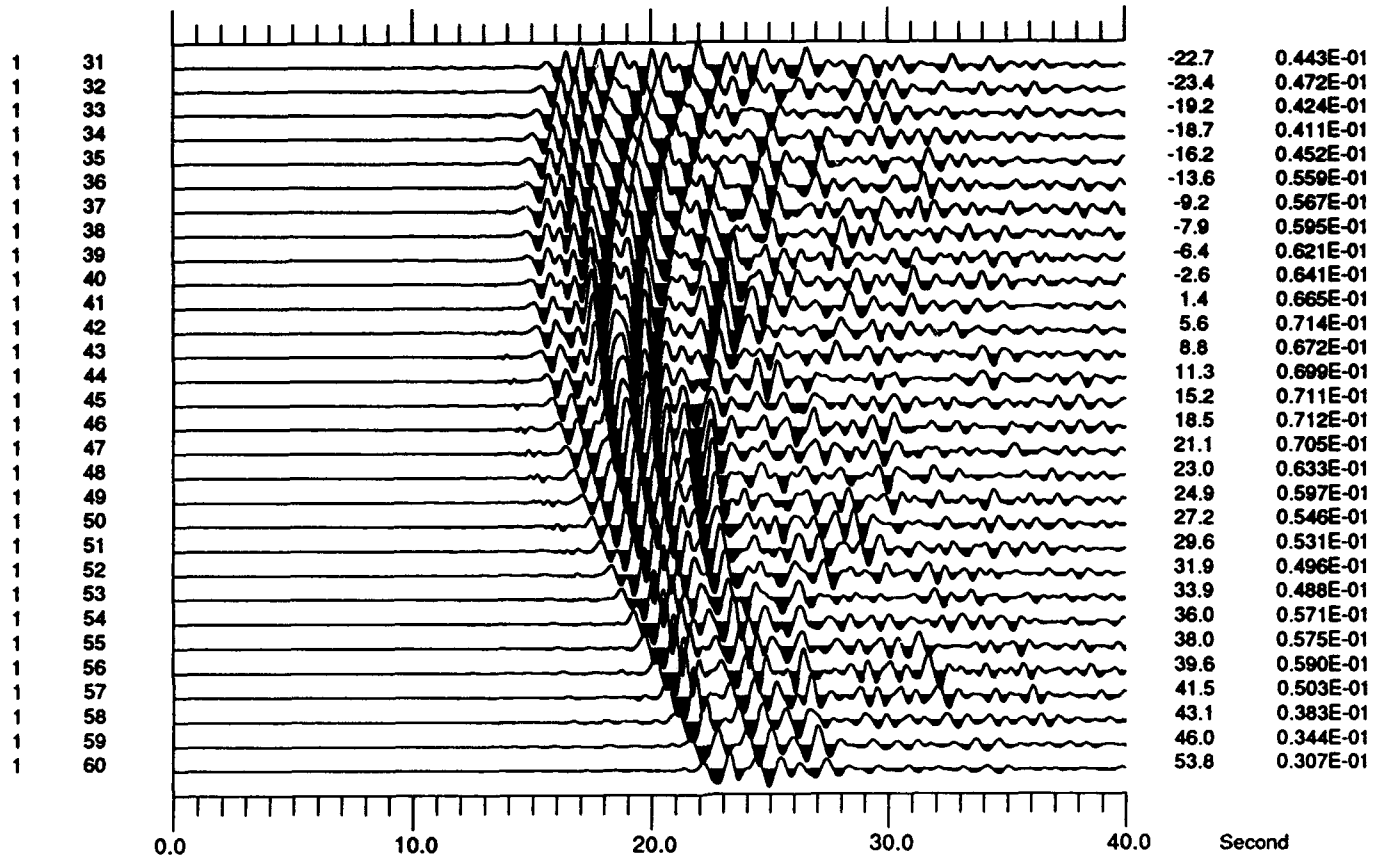
hori, same scale, decimated by 5

Figure 109




P, Model 22(seed 93347, Pr(1)=0.10)

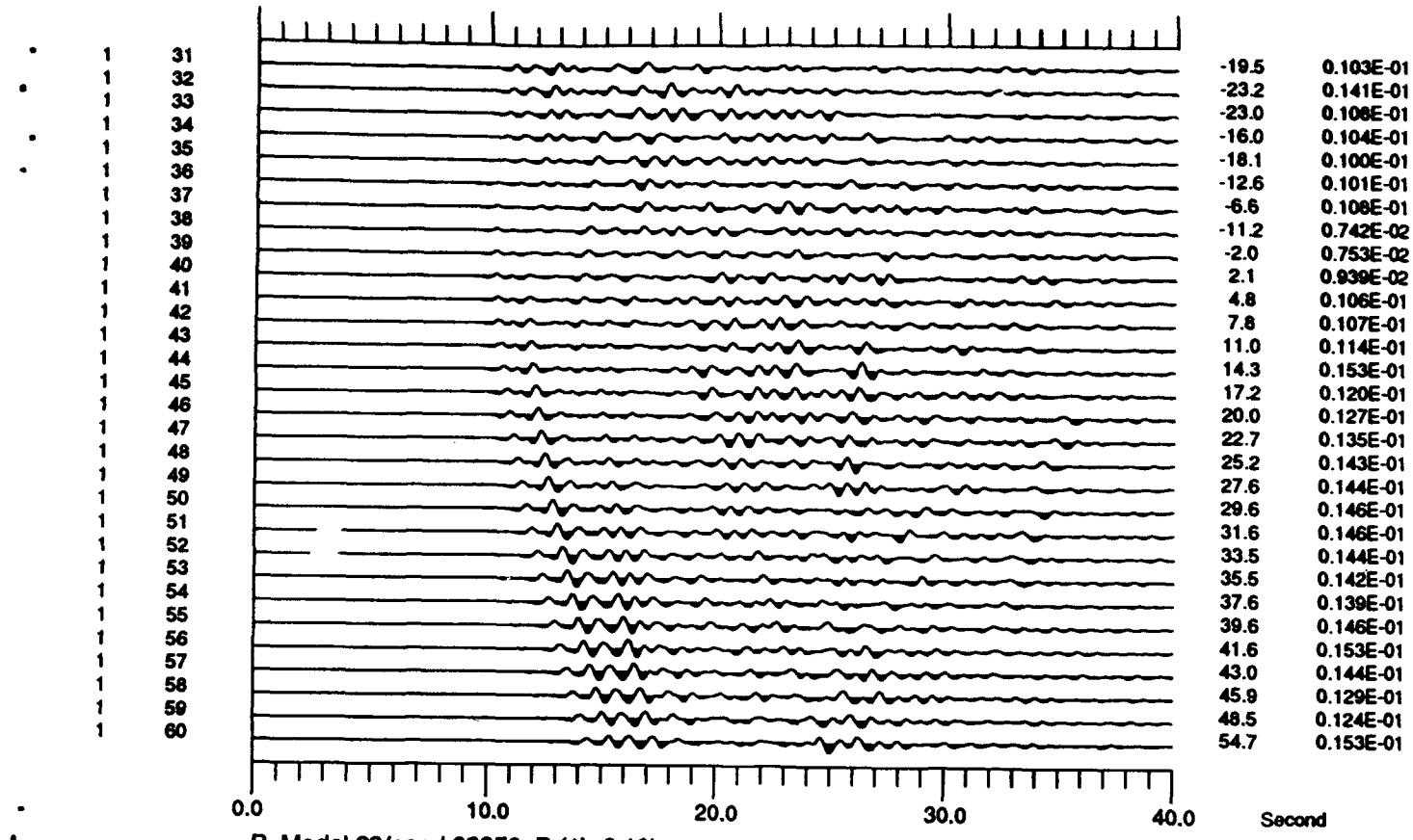
vert, same scale, decimated by 5




S, Model 22(seed 93347, Pr(1)=0.10)

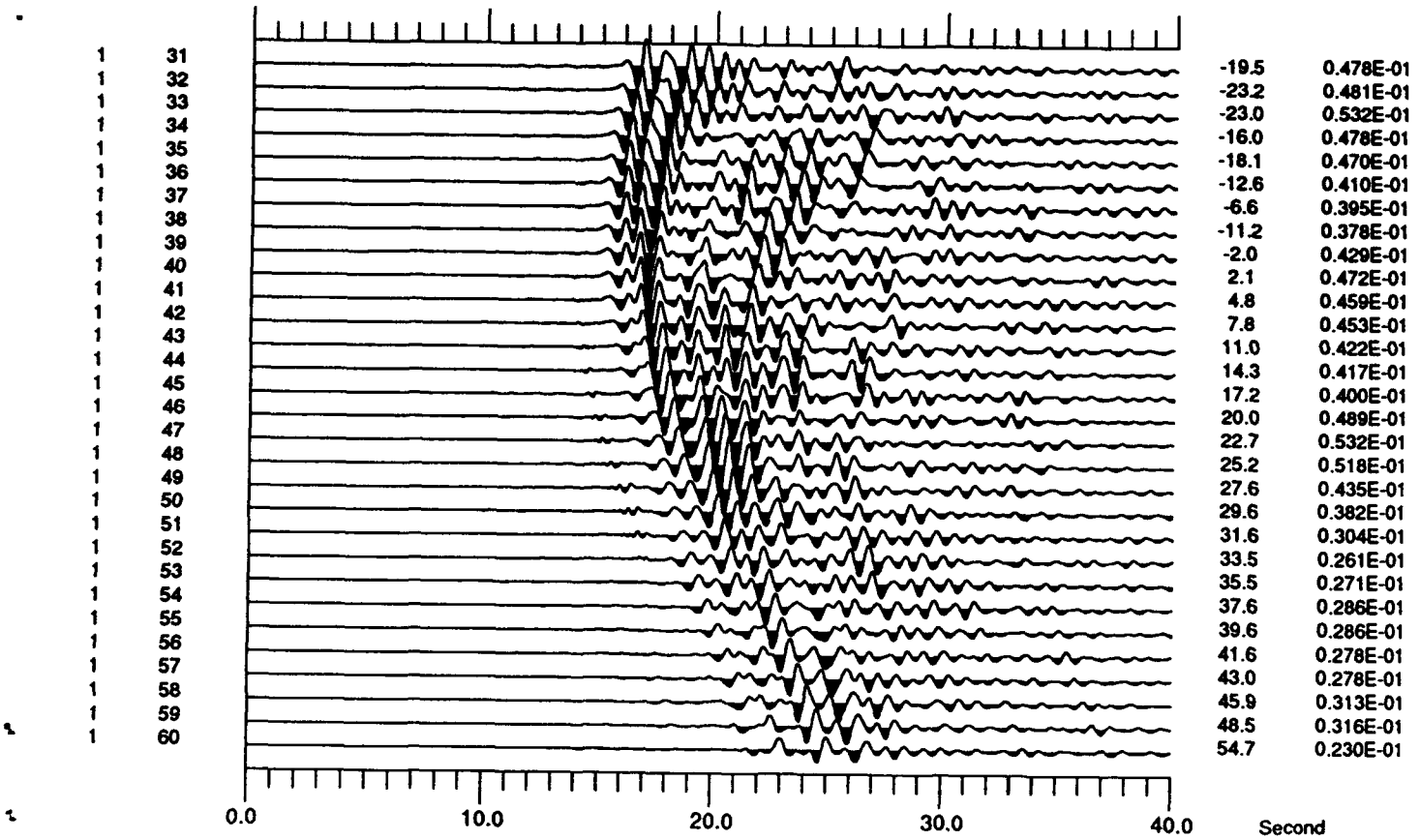
hori, same scale, decimated by 5

**Figure 110**




P, Model 23(seed 93356, Pr(1)=0.10)

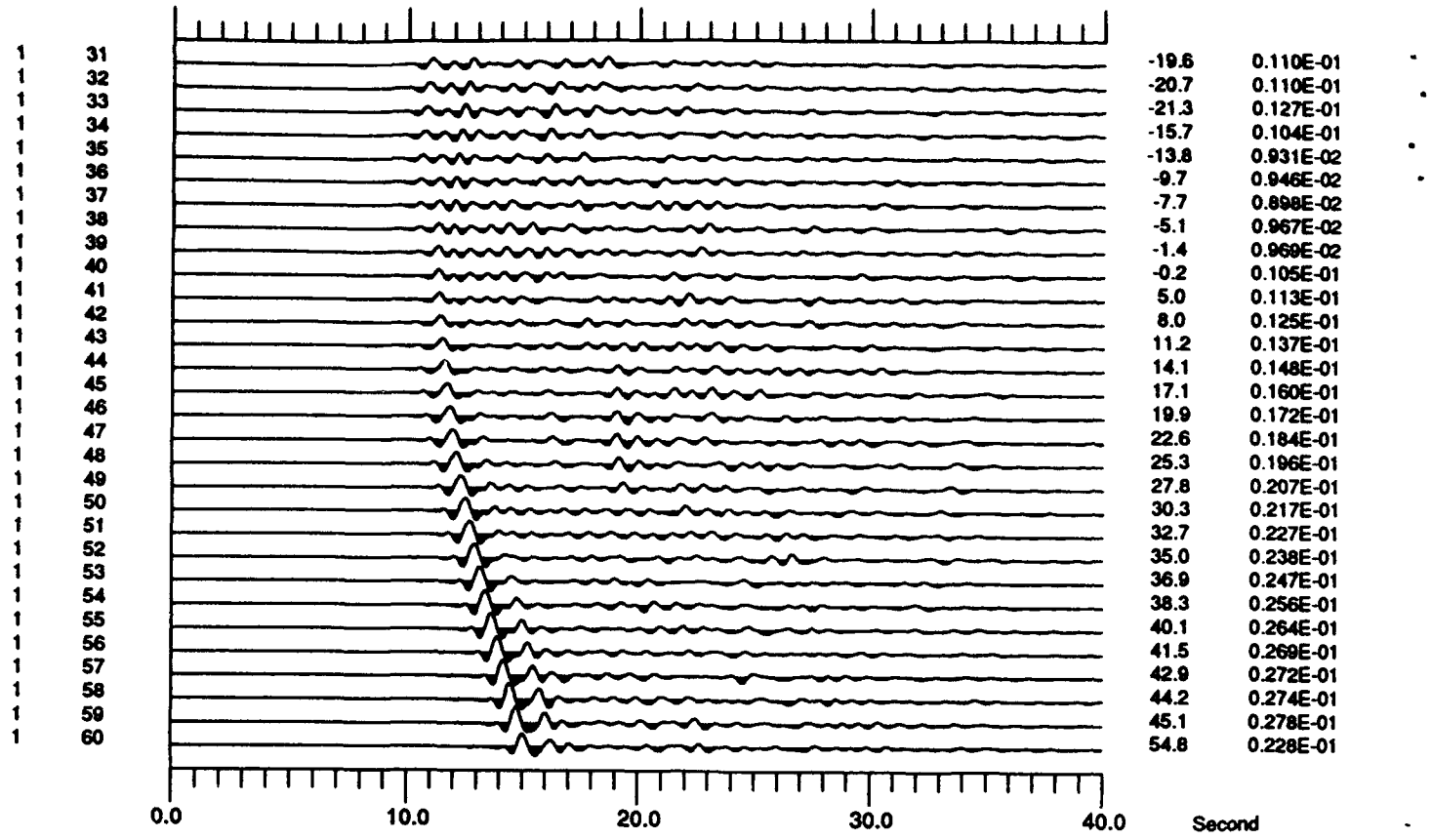
vert, same scale, decimated by 5




S, Model 23(seed 93356, Pr(1)=0.10)

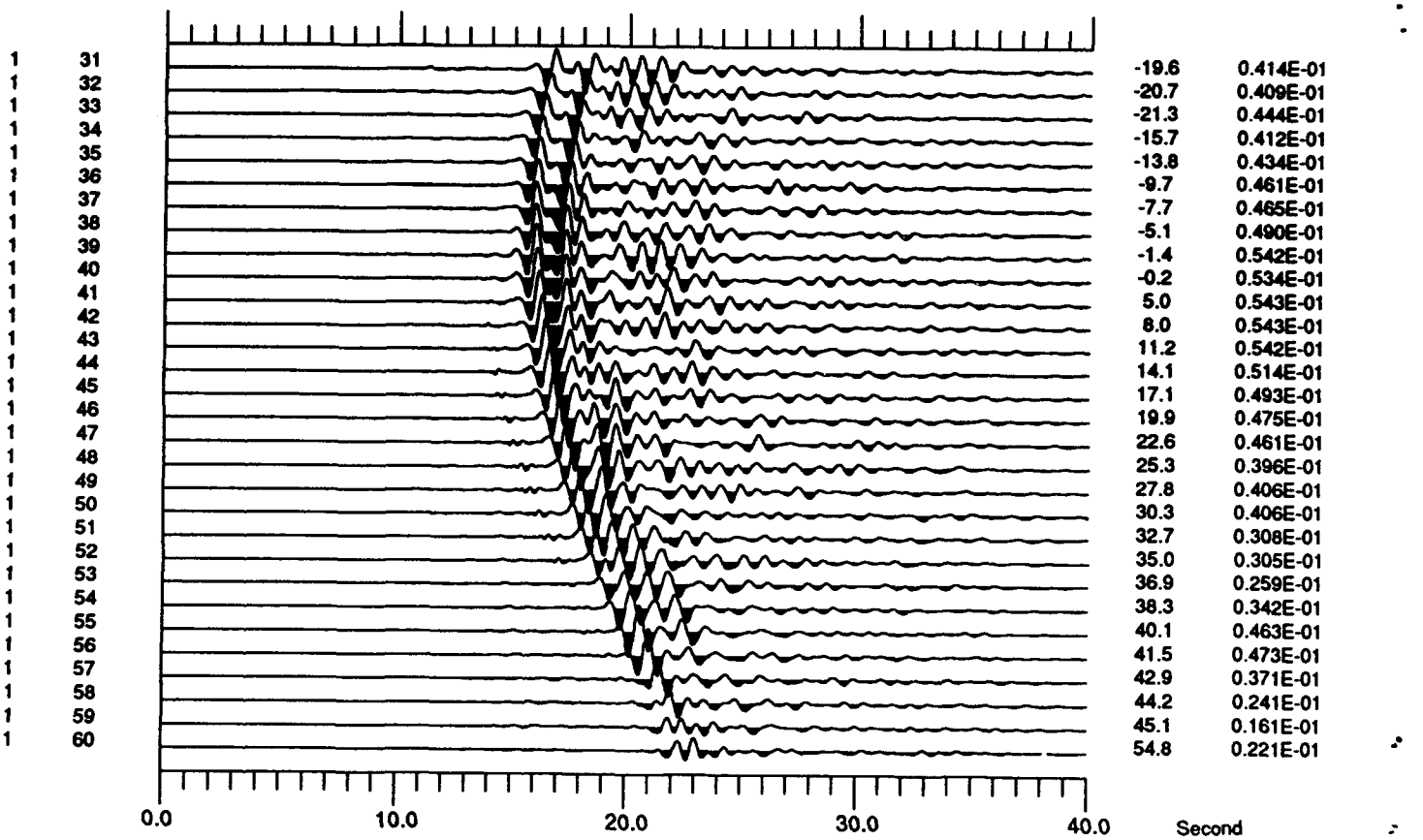
hori, same scale, decimated by 5

Figure 111




P, Model 31(seed 748546615, Pr(1)=0.15)

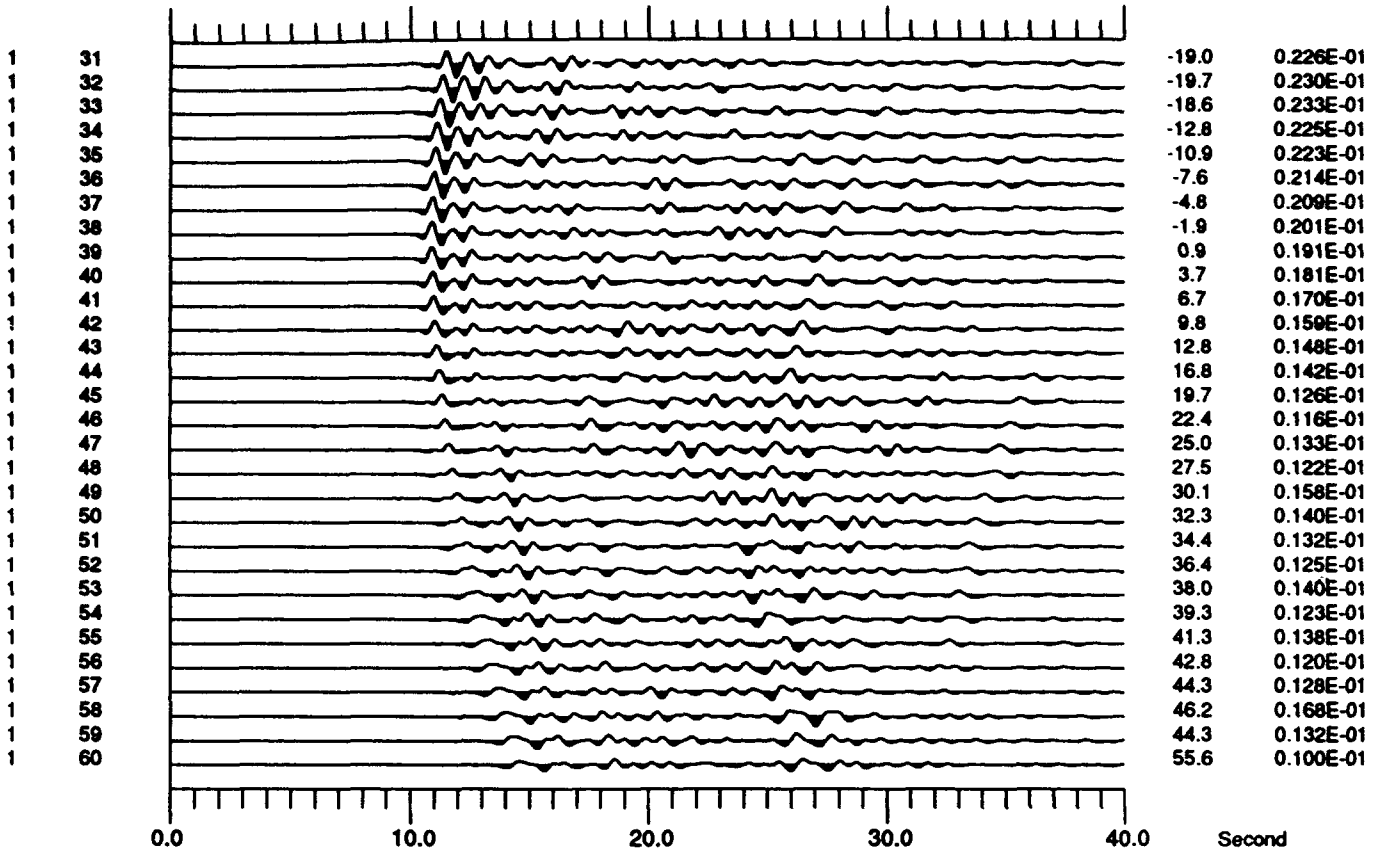
vert, same scale, decimated by 5




S, Model 31(seed 748546615, Pr(1)=0.15)

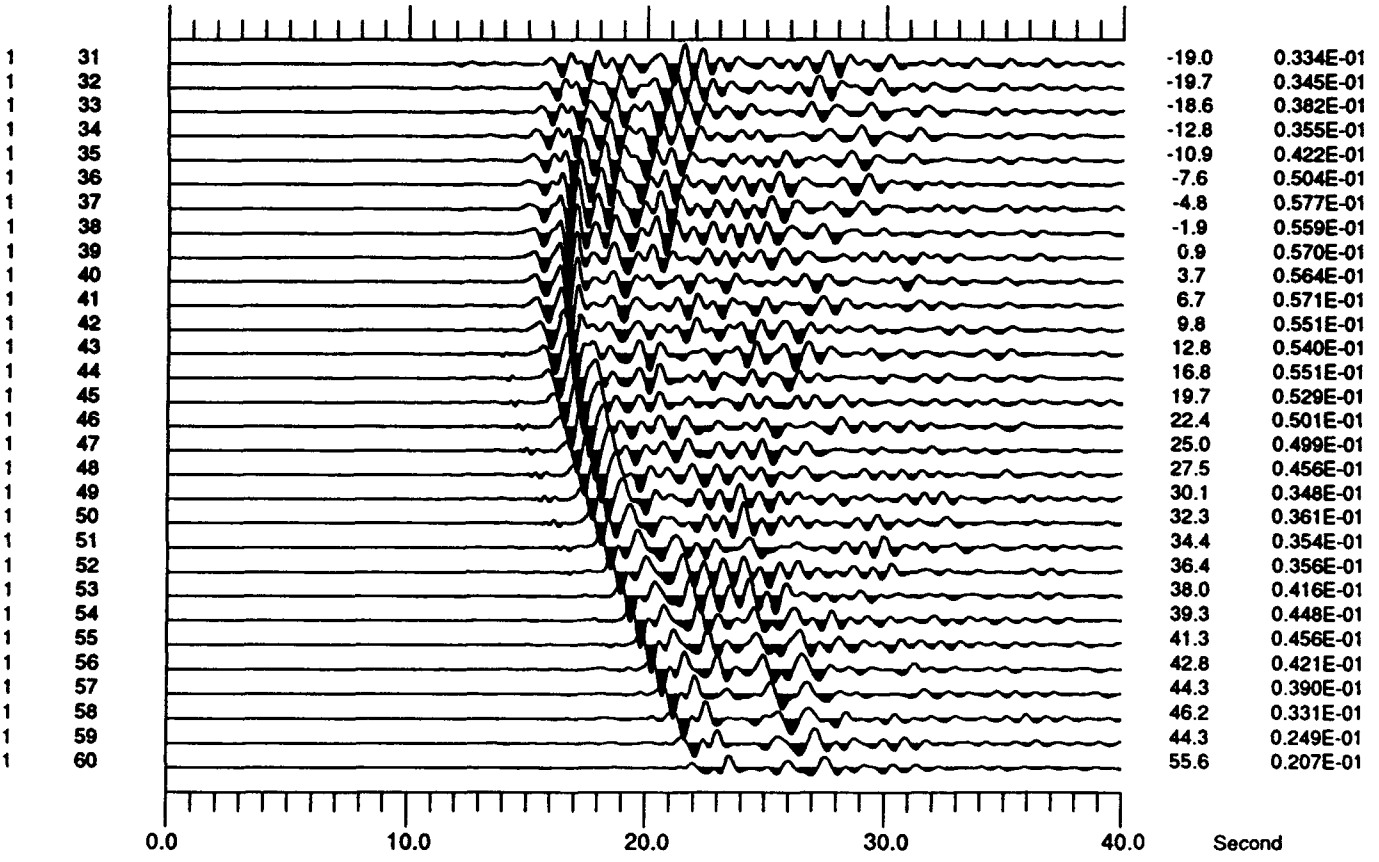
hori, same scale, decimated by 5

**Figure 112**




P, Model 32(seed 20333, Pr(1)=0.15)

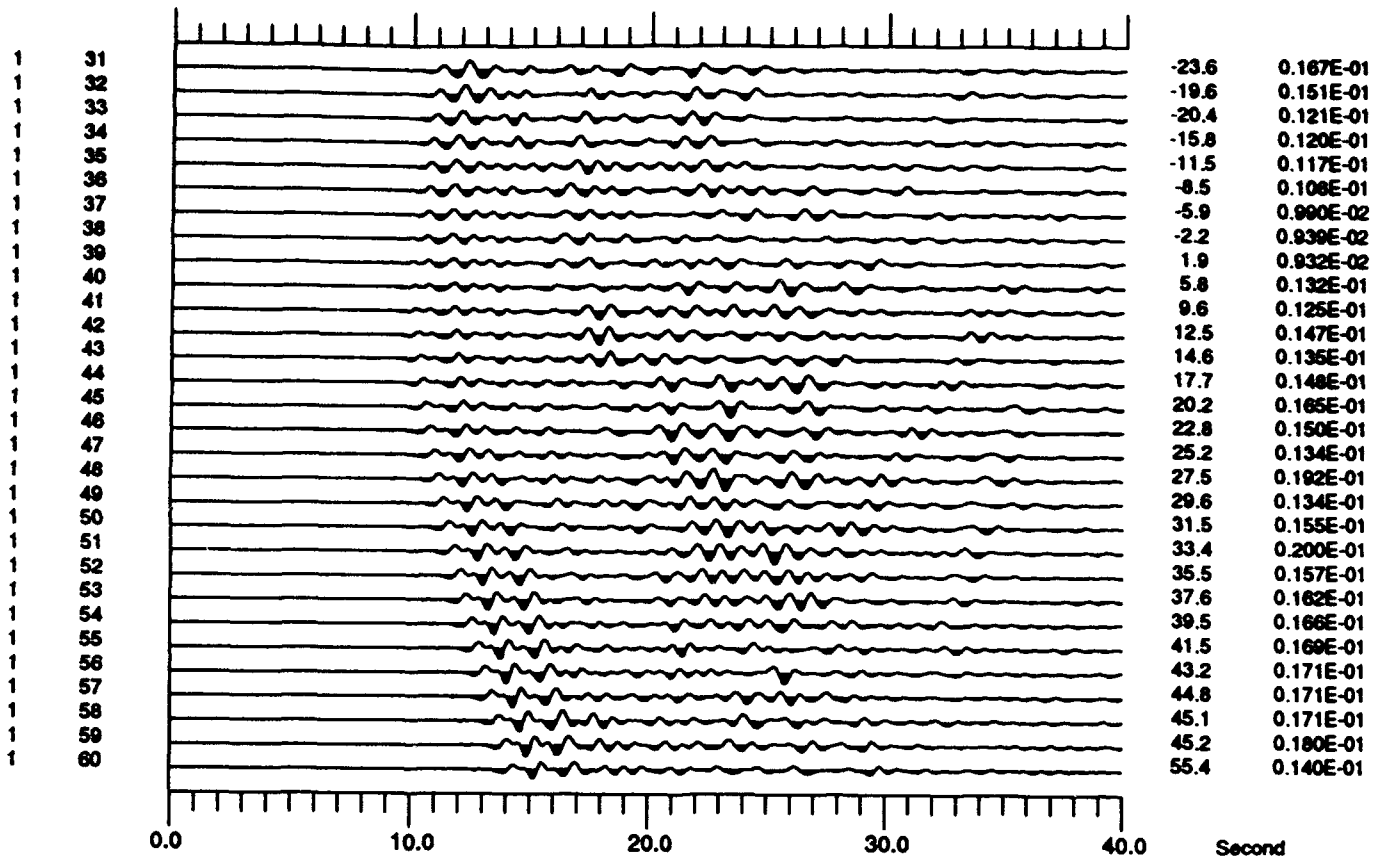
vert, same scale, decimated by 5




S, Model 32(seed 20333, Pr(1)=0.15)

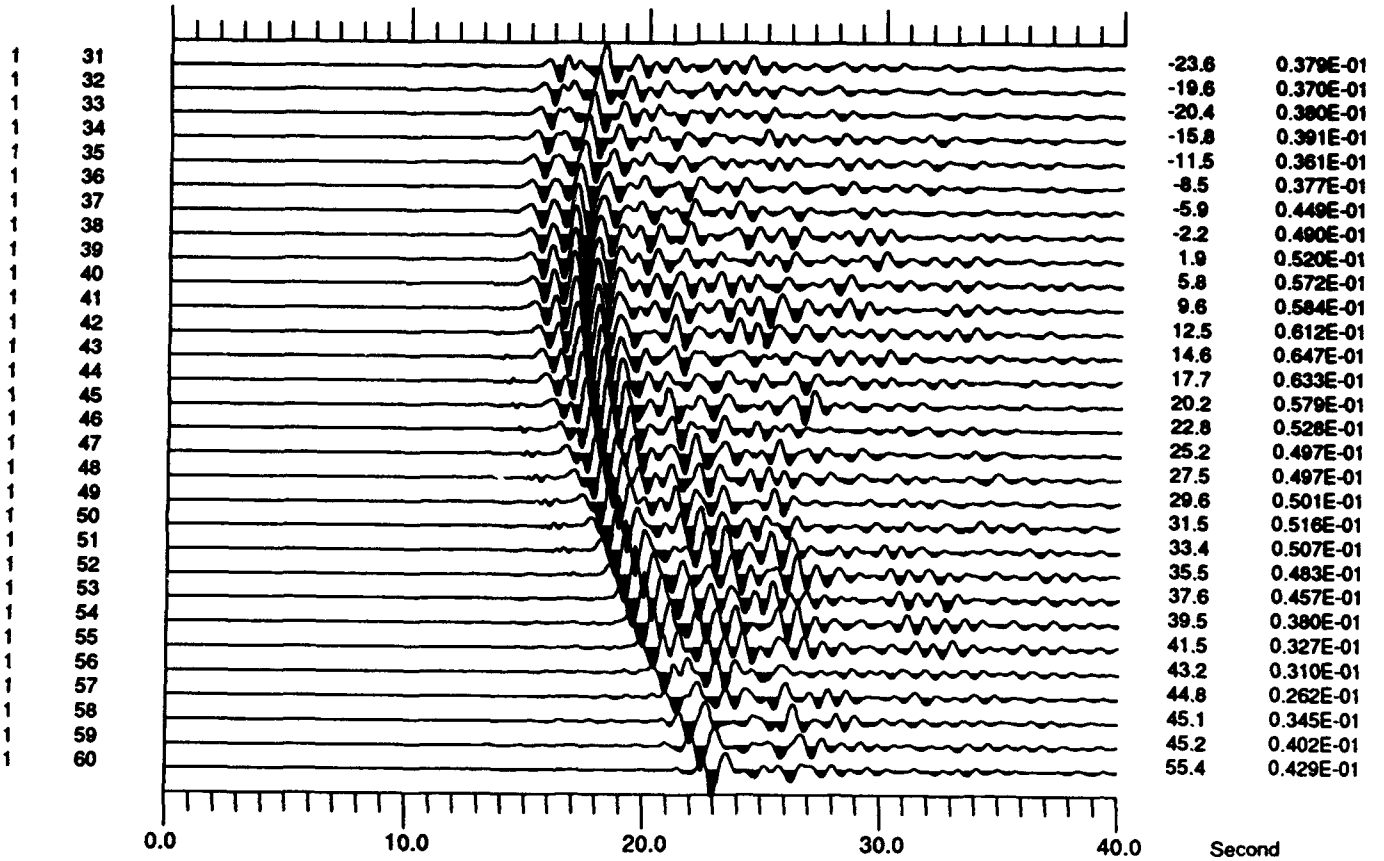
hori, same scale, decimated by 5

Figure 113




P, Model 33(seed 86016, Pr(1)=0.15)

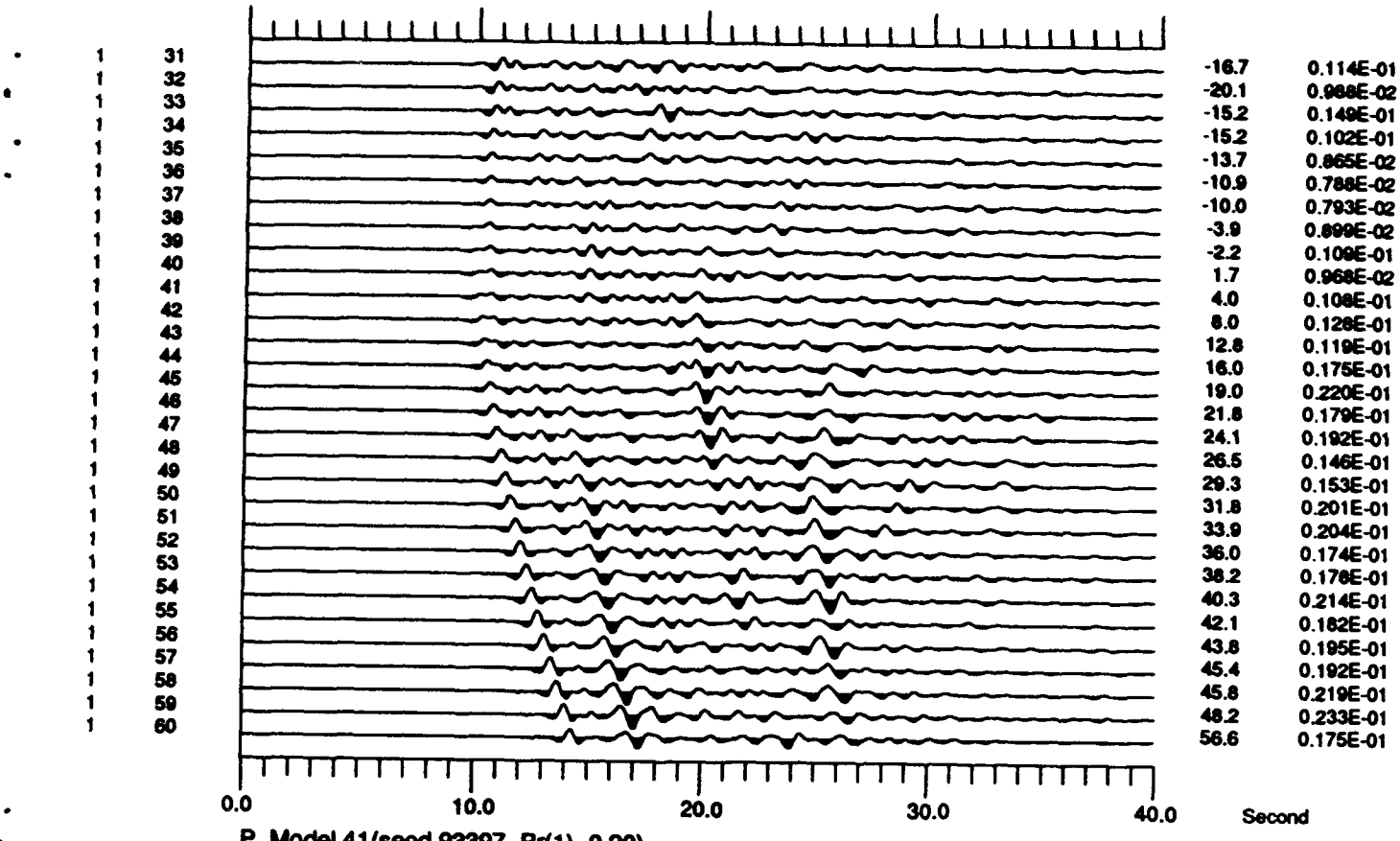
vert, same scale, decimated by 5




S, Model 33(seed 86016, Pr(1)=0.15)

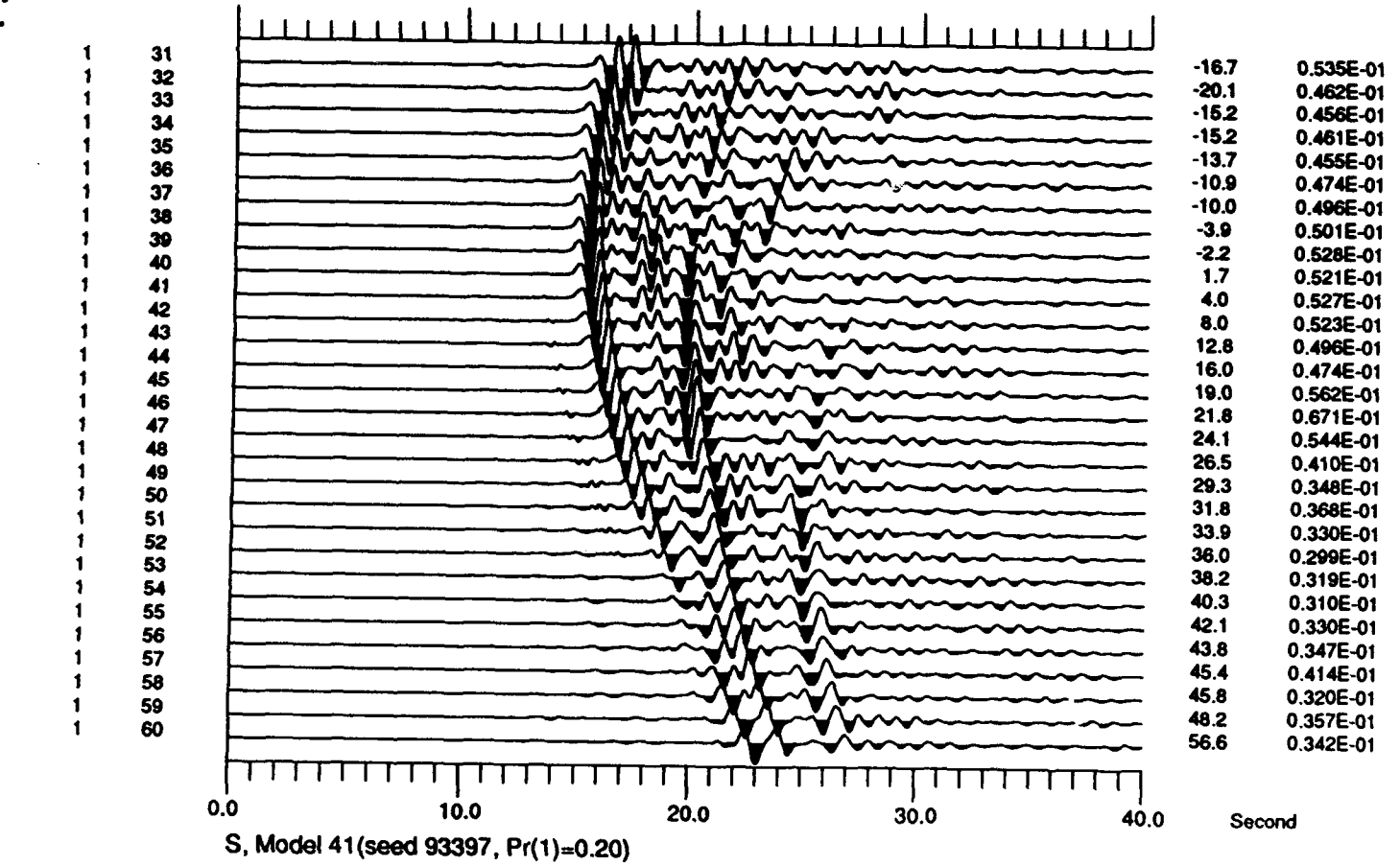
hori, same scale, decimated by 5

Figure 114




P, Model 41(seed 93397, Pr(1)=0.20)

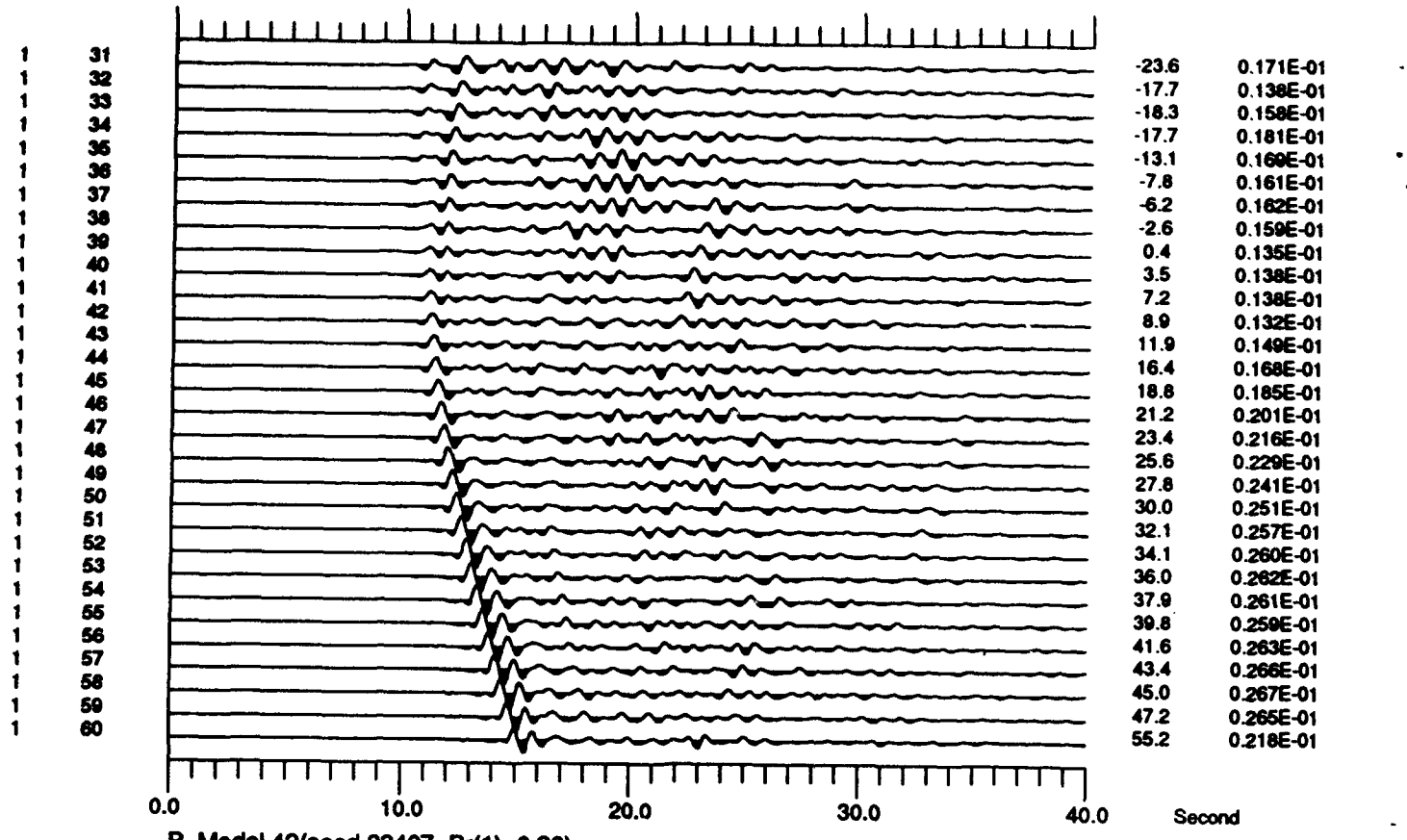
vert, same scale, decimated by 5




S, Model 41(seed 93397, Pr(1)=0.20)

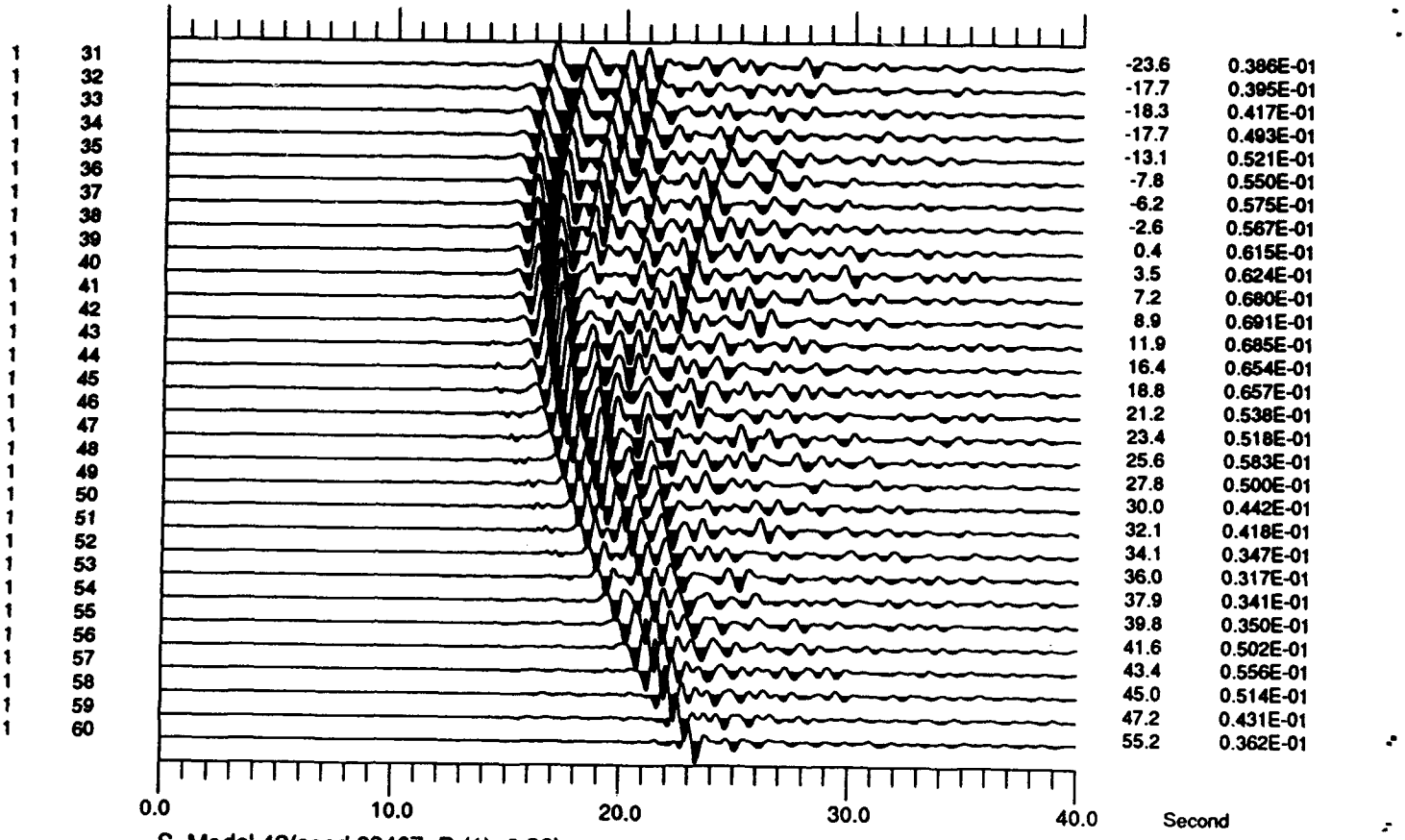
hori, same scale, decimated by 5

**Figure 115**




P, Model 42(seed 93407, Pr(1)=0.20)

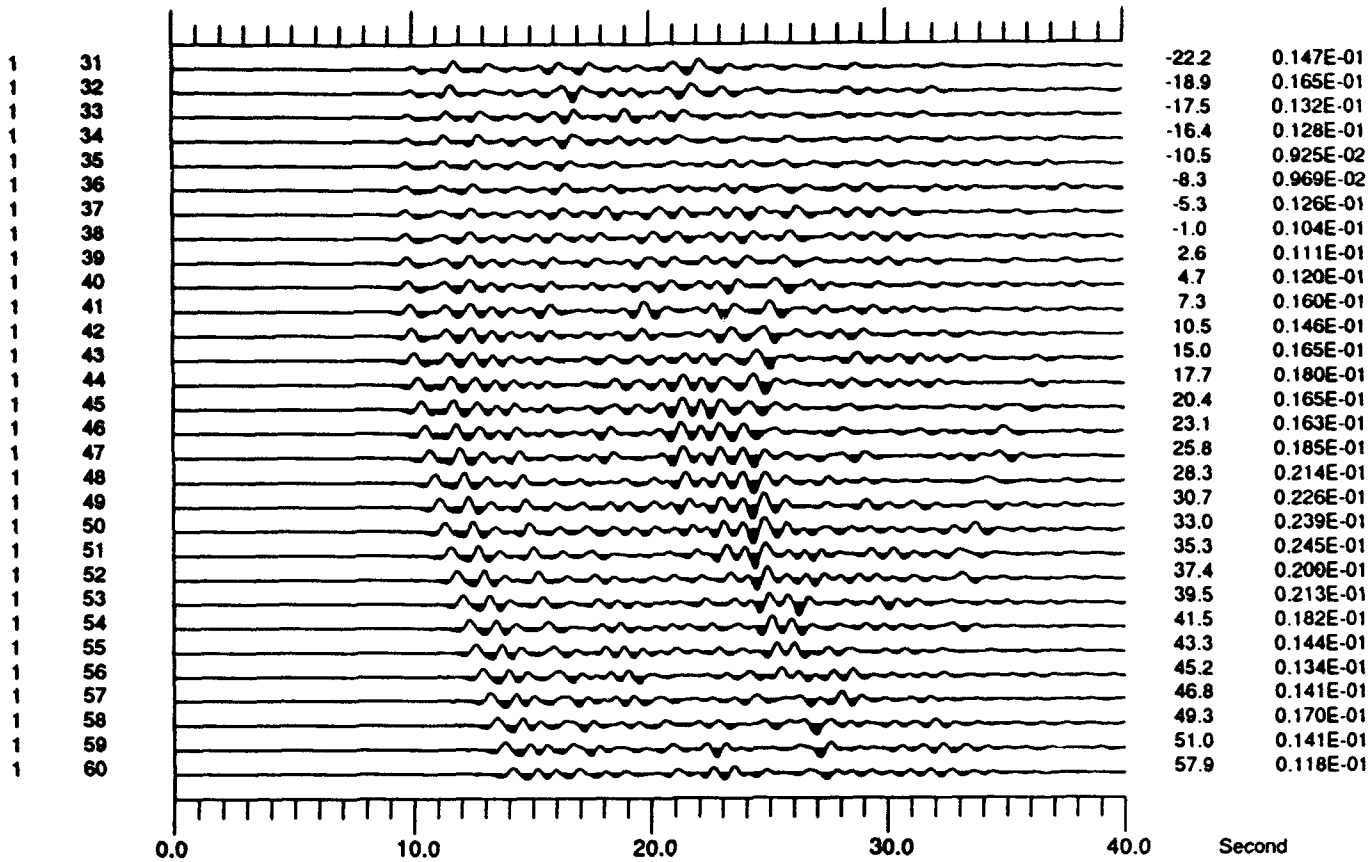
vert, same scale, decimated by 5




S, Model 42(seed 93407, Pr(1)=0.20)

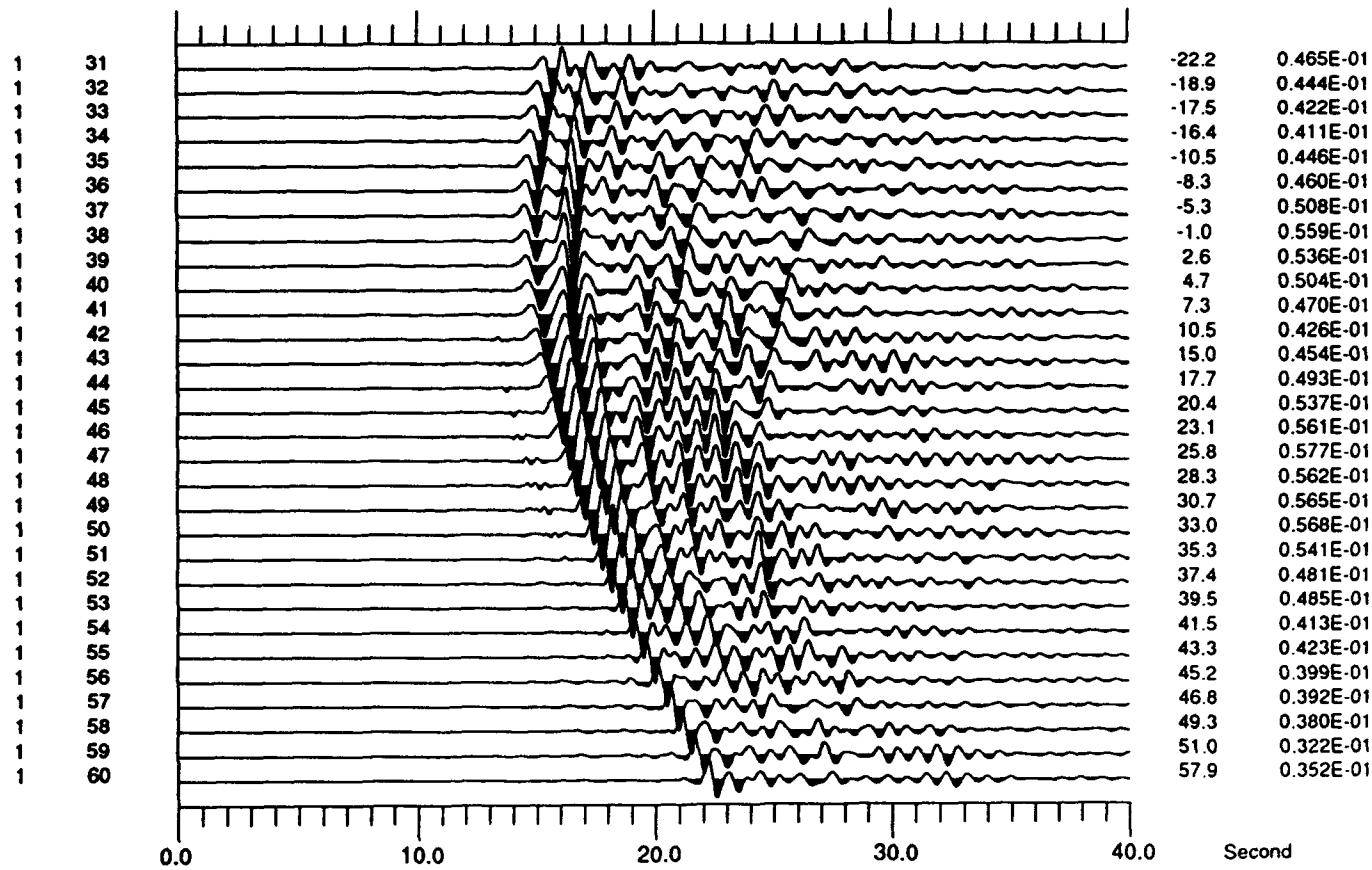
hori, same scale, decimated by 5

Figure 116




P, Model 43(seed 12345, Pr(1)=0.20)

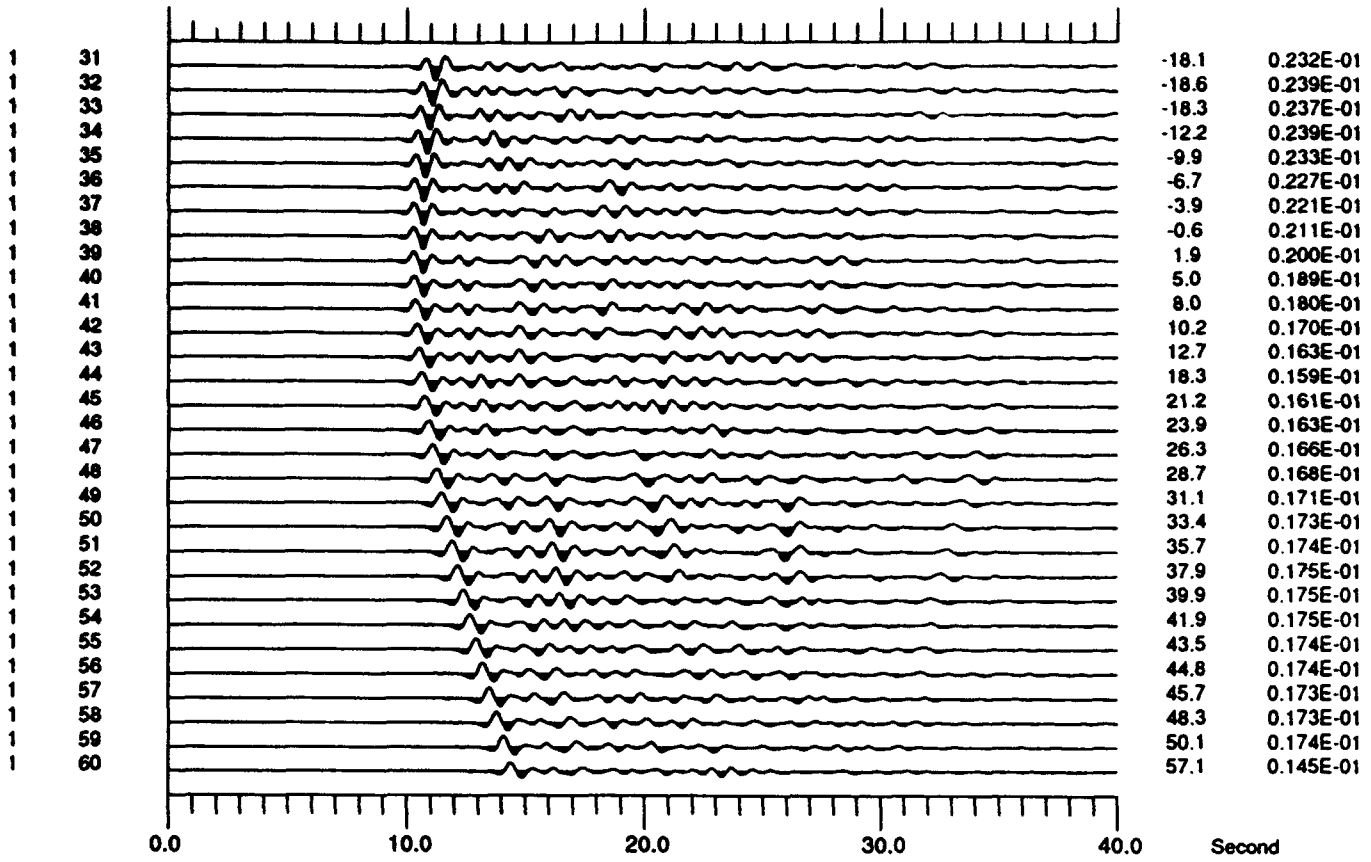
vert, same scale, decimated by 5




S, Model 43(seed 12345, Pr(1)=0.20)

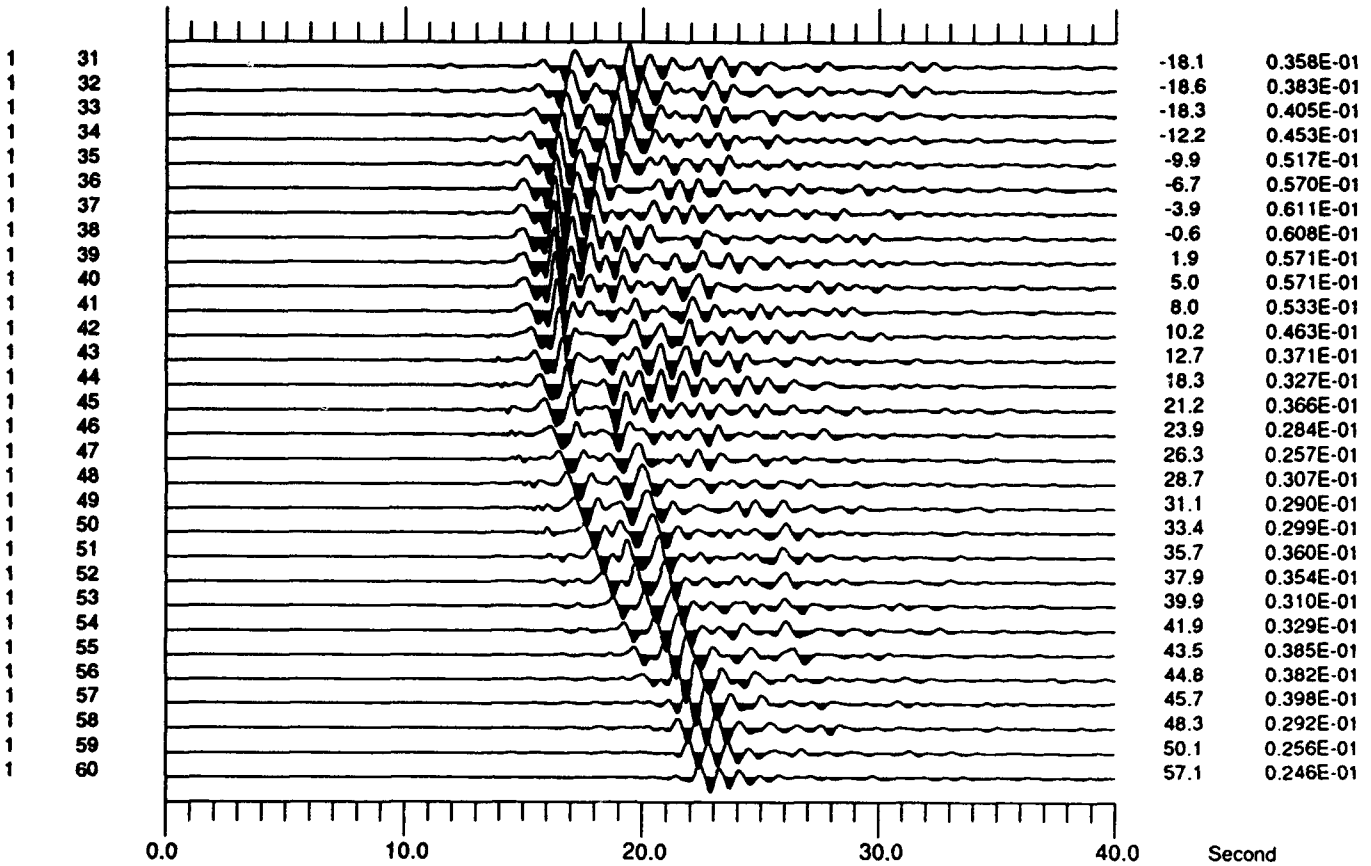
hori, same scale, decimated by 5

Figure 117




P, Model 51(seed 21691, Pr(1)=0.25)

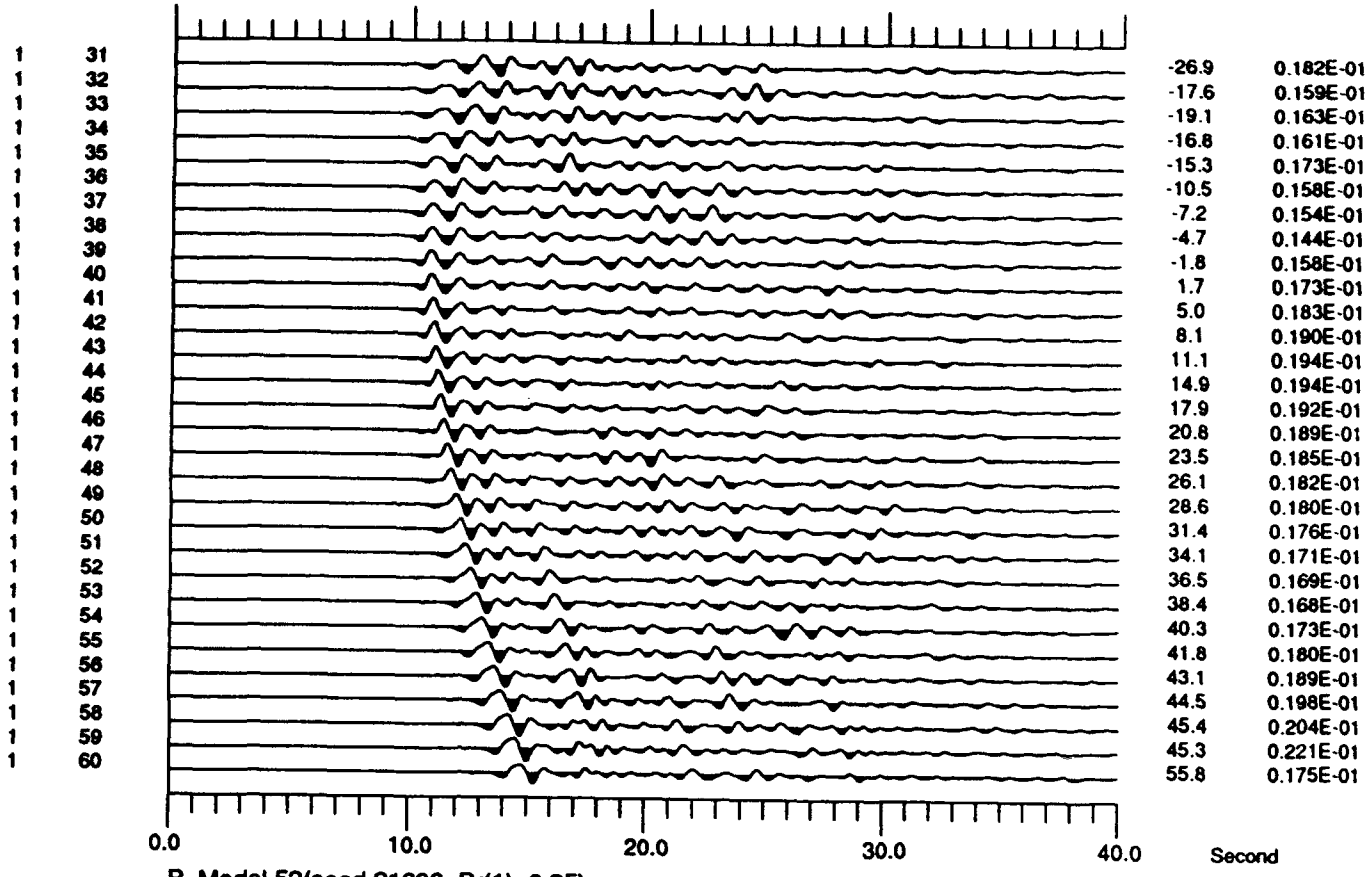
vert, same scale, decimated by 5




S, Model 51(seed 21691, Pr(1)=0.25)

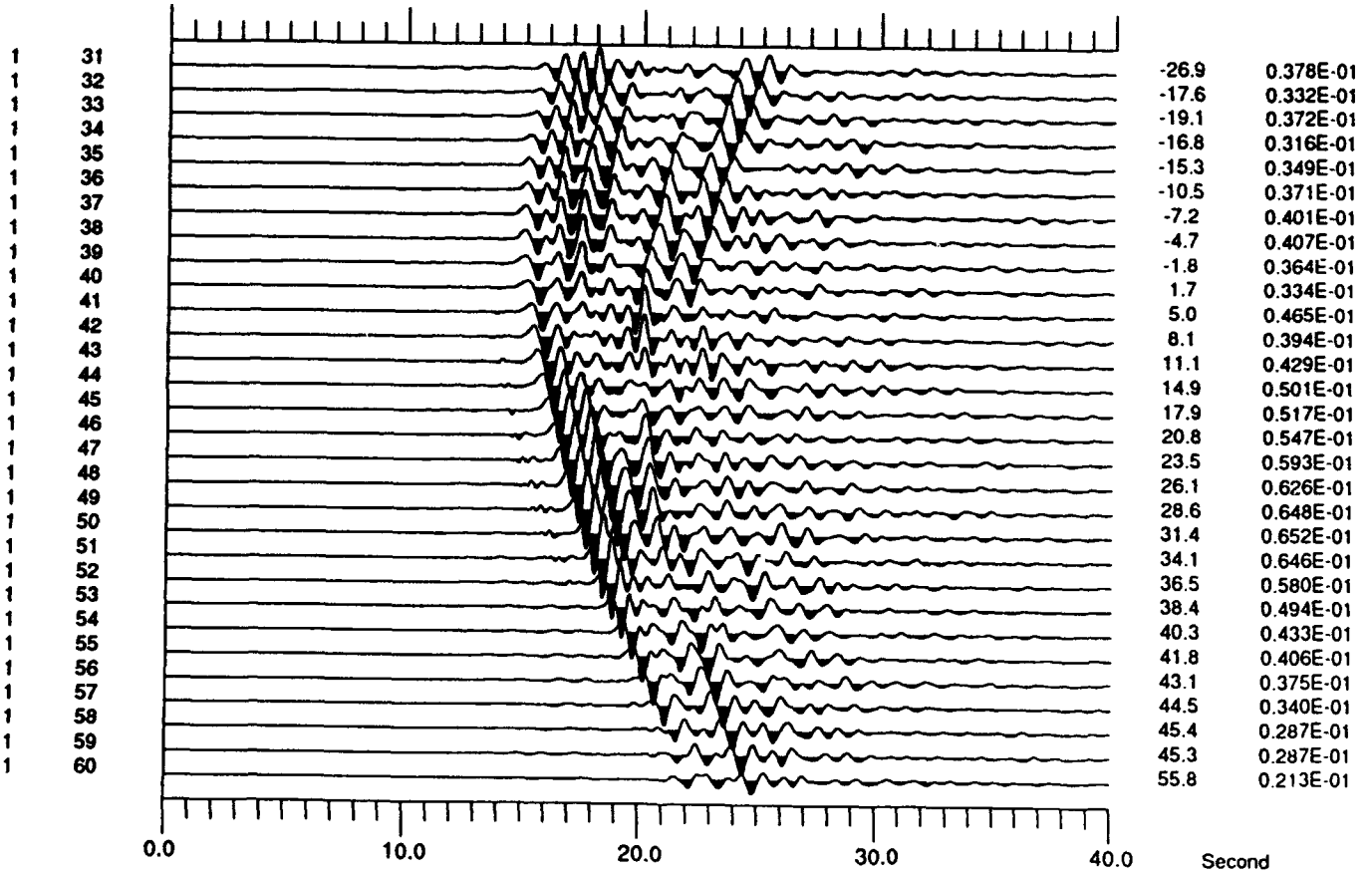
hori, same scale, decimated by 5

Figure 118




P, Model 52(seed 21696, Pr(1)=0.25)

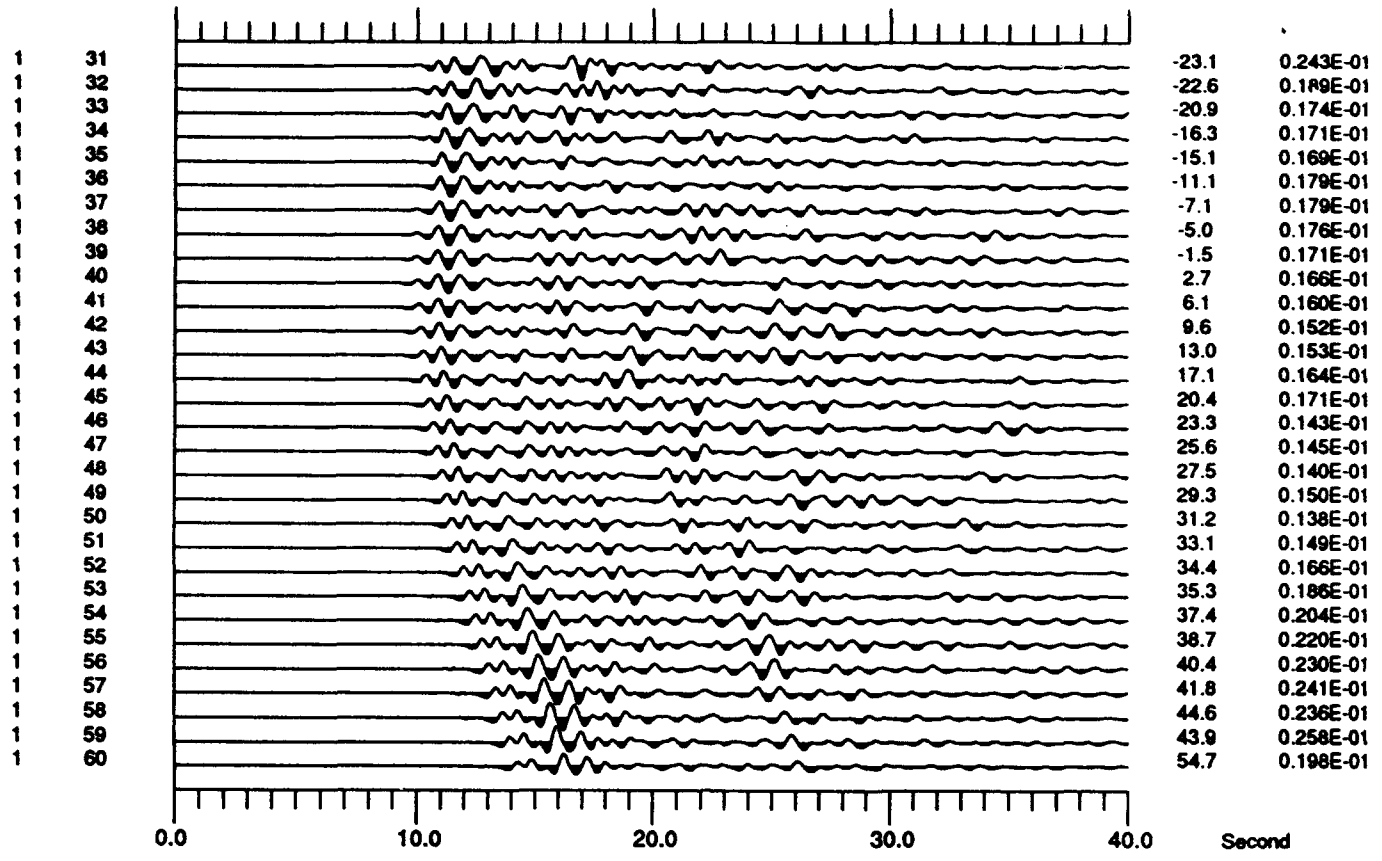
vert, same scale, decimated by 5




S, Model 52(seed 21696, Pr(1)=0.25)

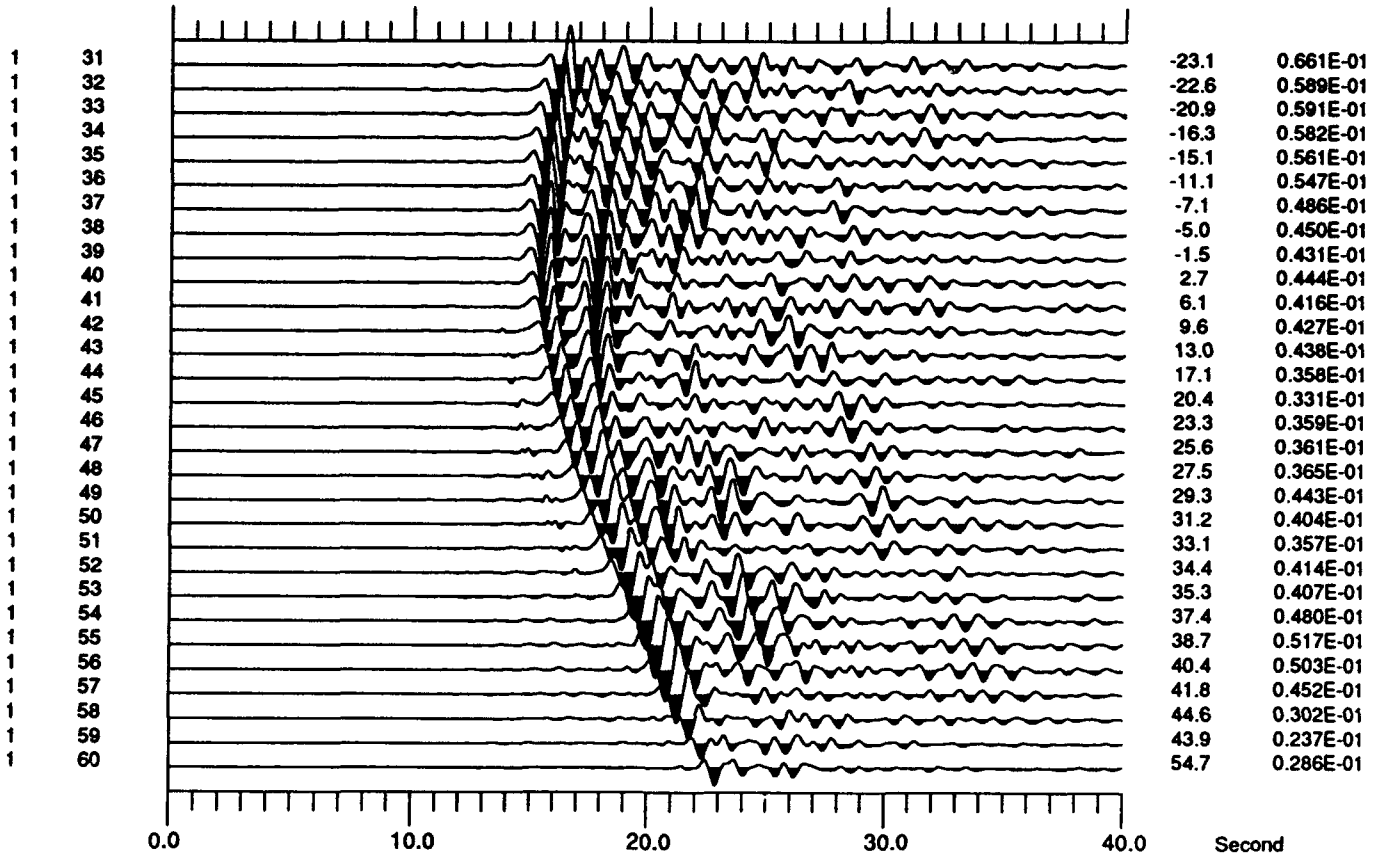
hori, same scale, decimated by 5

Figure 119




P, Model 53(seed 86037, Pr(1)=0.25)

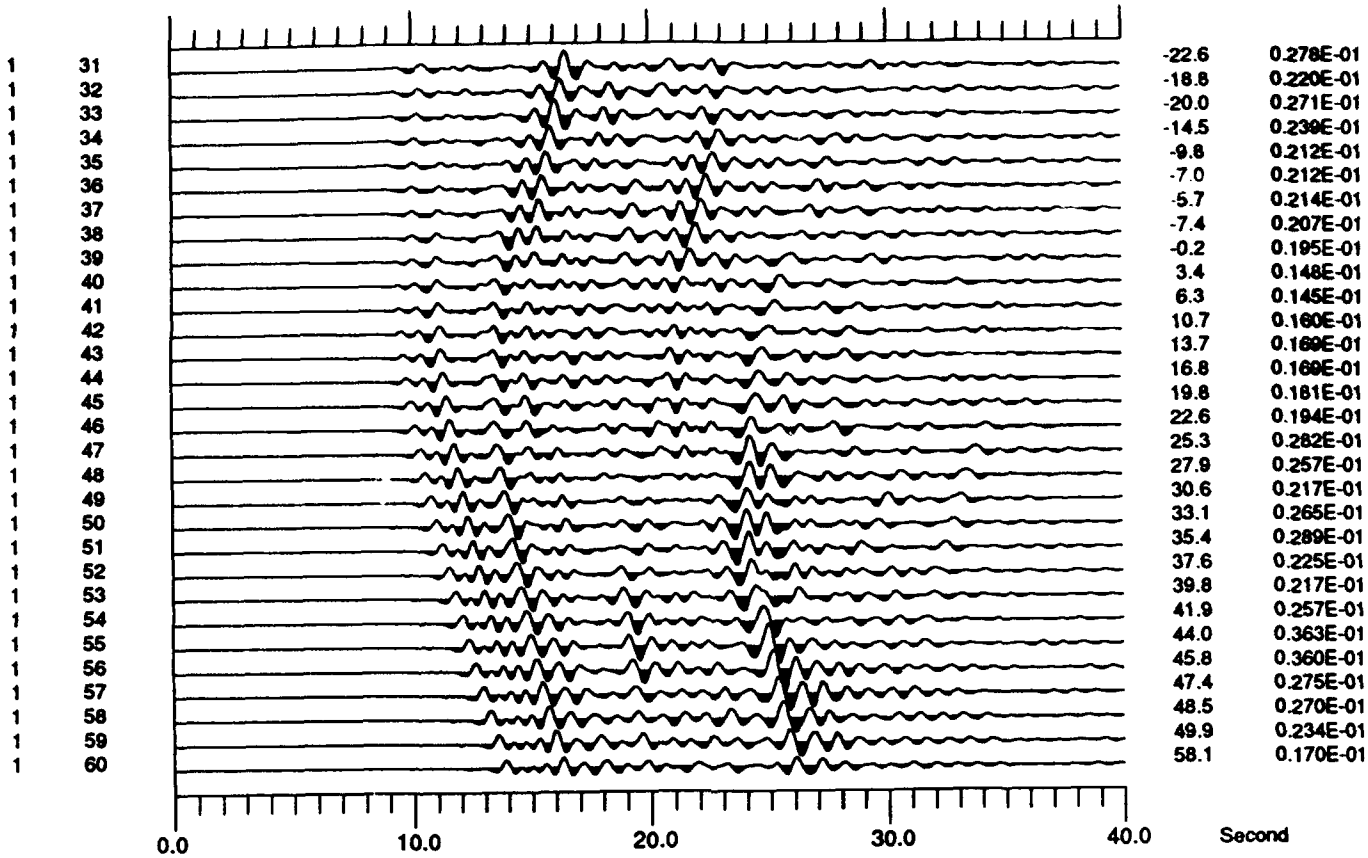
vert, same scale, decimated by 5




S, Model 53(seed 86037, Pr(1)=0.25)

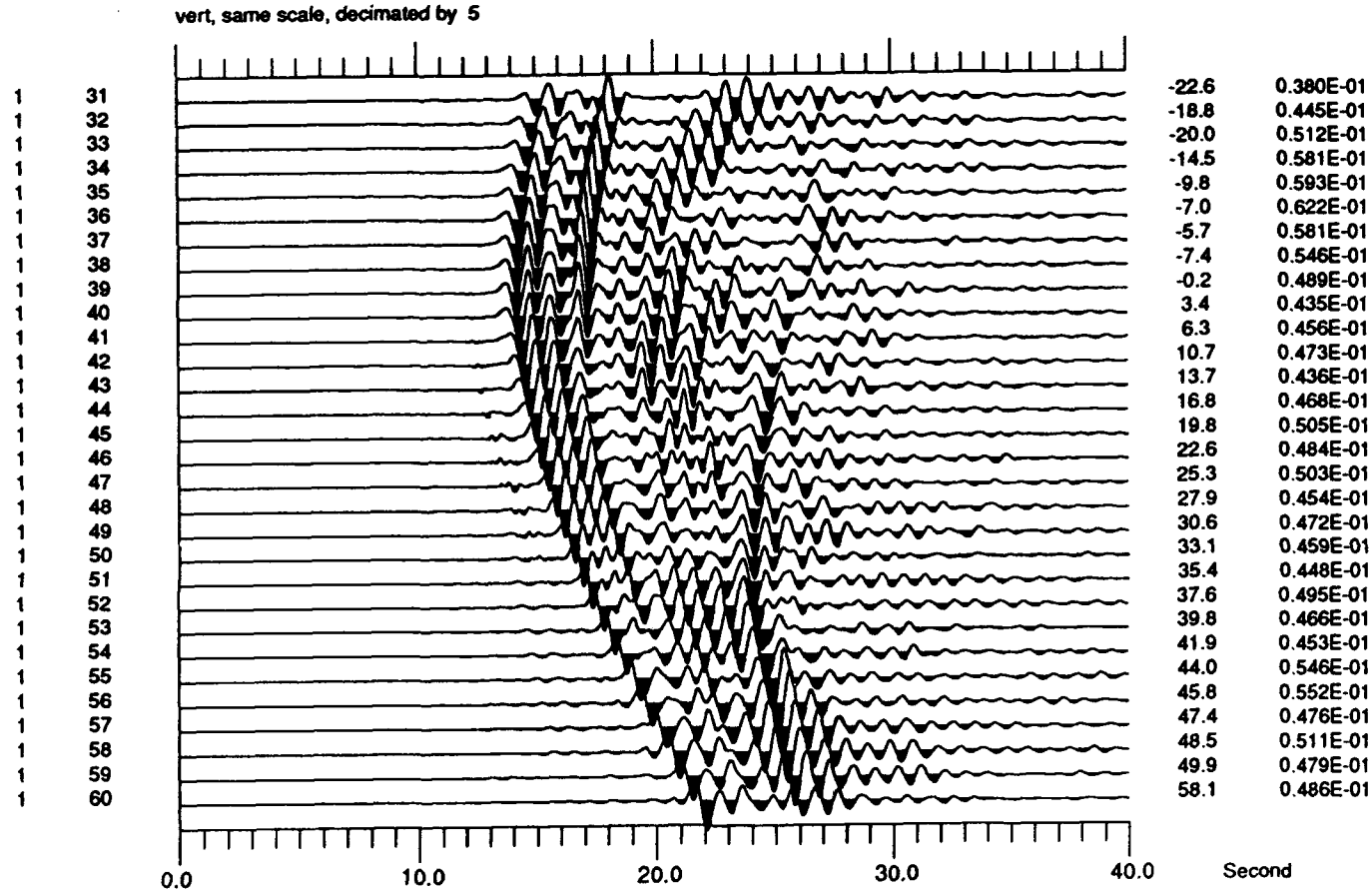
hori, same scale, decimated by 5

Figure 120




P, Model 61(seed 93459, Pr(1)=0.30)

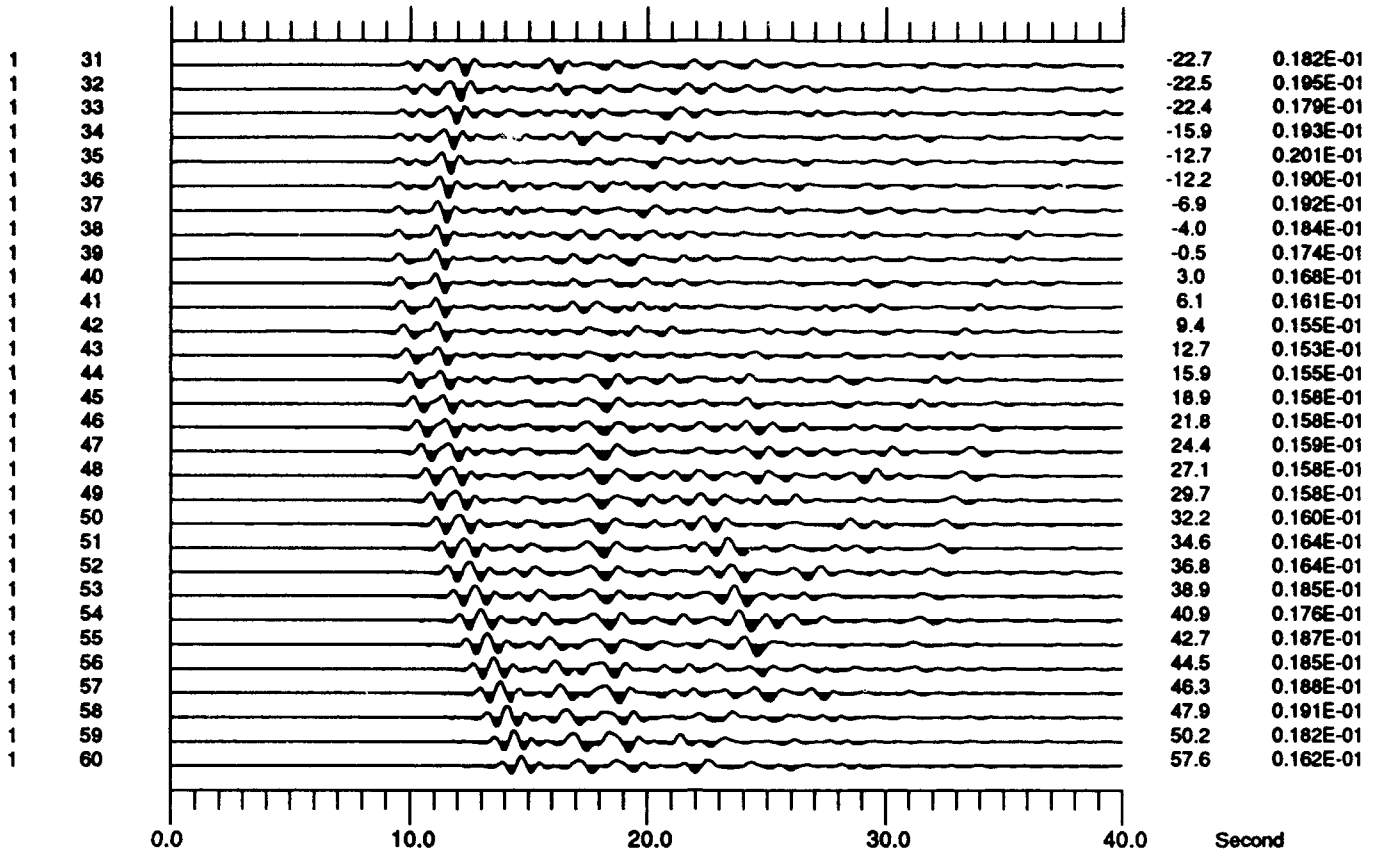
vert, same scale, decimated by 5




S, Model 61(seed 93459, Pr(1)=0.30)

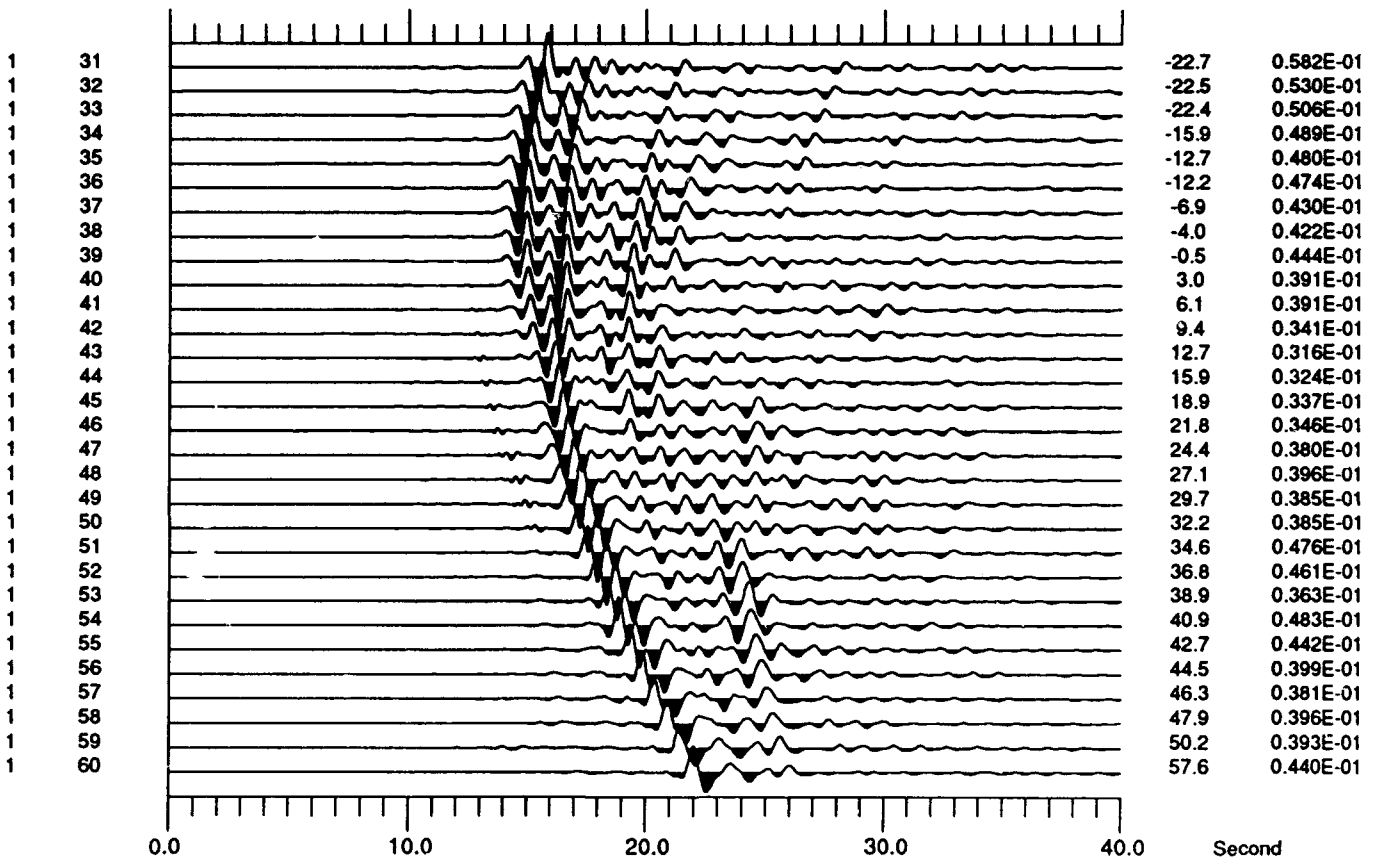
hori, same scale, decimated by 5

**Figure 121**




P, Model 62(seed 93468, Pr(1)=0.30)

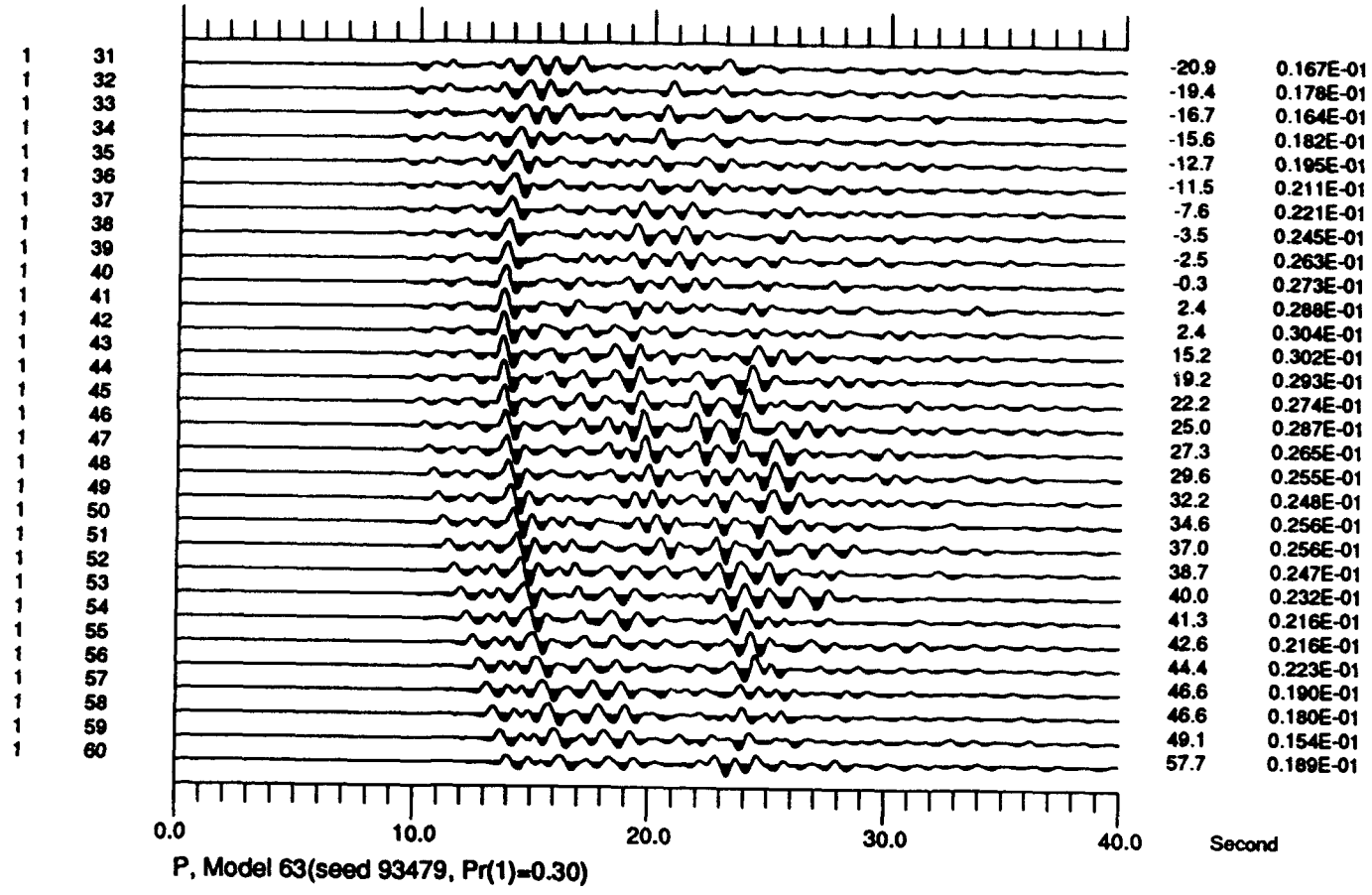
vert, same scale, decimated by 5




S, Model 62(seed 93468, Pr(1)=0.30)

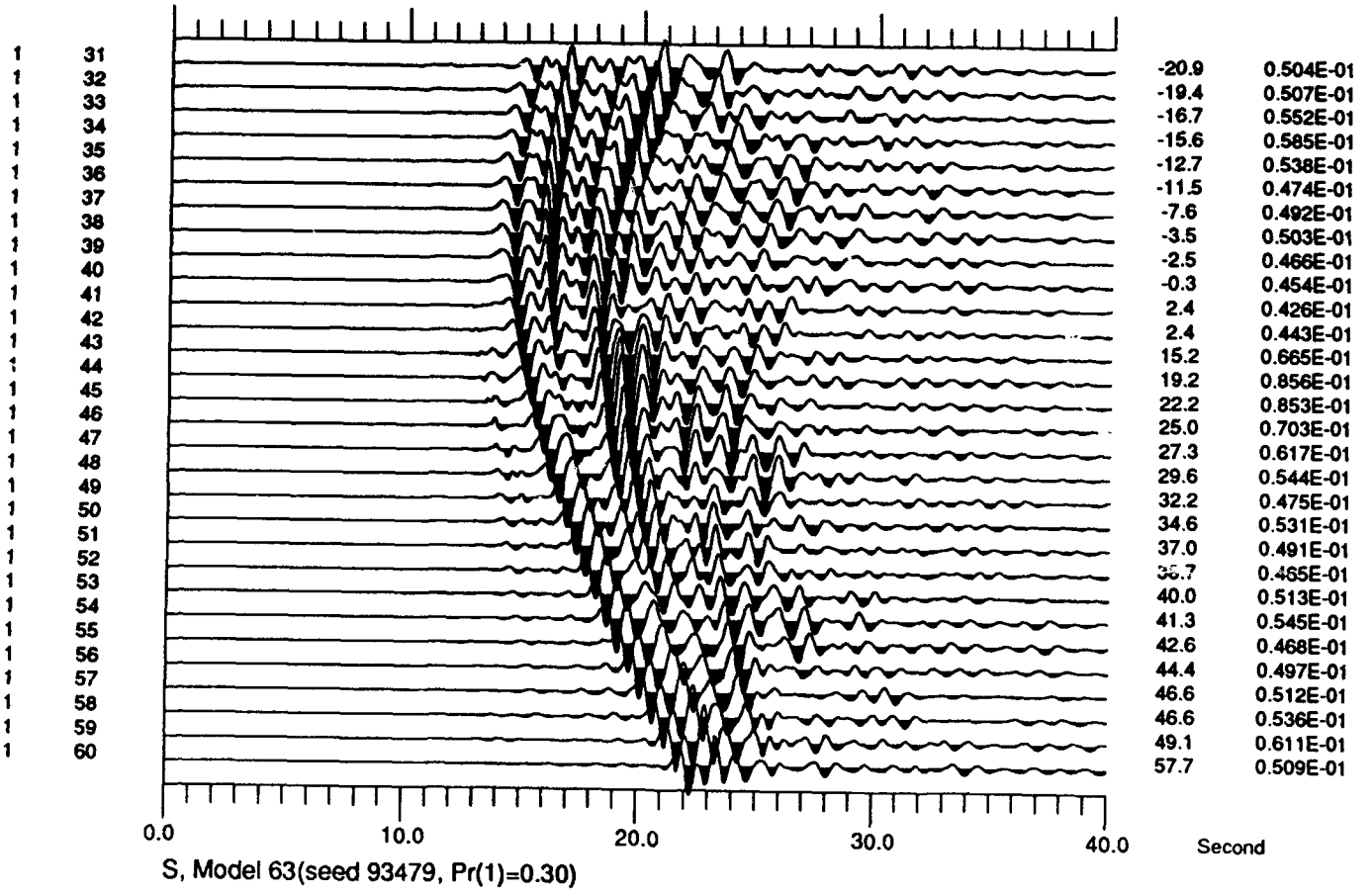
hori, same scale, decimated by 5

Figure 122




P, Model 63(seed 93479, Pr(1)=0.30)

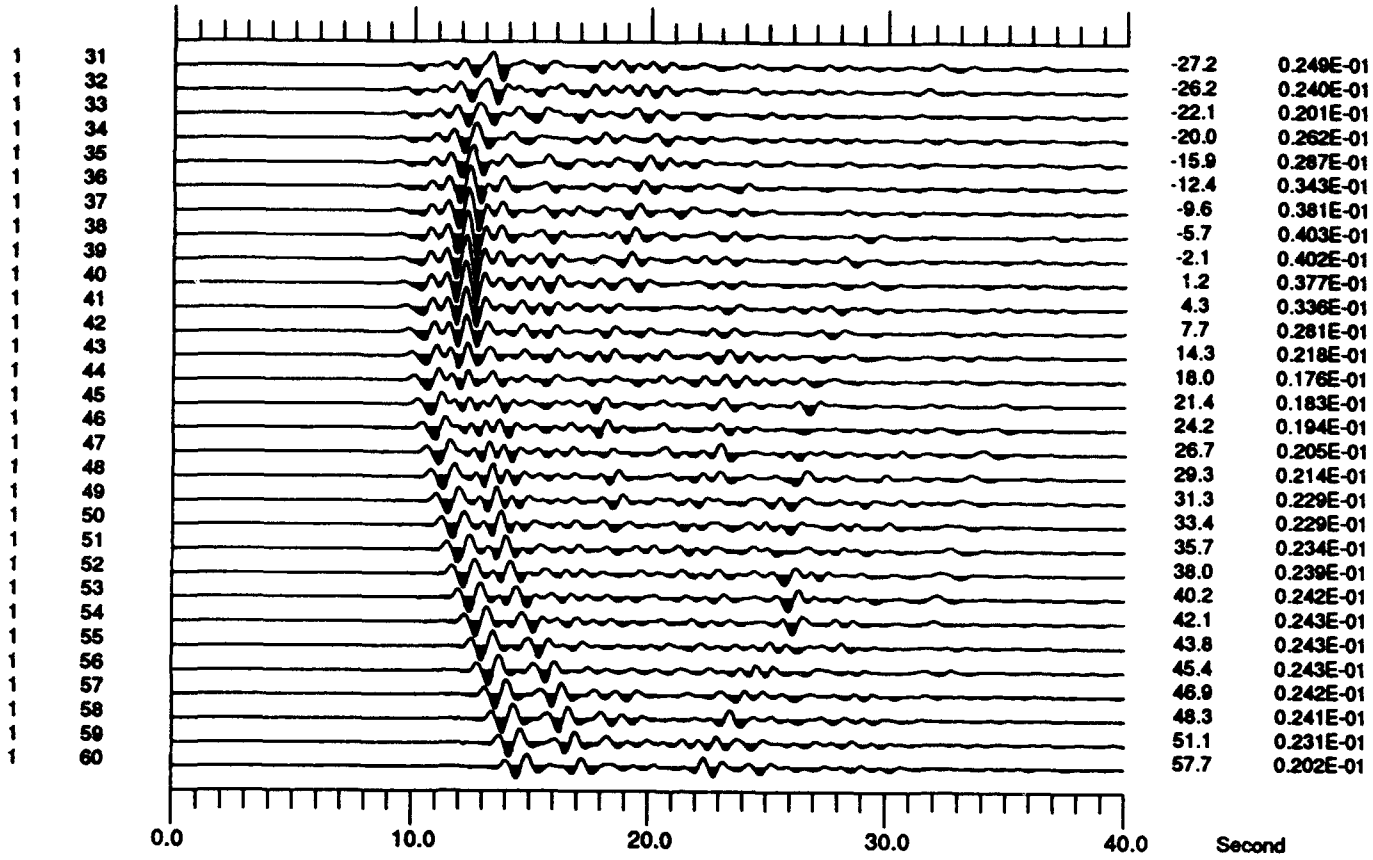
vert, same scale, decimated by 5




S, Model 63(seed 93479, Pr(1)=0.30)

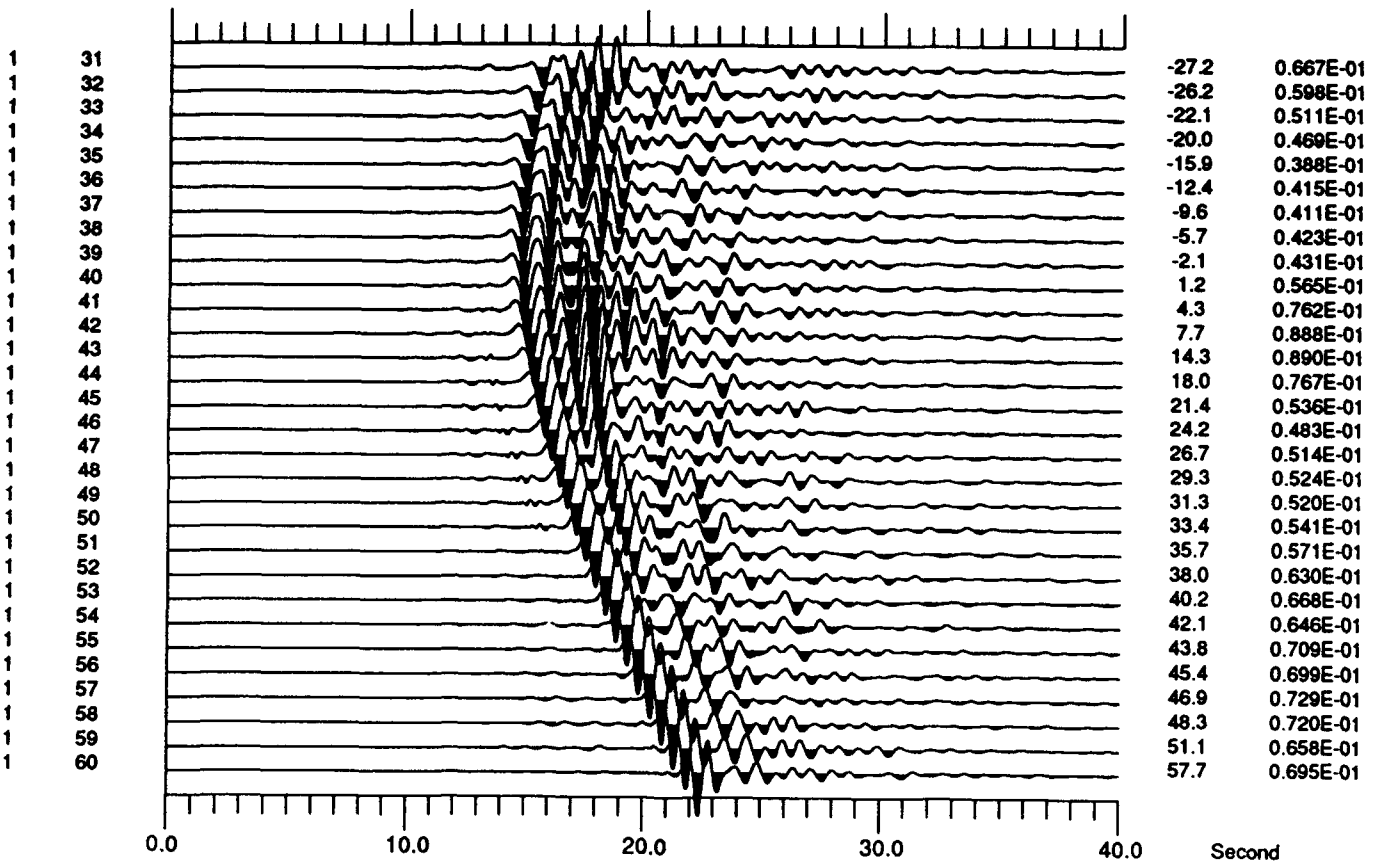
hori, same scale, decimated by 5

Figure 123




P, Model 64(seed 55473, Pr(1)=0.32)

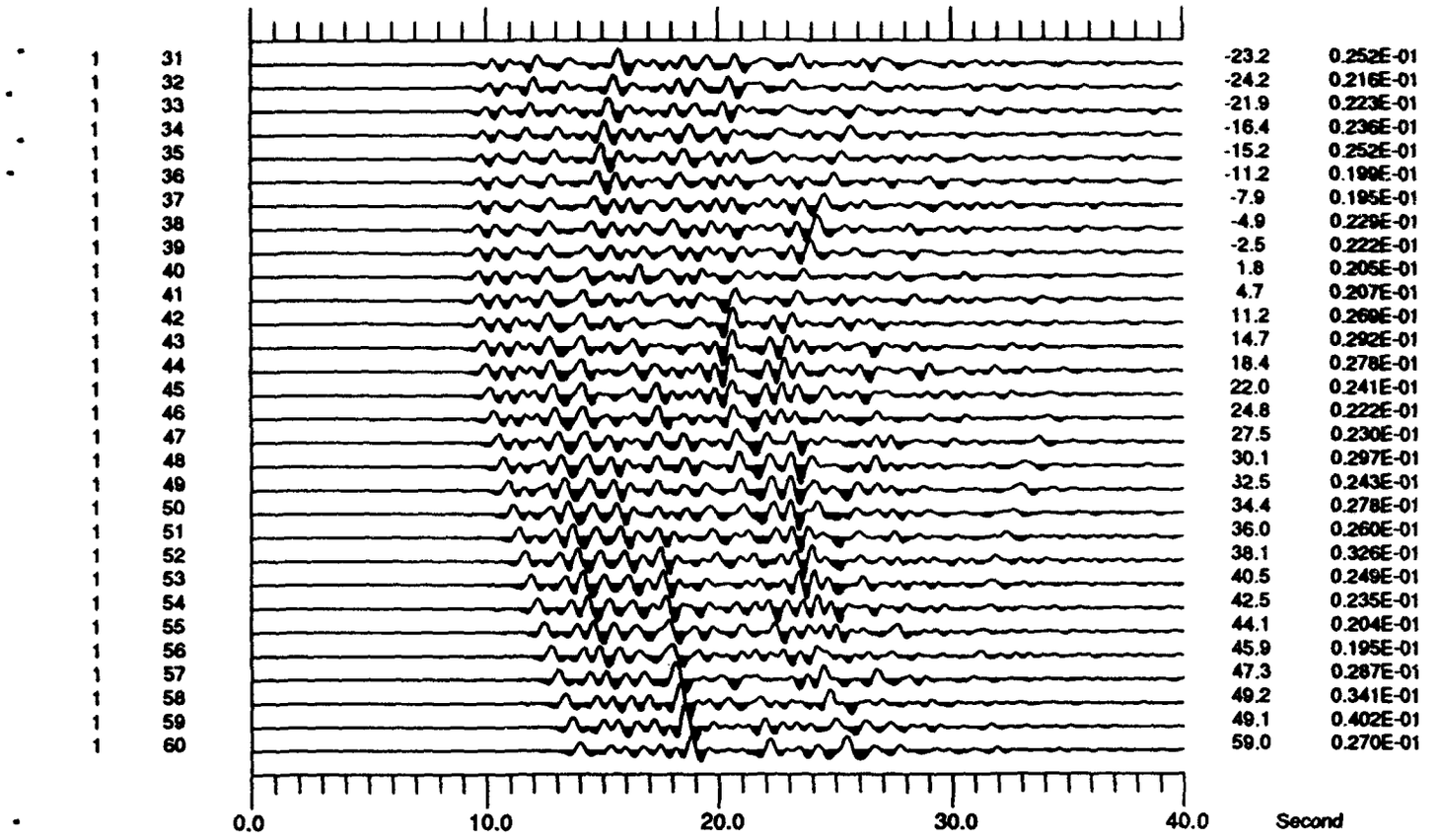
vert, same scale, decimated by 5




S, Model 64(seed 55473, Pr(1)=0.32)

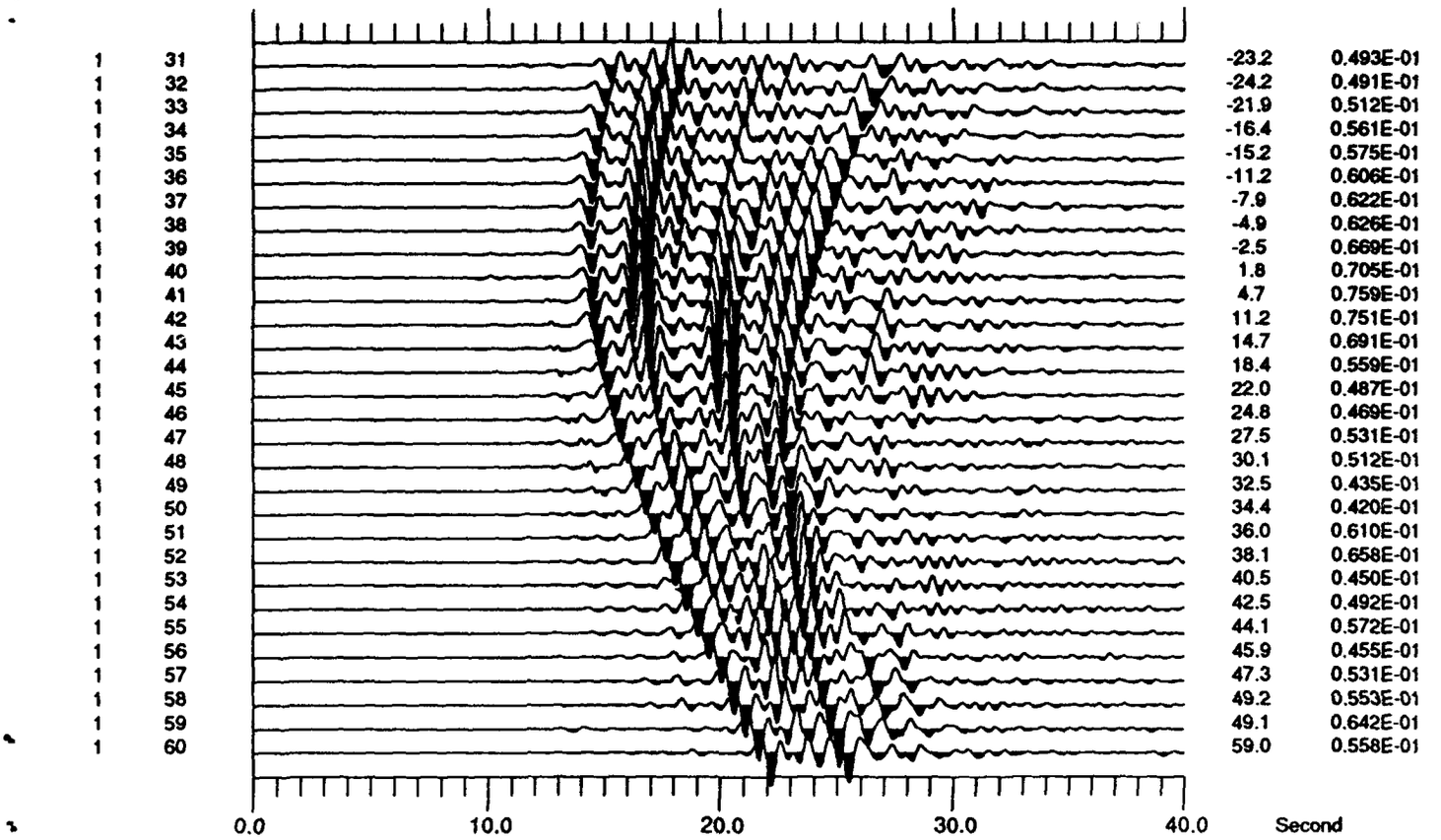
hori, same scale, decimated by 5

Figure 124




P, Model 65(seed 55499, Pr(1)=0.32)

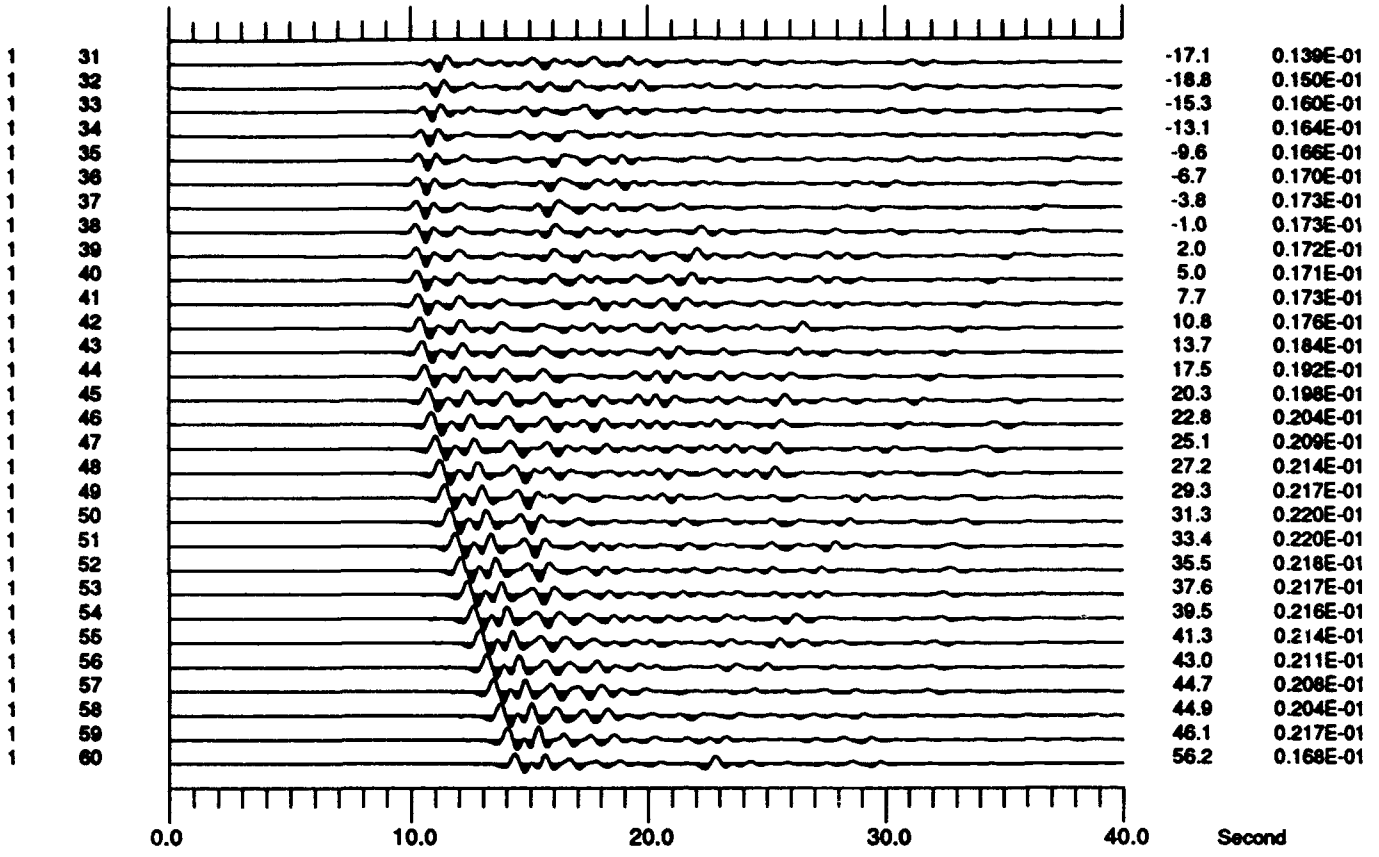
vert, same scale, decimated by 5




S, Model 65(seed 55499, Pr(1)=0.32)

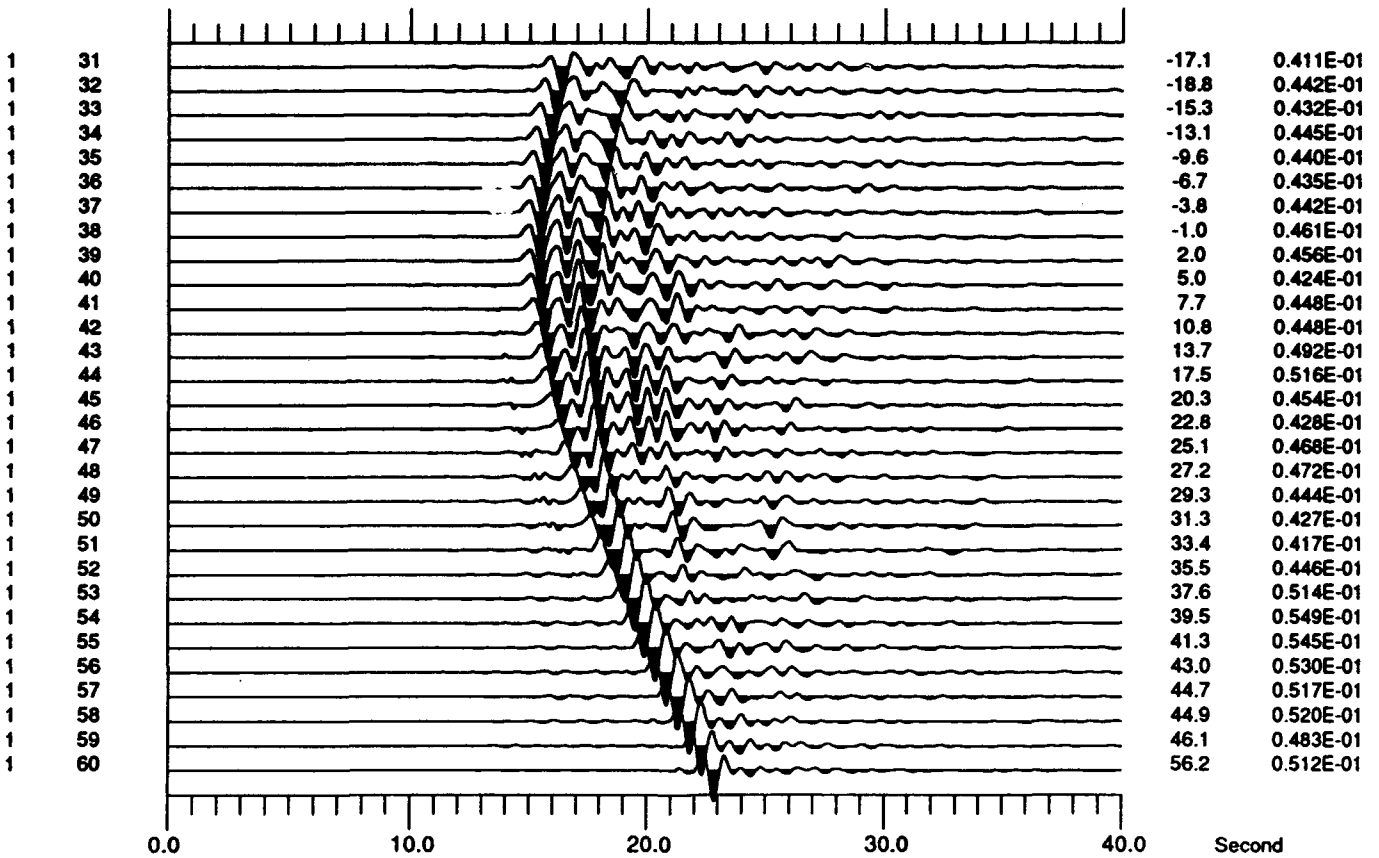
hori, same scale, decimated by 5

**Figure 125**




P, Model 66(seed 55446, Pr(1)=0.32)

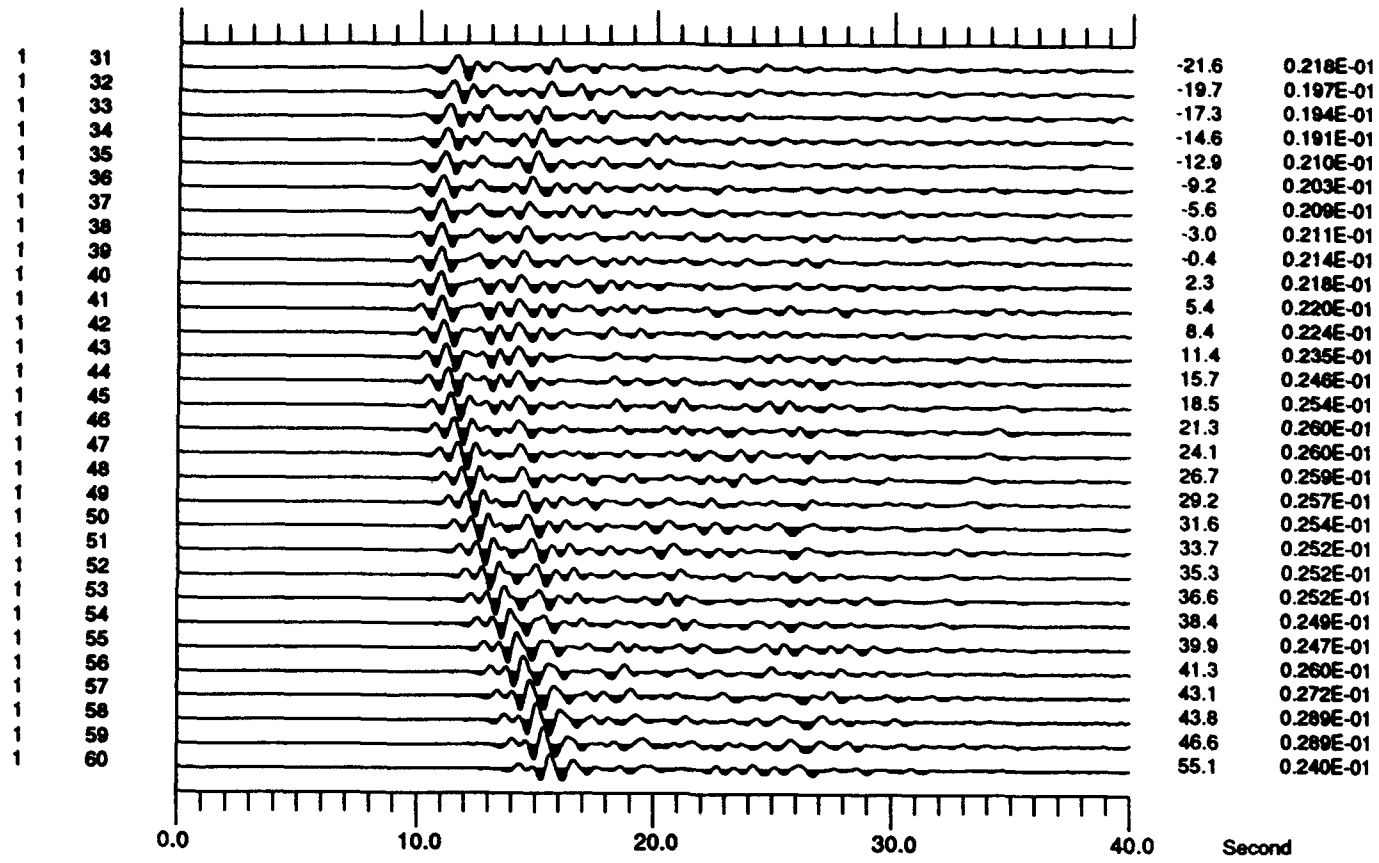
vert, same scale, decimated by 5




S, Model 66(seed 55446, Pr(1)=0.32)

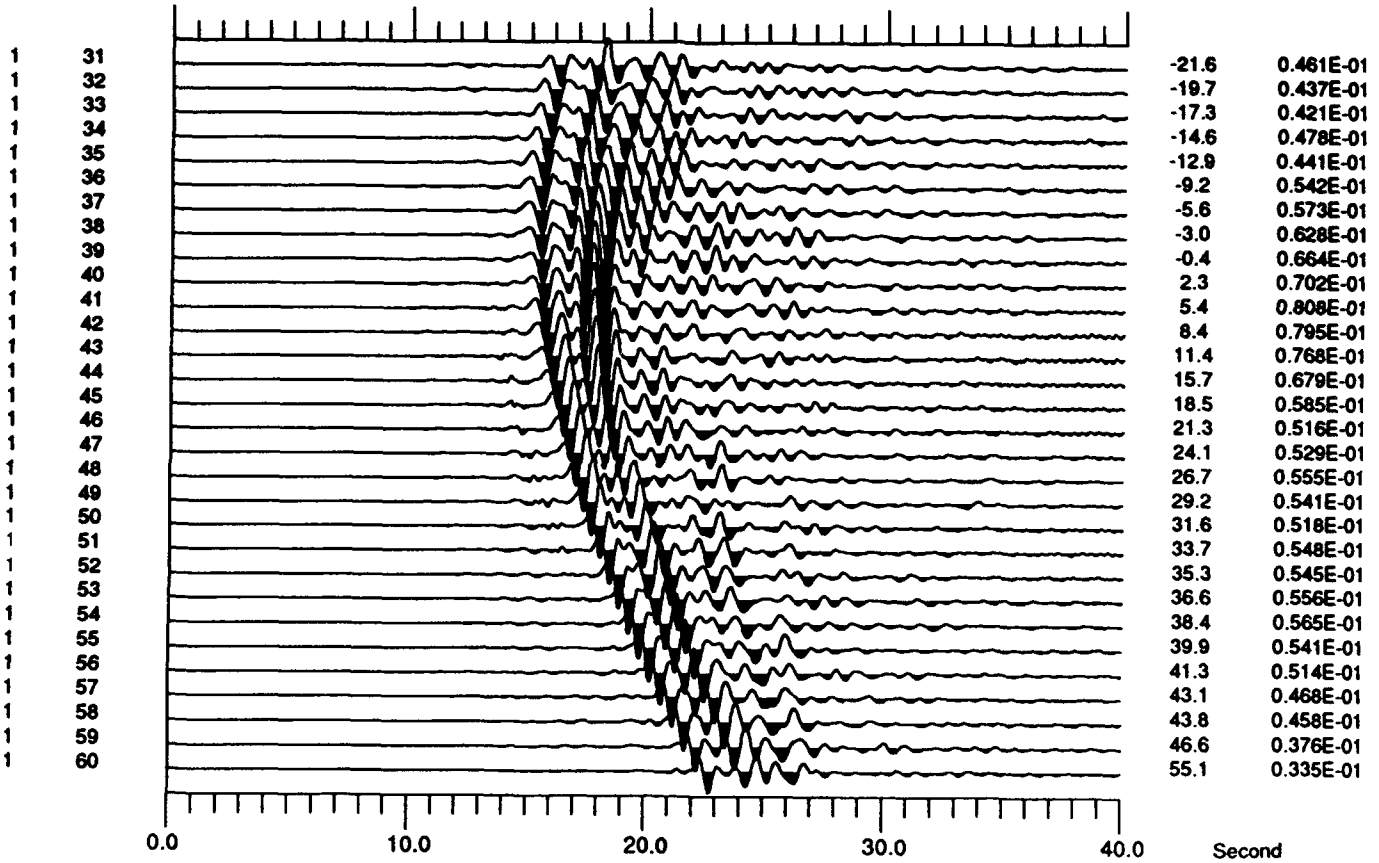
hori, same scale, decimated by 5

Figure 126




P, Model 71(seed 22192, Pr(1)=0.35)

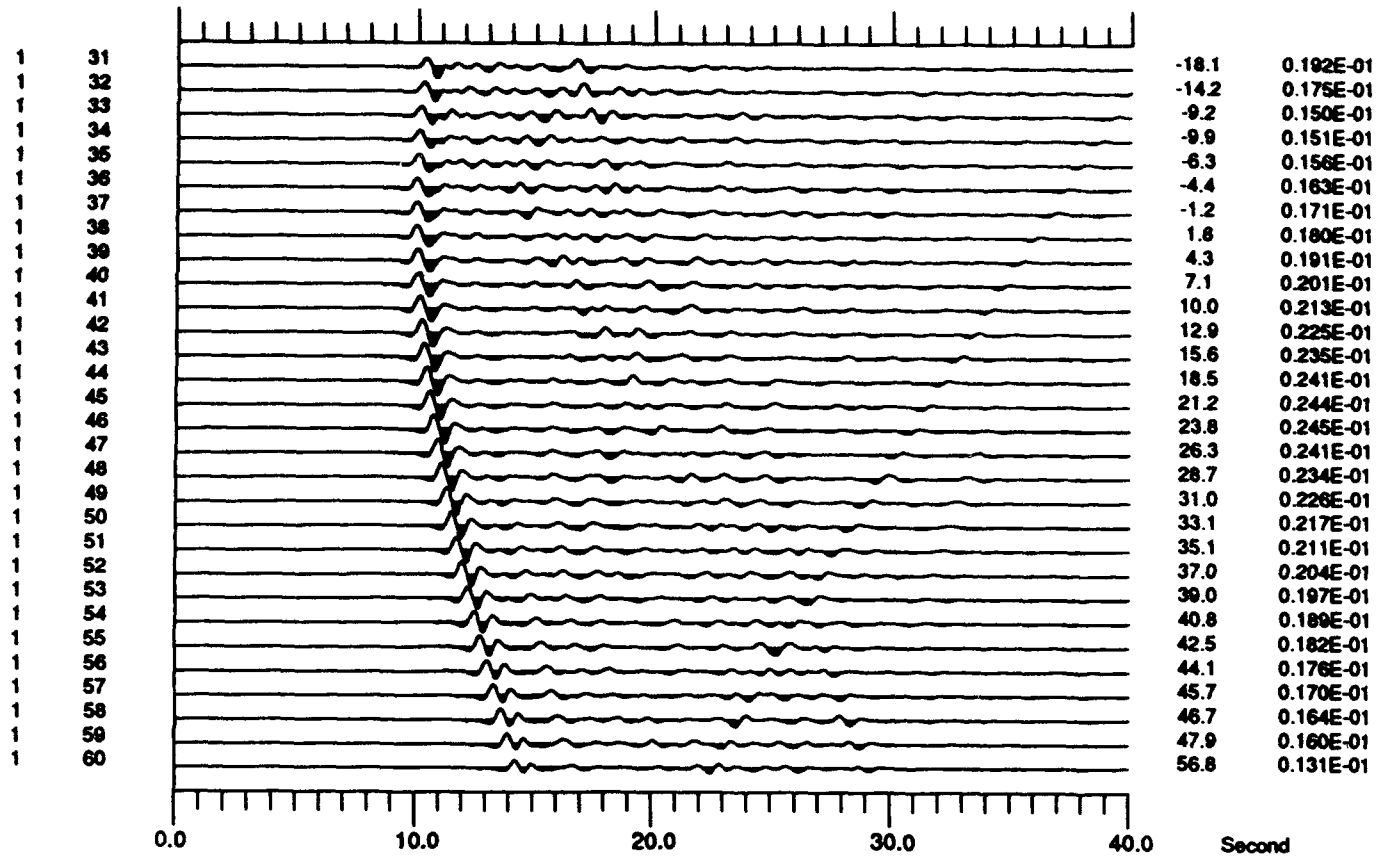
vert, same scale, decimated by 5




S, Model 71(seed 22192, Pr(1)=0.35)

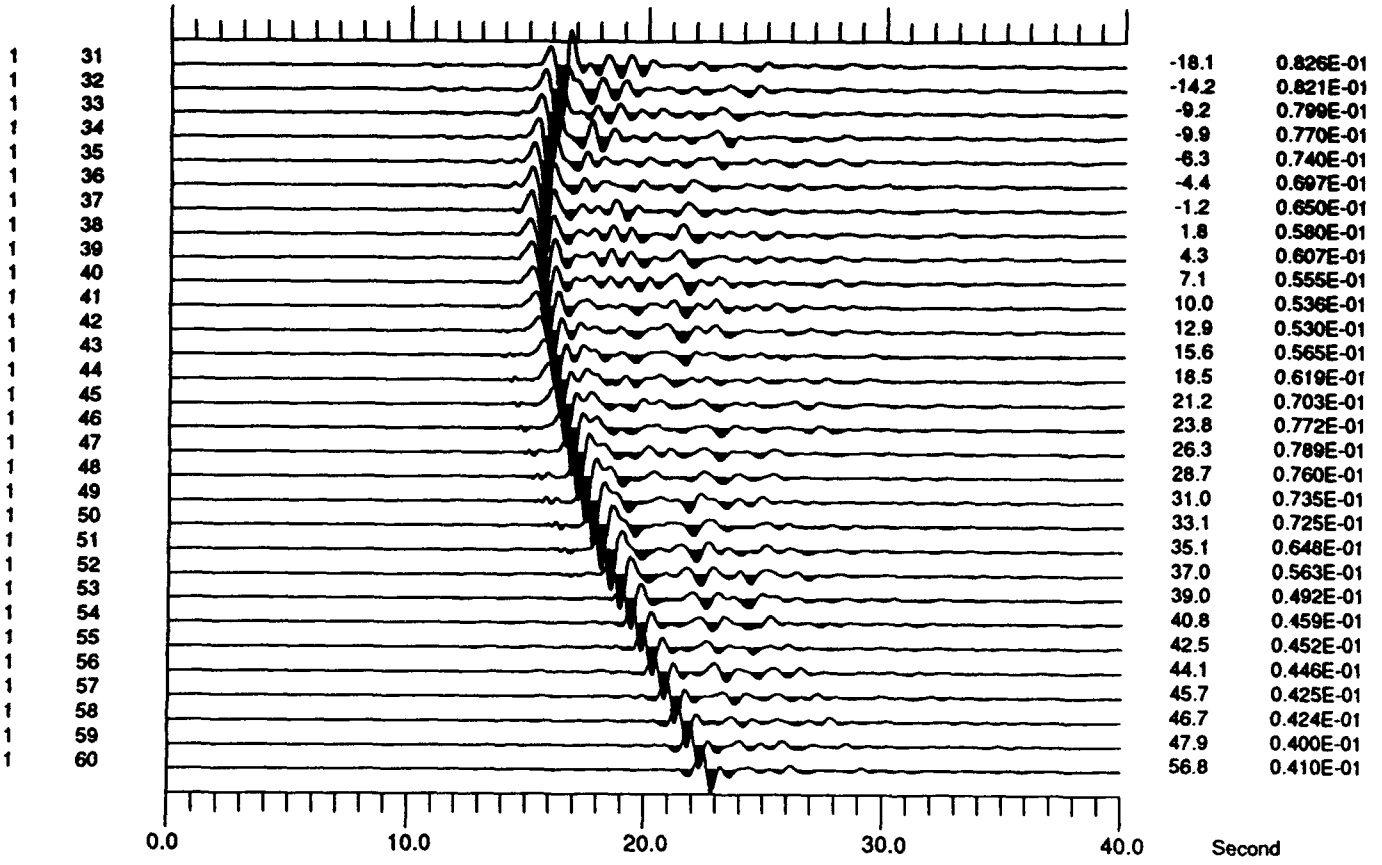
hori, same scale, decimated by 5

**Figure 127**




P, Model 72(seed 31087, Pr(1)=0.35)

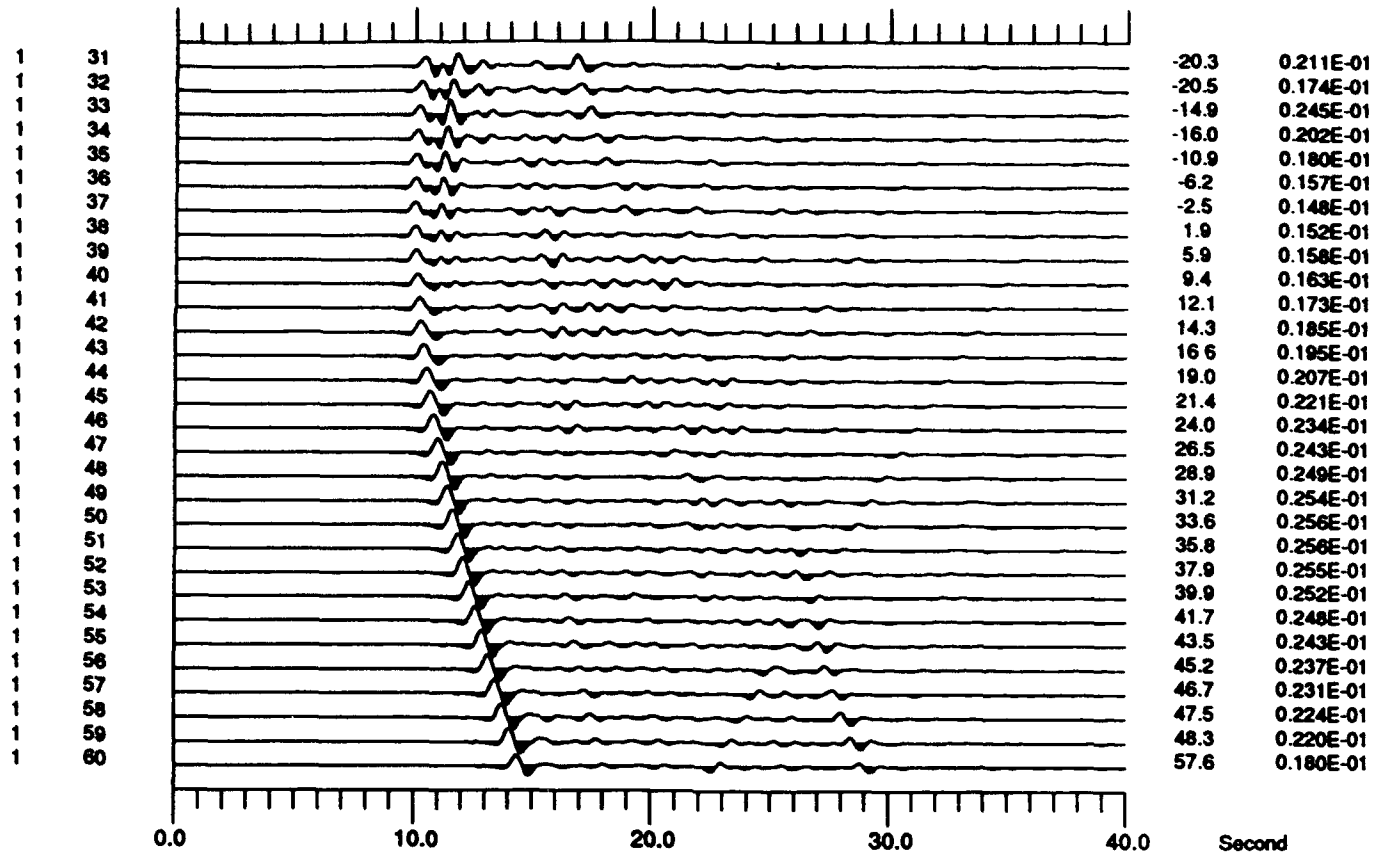
vert, same scale, decimated by 5




S, Model 72(seed 31087, Pr(1)=0.35)

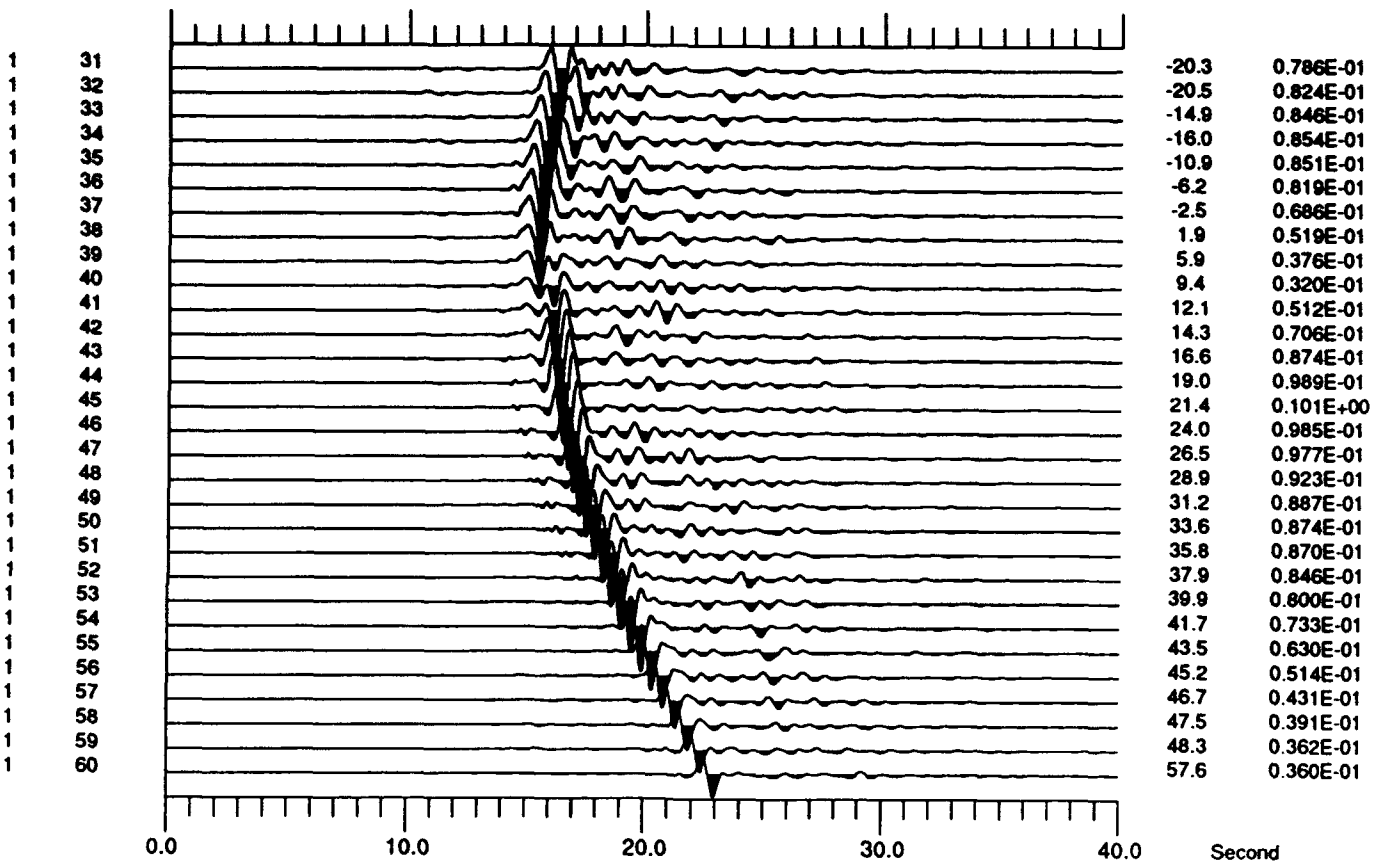
hori, same scale, decimated by 5

Figure 128




P, Model 73(seed 86061, Pr(1)=0.35)

vert, same scale, decimated by 5




S, Model 73(seed 86061, Pr(1)=0.35)

hori, same scale, decimated by 5

Figure 129

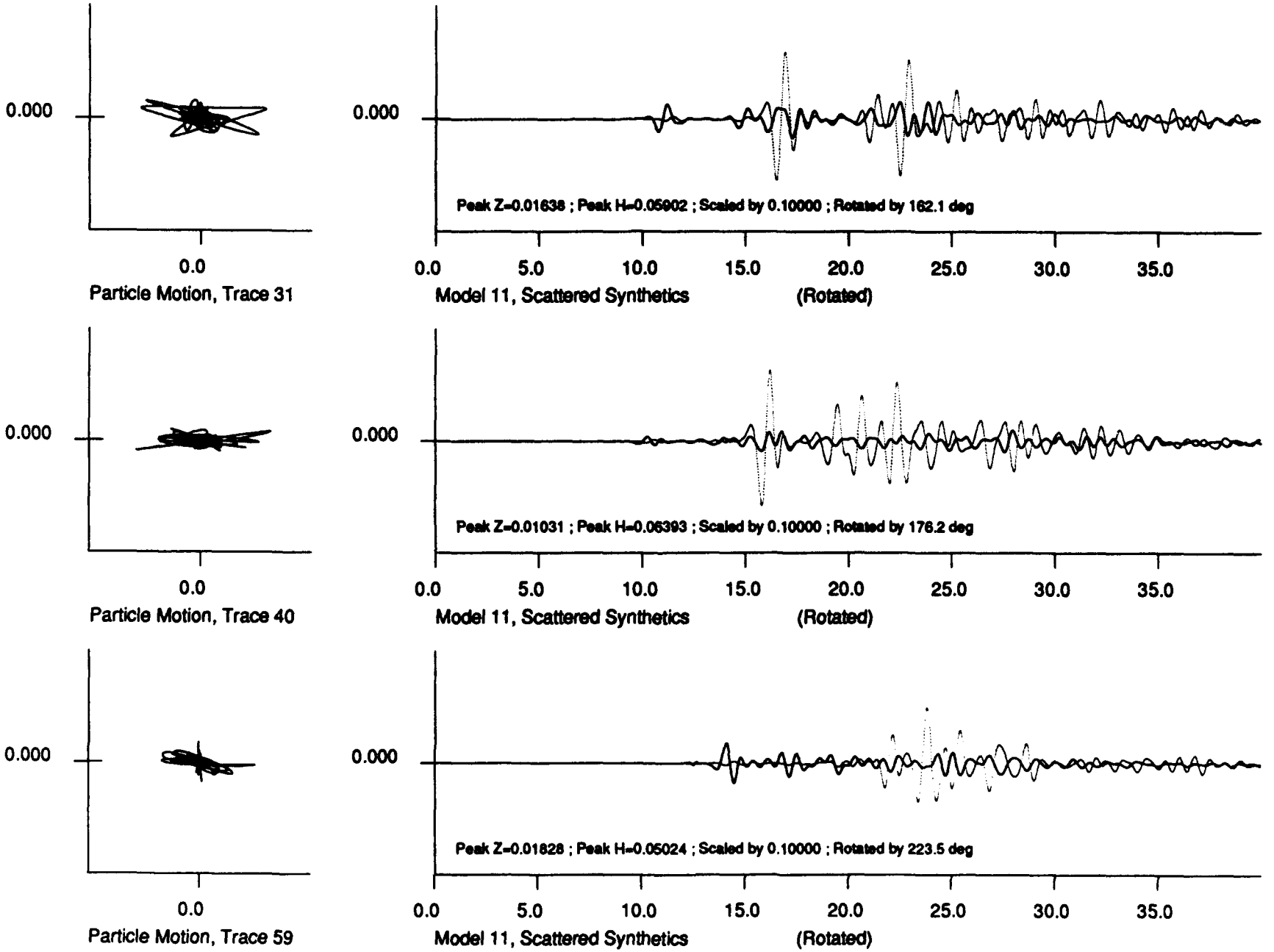

0.000
0.000
Peak Z=0.01638 ; Peak H=0.05902 ; Scaled by 0.10000 ; Rotated by 162.1 deg
0.0
Particle Motion, Trace 31
0.0 5.0 10.0 15.0 20.0 25.0 30.0 35.0
Model 11, Scattered Synthetics (Rotated)
0.000
0.000
Peak Z=0.01031 ; Peak H=0.06393 ; Scaled by 0.10000 ; Rotated by 176.2 deg
0.0
Particle Motion, Trace 40
0.0 5.0 10.0 15.0 20.0 25.0 30.0 35.0
Model 11, Scattered Synthetics (Rotated)
0.000
0.000
Peak Z=0.01628 ; Peak H=0.05024 ; Scaled by 0.10000 ; Rotated by 223.5 deg
0.0
Particle Motion, Trace 59
0.0 5.0 10.0 15.0 20.0 25.0 30.0 35.0
Model 11, Scattered Synthetics (Rotated)

**Figure 130**

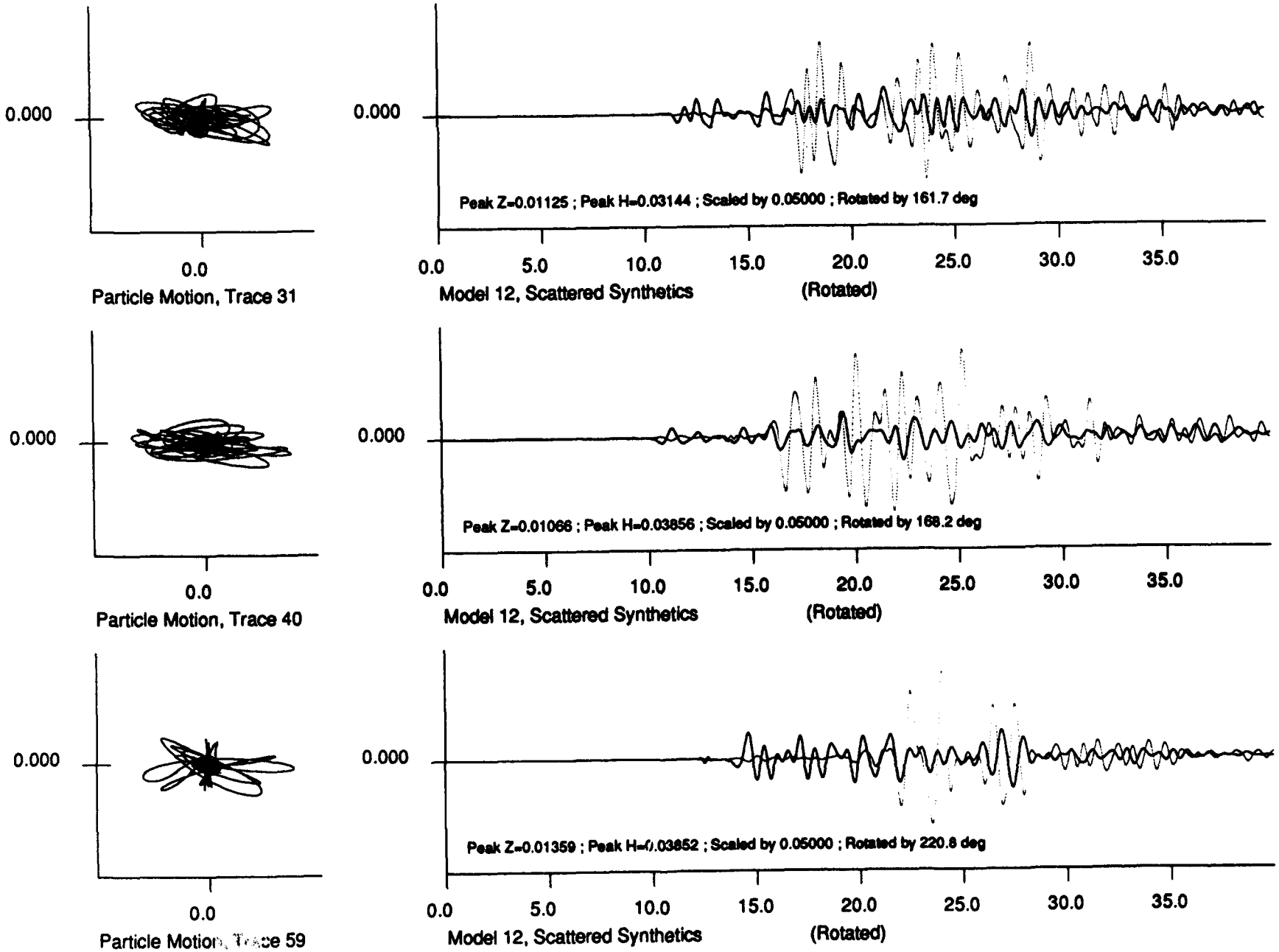

0.000
0.0
Particle Motion, Trace 31
0.000
Peak Z=0.01125 ; Peak H=0.03144 ; Scaled by 0.05000 ; Rotated by 161.7 deg
0.0
5.0
10.0
15.0
20.0
25.0
30.0
35.0
Model 12, Scattered Synthetics
(Rotated)
0.000
0.0
Particle Motion, Trace 40
0.000
Peak Z=0.01066 ; Peak H=0.03856 ; Scaled by 0.05000 ; Rotated by 168.2 deg
0.0
5.0
10.0
15.0
20.0
25.0
30.0
35.0
Model 12, Scattered Synthetics
(Rotated)
0.000
0.0
Particle Motion, Trace 59
0.000
Peak Z=0.01359 ; Peak H=0.03852 ; Scaled by 0.05000 ; Rotated by 220.8 deg
0.0
5.0
10.0
15.0
20.0
25.0
30.0
35.0
Model 12, Scattered Synthetics
(Rotated)

**Figure 131**

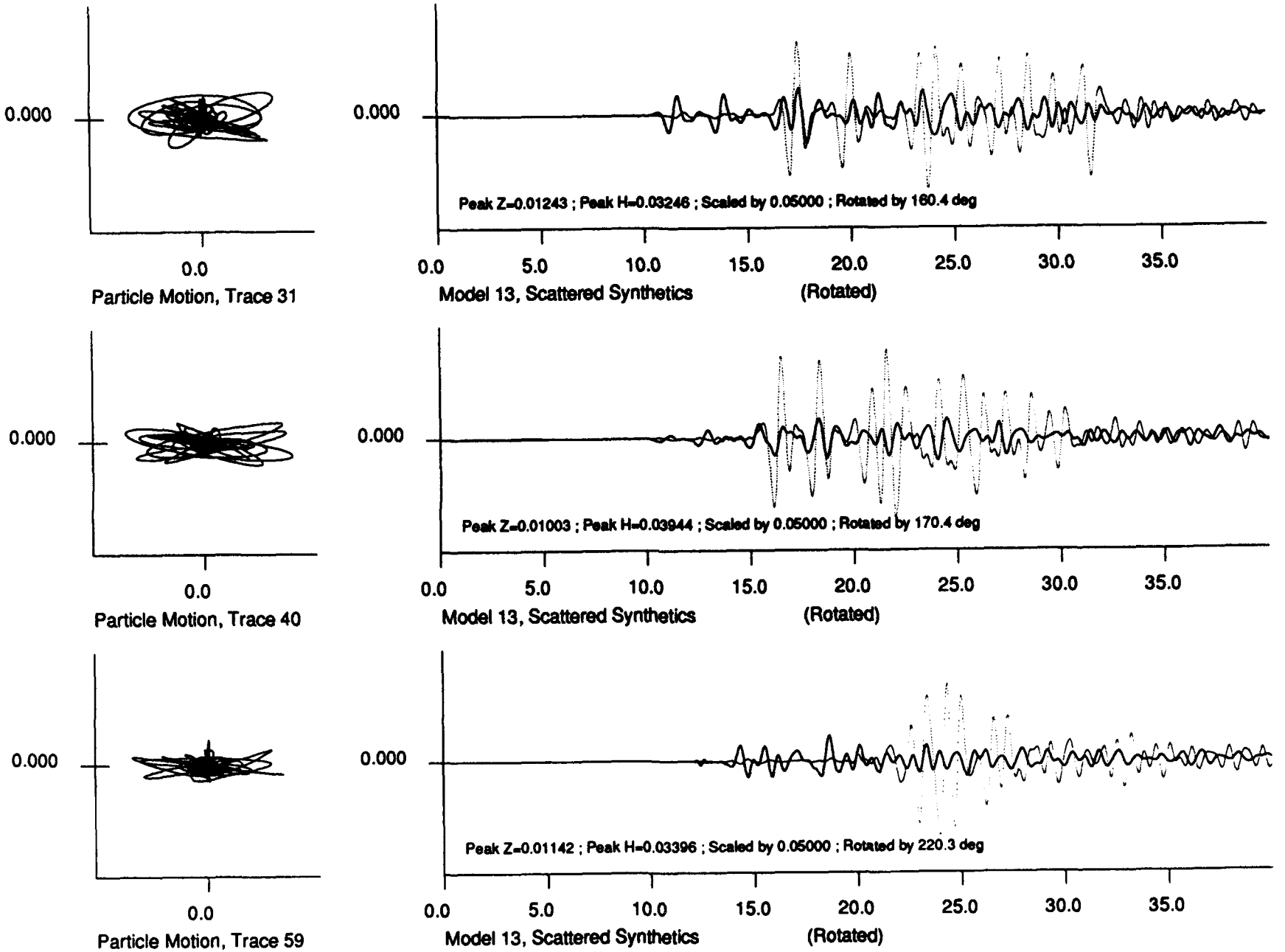

0.000
0.0
Particle Motion, Trace 31
0.000
Peak Z=0.01243 ; Peak H=0.03246 ; Scaled by 0.05000 ; Rotated by 160.4 deg
0.0 5.0 10.0 15.0 20.0 25.0 30.0 35.0
Model 13, Scattered Synthetics (Rotated)
0.000
0.0
Particle Motion, Trace 40
0.000
Peak Z=0.01003 ; Peak H=0.03944 ; Scaled by 0.05000 ; Rotated by 170.4 deg
0.0 5.0 10.0 15.0 20.0 25.0 30.0 35.0
Model 13, Scattered Synthetics (Rotated)
0.000
0.0
Particle Motion, Trace 59
0.000
Peak Z=0.01142 ; Peak H=0.03396 ; Scaled by 0.05000 ; Rotated by 220.3 deg
0.0 5.0 10.0 15.0 20.0 25.0 30.0 35.0
Model 13, Scattered Synthetics (Rotated)

**Figure 132**

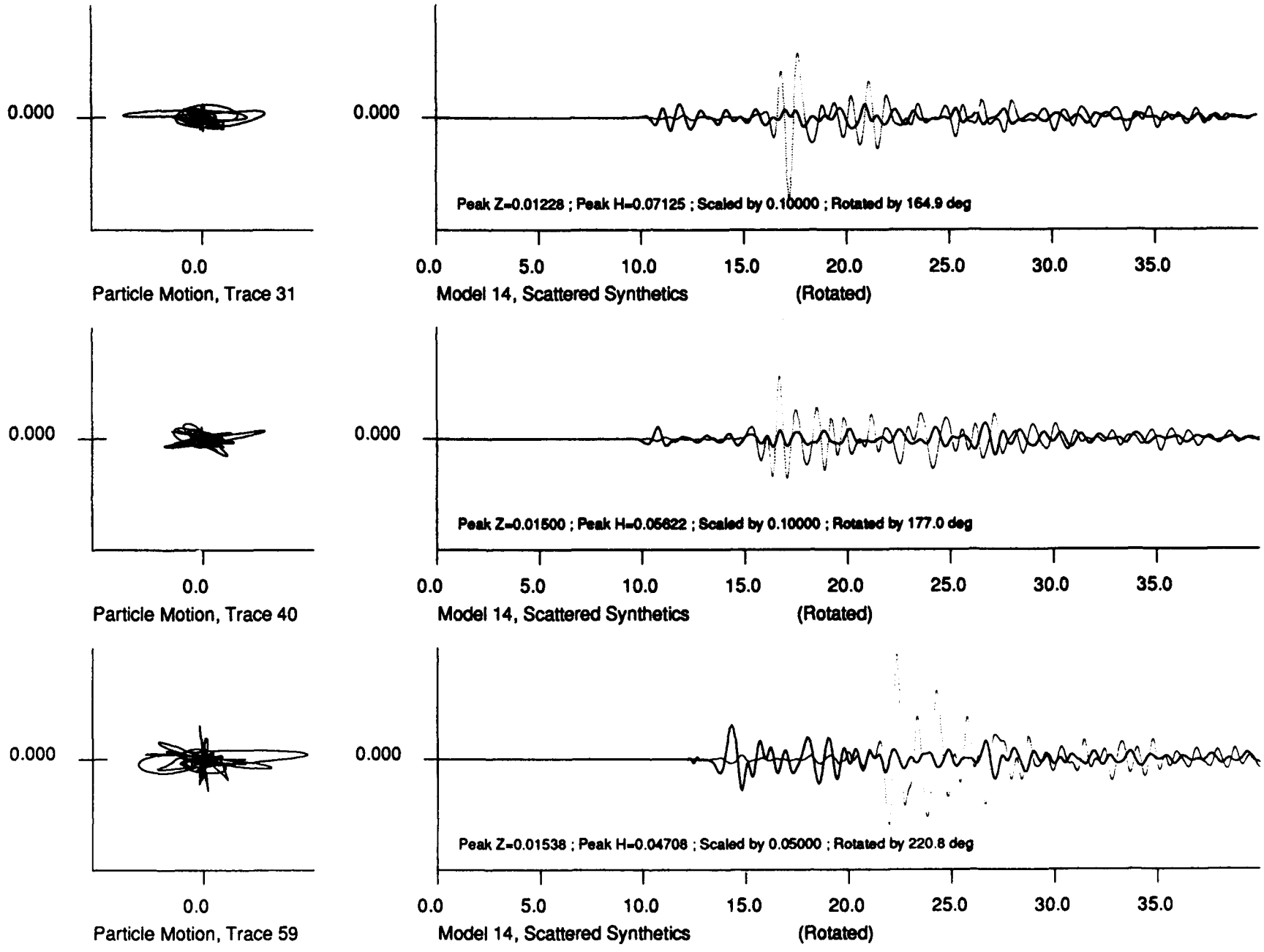

0.000
0.0
Particle Motion, Trace 31
0.000
Peak Z=0.01228 ; Peak H=0.07125 ; Scaled by 0.10000 ; Rotated by 164.9 deg
0.0 5.0 10.0 15.0 20.0 25.0 30.0 35.0
Model 14, Scattered Synthetics (Rotated)
0.000
0.0
Particle Motion, Trace 40
0.000
Peak Z=0.01500 ; Peak H=0.05622 ; Scaled by 0.10000 ; Rotated by 177.0 deg
0.0 5.0 10.0 15.0 20.0 25.0 30.0 35.0
Model 14, Scattered Synthetics (Rotated)
0.000
0.0
Particle Motion, Trace 59
0.000
Peak Z=0.01538 ; Peak H=0.04708 ; Scaled by 0.05000 ; Rotated by 220.8 deg
0.0 5.0 10.0 15.0 20.0 25.0 30.0 35.0
Model 14, Scattered Synthetics (Rotated)

**Figure 133**

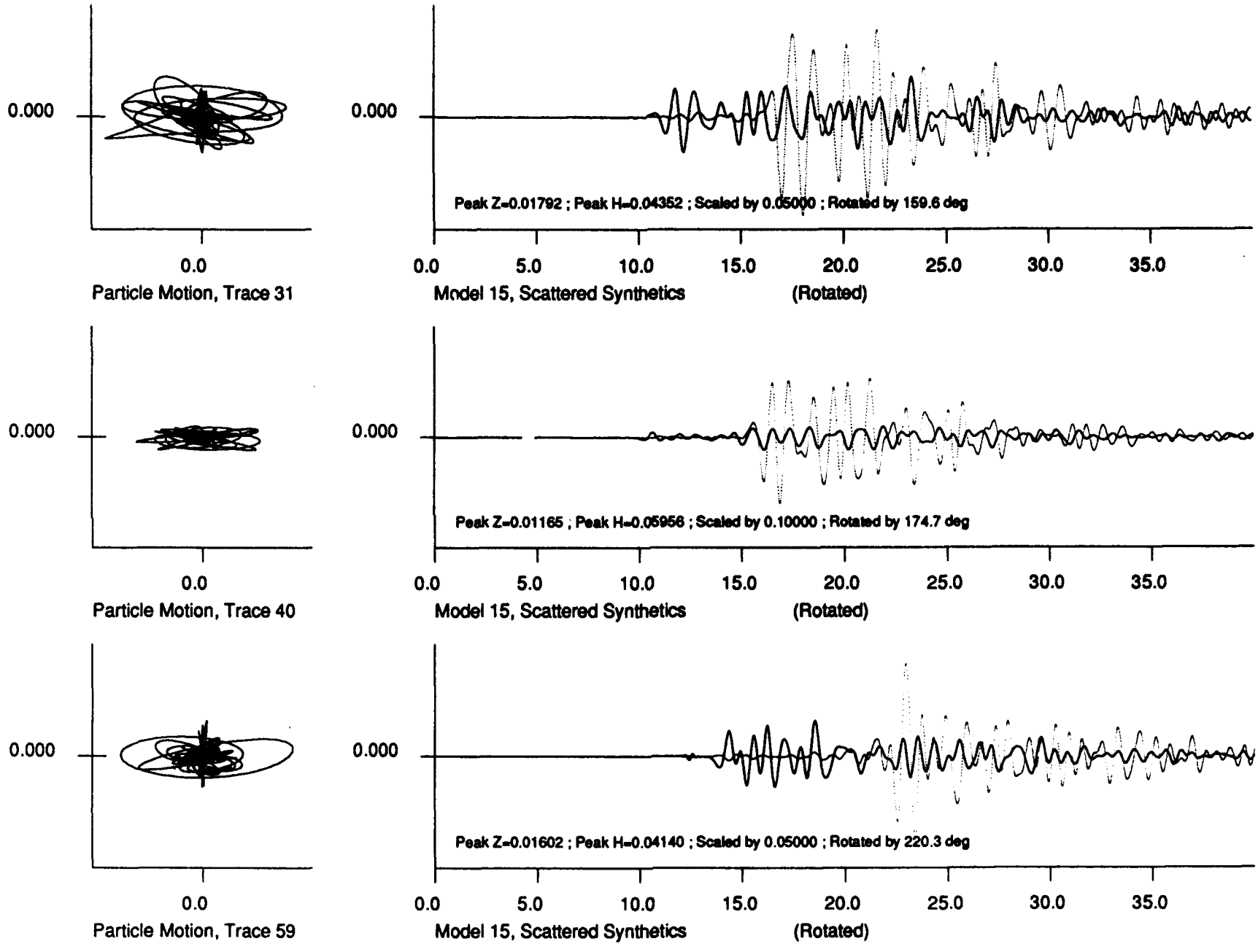

0.000
0.0
Particle Motion, Trace 31
0.000
Peak Z=0.01792 ; Peak H=0.04352 ; Scaled by 0.05000 ; Rotated by 159.6 deg
0.0 5.0 10.0 15.0 20.0 25.0 30.0 35.0
Model 15, Scattered Synthetics (Rotated)
0.000
0.0
Particle Motion, Trace 40
0.000
Peak Z=0.01165 ; Peak H=0.05956 ; Scaled by 0.10000 ; Rotated by 174.7 deg
0.0 5.0 10.0 15.0 20.0 25.0 30.0 35.0
Model 15, Scattered Synthetics (Rotated)
0.000
0.0
Particle Motion, Trace 59
0.000
Peak Z=0.01602 ; Peak H=0.04140 ; Scaled by 0.05000 ; Rotated by 220.3 deg
0.0 5.0 10.0 15.0 20.0 25.0 30.0 35.0
Model 15, Scattered Synthetics (Rotated)

**Figure 134**

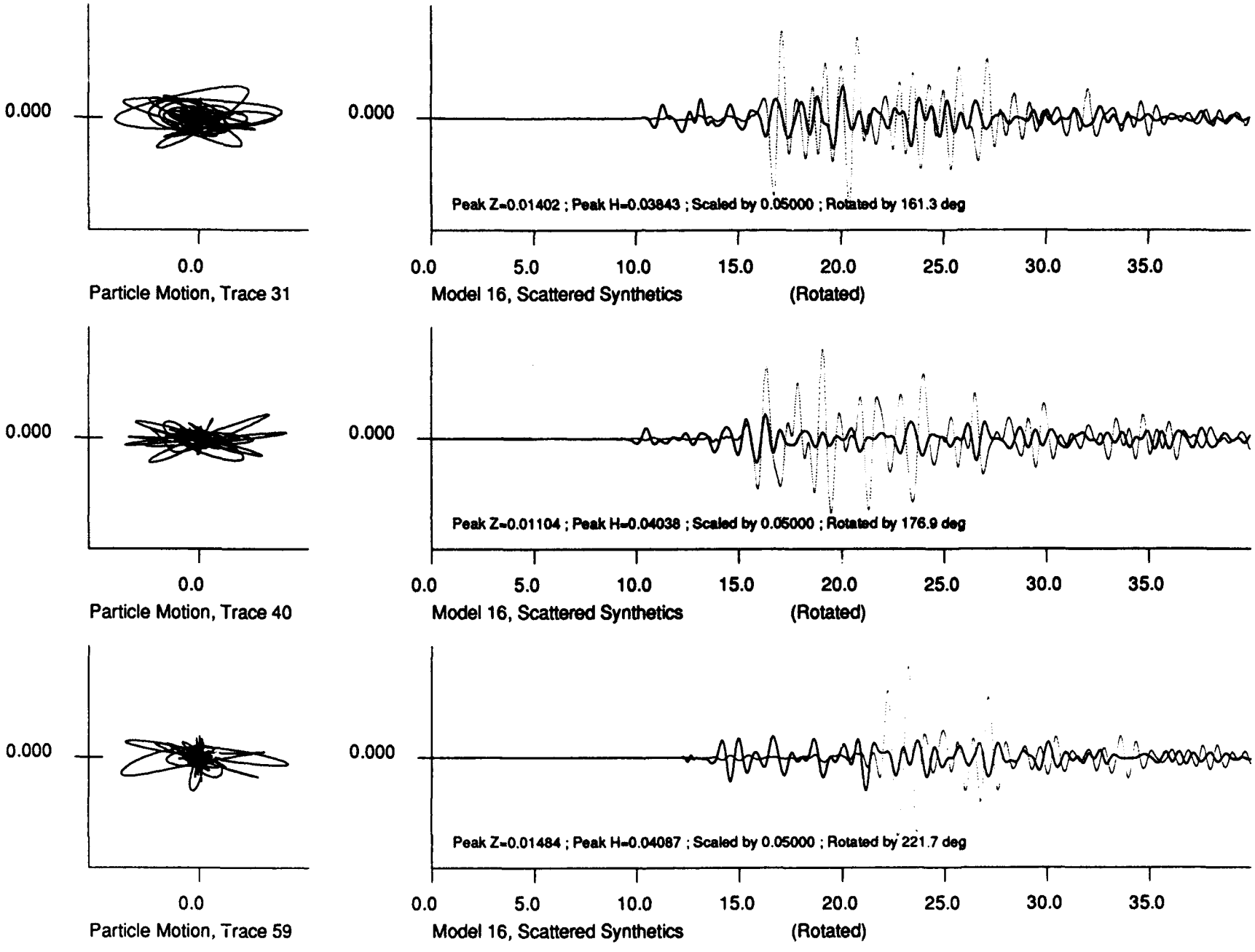

0.000
0.000
Peak Z=0.01402 ; Peak H=0.03843 ; Scaled by 0.05000 ; Rotated by 161.3 deg
0.0
5.0
10.0
15.0
20.0
25.0
30.0
35.0
0.0
Particle Motion, Trace 31
Model 16, Scattered Synthetics
(Rotated)
0.000
0.000
Peak Z=0.01104 ; Peak H=0.04038 ; Scaled by 0.05000 ; Rotated by 176.9 deg
0.0
5.0
10.0
15.0
20.0
25.0
30.0
35.0
0.0
Particle Motion, Trace 40
Model 16, Scattered Synthetics
(Rotated)
0.000
0.000
Peak Z=0.01484 ; Peak H=0.04087 ; Scaled by 0.05000 ; Rotated by 221.7 deg
0.0
5.0
10.0
15.0
20.0
25.0
30.0
35.0
0.0
Particle Motion, Trace 59
Model 16, Scattered Synthetics
(Rotated)

**Figure 135**

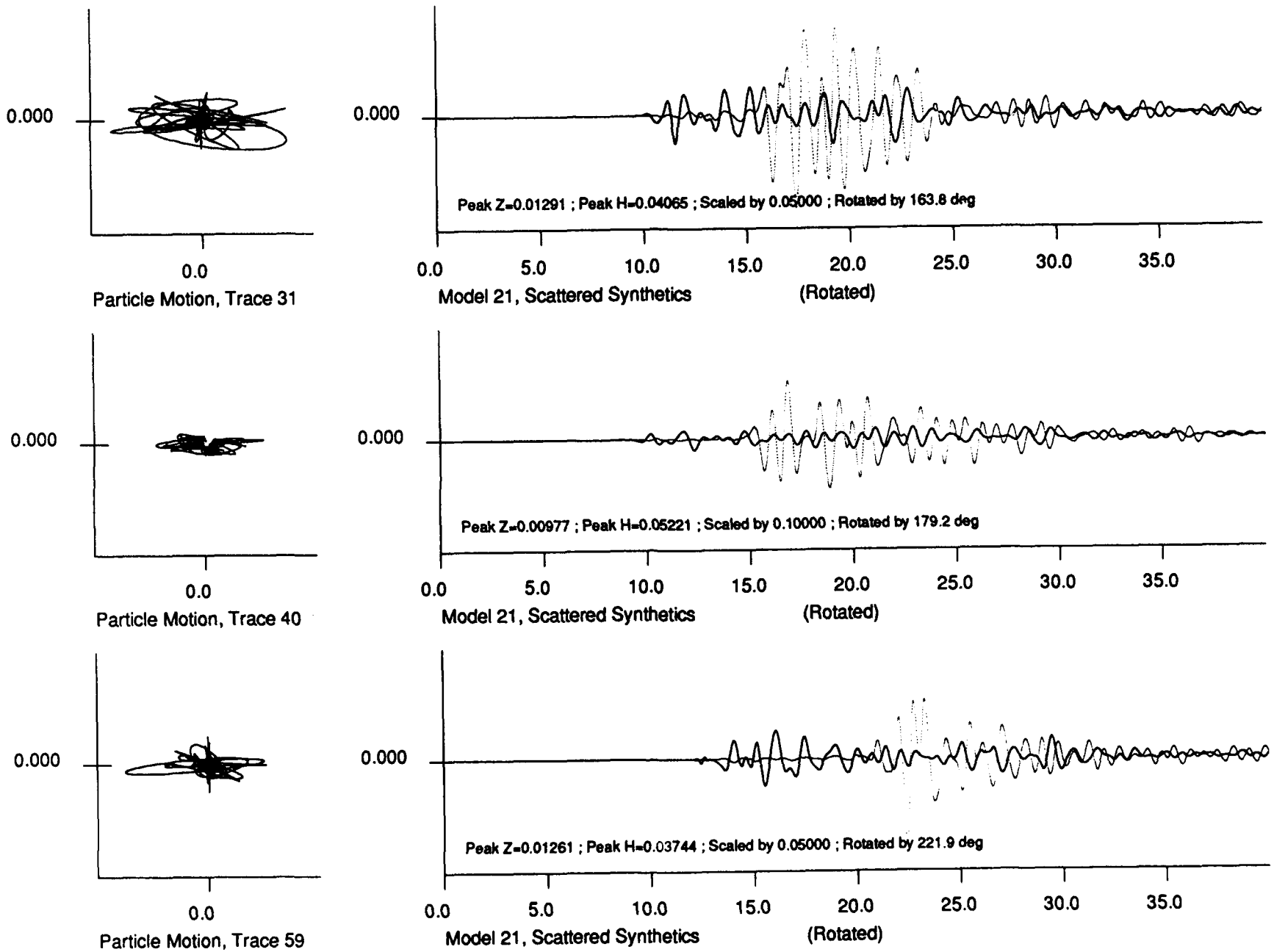

0.000
0.0
Particle Motion, Trace 31
0.000
Peak Z=0.01291 ; Peak H=0.04065 ; Scaled by 0.05000 ; Rotated by 163.8 deg
0.0 5.0 10.0 15.0 20.0 25.0 30.0 35.0
Model 21, Scattered Synthetics (Rotated)
0.000
0.0
Particle Motion, Trace 40
0.000
Peak Z=0.00977 ; Peak H=0.05221 ; Scaled by 0.10000 ; Rotated by 179.2 deg
0.0 5.0 10.0 15.0 20.0 25.0 30.0 35.0
Model 21, Scattered Synthetics (Rotated)
0.000
0.0
Particle Motion, Trace 59
0.000
Peak Z=0.01261 ; Peak H=0.03744 ; Scaled by 0.05000 ; Rotated by 221.9 deg
0.0 5.0 10.0 15.0 20.0 25.0 30.0 35.0
Model 21, Scattered Synthetics (Rotated)

**Figure 136**

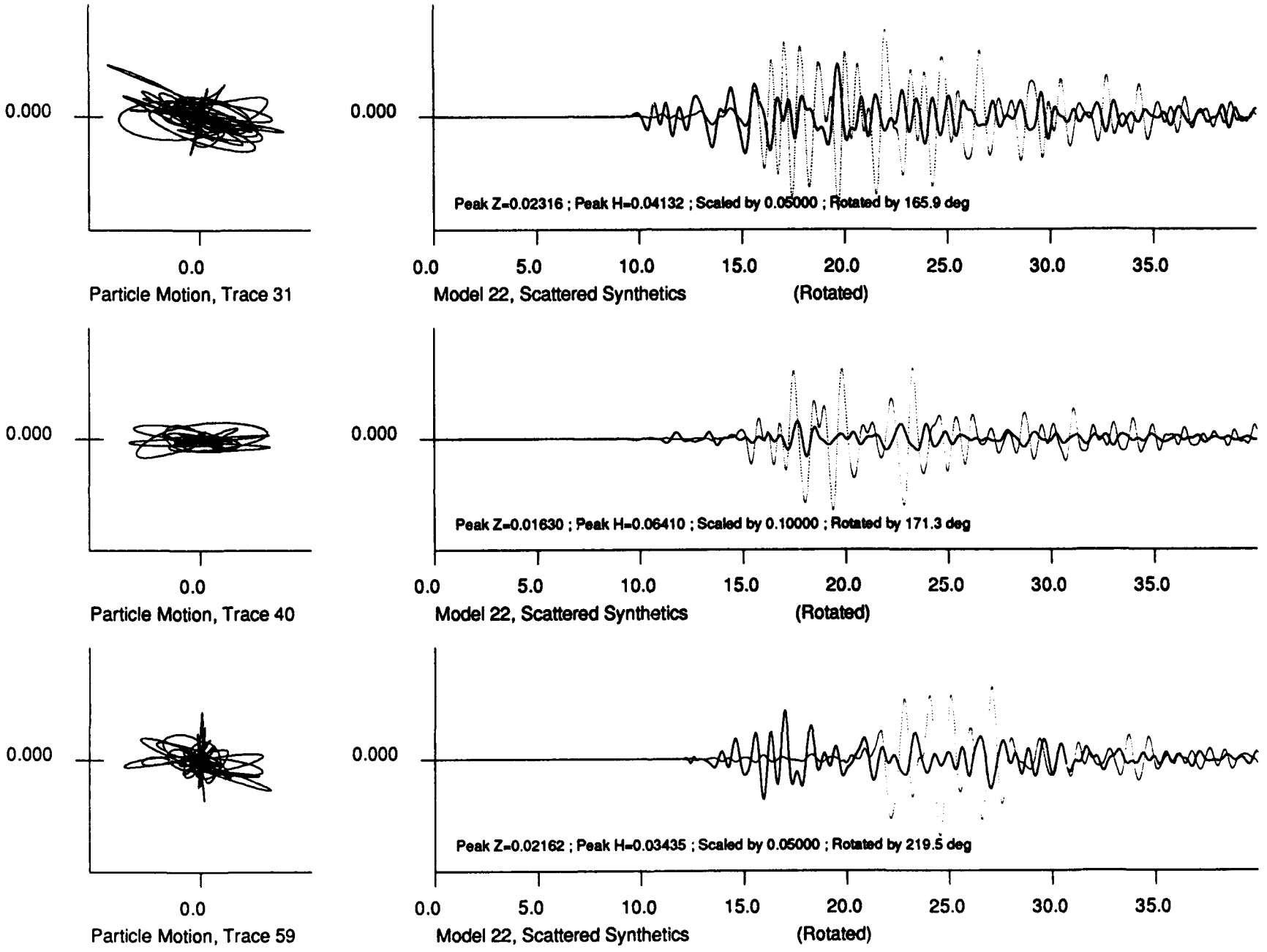

0.000
0.0
Particle Motion, Trace 31
0.000
Peak Z=0.02316 ; Peak H=0.04132 ; Scaled by 0.05000 ; Rotated by 165.9 deg
0.0 5.0 10.0 15.0 20.0 25.0 30.0 35.0
Model 22, Scattered Synthetics (Rotated)
0.000
0.0
Particle Motion, Trace 40
0.000
Peak Z=0.01630 ; Peak H=0.06410 ; Scaled by 0.10000 ; Rotated by 171.3 deg
0.0 5.0 10.0 15.0 20.0 25.0 30.0 35.0
Model 22, Scattered Synthetics (Rotated)
0.000
0.0
Particle Motion, Trace 59
0.000
Peak Z=0.02162 ; Peak H=0.03435 ; Scaled by 0.05000 ; Rotated by 219.5 deg
0.0 5.0 10.0 15.0 20.0 25.0 30.0 35.0
Model 22, Scattered Synthetics (Rotated)

**Figure 137**

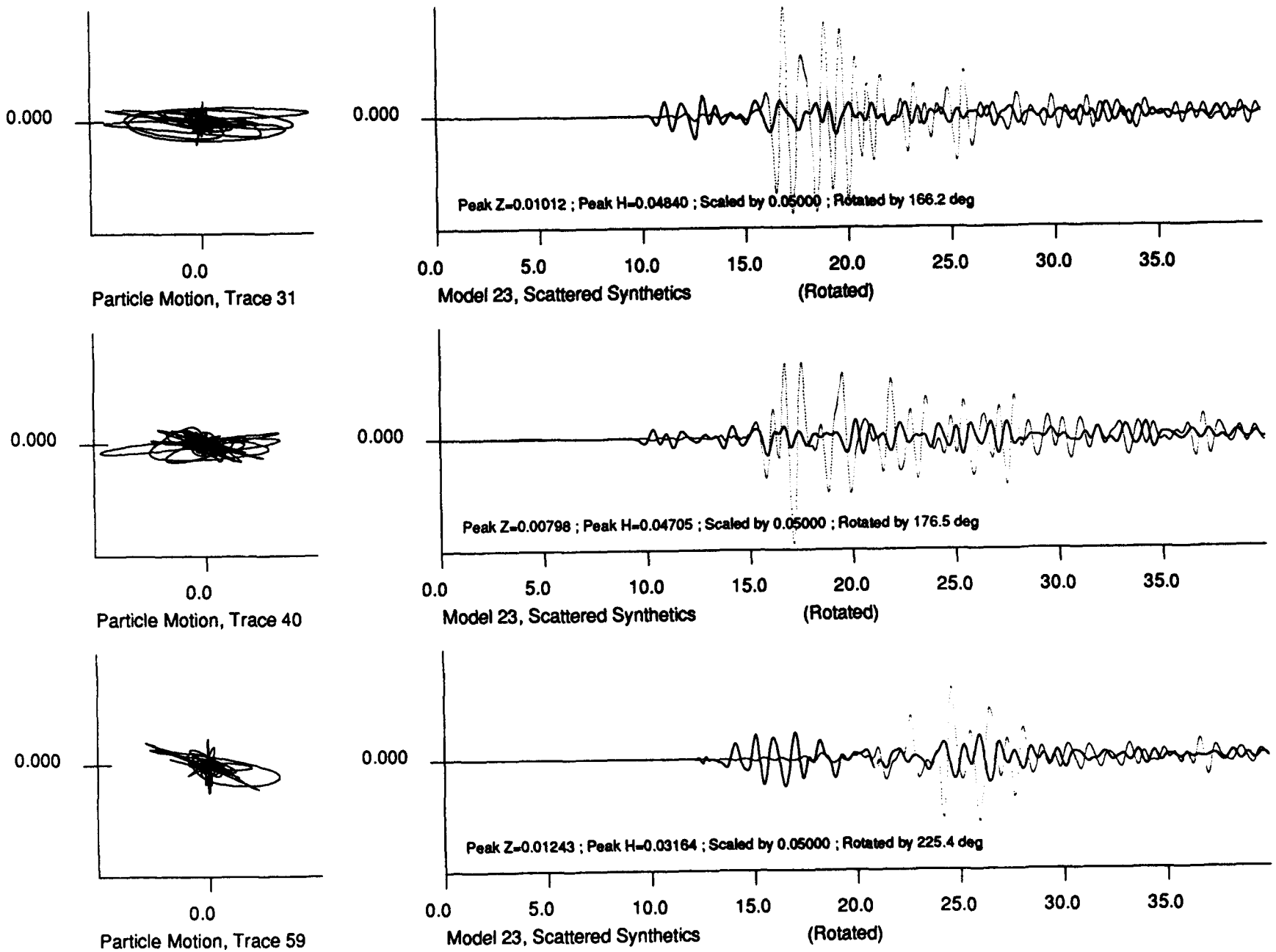

0.000
0.0
Particle Motion, Trace 31
0.000
Peak Z=0.01012 ; Peak H=0.04840 ; Scaled by 0.05000 ; Rotated by 166.2 deg
0.0 5.0 10.0 15.0 20.0 25.0 30.0 35.0
Model 23, Scattered Synthetics (Rotated)
0.000
0.0
Particle Motion, Trace 40
0.000
Peak Z=0.00798 ; Peak H=0.04705 ; Scaled by 0.05000 ; Rotated by 176.5 deg
0.0 5.0 10.0 15.0 20.0 25.0 30.0 35.0
Model 23, Scattered Synthetics (Rotated)
0.000
0.0
Particle Motion, Trace 59
0.000
Peak Z=0.01243 ; Peak H=0.03164 ; Scaled by 0.05000 ; Rotated by 225.4 deg
0.0 5.0 10.0 15.0 20.0 25.0 30.0 35.0
Model 23, Scattered Synthetics (Rotated)

**Figure 138**

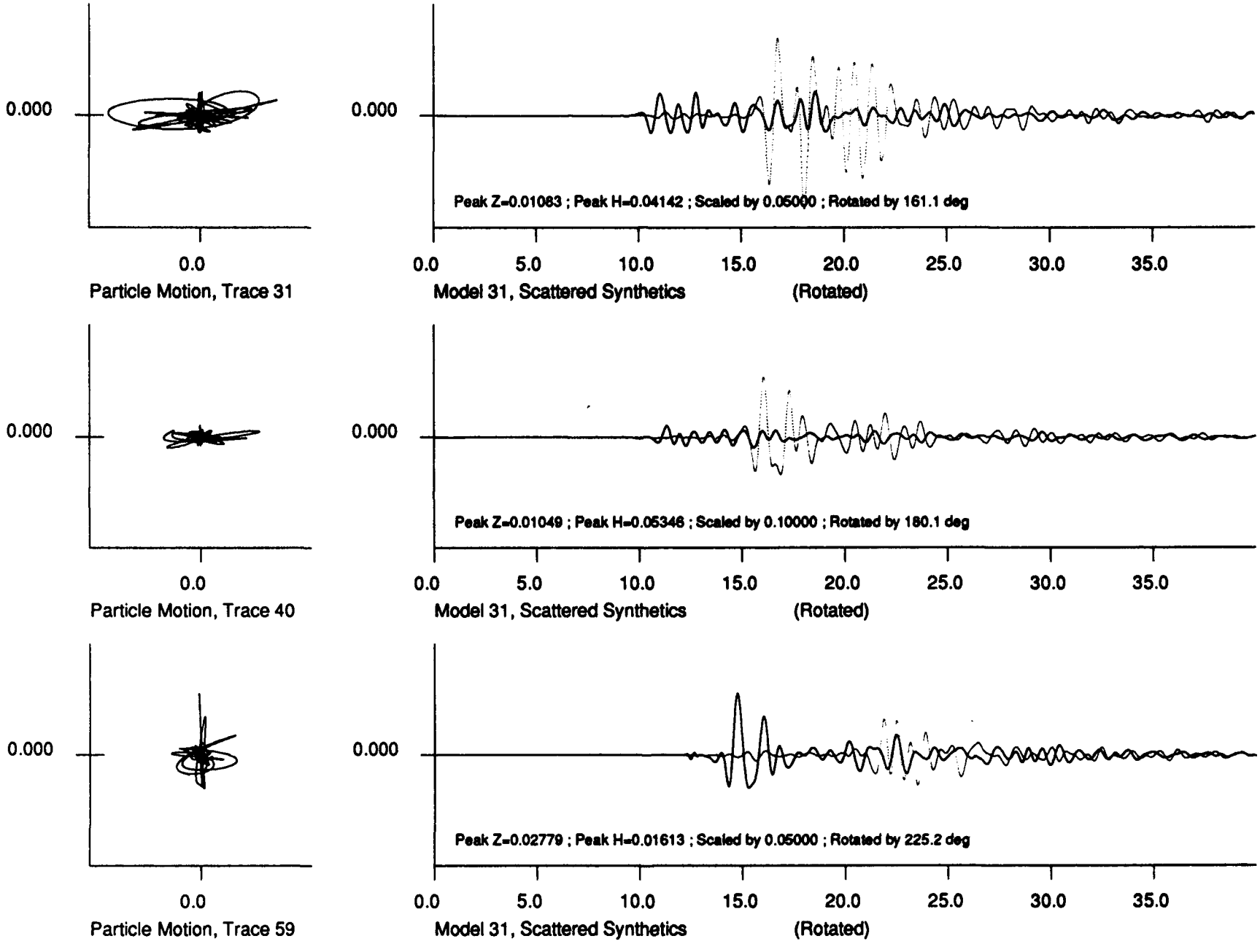

0.000
0.0
Particle Motion, Trace 31
0.000
Peak Z=0.01083 ; Peak H=0.04142 ; Scaled by 0.05000 ; Rotated by 161.1 deg
0.0 5.0 10.0 15.0 20.0 25.0 30.0 35.0
Model 31, Scattered Synthetics (Rotated)
0.000
0.0
Particle Motion, Trace 40
0.000
Peak Z=0.01049 ; Peak H=0.05346 ; Scaled by 0.10000 ; Rotated by 180.1 deg
0.0 5.0 10.0 15.0 20.0 25.0 30.0 35.0
Model 31, Scattered Synthetics (Rotated)
0.000
0.0
Particle Motion, Trace 59
0.000
Peak Z=0.02779 ; Peak H=0.01613 ; Scaled by 0.05000 ; Rotated by 225.2 deg
0.0 5.0 10.0 15.0 20.0 25.0 30.0 35.0
Model 31, Scattered Synthetics (Rotated)

**Figure 139**

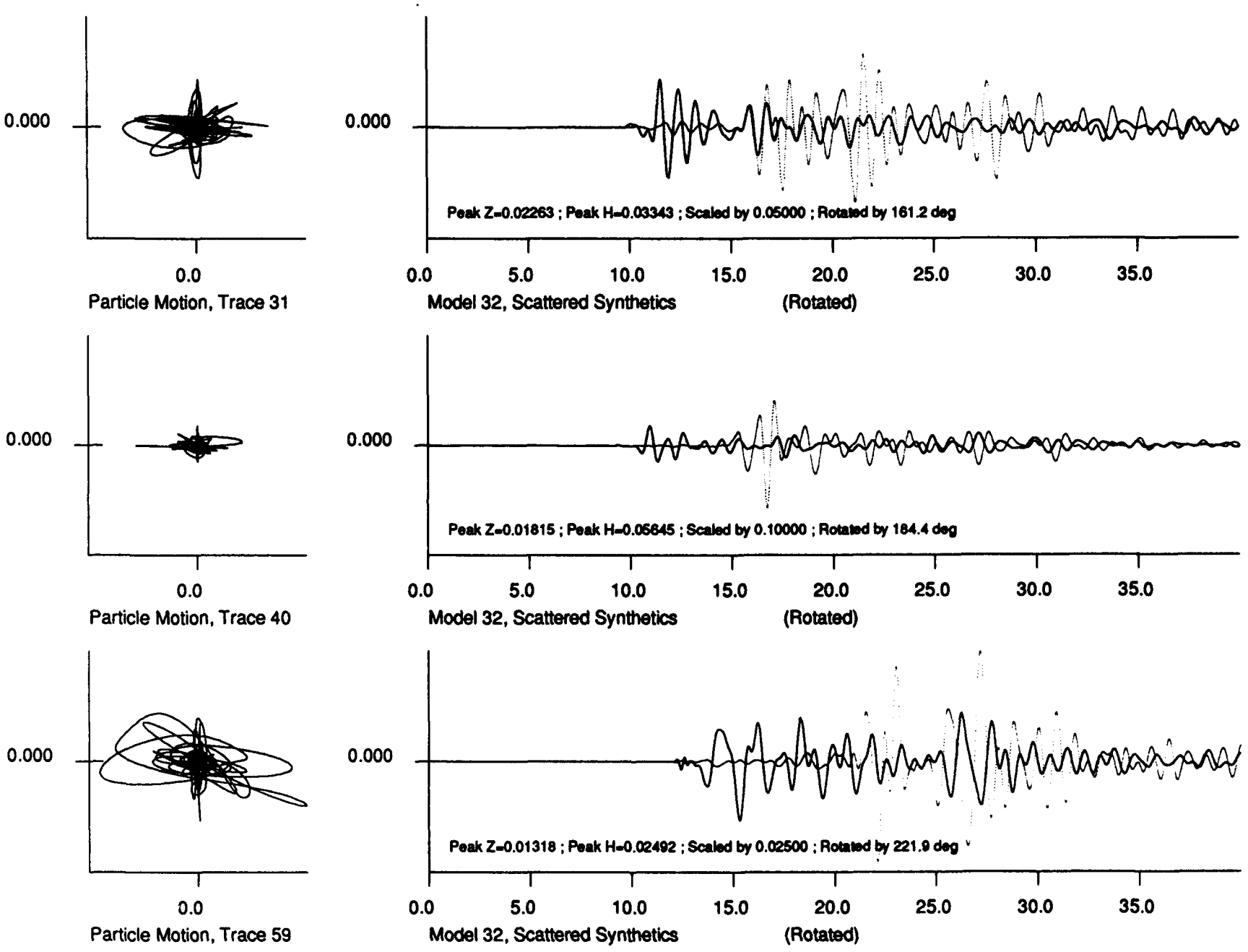

0.000
0.0
Particle Motion, Trace 31
0.000
Peak Z=0.02263 ; Peak H=0.03343 ; Scaled by 0.05000 ; Rotated by 161.2 deg
0.0 5.0 10.0 15.0 20.0 25.0 30.0 35.0
Model 32, Scattered Synthetics (Rotated)
0.000
0.0
Particle Motion, Trace 40
0.000
Peak Z=0.01815 ; Peak H=0.05645 ; Scaled by 0.10000 ; Rotated by 184.4 deg
0.0 5.0 10.0 15.0 20.0 25.0 30.0 35.0
Model 32, Scattered Synthetics (Rotated)
0.000
0.0
Particle Motion, Trace 59
0.000
Peak Z=0.01318 ; Peak H=0.02492 ; Scaled by 0.02500 ; Rotated by 221.9 deg
0.0 5.0 10.0 15.0 20.0 25.0 30.0 35.0
Model 32, Scattered Synthetics (Rotated)

**Figure 140**

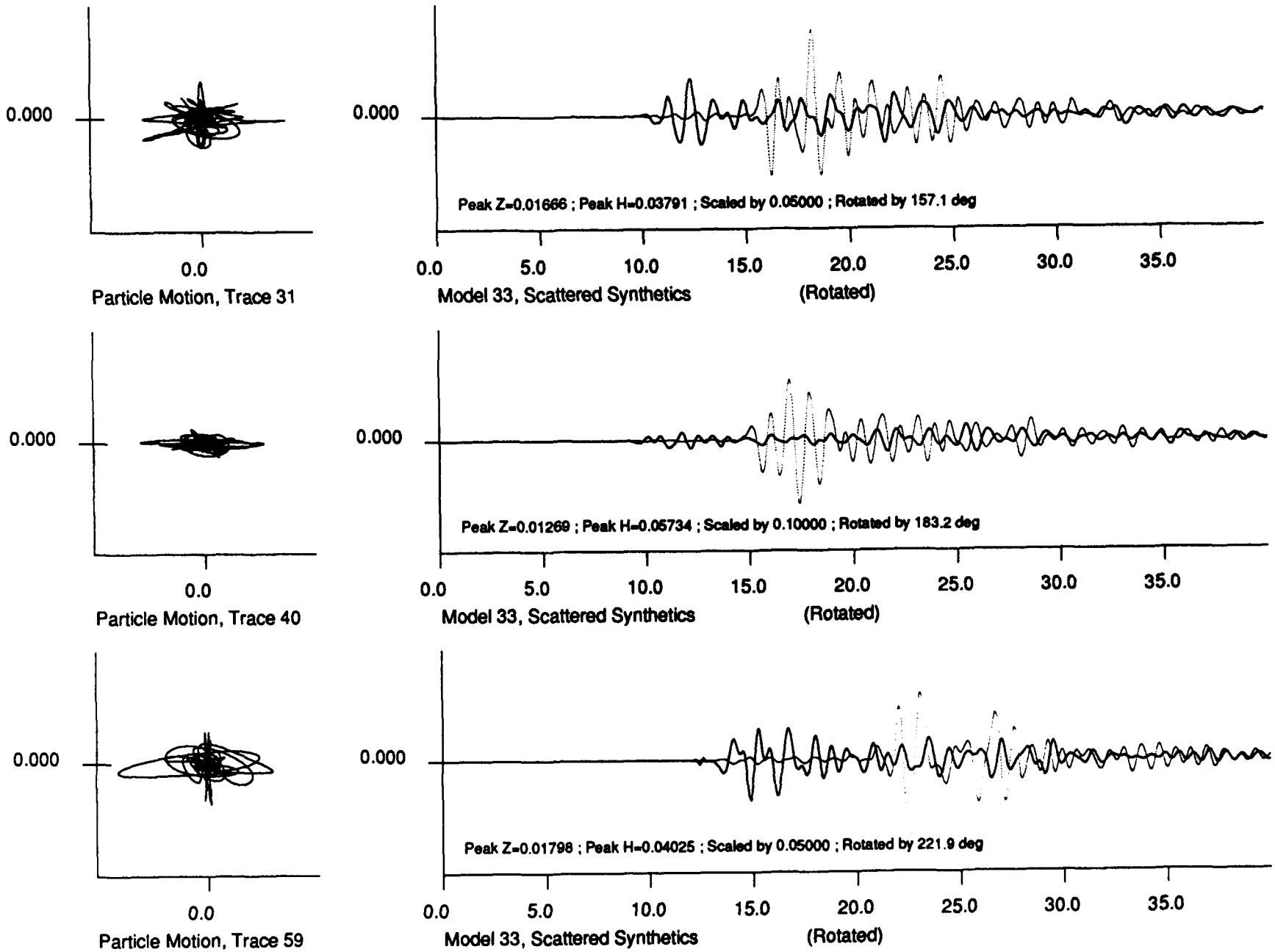

0.000
0.0
Particle Motion, Trace 31
0.000
Peak Z=0.01666 ; Peak H=0.03791 ; Scaled by 0.05000 ; Rotated by 157.1 deg
0.0 5.0 10.0 15.0 20.0 25.0 30.0 35.0
Model 33, Scattered Synthetics (Rotated)
0.000
0.0
Particle Motion, Trace 40
0.000
Peak Z=0.01269 ; Peak H=0.05734 ; Scaled by 0.10000 ; Rotated by 183.2 deg
0.0 5.0 10.0 15.0 20.0 25.0 30.0 35.0
Model 33, Scattered Synthetics (Rotated)
0.000
0.0
Particle Motion, Trace 59
0.000
Peak Z=0.01798 ; Peak H=0.04025 ; Scaled by 0.05000 ; Rotated by 221.9 deg
0.0 5.0 10.0 15.0 20.0 25.0 30.0 35.0
Model 33, Scattered Synthetics (Rotated)

**Figure 141**

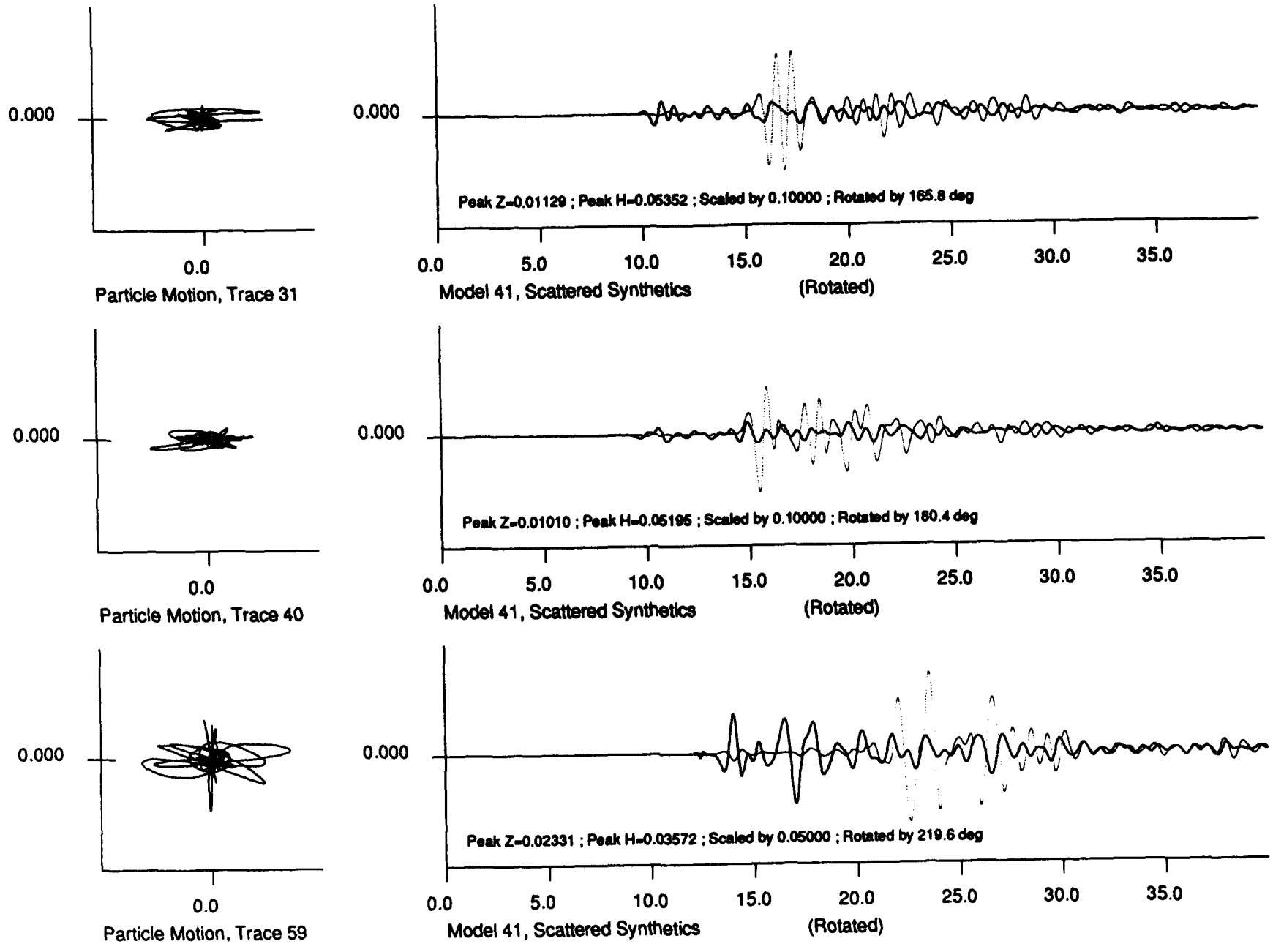

0.000
0.0
Particle Motion, Trace 31
0.000
Peak Z=0.01129 ; Peak H=0.05352 ; Scaled by 0.10000 ; Rotated by 165.8 deg
0.0 5.0 10.0 15.0 20.0 25.0 30.0 35.0
Model 41, Scattered Synthetics (Rotated)
0.000
0.0
Particle Motion, Trace 40
0.000
Peak Z=0.01010 ; Peak H=0.05195 ; Scaled by 0.10000 ; Rotated by 180.4 deg
0.0 5.0 10.0 15.0 20.0 25.0 30.0 35.0
Model 41, Scattered Synthetics (Rotated)
0.000
0.0
Particle Motion, Trace 59
0.000
Peak Z=0.02331 ; Peak H=0.03572 ; Scaled by 0.05000 ; Rotated by 219.6 deg
0.0 5.0 10.0 15.0 20.0 25.0 30.0 35.0
Model 41, Scattered Synthetics (Rotated)

**Figure 142**

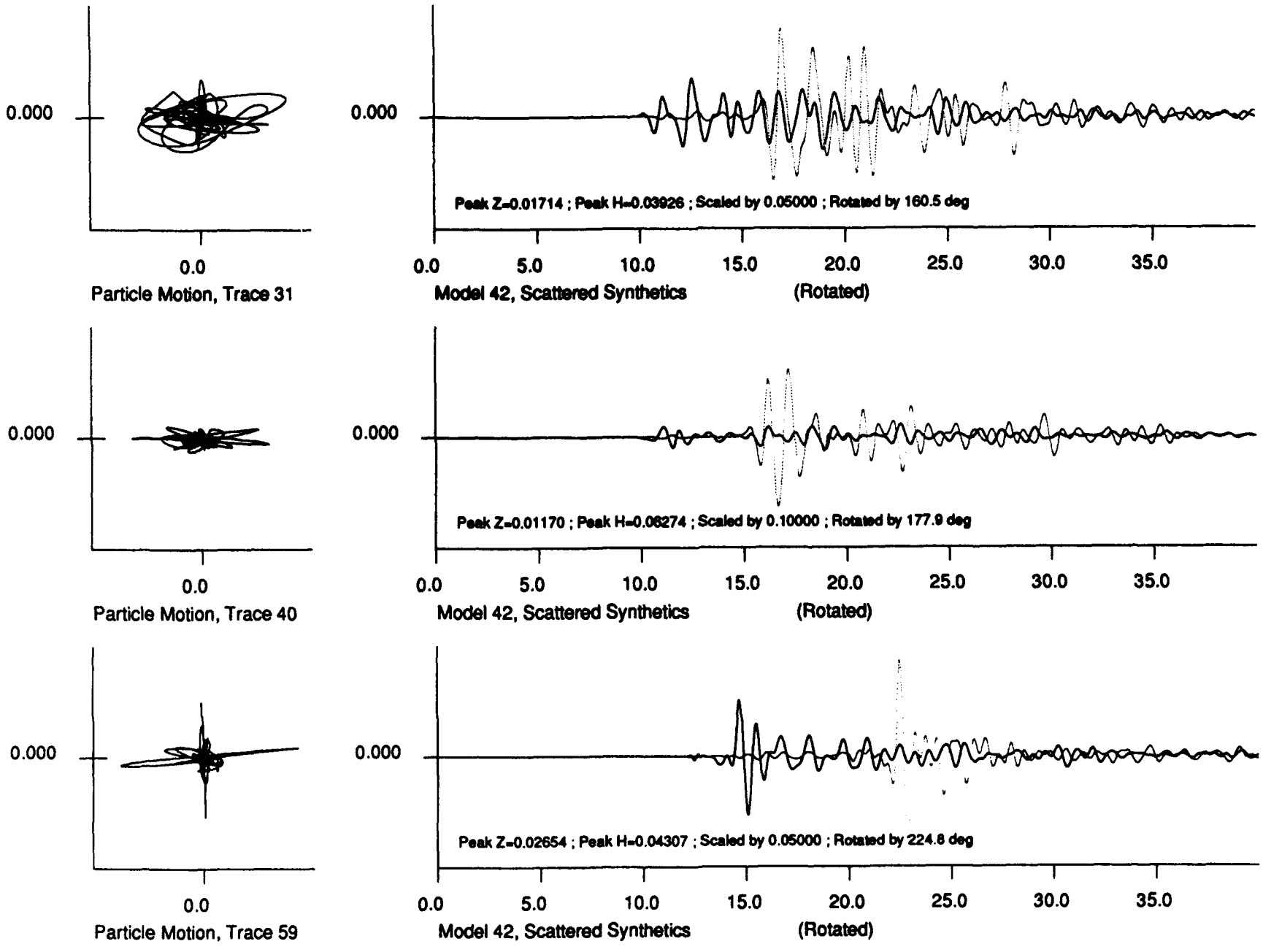

0.000
0.0
Particle Motion, Trace 31
0.000
Peak Z=0.01714 ; Peak H=0.03926 ; Scaled by 0.05000 ; Rotated by 160.5 deg
0.0 5.0 10.0 15.0 20.0 25.0 30.0 35.0
Model 42, Scattered Synthetics (Rotated)
0.000
0.0
Particle Motion, Trace 40
0.000
Peak Z=0.01170 ; Peak H=0.06274 ; Scaled by 0.10000 ; Rotated by 177.9 deg
0.0 5.0 10.0 15.0 20.0 25.0 30.0 35.0
Model 42, Scattered Synthetics (Rotated)
0.000
0.0
Particle Motion, Trace 59
0.000
Peak Z=0.02654 ; Peak H=0.04307 ; Scaled by 0.05000 ; Rotated by 224.8 deg
0.0 5.0 10.0 15.0 20.0 25.0 30.0 35.0
Model 42, Scattered Synthetics (Rotated)

**Figure 143**

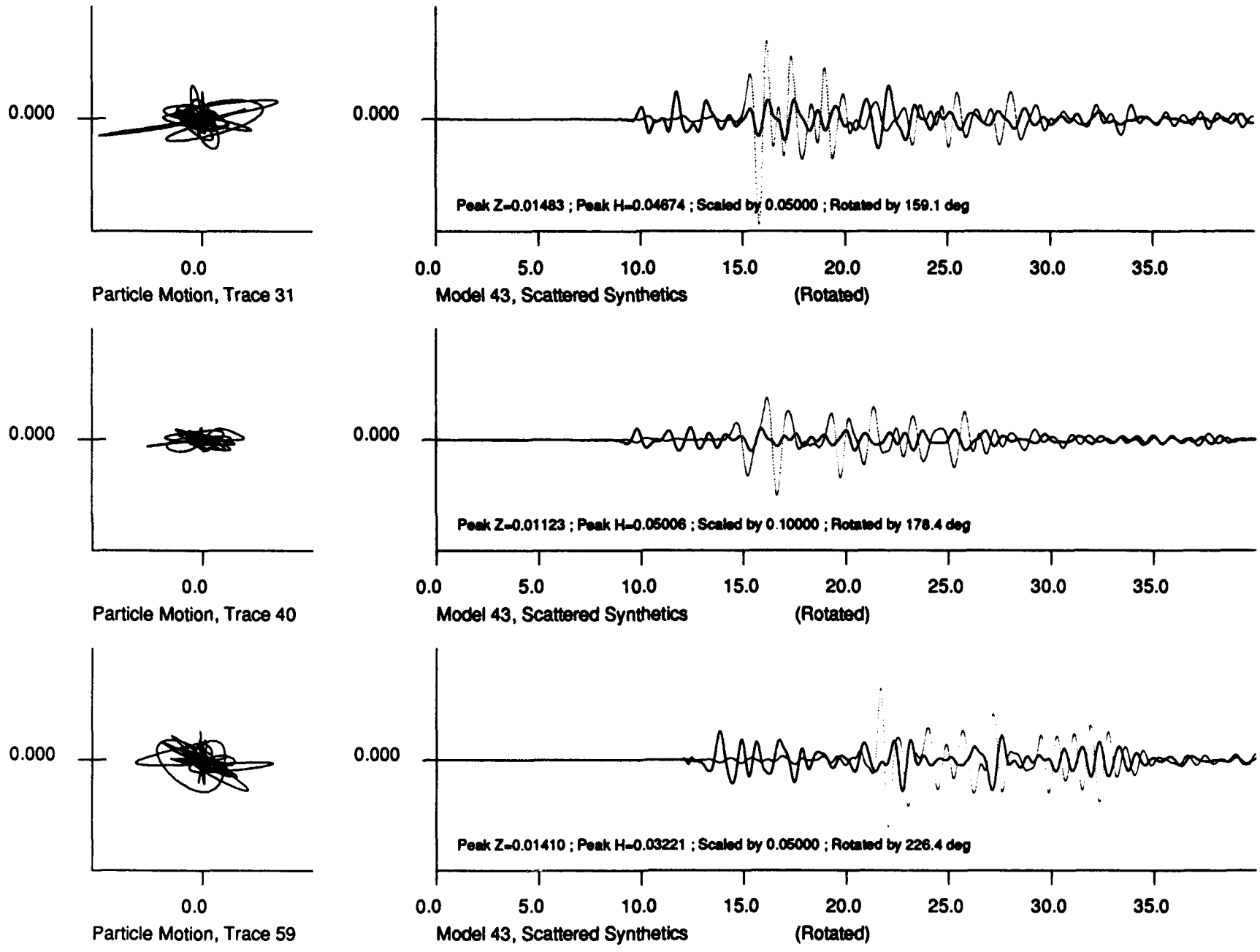

0.000
0.0
Particle Motion, Trace 31
0.000
Peak Z=0.01483 ; Peak H=0.04674 ; Scaled by 0.05000 ; Rotated by 159.1 deg
0.0 5.0 10.0 15.0 20.0 25.0 30.0 35.0
Model 43, Scattered Synthetics (Rotated)
0.000
0.0
Particle Motion, Trace 40
0.000
Peak Z=0.01123 ; Peak H=0.05006 ; Scaled by 0.10000 ; Rotated by 178.4 deg
0.0 5.0 10.0 15.0 20.0 25.0 30.0 35.0
Model 43, Scattered Synthetics (Rotated)
0.000
0.0
Particle Motion, Trace 59
0.000
Peak Z=0.01410 ; Peak H=0.03221 ; Scaled by 0.05000 ; Rotated by 226.4 deg
0.0 5.0 10.0 15.0 20.0 25.0 30.0 35.0
Model 43, Scattered Synthetics (Rotated)

**Figure 144**

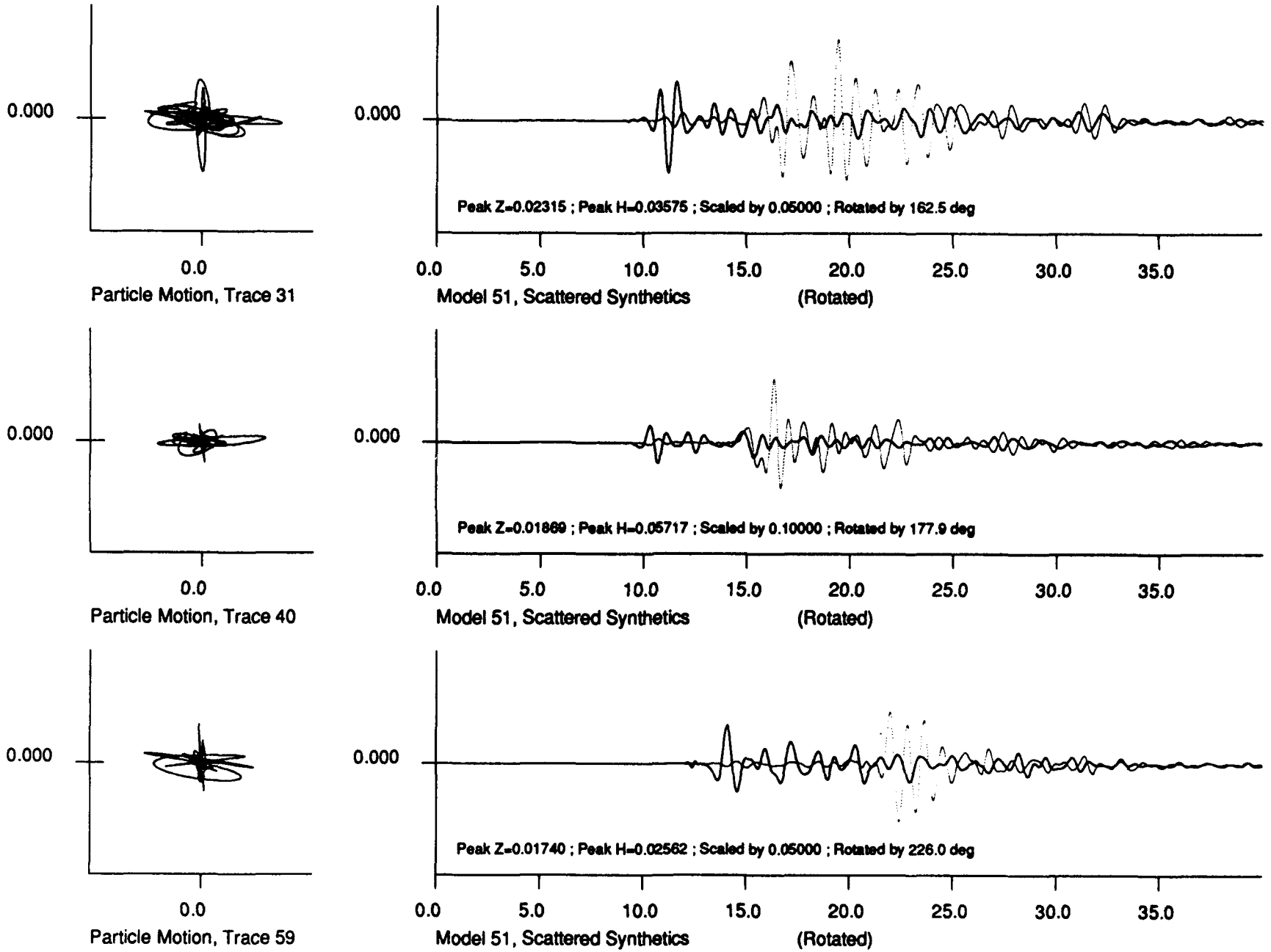

0.000
0.0
Particle Motion, Trace 31
0.000
Peak Z=0.02315 ; Peak H=0.03575 ; Scaled by 0.05000 ; Rotated by 162.5 deg
0.0 5.0 10.0 15.0 20.0 25.0 30.0 35.0
Model 51, Scattered Synthetics (Rotated)
0.000
0.0
Particle Motion, Trace 40
0.000
Peak Z=0.01869 ; Peak H=0.05717 ; Scaled by 0.10000 ; Rotated by 177.9 deg
0.0 5.0 10.0 15.0 20.0 25.0 30.0 35.0
Model 51, Scattered Synthetics (Rotated)
0.000
0.0
Particle Motion, Trace 59
0.000
Peak Z=0.01740 ; Peak H=0.02562 ; Scaled by 0.05000 ; Rotated by 226.0 deg
0.0 5.0 10.0 15.0 20.0 25.0 30.0 35.0
Model 51, Scattered Synthetics (Rotated)

**Figure 145**

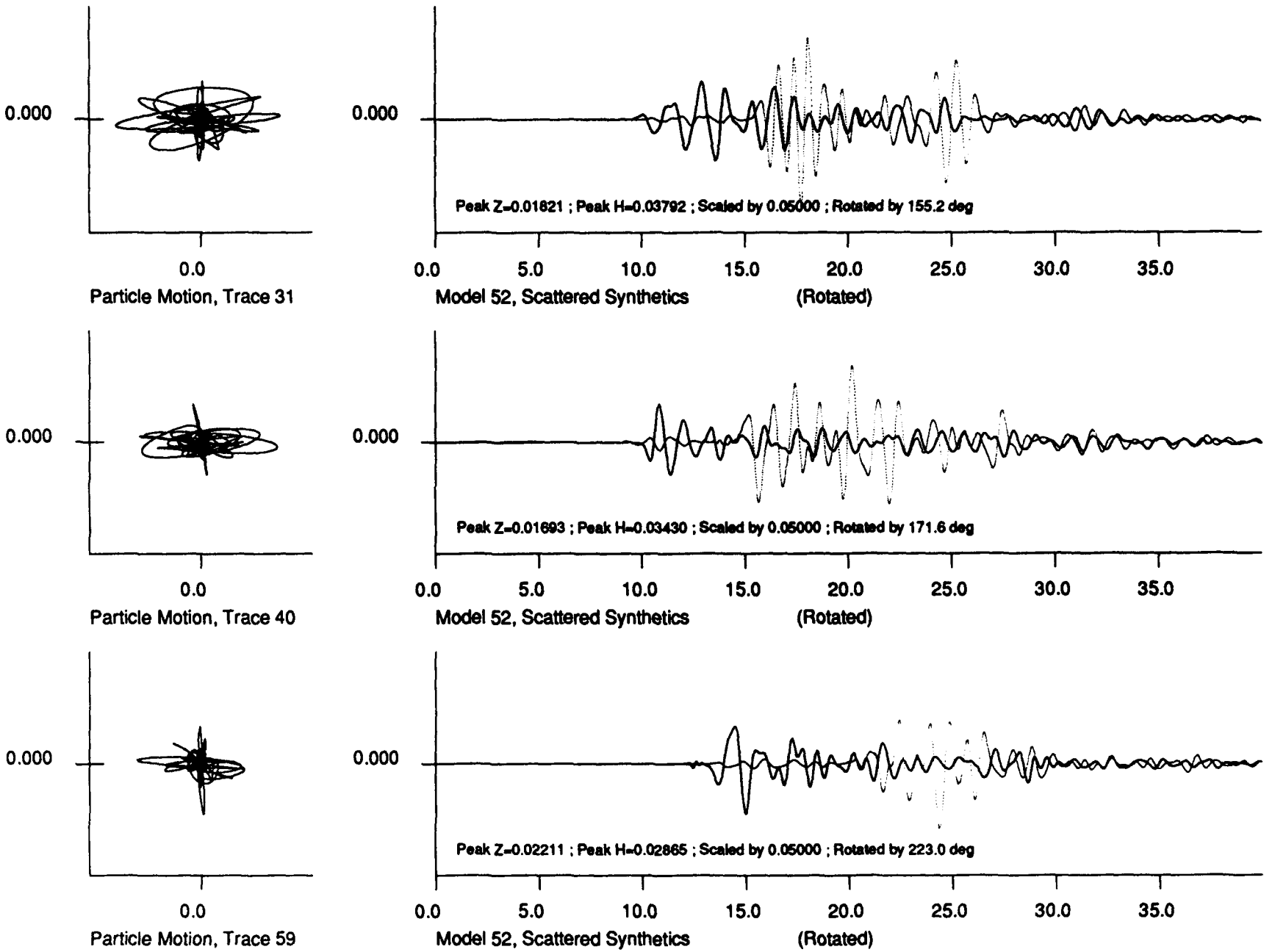

0.000
0.0
Particle Motion, Trace 31
0.000
Peak Z=0.01821 ; Peak H=0.03792 ; Scaled by 0.05000 ; Rotated by 155.2 deg
0.0 5.0 10.0 15.0 20.0 25.0 30.0 35.0
Model 52, Scattered Synthetics (Rotated)
0.000
0.0
Particle Motion, Trace 40
0.000
Peak Z=0.01693 ; Peak H=0.03430 ; Scaled by 0.05000 ; Rotated by 171.6 deg
0.0 5.0 10.0 15.0 20.0 25.0 30.0 35.0
Model 52, Scattered Synthetics (Rotated)
0.000
0.0
Particle Motion, Trace 59
0.000
Peak Z=0.02211 ; Peak H=0.02865 ; Scaled by 0.05000 ; Rotated by 223.0 deg
0.0 5.0 10.0 15.0 20.0 25.0 30.0 35.0
Model 52, Scattered Synthetics (Rotated)

**Figure 146**

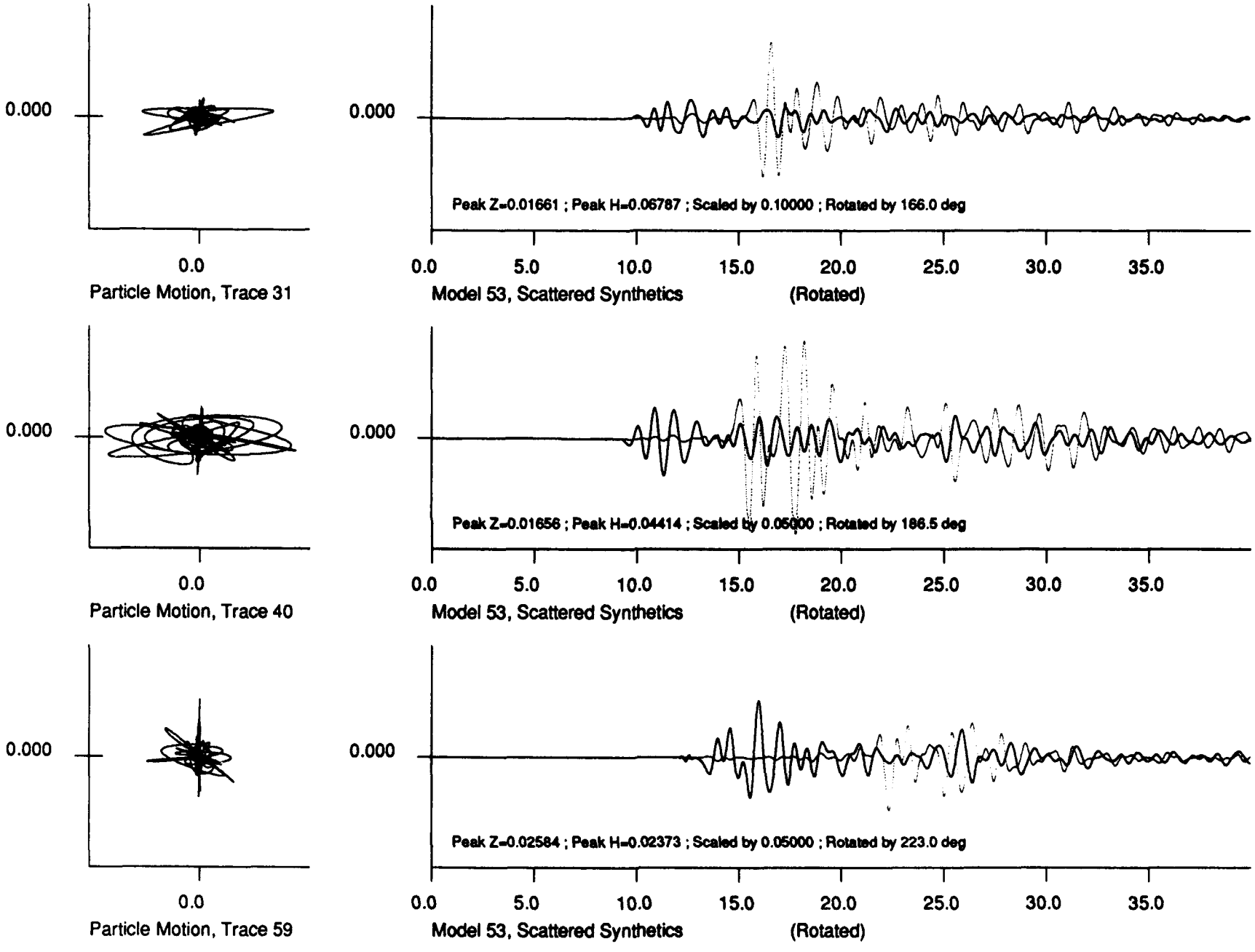

0.000
0.0
Particle Motion, Trace 31
0.000
Peak Z=0.01661 ; Peak H=0.06787 ; Scaled by 0.10000 ; Rotated by 166.0 deg
0.0 5.0 10.0 15.0 20.0 25.0 30.0 35.0
Model 53, Scattered Synthetics (Rotated)
0.000
0.0
Particle Motion, Trace 40
0.000
Peak Z=0.01656 ; Peak H=0.04414 ; Scaled by 0.05000 ; Rotated by 186.5 deg
0.0 5.0 10.0 15.0 20.0 25.0 30.0 35.0
Model 53, Scattered Synthetics (Rotated)
0.000
0.0
Particle Motion, Trace 59
0.000
Peak Z=0.02584 ; Peak H=0.02373 ; Scaled by 0.05000 ; Rotated by 223.0 deg
0.0 5.0 10.0 15.0 20.0 25.0 30.0 35.0
Model 53, Scattered Synthetics (Rotated)

**Figure 147**

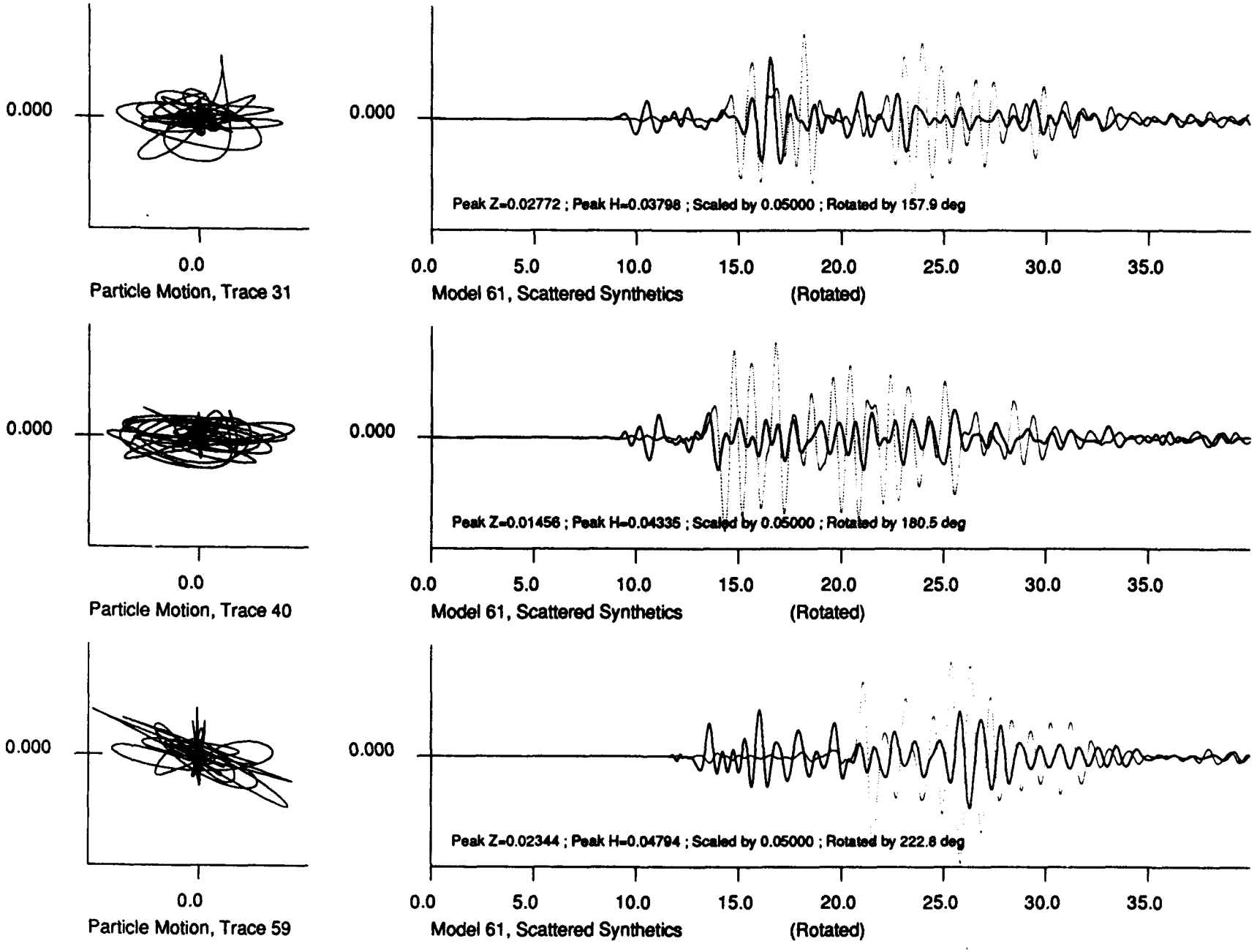

0.000
0.0
Particle Motion, Trace 31
0.000
Peak Z=0.02772 ; Peak H=0.03798 ; Scaled by 0.05000 ; Rotated by 157.9 deg
0.0 5.0 10.0 15.0 20.0 25.0 30.0 35.0
Model 61, Scattered Synthetics (Rotated)
0.000
0.0
Particle Motion, Trace 40
0.000
Peak Z=0.01456 ; Peak H=0.04335 ; Scaled by 0.05000 ; Rotated by 180.5 deg
0.0 5.0 10.0 15.0 20.0 25.0 30.0 35.0
Model 61, Scattered Synthetics (Rotated)
0.000
0.0
Particle Motion, Trace 59
0.000
Peak Z=0.02344 ; Peak H=0.04794 ; Scaled by 0.05000 ; Rotated by 222.8 deg
0.0 5.0 10.0 15.0 20.0 25.0 30.0 35.0
Model 61, Scattered Synthetics (Rotated)

**Figure 148**

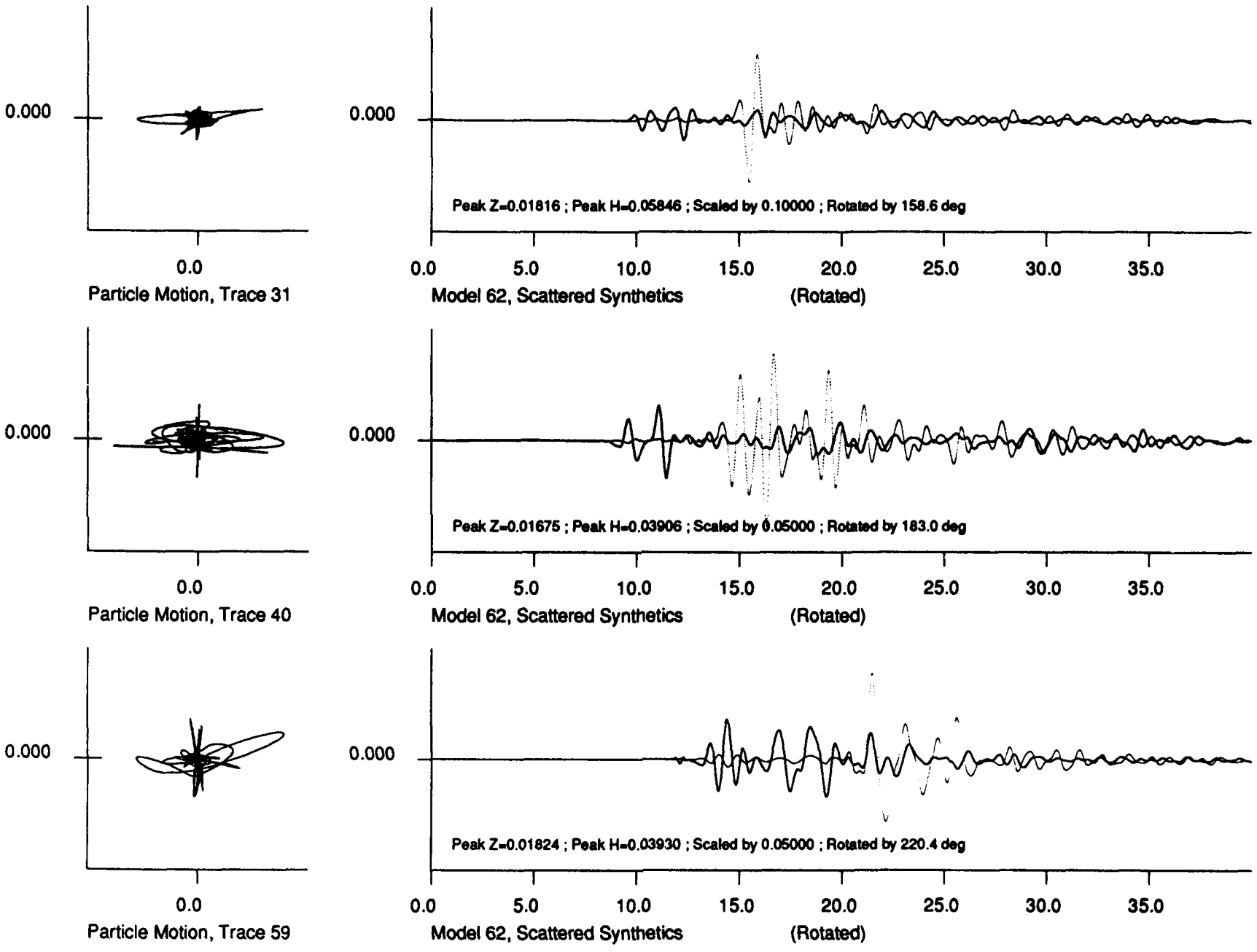

0.000
0.000
Peak Z=0.01816 ; Peak H=0.05846 ; Scaled by 0.10000 ; Rotated by 158.6 deg
0.0
5.0
10.0
15.0
20.0
25.0
30.0
35.0
0.0
Particle Motion, Trace 31
Model 62, Scattered Synthetics
(Rotated)
0.000
0.000
Peak Z=0.01675 ; Peak H=0.03906 ; Scaled by 0.05000 ; Rotated by 183.0 deg
0.0
5.0
10.0
15.0
20.0
25.0
30.0
35.0
0.0
Particle Motion, Trace 40
Model 62, Scattered Synthetics
(Rotated)
0.000
0.000
Peak Z=0.01824 ; Peak H=0.03930 ; Scaled by 0.05000 ; Rotated by 220.4 deg
0.0
5.0
10.0
15.0
20.0
25.0
30.0
35.0
0.0
Particle Motion, Trace 59
Model 62, Scattered Synthetics
(Rotated)

**Figure 149**

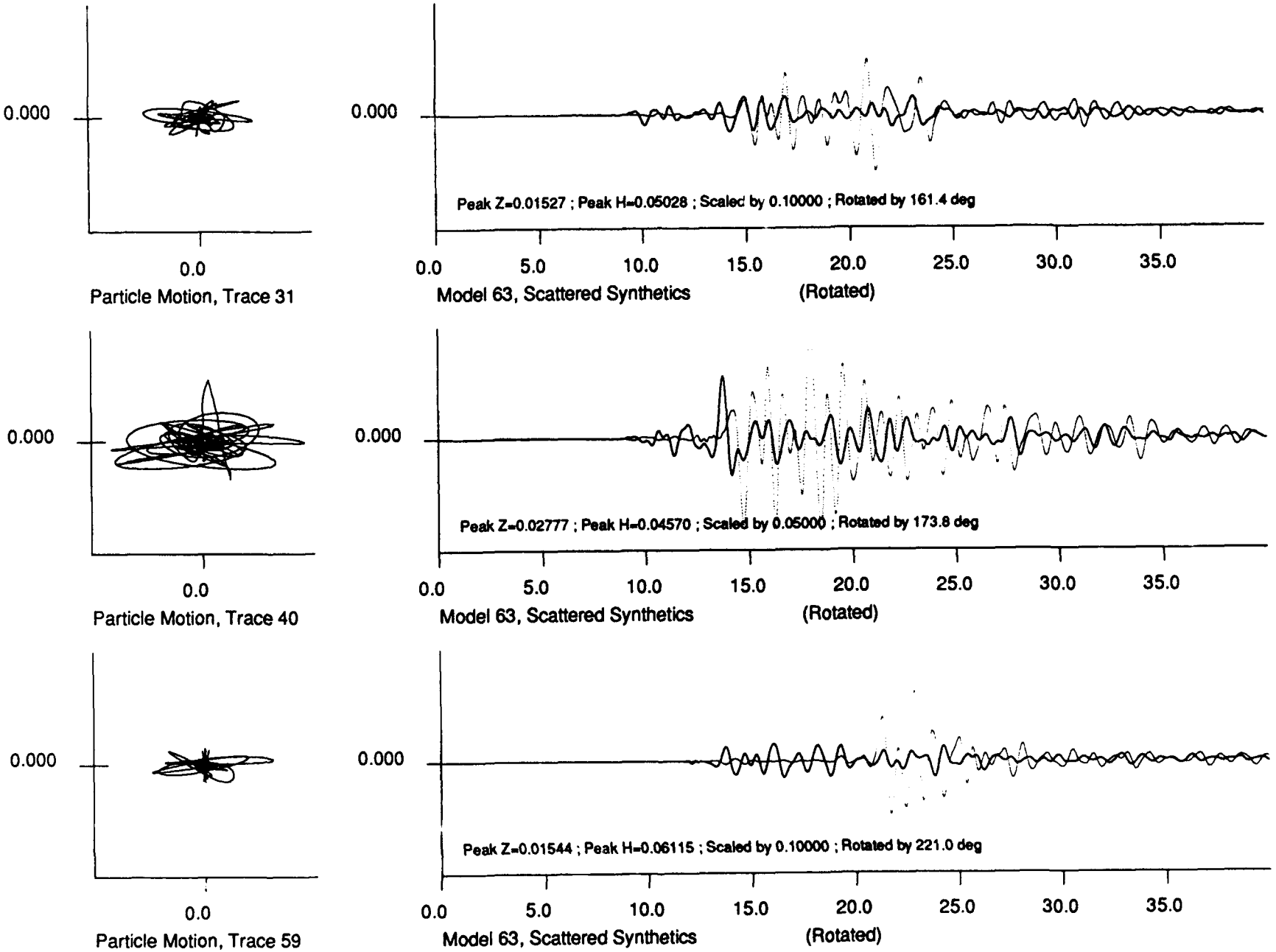

0.000
0.0
Particle Motion, Trace 31
0.000
Peak Z=0.01527 ; Peak H=0.05028 ; Scaled by 0.10000 ; Rotated by 161.4 deg
0.0 5.0 10.0 15.0 20.0 25.0 30.0 35.0
Model 63, Scattered Synthetics (Rotated)
0.000
0.0
Particle Motion, Trace 40
0.000
Peak Z=0.02777 ; Peak H=0.04570 ; Scaled by 0.05000 ; Rotated by 173.8 deg
0.0 5.0 10.0 15.0 20.0 25.0 30.0 35.0
Model 63, Scattered Synthetics (Rotated)
0.000
0.0
Particle Motion, Trace 59
0.000
Peak Z=0.01544 ; Peak H=0.06115 ; Scaled by 0.10000 ; Rotated by 221.0 deg
0.0 5.0 10.0 15.0 20.0 25.0 30.0 35.0
Model 63, Scattered Synthetics (Rotated)

**Figure 150**

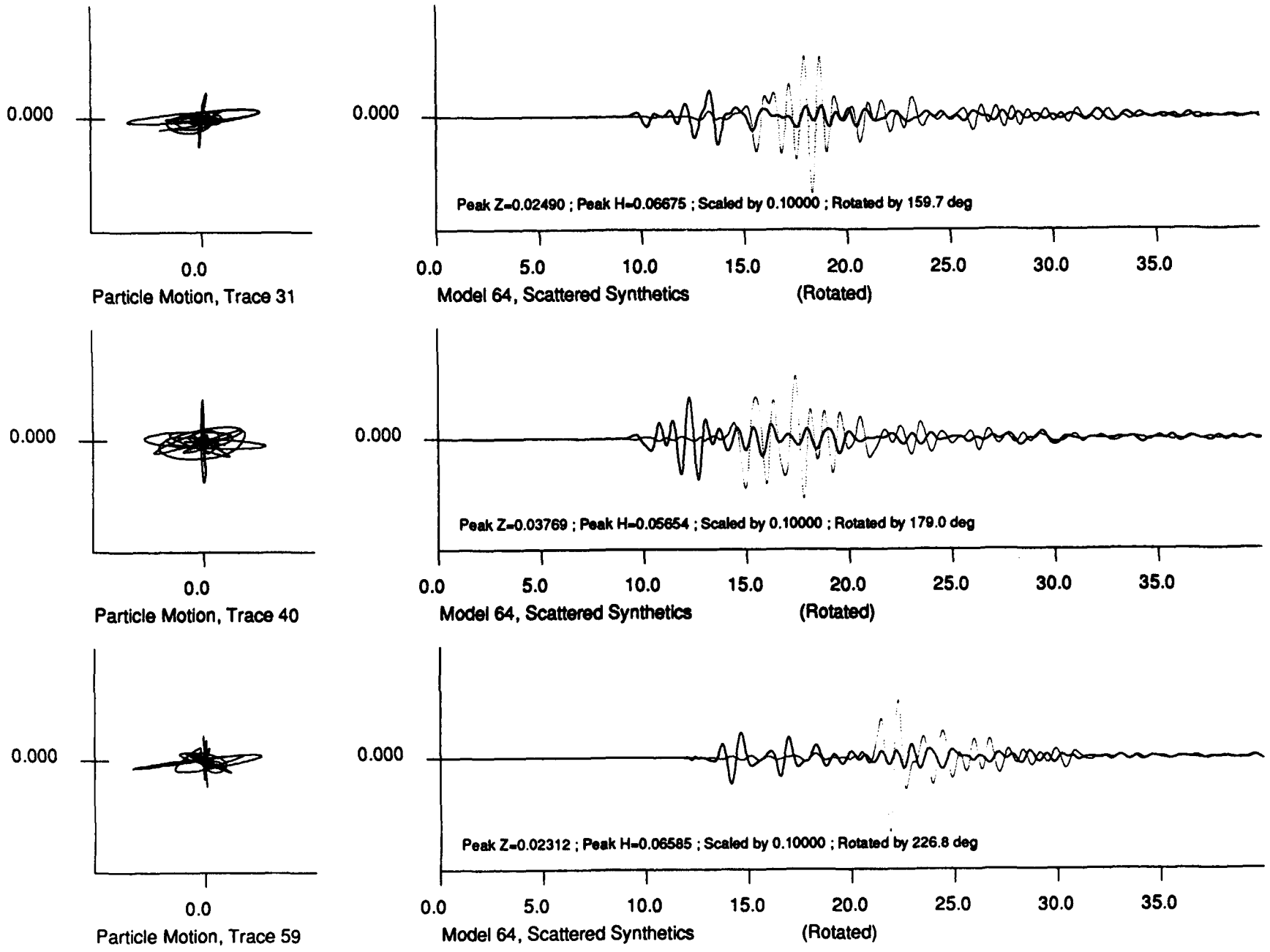

0.000
0.0
Particle Motion, Trace 31
0.000
Peak Z=0.02490 ; Peak H=0.06675 ; Scaled by 0.10000 ; Rotated by 159.7 deg
0.0 5.0 10.0 15.0 20.0 25.0 30.0 35.0
Model 64, Scattered Synthetics (Rotated)
0.000
0.0
Particle Motion, Trace 40
0.000
Peak Z=0.03769 ; Peak H=0.05654 ; Scaled by 0.10000 ; Rotated by 179.0 deg
0.0 5.0 10.0 15.0 20.0 25.0 30.0 35.0
Model 64, Scattered Synthetics (Rotated)
0.000
0.0
Particle Motion, Trace 59
0.000
Peak Z=0.02312 ; Peak H=0.06585 ; Scaled by 0.10000 ; Rotated by 226.8 deg
0.0 5.0 10.0 15.0 20.0 25.0 30.0 35.0
Model 64, Scattered Synthetics (Rotated)

**Figure 151**

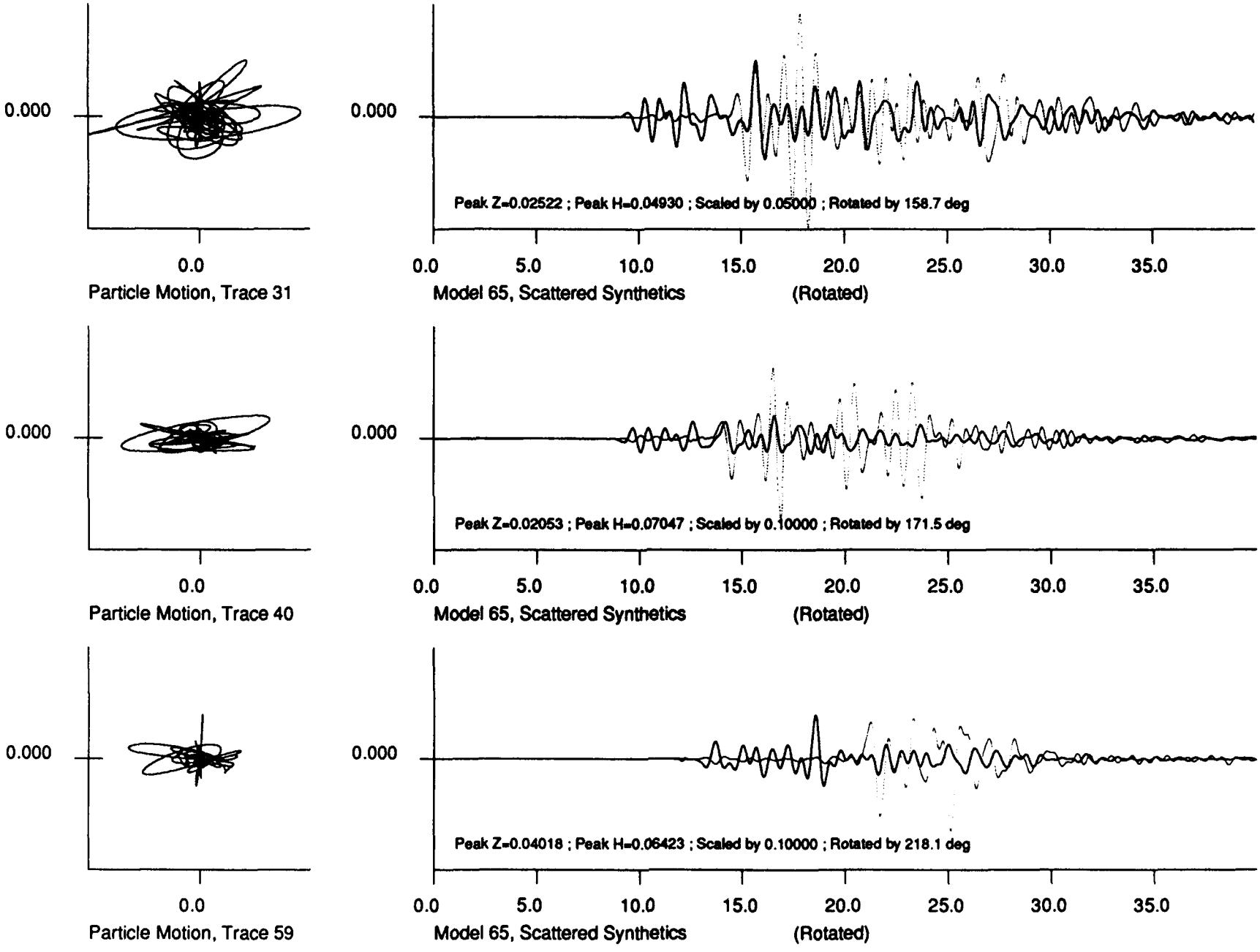

0.000
0.0
Particle Motion, Trace 31
0.000
Peak Z=0.02522 ; Peak H=0.04930 ; Scaled by 0.05000 ; Rotated by 158.7 deg
0.0 5.0 10.0 15.0 20.0 25.0 30.0 35.0
Model 65, Scattered Synthetics (Rotated)
0.000
0.0
Particle Motion, Trace 40
0.000
Peak Z=0.02053 ; Peak H=0.07047 ; Scaled by 0.10000 ; Rotated by 171.5 deg
0.0 5.0 10.0 15.0 20.0 25.0 30.0 35.0
Model 65, Scattered Synthetics (Rotated)
0.000
0.0
Particle Motion, Trace 59
0.000
Peak Z=0.04018 ; Peak H=0.06423 ; Scaled by 0.10000 ; Rotated by 218.1 deg
0.0 5.0 10.0 15.0 20.0 25.0 30.0 35.0
Model 65, Scattered Synthetics (Rotated)

**Figure 152**

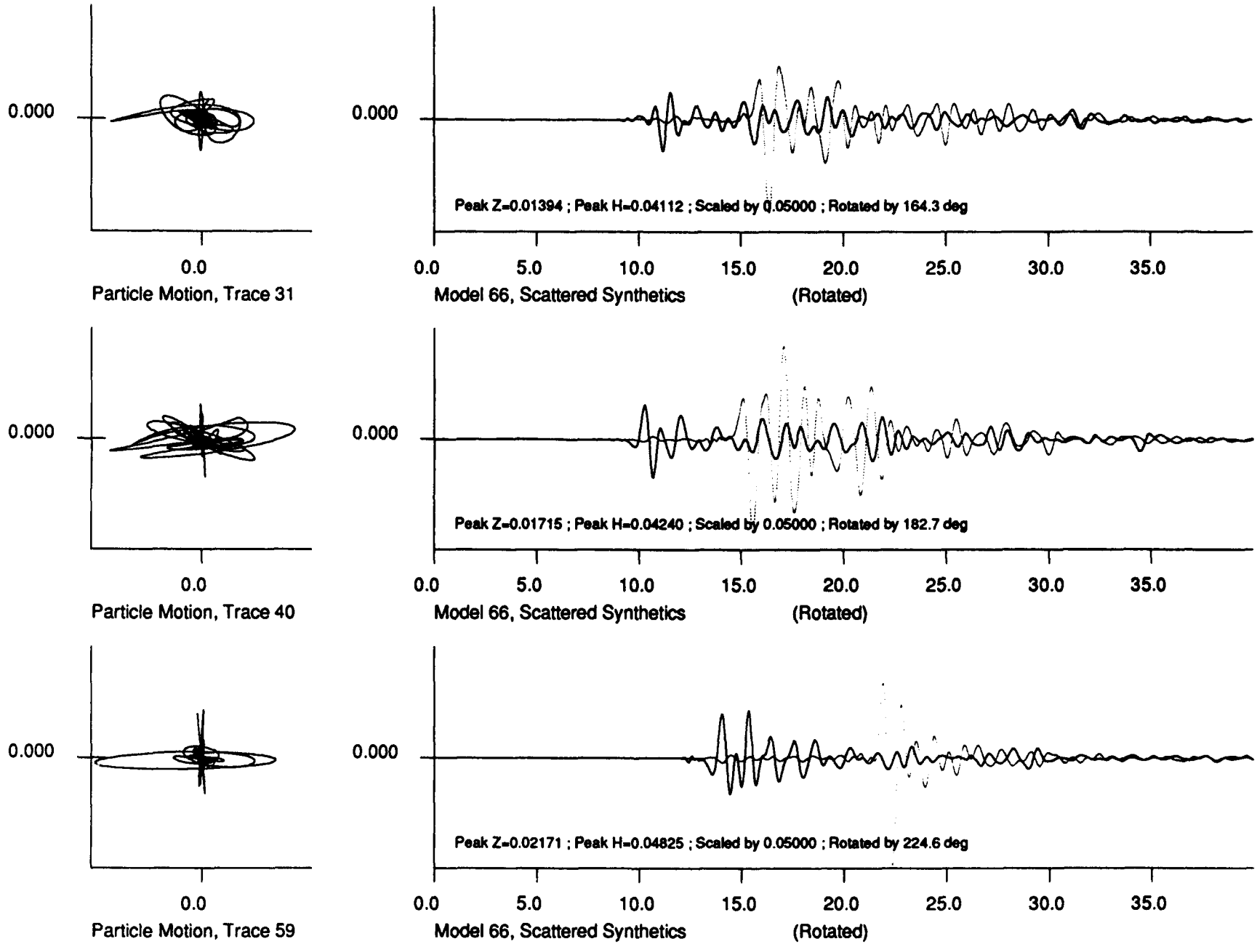

0.000
0.0
Particle Motion, Trace 31
0.000
Peak Z=0.01394 ; Peak H=0.04112 ; Scaled by 0.05000 ; Rotated by 164.3 deg
0.0 5.0 10.0 15.0 20.0 25.0 30.0 35.0
Model 66, Scattered Synthetics (Rotated)
0.000
0.0
Particle Motion, Trace 40
0.000
Peak Z=0.01715 ; Peak H=0.04240 ; Scaled by 0.05000 ; Rotated by 182.7 deg
0.0 5.0 10.0 15.0 20.0 25.0 30.0 35.0
Model 66, Scattered Synthetics (Rotated)
0.000
0.0
Particle Motion, Trace 59
0.000
Peak Z=0.02171 ; Peak H=0.04825 ; Scaled by 0.05000 ; Rotated by 224.6 deg
0.0 5.0 10.0 15.0 20.0 25.0 30.0 35.0
Model 66, Scattered Synthetics (Rotated)

**Figure 153**

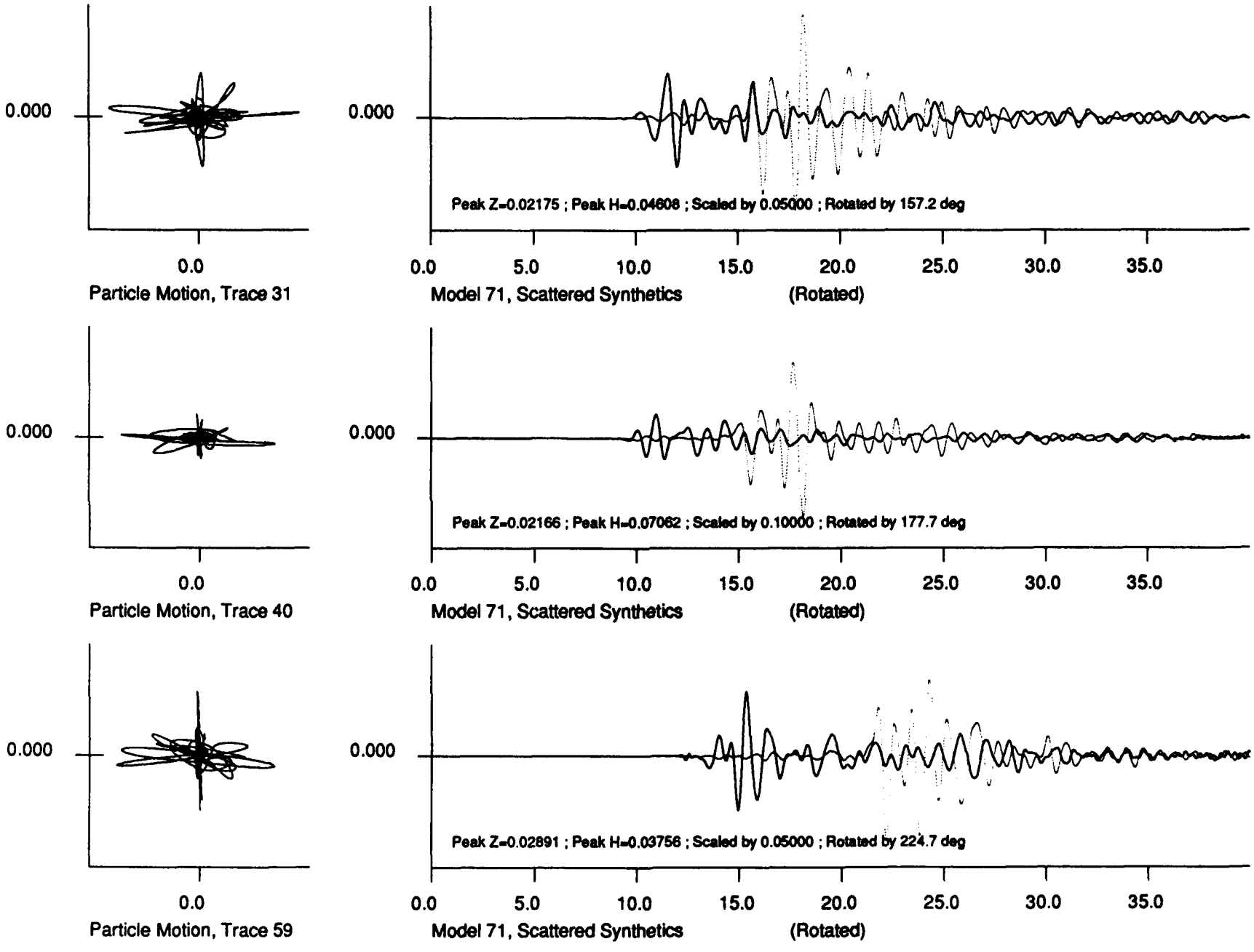

0.000
0.0
Particle Motion, Trace 31
0.000
Peak Z=0.02175 ; Peak H=0.04608 ; Scaled by 0.05000 ; Rotated by 157.2 deg
0.0 5.0 10.0 15.0 20.0 25.0 30.0 35.0
Model 71, Scattered Synthetics (Rotated)
0.000
0.0
Particle Motion, Trace 40
0.000
Peak Z=0.02166 ; Peak H=0.07062 ; Scaled by 0.10000 ; Rotated by 177.7 deg
0.0 5.0 10.0 15.0 20.0 25.0 30.0 35.0
Model 71, Scattered Synthetics (Rotated)
0.000
0.0
Particle Motion, Trace 59
0.000
Peak Z=0.02891 ; Peak H=0.03756 ; Scaled by 0.05000 ; Rotated by 224.7 deg
0.0 5.0 10.0 15.0 20.0 25.0 30.0 35.0
Model 71, Scattered Synthetics (Rotated)

**Figure 154**

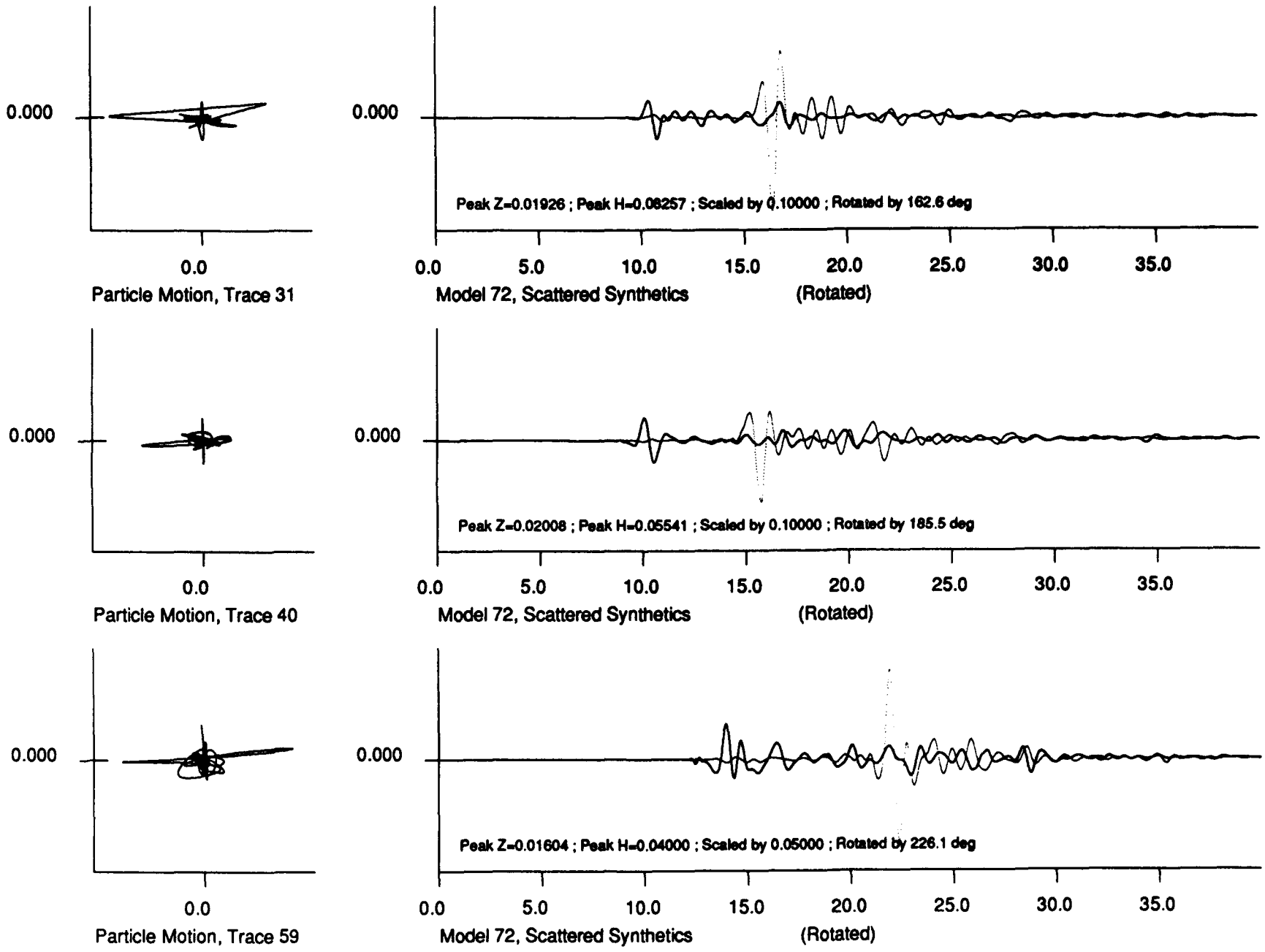

0.000
0.0
Particle Motion, Trace 31
0.000
Peak Z=0.01926 ; Peak H=0.08257 ; Scaled by 0.10000 ; Rotated by 162.6 deg
0.0 5.0 10.0 15.0 20.0 25.0 30.0 35.0
Model 72, Scattered Synthetics (Rotated)
0.000
0.0
Particle Motion, Trace 40
0.000
Peak Z=0.02008 ; Peak H=0.05541 ; Scaled by 0.10000 ; Rotated by 185.5 deg
0.0 5.0 10.0 15.0 20.0 25.0 30.0 35.0
Model 72, Scattered Synthetics (Rotated)
0.000
0.0
Particle Motion, Trace 59
0.000
Peak Z=0.01604 ; Peak H=0.04000 ; Scaled by 0.05000 ; Rotated by 226.1 deg
0.0 5.0 10.0 15.0 20.0 25.0 30.0 35.0
Model 72, Scattered Synthetics (Rotated)

**Figure 155**

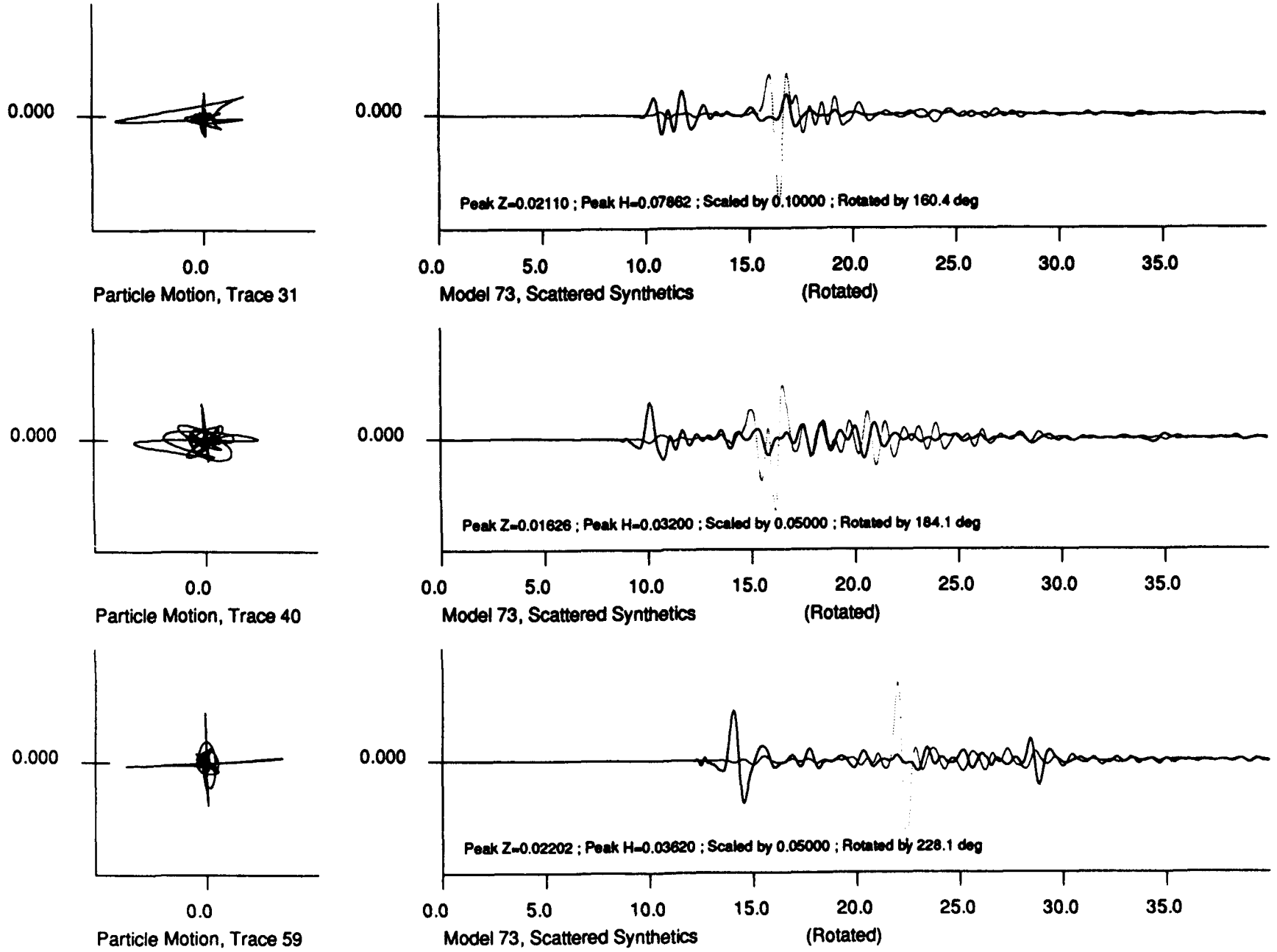

0.000
0.0
Particle Motion, Trace 31
0.000
Peak Z=0.02110 ; Peak H=0.07862 ; Scaled by 0.10000 ; Rotated by 160.4 deg
0.0 5.0 10.0 15.0 20.0 25.0 30.0 35.0
Model 73, Scattered Synthetics (Rotated)
0.000
0.0
Particle Motion, Trace 40
0.000
Peak Z=0.01626 ; Peak H=0.03200 ; Scaled by 0.05000 ; Rotated by 184.1 deg
0.0 5.0 10.0 15.0 20.0 25.0 30.0 35.0
Model 73, Scattered Synthetics (Rotated)
0.000
0.0
Particle Motion, Trace 59
0.000
Peak Z=0.02202 ; Peak H=0.03620 ; Scaled by 0.05000 ; Rotated by 228.1 deg
0.0 5.0 10.0 15.0 20.0 25.0 30.0 35.0
Model 73, Scattered Synthetics (Rotated)

**Figure 156**

# DISTRIBUTION LIST

## NON-GOVERNMENT CONTRACTORS

Prof. Thomas Ahrens
Seismological Lab, 252-21
Div. of Geol. & Planetary Sciences
California Institute of Technology
Pasadena, CA 91125

Dr. Thomas C. Bache, Jr.
Dr. Thomas J. Sereno, Jr.
Science Applications Int'l Corp.
10260 Campus Point Drive
San Diego, CA 92121 (2)

Dr. Peter Basham
Dr. Robert North
Earth Physics Branch
Geological Survey of Canada
1 Observatory Crescent
Ottawa, Ontario,CANADA K1A OY3

Dr. Douglas R. Baumgardt
Dr. Zoltan A. Der
ENSCO, Inc.
5400 Port Royal Road
Springfield, VA 22151-2388

Prof. Jonathan Berger
IGPP, A-025
Scripps Institution of Oceanography
University of California, San Diego
La Jolla, CA 92093

Dr. G. A. Bollinger
Department of Geological Sciences
Virginia Polytechnic Institute
21044 Derring Hall
Blacksburg, VA 24061

The Librarian
Dr. Jerry Carter
Dr. Stephen Bratt
Center for Seismic Studies
1300 North 17th Street, Suite 1450
Arlington, VA 22209-2308 (3)

Michael Browne
Teledyne Brown Engineering
3401 Shiloh Road
Garland, TX 75041

Dr. Lawrence J. Burdick
Woodward-Clyde Consultants
566 El Dorado Street
Pasadena, CA 91109-3245

Dr. Theodore Cherry
Science Horizons, Inc.
710 Encinitas Blvd, Suite 200
Encinitas, CA 92024 (2)

Dr. Kin-Yip Chun
Geophysics Division
Physics Department
University of Toronto
Ontario, CANADA M5S IA7

Dr. Paul M. Davis
Dept. Earth & Space Sciences
University of California (UCLA)
Los Angeles, CA 90024

Prof. Steven Day
Department of Geological Sciences
San Diego State University
San Diego, CA 92182

Ms. Eva Johannisson
Senior Research Officer
National Defense Research Institute
P.O. Box 27322
S-102 54 Stockholm, SWEDEN

Dr. Mark D. Fisk
Mission Research Corporation
735 State Street
P.O. Drawer 719
Santa Barbara, CA 93102

Prof. Stanley Flatte
Applied Sciences Building
University of California
Santa Cruz, CA 95064

Dr. Roger Fritzel
Pacific Sierra Research
1401 Wilson Blvd., Suite 1100
Arlington, VA 22209

Dr. Holly K. Given
Inst. Geophys. & Planet. Phys.
Scripps Inst. Oceanography (A-025)
University of California, San Diego
La Jolla, CA 92093

Prof. Hans-Peter Harjes
Institute for Geophysik
Ruhr University/Bochum
P.O. Box 102148
463 Bochum 1, FRG

Prof. Donald V. Helmberger
Seismological Laboratory
Div. of Geol. & Planetary Sciences
California Institute of Technology
Pasadena, CA 91125

Prof. Eugene Herrin
Prof. Brian Stump
Inst. for the Study of Earth and Man
Geophysical Laboratory
Southern Methodist University
Dallas, TX 75275

Prof. Bryan Isacks
Prof. Muawia Barazangi
Cornell University
Department of Geological Sciences
SNEE Hall
Ithaca, NY 14850

Prof. Lane R. Johnson
Prof. Thomas V. McEvilly
Seismographic Station
University of California
Berkeley, CA 94720

Robert C. Kemerait
ENSCO, Inc.
445 Pineda Court
Melbourne, FL 32940

Prof. Brian L.N. Kennett
Research School of Earth Sciences
Institute of Advanced Studies
G.P.O. Box 4
Canberra 2601, AUSTRALIA

Dr. Richard LaCoss
MIT-Lincoln Laboratory
M-200B
P.O. Box 73
Lexington, MA 02173-0073

Prof. Fred K. Lamb
Univ. of Illinois
Department of Physics
110 West Green Street
Urbana, IL 61801

Prof. Charles A. Langston
Geosciences Department
403 Deike Building
The Pennsylvania State University
University Park, PA 16802

Prof. Thorne Lay
Dr. Susan Schwartz
Institute of Tectonics
Earth Science Board
University of California, Santa Cruz
Santa Cruz, CA 95064

Prof. Arthur Lerner-Lam
Prof. Paul Richards
Prof. C.H. Scholz
Lamont-Doherty Geol. Observatory
of Columbia University
Palisades, NY 10964

Dr. Manfred Henger
Fed. Inst. for Geosci. & Nat'l Res.
Postfach 510153
D-3000 Hanover 51, FRG

Dr. Peter Marshall
Dr. Alan Douglas
Procurement Executive
Ministry of Defense
Blacknest, Brimpton
Reading FG7-4RS, United Kingdom

Dr. Randolph Martin, III
New England Research , Inc.
76 Olcott Drive
White River Junction, VT 05001

Dr. Bernard Massinon
Societe Radiomana
27 rue Claude Bernard
75005 Paris, FRANCE (2)

Dr. Gary McCartor
Prof. Henry L. Gray
Department of Physics
Southern Methodist University
Dallas, TX 75275

Dr. Keith L. McLaughlin
S-Cubed
P.O. Box 1620
La Jolla, CA 92038-1620

Dr. Pierre Mecheler
Societe Radioman
27 rue Claude Bernard
75005 Paris, FRANCE

Prof. Bernard Minster
Prof. John Orcutt
IGPP, A-025
Scripps Institute of Oceanography
University of California, San Diego
La Jolla, CA 92093

Prof. Brian J. Mitchell
Dr. Robert Herrmann
Dept. of Earth & Atmospheric Sciences
St. Louis University
St. Louis, MO 63156

Mr. Jack Murphy
S-Cubed
11800 Sunrise Valley Drive
Suite 1212
Reston, VA 22091 (2)

Dr. Jay J. Pulli
Radix Systems, Inc.
2 Taft Court, Suite 203
Rockville, MD 20850

Dr. Frode Ringdal
Dr. Svein Mykkeltveit
NTNF/NORSAR
P.O. Box 51
N-2007 Kjeller, NORWAY (2)

Mr. Wilmer Rivers, Jr.
Teledyne Geotech Alexandria Laboratory
314 Montgomery Street
Alexandria, VA 22314-1581

Dr. Richard Sailor
TASC, Inc.
55 Walkers Brook Drive
Reading, MA 01867

Prof. Charles G. Sammis
Prof. Kei Aki
Center for Earth Sciences
University of Southern California
University Park
Los Angeles, CA 90089-0741

Prof. David G. Simpson
Lamont-Doherty Geological Observatory
of Columbia University
Palisades, NY 10964

Dr. Stewart W. Smith
Geophysics AK-50
University of Washington
Seattle, WA 98195

Prof. Clifford Thurber
Prof. Robert P. Meyer
University of Wisconsin-Madison
Department of Geology & Geophysics
1215 West Dayton Street
Madison, WS 53706

Prof. M. Nafi Toksoz
Earth Resources Lab
Mass. Institute of Technology
42 Carleton Street
Cambridge, MA 02142

Prof. Terry C. Wallace
Dept. of Geosciences
Building #77
University of Arizona
Tucson, AZ 85721

Dr. William Wortman
Mission Research Corporation
8560 Cinderbed Road
Suite 700
Newington, VA 22122

## U.S. GOVERNMENT AGENCIES

Mr. Alfred Lieberman
ACDA/VI-OA, Room 5726
320 21st Street, N.W.
Washington, D.C. 20451

Colonel Jerry J. Perrizo
AFOSR/NP, Building 410
Bolling AFB
Washington, D.C. 20331-6448

Dr. Robert R. Blandford
AFTAC/CSS
1300 N. 17th Street, Suite 1450
Arlington, VA 22209

AFTAC/CA
(STINFO)
Patrick AFB, FL 32925-6001

Dr. Frank F. Pilotte
HQ AFTAC/TT
Patrick AFB, FL 32925-6001

Katie Poley
CIA-ACIS/TMC
Room 4X16NHB
Washington, D.C. 20505

Dr. Larry Turnbull
CIA-OSWR/NED
Washington, DC 20505

Dr. Ralph W. Alewine, III
Dr. Alan S. Ryall, Jr.
DARPA/NMRO
3701 N. Fairfax Drive
Arlington, VA 22303-1714 (7)

DARPA/OASB/Librarian
3701 N. Fairfax Drive
Arlington, VA 22303-1714

Dr. Dale Glover
DIA/DT-1B
Washington, D.C. 20301

Dr. Michael Shore
Defense Nuclear Agency/SPSS
6801 Telegraph Road
Alexandria, VA 22310

Dr. Max Koontz
U.S. Dept. of Energy/DP-5
Forrestal Building
1000 Independence Avenue
Washington, D.C. 20585

Defense Technical Information Center
Cameron Station
Alexandria, VA 22314 (2)

Dr. John J. Cipar, PL/GPEH
Dr. Anton W. Dainty
Phillips Lab/Geophysics Directorate
Hanscom AFB, MA 01731 (2)

James F. Lewkowicz, PL/GPEH
Phillips Lab/Geophysics Directorate
Hanscom AFB, MA 01731

Phillips Laboratory (PL/XO)
Hanscom AFB, MA 01731

Dr. James Hannon
Lawrence Livermore National Laboratory
P.O. Box 808
Livermore, Ca 94550 (2)

Office of the Secretary of Defense
DDR&E
Washington, D.C. 20330

Eric Chael
Division 9241
Sandia Laboratory
Albuquerque, NM 87185

Dr. William Leith
U.S. Geological Survey
Mail Stop 928
Reston, VA 22092

Dr. Robert Masse
Box 25046, Mail Stop 967
Denver Federal Center
Denver, CO 80225

Dr. Robert Reinke
WL/NTESG
Kirtland, AFB, NM 87117-6008